frontiers | Research Topics

Current advances in precision microscopy

Edited by
Rupert Ecker, Quan Nguyen, Jyotsna Batra
and Felicitas Mungenast

Published in
Frontiers in Medicine

ISSN 1664-8714
ISBN 978-2-8325-6060-0
DOI 10.3389/978-2-8325-6060-0

About Frontiers

Frontiers is more than just an open access publisher of scholarly articles: it is a pioneering approach to the world of academia, radically improving the way scholarly research is managed. The grand vision of Frontiers is a world where all people have an equal opportunity to seek, share and generate knowledge. Frontiers provides immediate and permanent online open access to all its publications, but this alone is not enough to realize our grand goals.

Frontiers journal series

The Frontiers journal series is a multi-tier and interdisciplinary set of open-access, online journals, promising a paradigm shift from the current review, selection and dissemination processes in academic publishing. All Frontiers journals are driven by researchers for researchers; therefore, they constitute a service to the scholarly community. At the same time, the *Frontiers journal series* operates on a revolutionary invention, the tiered publishing system, initially addressing specific communities of scholars, and gradually climbing up to broader public understanding, thus serving the interests of the lay society, too.

Dedication to quality

Each Frontiers article is a landmark of the highest quality, thanks to genuinely collaborative interactions between authors and review editors, who include some of the world's best academicians. Research must be certified by peers before entering a stream of knowledge that may eventually reach the public - and shape society; therefore, Frontiers only applies the most rigorous and unbiased reviews. Frontiers revolutionizes research publishing by freely delivering the most outstanding research, evaluated with no bias from both the academic and social point of view. By applying the most advanced information technologies, Frontiers is catapulting scholarly publishing into a new generation.

What are Frontiers Research Topics?

Frontiers Research Topics are very popular trademarks of the *Frontiers journals series*: they are collections of at least ten articles, all centered on a particular subject. With their unique mix of varied contributions from Original Research to Review Articles, Frontiers Research Topics unify the most influential researchers, the latest key findings and historical advances in a hot research area.

Find out more on how to host your own Frontiers Research Topic or contribute to one as an author by contacting the Frontiers editorial office: frontiersin.org/about/contact

Current advances in precision microscopy

Topic editors
Rupert Ecker — TissueGnostics GmbH, Austria
Quan Nguyen — The University of Queensland, Australia
Jyotsna Batra — Queensland University of Technology, Australia
Felicitas Mungenast — TissueGnostics GmbH, Austria

Citation
Ecker, R., Nguyen, Q., Batra, J., Mungenast, F., eds. (2025). *Current advances in precision microscopy*. Lausanne: Frontiers Media SA.
doi: 10.3389/978-2-8325-6060-0

Topic Editor R.E. is the CEO of TissueGnostic. Topic Editor F.M. is employed at TissueGnostic. The other Topic Editors declare no conflicts of interest in regards to the Research Topic subject.

Table of contents

05 Editorial: Current advances in precision microscopy
Rupert C. Ecker, Felicitas Mungenast, Quan Nguyen and Jyotsna Batra

08 Establishment and Verification of Neural Network for Rapid and Accurate Cytological Examination of Four Types of Cerebrospinal Fluid Cells
Luyue Jiang, Gang Niu, Yangyang Liu, Wenjin Yu, Heping Wu, Zhen Xie, Matthew Xinhu Ren, Yi Quan, Zhuangde Jiang, Gang Zhao and Wei Ren

16 Quantitative Characterization of Macrophage, Lymphocyte, and Neutrophil Subtypes Within the Foreign Body Granuloma of Human Mesh Explants by 5-Marker Multiplex Fluorescence Microscopy
Uwe Klinge, Axel Dievernich and Johannes Stegmaier

31 A dual decoder U-Net-based model for nuclei instance segmentation in hematoxylin and eosin-stained histological images
Amirreza Mahbod, Gerald Schaefer, Georg Dorffner, Sepideh Hatamikia, Rupert Ecker and Isabella Ellinger

42 Human intravital microscopy in the study of sarcomas: an early trial of feasibility
Emmanuel M. Gabriel, Kulkaew Sukniam, Kyle Popp and Sanjay P. Bagaria

50 Using quantitative single molecule localization microscopy to optimize multivalent HER2-targeting ligands
Devin L. Wakefield, Ottavia Golfetto, Raphael Jorand, Sunetra Biswas, Kassondra Meyer, Kendra N. Avery, Cindy Zer, Eliedonna E. Cacao, Steven J. Tobin, Ian J. Talisman, John C. Williams and Tijana Jovanovic-Talisman

62 Single cell analysis of the localization of the hematopoietic stem cells within the bone marrow architecture identifies niche-specific proliferation dynamics
Maria Mazzarini, Francesca Arciprete, Orietta Picconi, Mauro Valeri, Paola Verachi, Fabrizio Martelli, Anna Rita Migliaccio, Mario Falchi and Maria Zingariello

74 *In situ* veritas: combining omics and multiplex imaging can facilitate the detection and characterization of cell-cell interactions in tissues
Uwe Ritter

80 Trapalyzer: a computer program for quantitative analyses in fluorescent live-imaging studies of neutrophil extracellular trap formation
Michał Aleksander Ciach, Grzegorz Bokota, Aneta Manda-Handzlik, Weronika Kuźmicka, Urszula Demkow and Anna Gambin

92 Analysis of organoid and immune cell co-cultures by machine learning-empowered image cytometry
Philipp Stüve, Benedikt Nerb, Selina Harrer, Marina Wuttke, Markus Feuerer, Henrik Junger, Elke Eggenhofer, Bianca Lungu, Simina Laslau and Uwe Ritter

frontiers | Frontiers in Medicine

TYPE Editorial
PUBLISHED 18 February 2025
DOI 10.3389/fmed.2025.1561485

OPEN ACCESS

EDITED AND REVIEWED BY
Alice Chen,
Consultant, Potomac, MD, United States

*CORRESPONDENCE
Rupert C. Ecker
✉ rupert.ecker@tissuegnostics.com
Jyotsna Batra
✉ jyotsna.batra@qut.edu.au

RECEIVED 16 January 2025
ACCEPTED 30 January 2025
PUBLISHED 18 February 2025

CITATION
Ecker RC, Mungenast F, Nguyen Q and Batra J (2025) Editorial: Current advances in precision microscopy. *Front. Med.* 12:1561485. doi: 10.3389/fmed.2025.1561485

Editorial: Current advances in precision microscopy

Rupert C. Ecker[1,2,3,4]*, Felicitas Mungenast[4], Quan Nguyen[5] and Jyotsna Batra[1,2,3,6]*

[1]Translational Research Institute, Queensland University of Technology, Brisbane, QLD, Australia, [2]School of Biomedical Sciences, Faculty of Health, Queensland University of Technology, Brisbane, QLD, Australia, [3]ARC Training Centre for Cell and Tissue Engineering Technologies (CTET), Queensland University of Technology, Brisbane, QLD, Australia, [4]TissueGnostics GmbH, Vienna, Austria, [5]Institute for Molecular Bioscience, The University of Queensland, Brisbane, QLD, Australia, [6]Centre for Genomics and Personalised Health, Queensland University of Technology, Brisbane, QLD, Australia

KEYWORDS

precision microscopy, image cytometry, organoid, single cell analysis, multiplexing, intravital microscopy, deep learning, machine learning

Editorial on the Research Topic
Current advances in precision microscopy

The field of precision microscopy has undergone a transformative evolution, driven by the integration of advanced imaging techniques, multiplex staining methods, as well as the application of computer vision techniques in artificial intelligence (AI) for image analysis. These innovations are not only enhancing our ability to visualize and analyze biological samples with unprecedented precision but are also paving the way for significant advancements in personalized medicine and precision diagnostics. The articles in this Research Topic collectively highlight the cutting-edge developments in precision microscopy, showcasing how these technologies are being leveraged to gain deeper insights into cellular and molecular processes, improve diagnostic accuracy, and ultimately, contribute to better clinical outcomes.

From the development of high-throughput imaging platforms that integrate machine learning algorithms for the analysis of 3D organoids and immune cell co-cultures, to the creation of novel software tools like Trapalyzer for the quantitative analysis of neutrophil extracellular trap formation, the advancements in precision microscopy are revolutionizing the way we study and understand complex biological systems across millions of cells, through 2D to 3D tissue spatial dimensions, incorporating temporal aspects. The integrative analyses of omics data and multiplex imaging, as discussed in one of the opinion articles, exemplifies the potential of these integrated approaches to provide a comprehensive understanding of cellular communication and its implications for disease progression and treatment.

The application of advanced light and fluorescence microscopy techniques, such as super-resolution microscopy and single-molecule imaging, is enabling researchers to visualize cellular processes with remarkable detail, aiding in the mechanistic understandings required for the development of targeted therapies. The integration of machine learning and deep learning techniques is further enhancing the accuracy and automation of biomarker identification and disease state analysis. Furthermore, multiplex staining methods are allowing for the simultaneous detection of multiple biomarkers, significantly improving the diagnostic capabilities at the molecular level.

The collective contributions of these articles underscore the transformative potential of precision microscopy in advancing our understanding of biological systems and improving clinical outcomes. By leveraging cutting-edge technologies and interdisciplinary approaches, researchers are making significant strides toward the realization of precision medicine. The integration of advanced imaging techniques, multiplex staining methods, and AI-driven analysis for patient samples, pre-clinical models and *in vitro* cell cultures is not only enhancing our ability to visualize and analyze biological structures with unprecedented precision but is also paving the way for significant advancements in personalized medicine and precision diagnostics.

As we continue to push the boundaries of what is possible with precision microscopy, it is essential to foster global collaboration, implement rigorous governance, and address ethical dilemmas head-on. By doing so, we can harness the full potential of these technologies for societal benefit, ensuring that precision microscopy aligns with humanity's highest aspirations. The future of precision microscopy is bright, and with continued innovation and interdisciplinary engagement, we are poised to make groundbreaking discoveries that will shape the future of medicine and healthcare.

1. Analysis of organoid and immune cell co-cultures by machine learning-empowered image cytometry.

This study presents a high-throughput imaging analysis platform that integrates automated imaging techniques and advanced image processing tools to analyze 3D organoids in co-cultures with immune cells (Stüve et al.). By employing machine learning algorithms, the platform can accurately identify and classify organoids, facilitating the study of organ development, immune disorders, and drug discovery.

2. Single cell analysis of the localization of the hematopoietic stem cells within the bone marrow architecture identifies niche-specific proliferation dynamics.

The publication combines flow cytometry with confocal microscopy and image analysis to investigate the location as well as the dynamics of HSCs (Mazzarini et al.). The results indicate that in aged mice, hematopoietic stem cells exhibit highly dynamic cycling and show a preference for interactions within the niche that directs their differentiation.

3. *In situ* Veritas: Combining omics and multiplex imaging to facilitate the detection and characterization of cell-cell interactions in tissues.

This opinion article discusses the potential of combining omics data with multiplex imaging to detect and characterize cell-cell interactions within tissues (Ritter). Such an approach can provide a comprehensive understanding of cellular communication and its implications for disease progression and treatment.

4. Human intravital microscopy in the study of sarcomas: an early trial of feasibility.

This brief report highlights the successful utilization of real-time intravital microscopy during the surgical removal of large sarcomas (Gabriel et al.). This method gives critical and immediate insight into data such as tumor vessel characteristics as well as their potential impact on administration and effectiveness of drug treatments.

5. Using quantitative single molecule localization microscopy to optimize multivalent HER2-targeting ligands.

This publication investigates the effect of different treatment regimens in cultured breast cancer cells on the organization of HER2 receptor (Wakefield et al.). The group used super-resolution microscopy in combination with other techniques to spatially analyse HER2 distribution. These findings give valuable new insights and may improve treatment strategies for HER+ breast cancer patients.

6. Trapalyzer: A computer program for quantitative analyses in fluorescent live-imaging studies of neutrophil extracellular trap formation.

Trapalyzer is a novel software tool designed for the quantitative analysis of neutrophil extracellular trap (NET) formation in live-imaging studies (Ciach et al.). This tool enhances the precision of NET quantification, providing valuable insights into the role of neutrophils in immune responses and inflammatory diseases.

7. A dual decoder U-net-based model for nuclei instance segmentation in hematoxylin and eosin-stained histological images.

The publication is introducing a dual decoder U-Net-based model for the segmentation of nuclei stained by hematoxylin in histological tissue images (Mahbod et al.). This algorithm is showing excellent segmentation performance and is the top-ranked method in the MoNuSAC post-challenge leaderboard.

8. Quantitative characterization of macrophage, lymphocyte and neutrophil subtypes within the foreign body granuloma of human mesh explants by 5 marker multiplex fluorescence microscopy.

This study emphasizes the potential for detailed characterization and spatial distribution analysis of immune phenotypes at inflammatory sites caused by surgical mesh (Klinge et al.). It offers insights into the complex interactions within this process and may contribute to the development of new treatment strategies.

9. Establishment and verification of neural network for rapid and accurate cytological examination of four types of cerebrospinal fluid cells.

This study introduces a deep neural network (DNN) for counting and classifying cerebrospinal fluid (CSF) cells,

improving diagnostic efficiency (Jiang et al.). Using May-Grünwald-Giemsa stained images, the DNN accurately identifies key cell types and outperforms expert examination with 95% accuracy and an 86% reduction in turnaround time. The results demonstrate the potential of DNN classifier in clinical CSF cytology.

This Research Topic on *Current advances in precision microscopy* provides a snapshot of technological development in a highly innovative and vibrant scientific environment. We hope that this Research Topic will help spread the excitement the authors share with regards to this Research Topic and we wish our readers an insightful read!

Author contributions

RE: Conceptualization, Project administration, Supervision, Writing – original draft, Writing – review & editing. FM: Supervision, Writing – review & editing. QN: Supervision, Writing – review & editing. JB: Conceptualization, Supervision, Writing – original draft, Writing – review & editing.

Conflict of interest

RE and FM were employed by TissueGnostics GmbH.

The remaining authors declare that the research was conducted in the absence of any commercial or financial relationships that could be construed as a potential conflict of interest.

Publisher's note

frontiers in Medicine

ORIGINAL RESEARCH
published: 24 January 2022
doi: 10.3389/fmed.2021.749146

Establishment and Verification of Neural Network for Rapid and Accurate Cytological Examination of Four Types of Cerebrospinal Fluid Cells

Luyue Jiang[1], Gang Niu[1], Yangyang Liu[1], Wenjin Yu[2], Heping Wu[1], Zhen Xie[2], Matthew Xinhu Ren[3], Yi Quan[1,4], Zhuangde Jiang[5], Gang Zhao[2]* and Wei Ren[1]**

[1] Electronic Materials Research Laboratory, School of Electronic Science and Engineering, The International Joint Laboratory for Micro/Nano Manufacturing and Measurement Technology, Xi'an Jiaotong University, Xi'an, China, [2] The College of Life Sciences and Medicine, Northwest University, Xi'an, China, [3] Biology Program, Faculty of Science, The University of British Columbia, Vancouver, BC, Canada, [4] School of Microelectronics, Xidian University, Xi'an, China, [5] The State Key Laboratory for Manufacturing Systems Engineering, The International Joint Laboratory for Micro/Nano Manufacturing and Measurement Technology, Xi'an Jiaotong University, Xi'an, China

OPEN ACCESS

Edited by:
Kuanquan Wang,
Harbin Institute of Technology, China

Reviewed by:
Dimitrios Tamiolakis,
University of Crete, Greece
Chunpeng Wu,
Duke University, United States

***Correspondence:**
Gang Niu
gangniu@xjtu.edu.cn
Gang Zhao
zhaogang@nwu.edu.cn
Wei Ren
wren@xjtu.edu.cn

Specialty section:
This article was submitted to Precision Medicine, a section of the journal Frontiers in Medicine

Received: 29 July 2021
Accepted: 09 December 2021
Published: 24 January 2022

Citation:
Jiang L, Niu G, Liu Y, Yu W, Wu H, Xie Z, Ren MX, Quan Y, Jiang Z, Zhao G and Ren W (2022) Establishment and Verification of Neural Network for Rapid and Accurate Cytological Examination of Four Types of Cerebrospinal Fluid Cells. Front. Med. 8:749146. doi: 10.3389/fmed.2021.749146

Fast and accurate cerebrospinal fluid cytology is the key to the diagnosis of many central nervous system diseases. However, in actual clinical work, cytological counting and classification of cerebrospinal fluid are often time-consuming and prone to human error. In this report, we have developed a deep neural network (DNN) for cell counting and classification of cerebrospinal fluid cytology. The May-Grünwald-Giemsa (MGG) stained image is annotated and input into the DNN network. The main cell types include lymphocytes, monocytes, neutrophils, and red blood cells. In clinical practice, the use of DNN is compared with the results of expert examinations in the professional cerebrospinal fluid room of a First-line 3A Hospital. The results show that the report produced by the DNN network is more accurate, with an accuracy of 95% and a reduction in turnaround time by 86%. This study shows the feasibility of applying DNN to clinical cerebrospinal fluid cytology.

Keywords: neural network, white blood cell, cerebral spinal fluid, classification, clinical, image recognition

INTRODUCTION

The central nervous system (CNS) is one of the most crucial systems in the human body. One important aspect of the CNS is the cerebral spinal fluid (CSF), which is typically sterile and only contains around 1–5 white blood cells (WBCs) per microliter (μl) under normal conditions. Many neurological diseases cause changes in cerebrospinal fluid cytology, especially in infectious diseases of the nervous system. When perturbed by an infectious disease, the human body responds by increasing WBC population leading to an inflammation of the CNS, which leads to increased mortality and morbidity if not correctly diagnosed and properly treated. The global burden of CNS infections in 2016 was tabulated in a recent study (1) and estimated to be 9.4 million incidences with a mortality rate of 5% or 458,000 deaths annually. With such a high clinical priority and impact, there is always a need for improvement on the aspect of rapid diagnose for CNS infection.

The current diagnostic method for CNS infections consists of a series of tests, such as CSF test, culturing, and gram staining. In developing countries, the sensitivity of culturing and gram staining is low (2). CSF test is the most commonly used and includes several crucial key factors, such as cell counting, cell staining, and cell identification. Treatment usually begins at the onset of signs of CNS inflammation, immediately after the cell count and differential cell count become abnormal. This WBC identification is typically achieved with the May-Grünwald-Giemsa (MGG) staining of the CSF, which stains the nucleus and granules of the WBCs. In the case of one of the biggest hospitals in the northwestern region in China where this study is conducted, the hospital annually treats 120,000 outpatients with neurological diseases and among these, 4,000 patients are suspected of CNS infections (3). Because of this number, the hospital employs a large number of resources with an estimated 10 working hours per day dedicated just for CSF cell counting, cell staining, and cell identification alone.

Recent years have seen the boon of machine learning for analyzing large datasets and in particular, deep neural network (DNN) has been used to help to analyze and differentiate red blood cells (RBCs) and WBCs in whole blood (4–10). These studies imply different tactics, such as image segmentation, clustering, thresholding, local binary pattern, and edge detection (6). However, the initial implementation of these strategies for this application resulted in low clinical accuracies, thus accommodating a more generalized model, a generic object-detection neural network, such as region-based convolutional neural network (R-CNN), was explored and found to be more successful (11). To date, there have not been any studies for WBC differentiation in CSF using any machine-learning algorithms to the best of our knowledge.

In this study, the objective is to explore the feasibility of letting DNN to completely replace the currently employed manual labor leading to significant improvement in cell counting accuracy and cost savings. DNN is utilized in the differentiation of lymphocyte, monocyte, neutrophil, and erythrocytes for CNS inflammation diagnosis. To highlight how DNN accomplishes this, there are three main pillars presented in this study: (1) systematic validation of the DNN to confirm the similar quality of care to current standards, (2) analysis of accuracy and precision in automation, and (3) analysis of time savings if applied to the real case. The data reported in the present study are expected to greatly improve patient care when it comes to the diagnosis of infectious CNS diseases.

MATERIALS AND METHODS

MGG Staining Procedure and OM Capture Details

Patients suspected of CNS inflammation had their CSF drawn from a typical lumbar puncture, where usually 10 ml of CSF was collected. The CSF was then split into two parts: (1) for cell count, 10 μl of CSF was dropped onto a hemocytometer and cells were counted, (2) based on the cell count, a proportional amount of CSF was used in the cytocentrifuge, and the cells were concentrated onto a microscope slide. MGG staining was done by first taking the microscope slide out and fixing them with acetone-formaldehyde. After they were fixed, the slides were stained with an MGG staining kit. The samples were then observed under a normal optical microscope (Leica DM2500) with the 20× lens used first to get a general idea of the patient's condition. Additional 100× images were subsequently taken when particular cells of interest were located; these 100× images were the type sent to the DNN for training and testing. Afterward, the fixed microscope slides were preserved in a sample bank in case of future analysis.

Preprocessing

All images were taken using an optical microscope (Leica DM2500) with the 100× lens. Images are in the format of 8-bit JPEG. Each image was individually labeled with the type of each cell using an open-source software called Labellmg (12) by trained technicians with cell identification experience of 10 y. The Labellmg also helps to establish spatial locations of each cell by the function of the "user draw boxes". Then, the saturation, the contrast, and the brightness of all images were randomly adjusted. All images were also randomly horizontally flipped.

Training and Inference

Model training was performed in Python 3.6 and TensorFlow 1.14 using two NVIDIA 2080Ti 11 GB graphics processing units. Models were based on the Faster R-CNN architecture. The DNN software is a region-based convolution neural network (CNN) so it has great edge detection capability. It uses label mapping to separate labeled areas from the non-labeled background areas. Labeled images were split into two sections with a ratio of 9:1 and were separately put into the training and the testing folders, respectively. Model weights were initialized with weights pre-trained on the COCO database. Models were trained for 4-way classification (lymphocytes, monocytes, neutrophils, and RBCs). The RMSprop optimizer was used with a softmax loss and an exponential decay rate schedule with an initial learning rate of 0.001. Models were trained for 32,000 steps. The batch size was 4 and the Intersection over Union (IOU) threshold was 0.5. The model for each training episode was selected based on the PASCAL VOC detection metrics on the validation set. Predictions were averaged across all models and all cell images to produce a final prediction for each case. An external test set comprised of images from the rest of the dataset was used to evaluate the generalization performance of the model. Preprocessing scripts were written in Python to organize the data for utilization in TensorFlow. And the training was done until the loss function was saturated and observed *via* Tensorboard. Once the newly trained model was frozen, validations were done on the test image folder and compared with the ground truths of the trained technicians. After a reasonable accuracy was achieved, additional unlabeled images were evaluated with the frozen DNN model. For the training process of the DNN, 1,300 images, which include around 30,000 cells, were individually labeled and fed into the program.

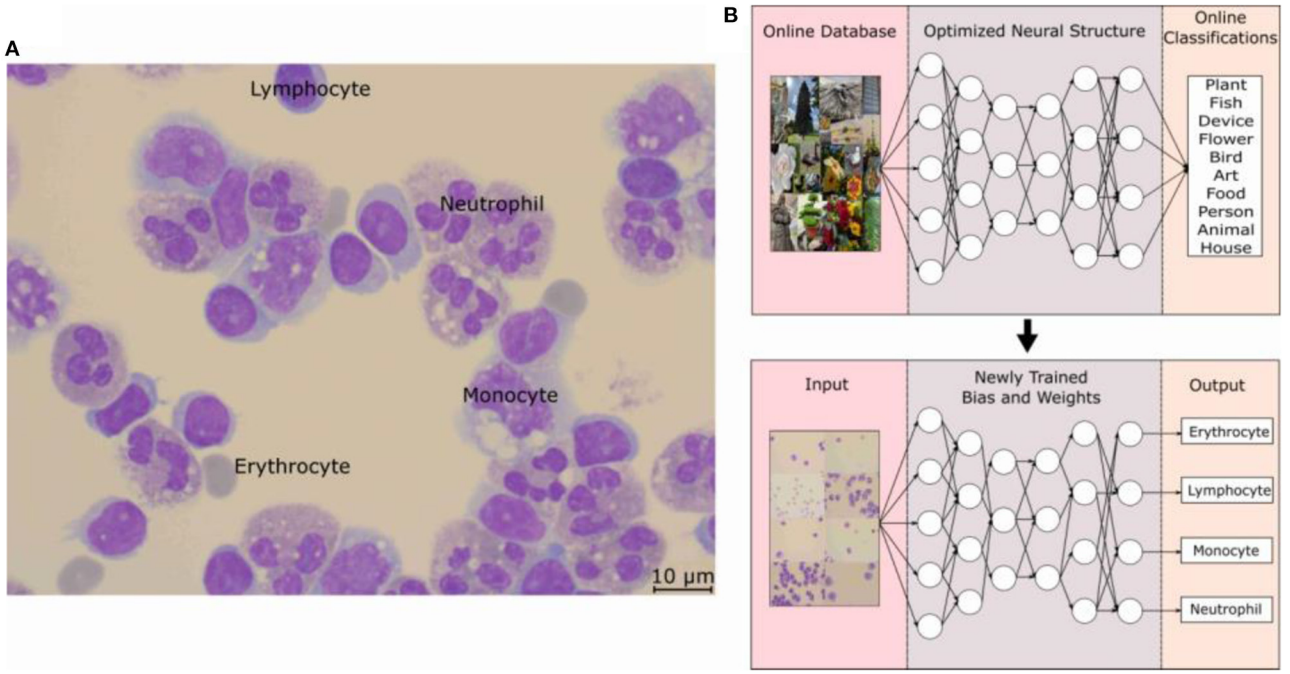

FIGURE 1 | (A) Optical microscope image taken at 100× with a scale bar of 10 μm. Cells were fixed and stained with MGG, which provides a light color to the cytoplasm of the cell and purple color to the lobes of the nucleus. Labels for the three WBCs and the RBCs can be seen in the picture. **(B)** Schematic of how the object-detection DNN model is trained to form its basic architecture. The model structure is Faster R-CNN with an initial learning rate of 0.001, a batch size of 4, and an IOU threshold of 0.5. The structure along with an online database was used to train the DNN model and then with the basic architecture, the weights and biases are optimized for the MGG-stained cell images of each classification. MGG, The May-Grünwald-Giemsa; DNN, deep neural network; RBC, red blood count; WBC, white blood cell.

RESULTS/DISCUSSION

Validating the DNN

The application of the DNN in this study is in the identification of the 4 main types of cells found in infectious CNS disease patients' CSF. The four main types of cells typically found are lymphocyte, monocyte, neutrophil, and erythrocytes. When a doctor suspects a CNS infection, the routine procedure of lumbar puncture is done and CSF is withdrawal from the patient, which will be stained for clear cell identification by the hospital technicians. The MGG staining provides a red acidic stain, a blue basic stain, and a purple color for cellular components (13, 14). This effectively gives the RBCs a dark gray or red-pink color, the WBCs a blue color with the lymphocyte a distinctive singular round purple nucleus, the monocyte with a large and bean-shaped purple nucleus, and finally the neutrophil with multi-lobed purple-colored nucleus (15). An example of MGG staining is shown in **Figure 1A**, where all four types of cells can be seen from CSF for one patient.

The DNN model employed for this study is based on an object-detection image-based neural network built on the TensorFow and pre-trained on the COCO dataset (16). The basics of a neural network can be considered as a repeating algorithm that classifies the importance of an input based on an activation function. An activation function is similar to the action potential of a human neuron cell, where a necessary stimulus causes the firing of the neuron, which is an all-or-nothing process. This is analogous to artificial neural networks where the activation function is a mathematical threshold value and once that is met, the result is similar to the firing of a human neuron. There are additional nuances to this mathematical equation with a coupling of weights and bias values, and the resultant firing is not a step function, but a specialized mathematical function containing in-between 0 and 1 activation values; an example is the sigmoid function. However, the main concepts translate to the idea that only the important characteristics of an image will be filtered through this activation function with each of these characteristics being represented as a neuron in one layer of the neural network. The addition of multiple layers gives rise to the non-linearly of a DNN and these features allow a DNN to recognize an image, similar to mimicking the image processing of a human brain. Coupled with the introduction of CNN, the processing requirement for image-based neural networks dropped significantly, paving the way for large advancements in the field (17). However, the detailed description and workings of each of these improvements are beyond the scope of this study, and a sample of this literature can be found in References. (11, 18, 19).

The application of the DNN to recognize WBCs and RBCs was made possible by first applying the pre-trained DNN to a database of optical microscope (OM) images labeled by doctors for each cell classification. The specifics of the Faster R-CNN

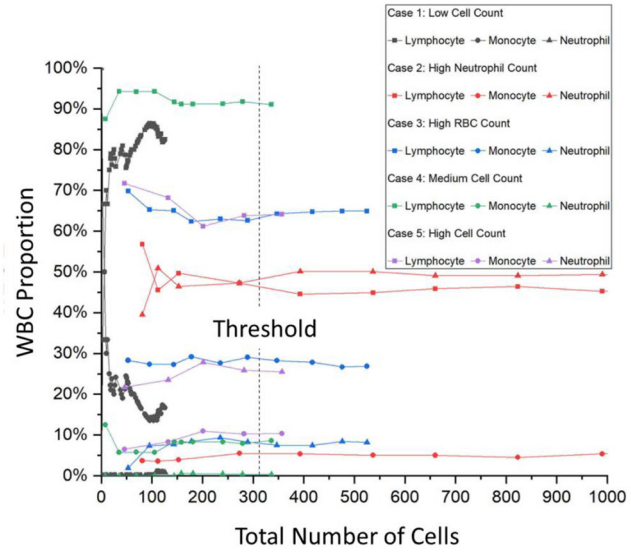

FIGURE 2 | A trend graph of the number of cells per patient needed for certain patient condition examples. It can be seen that after a certain amount of cells, the percentage of the WBC type saturates thus determining the number of cells needed for a successful and accurate hospital report. This trend graph shows that on average, 315 cells are needed with even the onset of saturation starting at around 150 cells. WBC, white blood cells.

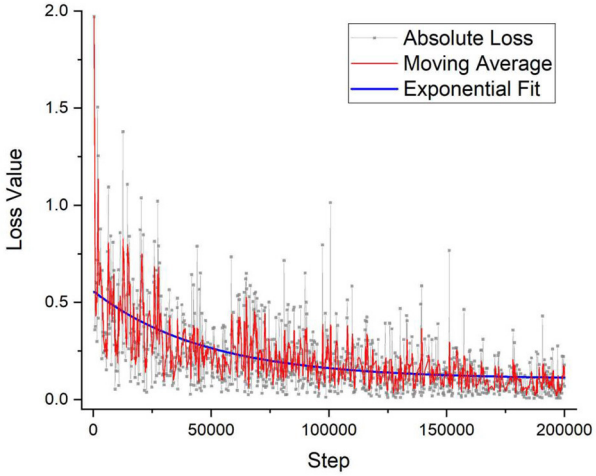

FIGURE 3 | The DNN model's training accuracy shows its precision vs. the number of iteration steps. As can be seen that the graph takes on a 1/x, asymptotic relationship with saturation quickly established within the first few thousand steps. After 200,000 iterations, the precision % has not improved that much and the training of the model stopped, which took around 2 days of nonstop training. DNN, deep neural network.

TABLE 1 | The number of cells labeled in the validation dataset between human and AI for each cell type.

	Erythrocyte	Lymphocyte	Monocyte	Neutrophil
Human				
Person 1	13	66	67	41
Person 2	12	43	48	40
Person 3	20	77	70	43
Person 4	27	80	73	54
Human std dev	7	17	11	6
DNN				
Round 1	28	77	66	50
Round 2	28	77	66	50
Round 3	28	77	66	50
Round 4	28	77	66	50
AI Std Dev	0	0	0	0

model used can be found in this study (11, 19) and the training on the open-source image database, COCO by Microsoft (16), allowed for a DNN architecture to handle the complexities of the various cell types. As can be seen in **Figure 1B**, this pre-trained DNN model has already predetermined the number of layers, and neurons are needed for an optimal score of the COCO database and by carrying out a process of transfer learning (20), this model has re-trained itself by adjusting its weights and biases for MGG-stained cell images. The specific structure of the DNN model is Faster R-CNN, and an initial learning rate was 0.001, the batch size was 4, and the IOU threshold was 0.5.

The typical hospital protocol in WBC type classification involves checking around 200 cells per patient. This is known as the cell classification step and it is one of the most time-consuming processes for the hospital. As can be seen in **Supplementary Table 1**, there are significant numbers of patients the hospital handles daily and as such, the hospital has the CSF Cytology Department to devote half-day daily to handle the suspected CSF samples. According to the hospital, the 200 cell minimum is an arbitrary standard set a while ago without much scientific basis but has not led to failure. As such, an objective study was also done to determine the minimum number of cells needed per patient and also to determine the minimum number of images needed to be taken per patient. **Figure 2** shows the result of this focused study where only the three main WBC types are compared with the total number of cells identified per patient. For a typical hospital CSF cytology report, the doctors base their diagnosis on the percentage of these WBCs. The CSF Cytology Department has stored cytological smears of more than 100,000 patients in the last 10 y. Among these cytological smears diseases, 5 different cases can be categorized: (1) low WBC count (W = 0–4), (2) high neutrophil cell count, (3) high RBC count, (4) medium WBC count (W = 5–50), and 5) high WBC count (W $\geq$ 50). According to the characteristics of these types, we selected the corresponding cytological smears. Then we collected OM images of cells on each smear to analyze the threshold number of cells and the percentage of each cell type and subsequently to determine the required collecting cell number for each smear.

For Case 1, the low cell count typically means that the CSF of the patient is within the normal range and that the symptoms exhibited by the patient are from a different cause. However, Case 1 also has another difficulty where the entire cytospin sample contains typically <200 cells. As can be seen in **Figure 2**, the gray curves depict this, and the saturation of the curves is not met. For

Cases 2–5, there are enough cells present and **Figure 2** shows that saturation of the curves occurs after 315 cells are labeled. This number was calculated from an average of all the curves and from interpolations between data points after the minimum condition of saturation occurred. The onset of saturation can also be seen around 150 cells, but the error margin of 5% can be calculated.

For the training of the DNN, 100× OM images were taken, and every cell in each image was labeled by a trained technician and cross-checked with specialized doctors. For the training process of the DNN, 1,300 images or around 30,000 cells were individually labeled and fed into the program. To verify the effectiveness of the training process, **Figure 3** shows the loss value plotted against the number of iterations. The lower the value of the loss function indicates the more fully trained the DNN model. The loss function has become to an absolute limit of 0, which indicates that the model is perfectly trained. Generally, all DNN models are given trained values with a certain amount of noise, or in this case, a variety of images of different situations, so that the DNN can have the flexibility and not be over-fitted to a degree that it cannot identify images perfectly matching its initial training dataset. **Figure 3** shows the output loss values in gray along with a moving average for a better visual representation of the graph. An exponential decay function is also fitted to highlight the saturation of the loss function. The training of this DNN took around 200,000 iterations and around 2.5 days. However, once a DNN is trained, it requires only around 7 s for an output.

The Precision of the Neural Network

Besides merely relying on the loss function plot, a cross-check of the validation was performed to verify the accuracy of the DNN model. A certain portion of the image dataset was kept from training as the testing validation set, and the ratio amount chosen was 9:1. For comparison, four trained technicians were also arranged to label the same validation dataset, and then their results were compared with the DNN's prediction. **Table 1**

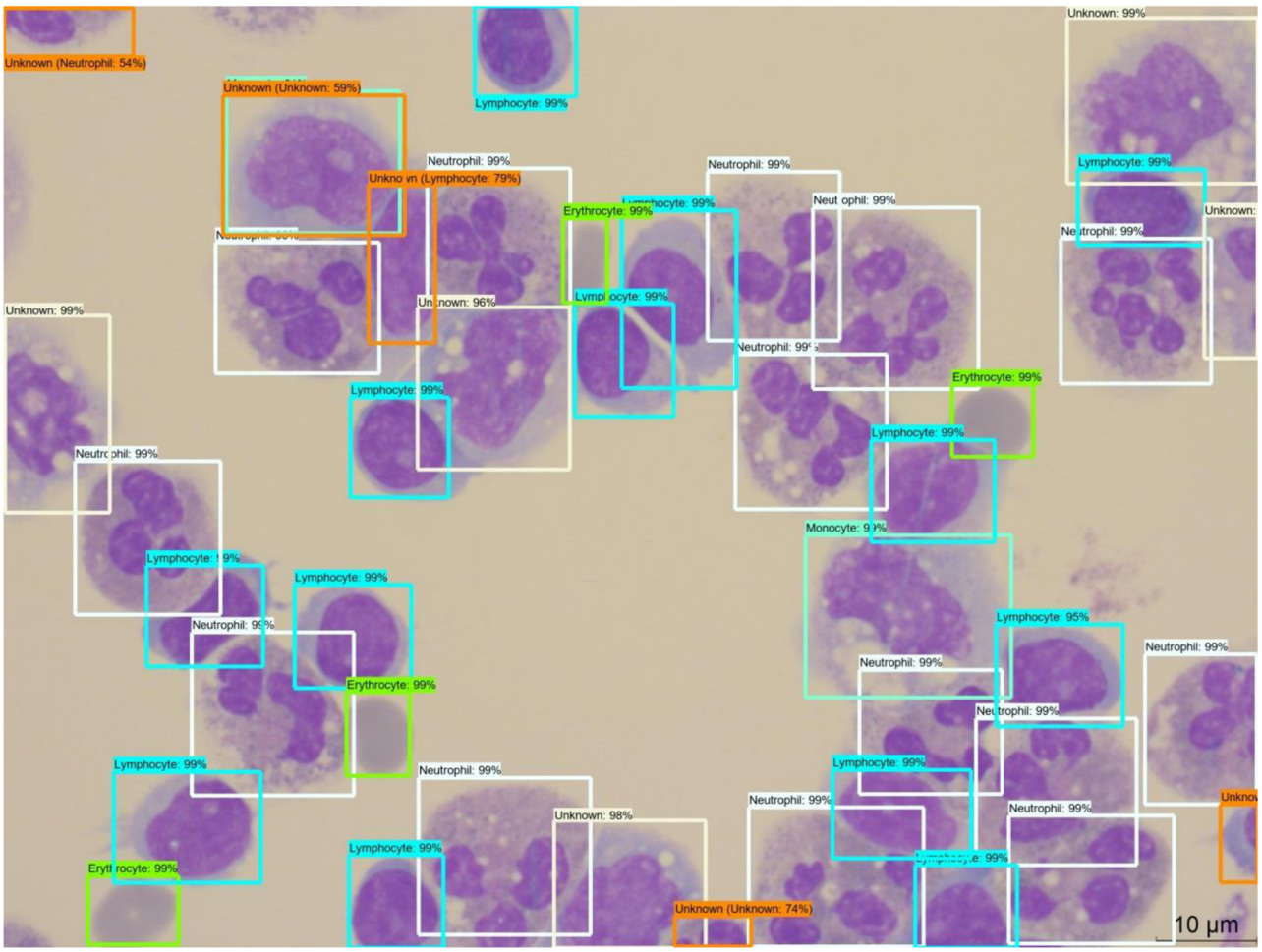

FIGURE 4 | An example output of the DNN model with boxed labels along with the model's percentage prediction. One can see the predicted outputs of neutrophil, monocyte, lymphocyte, and erythrocyte with their respective colors along with the DNN model's percentage prediction. In addition, some cells are labeled with the "unknown" label tag (tan and orange boxes) when the prediction percentage is below 80% or when the shape of the cell indicates a possibility of a rare cell type (i.e., basophil, eosinophil, mitotic, etc.). DNN, deep neural network.

TABLE 2 | Blind testing results of the DNN vs. the Hospital Diagnosis Report.

	% Lymphocyte	% Monocyte	% Neutrophil
Hospital Technician			
Patient 1 (ID# 190931)	5	3	92
Patient 2 (ID# 191155)	1	7	91
Patient 3 (ID# 191172)	18	23	59
Patient 4 (ID# 191158)	87	6	7
DNN			
Patient 1 (ID# 190931)	7	18	75
Patient 2 (ID# 191155)	4	7	90
Patient 3 (ID# 191172)	27	20	53
Patient 4 (ID# 191158)	89	8	3
Comparison Between Human vs AI			
Patient 1 (ID# 190931)	2	16	16
Patient 2 (ID# 191155)	3	0	1
Patient 3 (ID# 191172)	9	3	6
Patient 4 (ID# 191158)	2	2	3
Average Difference	4	5	7

TABLE 3 | The time-saving potential when compared between the DNN and hospital technician.

	Average time per day (mins)	Average time per patient (mins)	%
Hospital technician			
Cell classification	211 ± 25.3	13.4 ± 0.86	N/A
Report writing	70 ± 13.4	4.4 ± 0.20	N/A
Total time	281 ± 38.5	17.8 ± 0.92	N/A
DNN			
Cell classification	34 ± 4.5	2.2 ± 0.04	N/A
Report writing	3 ± 0.3	0.2 ± 0.00	N/A
Total time	37 ± 4.8	2.4 ± 0.04	N/A
Time saved	243 ± 38.8	15.5 ± 0.92	86 ± 4

DNN, deep neural network.

shows the labeling results of the validation dataset comparing the variations between the human labeling and the labeling of the DNN. The immediate takeaway is the confirmation that the multiple evaluation rounds of the DNN will produce the same result, however, that is not always the case. As can be seen in **Supplementary Figure 1**, there is a possibility for the DNN within the same validation round and with the same model version to produce two different image labeling outputs. In this case, the four validation rounds did not produce any variations. The other interesting factor comes from the human side with SD among the technicians producing large variability. However, such inaccuracy is suitable in the clinical setting where speed is more important and the WBC typing percentage can have a swing of ± 10% as the MGG cell classification report is only one of the many diagnostic tests typically done in series on a patient's CSF. This further shows the importance of implementing artificial intelligence (AI) in cell classification to improve the accuracy of the clinical results to reduce the reliance on subsequent tests in aiding the diagnosis of the doctor.

There are two outputs of the DNN program: (1) a labeled image with each DNN-recognized cell boxed with its prediction percentage, and (2) a report with the statistics of the recently run evaluation. An example of the output image can be seen in **Figure 4** where the four major cell types are labeled by the DNN program. The program puts a predicted boxed area around the target cell and then gives each cell a classification prediction percentage. If that percentage falls under 80%, then the program will instead add another orange box over the original label and give it the label "unknown" so that a human technician can manually check the cell. Moreover, the cells that the program outputs the light brown boxes correspond to the "unknown" label, which is the more rare cell types (lymphoid, mitotic, basophil, etc.) and these will require the human technicians to check them as well. While the spatial location is innovative, it has not been widely used for common diagnosis reports, the percentage of WBC types is important for diagnosis, and the program calculates and outputs a statistical report of the three major WBC types.

Accuracy of the Neural Network

To determine the effectiveness of the DNN in a real-world application setting, a blind test was performed and the comparison can be found in **Table 2**. During the blind test, the images were taken by operators without knowledge of the hospital report and given to a DNN operator, without any patient information except their ID number. The ID number is scrambled with the key being kept by a third party. From **Table 2**, the average differences show that the DNN model is fairly accurate when compared with the hospital report with the largest margin of error in cell classification with neutrophil and the largest patient variability with Patient #1. Overall, the DNN was able to handle the various infectious disease cases presented to it, they are as follows: (1) high neutrophil count, (2) high RBC count, (3) even distribution of WBC types, and (4) high lymphocyte count. The average accuracy of this DNN for these three WBC types is 95%. Compared to similar studies done on whole blood, our result is on similar levels of accuracy (6–8, 10). In addition, the average accuracy of this DNN is similar to these three WBC types of the same patient. Patient #2 provides a sample with a high neutrophil count. For Patient #2, the average error of this DNN for these three WBC types is minimal, i.e., only ∼1.3%. For Patient #3 with a close amount of three WBC types, the average error of this DNN for these three WBC types is ∼6%. In addition, for Patient #4 with a high lymphocyte count, the average error of this DNN for these three WBC types is ∼2.3%. For Patients #2–4, the error of this DNN for monocytes is minimal compared to those of lymphocytes and neutrophils. However, for Patient #1, neutrophils and monocytes showed large recognition errors. Upon closer inspection of the data discrepancy for Patient #1, it was found that the DNN had not previously encountered abnormal neutrophil images during its training phase. These abnormal neutrophil pictures had the individual nuclei lobes clustered together into a similar shape of the monocyte nuclei producing a false negative result; an example of this can be seen in **Supplementary Figure 2**.

These misclassifications led to the uneven monocyte/neutrophil percentage and thusly incorrect report. To better apply the DNN for future clinical situations, the training regime will have more of an emphasis on the number of patients trained rather than the number of cells trained for each cell classification to account for the complex clinical patient situations.

Time-Saving Potential

One of the main advantages of using the DNN program to replace the mundane task of cell type labeling is the time savings for the doctors so that their attention can be more focused on other tasks. To quantify these time savings, a short survey was conducted during a working week to estimate the time committed on each patient and daily basis. An example of the complete survey can be found in **Supplementary Table 1**, **Table 3** shows the time required by the hospital personnel for the two time-saving procedures that the DNN can contribute: 1) cell classification and 2) report writing. As can be seen in **Table 3**, the DNN can save around 16 min per patient and around 4 h per day; this amounts to a doctor time reduction of 86% daily. The DNN time was calculated from the validation dataset and extrapolated with an average number of patients from the short survey. The minimum number of cells per patient, extrapolated from **Figure 2**, and the average number of cells per image were also factors used. In addition, the DNN processing time required per image was also found to be independent of the number of cells present, with processing time slowing down as heat became more difficult to dissipate from the machine.

CONCLUSION

This study presents a pioneering application of image-based DNNs to patient samples in a clinical setting. Image analysis of MGG-stained patient samples is done for CSF cytology. By applying neural network technology to the clinical space of cell-type classification, a significant saving in time has been achieved. The daily saving in the time spent counting cells of hospital technicians is estimated to be approximately 86 $\pm$ 4%. DNN further rendered more consistent analyses capability against the large variability common to human classification analyses. Blind tests result in an average accuracy of 95% among the three WBC types, with the addendum being that the accuracy of the program can always be improved further with additional training from a wider variety of patients. This report clearly demonstrates the promise of DNN in clinical practices pertaining to infectious diseases of the CNSs.

DATA AVAILABILITY STATEMENT

The raw data supporting the conclusions of this article will be made available by the authors, without undue reservation.

ETHICS STATEMENT

This article does not contain any studies with human participants or animals performed by any of the authors. No modifications were done to this procedure, patients received routine care, and everything was approved in accordance with the local Ethics Committee. The MGG databank follows protocols in accordance with ethical standards of the Fourth Military Medical University and with the 1964 Helsinki declaration and its later amendments or comparable ethical standards. Images in the dataset do not contain any identifying information and patients willing consented to have their stained cell images stored in this MGG databank.

AUTHOR CONTRIBUTIONS

LJ, GN, ZJ, GZ, and WR contributed to conception and design of the study. LJ collected the pictures of cells and wrote the first draft of the manuscript. LJ, YQ, and WY performed the statistical analysis. LJ, MR, YL, and HW designed the DNN model. ZX proofread and edited the manuscript. All authors contributed to manuscript revision, read, and approved the submitted version.

FUNDING

Key R&D Program of Shaanxi Province of China (2020GY-271), the 111 Project of China (B14040), the National Natural Science Foundation of China (Program No. 81671185), the Natural Science Basic Research Program of Shaanxi (Program No. 2019JQ-251), the Hospital-level project of Xi'an International Medical Center (Program No. 2020ZD007).

ACKNOWLEDGMENTS

The authors acknowledge Dr. Owen Liang and Dr. Shan Huang for useful discussions and support for DNN. We acknowledge the funding support from the Key R&D Program of Shaanxi Province of China (2020GY-271), the 111 Project of China (B14040), the National Natural Science Foundation of China (Program No. 81671185), the Natural Science Basic Research Program of Shaanxi (Program No. 2019JQ-251), and the Hospital-level project of Xi'an International Medical Center (Program No. 2020ZD007).

SUPPLEMENTARY MATERIAL

The Supplementary Material for this article can be found online at: https://www.frontiersin.org/articles/10.3389/fmed.2021.749146/full#supplementary-material

REFERENCES

1. Feigin VL, Nichols E, Alam T, Bannick MS, Beghi E, Blake N, et al. Global, regional, and national burden of neurological disorders, 1990–2016: a systematic analysis for the Global Burden of Disease Study 2016. *Lancet Neurol.* (2019) 18:459–80. doi: 10.1016/S1474-4422(18)30499-X
2. Nagarathna S, Veenakumari HB, Chandramuki A. (2012). Laboratory diagnosis of meningitis. In: *Wireko-Brobby G (ed)*

Meningitis. FL: InTech, Croatia. pp. 185–208. doi: 10.5772/29081
3. Zhou L, Wu R, Shi X, Feng D, Feng G, Yang Y, et al. Simultaneous detection of five pathogens from cerebrospinal fluid specimens using Luminex technology. *Int J Environ Res Public Health*. (2016) 13:193. doi: 10.3390/ijerph13020193
4. Shahin AI, Guo Y, Amin KM, Sharawi AA. White blood cells identification system based on convolutional deep neural learning networks. *Comput Methods Programs Biomed.* (2019) 168:69–80. doi: 10.1016/j.cmpb.2017.11.015
5. Khashman A. Investigation of different neural models for blood cell type identification. *Neural Comput Appl.* (2012) 21:1177–83. doi: 10.1007/s00521-010-0476-3
6. Su MC, Cheng CY, Wang PC. A neural-network-based approach to white blood cell classification. *Sci World J.* (2014) 2014:796371. doi: 10.1155/2014/796371
7. Othman M, Mohammed T, Ali A. Neural network classification of white blood cell using microscopic images. *Int J Adv Comput Sci Appl.* (2017) 8:99–104. doi: 10.14569/IJACSA.2017.080513
8. Çelebi S, Burkay Çöteli M. Red and white blood cell classification using Artificial Neural Networks. *AIMS Bioeng.* (2018) 5:179–91. doi: 10.3934/bioeng.2018.3.179
9. Jiang M, Cheng L, Qin F, Du L, Zhang M. White blood cells classification with deep convolutional neural networks. *Int J Pattern Recognit Artif Intell.* (2018) 32:1857006. doi: 10.1142/S0218001418570069
10. Zhao J, Zhang M, Zhou Z, Chu J, Cao F. Automatic detection and classification of leukocytes using convolutional neural networks. *Med Biol Eng Comput.* (2017) 55:1287–301. doi: 10.1007/s11517-016-1590-x
11. Ren S, He K, Girshick R, Sun J. Faster R-CNN: towards real-time object detection with region proposal networks. *IEEE Trans Pattern Anal Mach Intell.* (2017) 39:1137–49. doi: 10.1109/TPAMI.2016.2577031
12. Tzutalin. *LabelImg*. (2015). Available online at: https://github.com/tzutalin/labelImg (accessed April 10, 2019).
13. Schmidt RM. *Cytological atlas of cerebrospinal fluid[M]*. FL: Johann Ambrosius Barth (1978).
14. Preusser M, Hainfellner J A. CSF and laboratory analysis (tumor markers). *Handb Clin Neurol.* (2012) 104:143–8. doi: 10.1016/B978-0-444-52138-5.00011-6
15. Rahimi J, Woehrer A. Overview of cerebrospinal fluid cytology. *Handb Clin Neurol.* (2017) 145:563–71. doi: 10.1016/B978-0-12-802395-2.00035-3
16. Lin TY, Maire M, Belongie S, Hays J, Perona P, Ramanan D, et al. Microsoft COCO: Common objects in context. *Lect Notes Comput Sci (including Subser Lect Notes Artif Intell Lect Notes Bioinformatics) LNCS:740–755*. (2014) 8693. doi: 10.1007/978-3-319-10602-1_48
17. Lecun Y, Bengio Y, Hinton G. Deep learning. *Nature*. (2015) 521:436–44. doi: 10.1038/nature14539
18. Liu W, Anguelov D, Erhan D, Szegedy C, ReedS, Fu CY, et al. SSD: Single shot multibox detector. *Lect Notes Comput Sci (including Subser Lect Notes Artif Intell Lect Notes Bioinformatics) LNCS:21–37*. (2016) 9905. doi: 10.1007/978-3-319-46448-0_2
19. Huang J, Rathod V, Sun C, Zhu M, Korattikara A, Fathi A, et al. Speed/accuracy trade-offs for modern convolutional object detectors. In: *Proc - 30th IEEE Conf Comput Vis Pattern Recognition, CVPR 2017 2017-Janua:3296–3305* (2017). doi: 10.1109/CVPR.2017.351
20. Kermany DS, Goldbaum M, Cai W, Valentim CCS, Liang H, Baxter SL, et al. Identifying Medical Diagnoses and Treatable Diseases by Image-Based Deep Learning. *Cell*. (2018) 172:1122–1131.e9. doi: 10.1016/j.cell.2018.02.010

Conflict of Interest: The authors declare that the research was conducted in the absence of any commercial or financial relationships that could be construed as a potential conflict of interest.

frontiers in Medicine

ORIGINAL RESEARCH
published: 15 February 2022
doi: 10.3389/fmed.2022.777439

Quantitative Characterization of Macrophage, Lymphocyte, and Neutrophil Subtypes Within the Foreign Body Granuloma of Human Mesh Explants by 5-Marker Multiplex Fluorescence Microscopy

Uwe Klinge[1]*, *Axel Dievernich*[2] and *Johannes Stegmaier*[3]

[1] Department of General, Visceral and Transplant Surgery at the University Hospital of the RWTH Aachen, Aachen, Germany, [2] Forschungs- und Entwicklungsgesellschaft FEG Textiltechnik, Aachen, Germany, [3] Institute of Imaging and Computer Vision, RWTH Aachen University, Aachen, Germany

OPEN ACCESS

Edited by:
Rupert Ecker,
TissueGnostics GmbH, Austria

Reviewed by:
Henning Ulrich,
University of São Paulo, Brazil
Diana Mechtcheriakova,
Medical University of Vienna, Austria

***Correspondence:**
Uwe Klinge
uklinge@ukaachen.de

Specialty section:
This article was submitted to Precision Medicine, a section of the journal Frontiers in Medicine

Received: *15 September 2021*
Accepted: *11 January 2022*
Published: *15 February 2022*

Citation:
Klinge U, Dievernich A and Stegmaier J (2022) Quantitative Characterization of Macrophage, Lymphocyte, and Neutrophil Subtypes Within the Foreign Body Granuloma of Human Mesh Explants by 5-Marker Multiplex Fluorescence Microscopy. Front. Med. 9:777439. doi: 10.3389/fmed.2022.777439

Foreign bodies such as fibers of a surgical mesh induce a typical reaction with an inflammatory infiltrate that forms a surrounding granuloma. This infiltrate is dominated by macrophages, lymphocytes, and neutrophils, whereas its extent of collaboration is widely unknown. In this study, we analyzed 12 samples of surgical meshes explanted from humans by multiplex analyses with three different 5-marker panels – 1. macrophage panel: CD68, CD86, CD105, CD163, and CD206; 2. lymphocyte panel: CD3, CD4, CD8, CD20, and CD68; and 3. neutrophil panel: CD15, histone, MPO, NE, and CD68. Measurement of fluorescence intensity within nuclear masks resulting from DAPI nuclear staining allows exact quantification of cells considered "positive" at a user-defined mean intensity threshold of > 100. Obviously, however, there is no natural threshold as a biological criterion for an intensity that separates "positive" stained cells from unstained cells ("negative"). Multiplex staining of 5 markers always reveals a high rate of coexpression for almost all of the 2^5 possible marker combinations (= 32 combinations, when using 5 markers simultaneously). The present staining results demonstrate that various morphological and functional subtypes of macrophages, lymphocytes, and neutrophils are abundant in the foreign body granuloma (FBG), which were investigated by regions of interest (ROI) with an area of 1 mm^2. The widespread coexpression of two or more markers underscores the complex collaboration network of the inflammatory infiltrate. The ability to combine spatial distribution with exact numerical analysis may offer new perspectives for our understanding of the complex interactions in this multidimensional process.

Keywords: foreign body granuloma, mesh, multiplex, fluorescence, macrophage, lymphocyte, neutrophil

INTRODUCTION

The repair of hernias as defects of the abdominal wall with possible protrusion of intestine is the most frequent procedure of visceral surgery. Within the past decades, the closure of the hernia orifice turned from simple suture to extended reinforcement with non-absorbable textile structures, the so-called meshes. These porous devices elicit a foreign body reaction that culminates in the formation of a foreign body granuloma (FBG), consisting of an inflammatory infiltrate surrounded by a fibrotic capsule. In some cases, revision surgery is required, mainly because of hernia recurrence, infection, or chronic pain, where these devices with ingrown and adherent tissue need to be removed or replaced.

Image cytometry with the use of various specific antibodies against cellular proteins and staining with several different fluorescent dyes enables the determination of various cell types and their functionality. Measurement of the mean intensities in the area of a nucleus offers the possibility of precise quantification of the number of "positive" cells and thus characterization of the local cellular response to the foreign body.

Quantified analysis of the foreign body reaction at the cell molecular level in terms of precision medicine is essential to determine the different risk profiles of mesh materials.

Macrophages have been shown to be the predominant actors of the chronic inflammation around these foreign bodies, with some of them fusing to multinucleated foreign body giant cells (FBGCs) (**Supplementary Figure 1A** in **Supplementary Material 1**). Characteristic surface markers are CD68 as pan-macrophage marker, CD86 for M1 subtype, CD105 indicates macrophage activation, and CD163 and also CD206 reflect M2 subtypes (1). Though these subtypes appear with distinct spatial distribution, they all can be found within a FBG. Recently, it has been shown that lymphocytes may also be the important components of the foreign body reaction (**Supplementary Figure 1B** in **Supplementary Material 1**). Corresponding surface markers are CD3 for T-lymphocytes, CD4 for T-helper cells, CD8 for cytotoxic T cells, and CD20 for B-lymphocytes (2). Besides macrophages and lymphocytes, neutrophils have been supposed to contribute to the inflammatory process (**Supplementary Figure 1C** in **Supplementary Material 1**), in particular by forming neutrophils extracellular traps (NETs) (3). Characteristic immune markers for NETs are CD15 for neutrophils, and antibodies against myeloperoxidase (MPO), neutrophil elastase (NE), and histone, and in particular the colocalization of all these.

However, it is not clear how many cells of the FBG show these surface markers and if there is some overlapping. As multiplex staining can provide this valuable information, we examined the macrophage pattern, lymphocyte pattern, and neutrophil pattern on 12 explanted mesh samples with 5 markers each and analyzed and quantified their coexpression profiles using the scanning system TissueFAXS PLUS with the StrataQuest Analysis Software from TissueGnostics, Vienna, Austria (4, 5).

MATERIALS AND METHODS

We analyzed 12 meshes, all of which have been used for abdominal wall hernia repair in humans: 2 plugs, 1 multifilament polyester (PES) mesh, 2 monofilament polyvinylidene fluoride (PVDF) meshes, 3 polypropylene (PP) meshes, and 4 composite PP meshes, combined with an absorbable part. Meshes with ingrown tissue were removed between 2001 and 2020 because of recurrence, pain, or infection after being incorporated for 2 months to 17 years (Ethics Committee approval: EK 239/19).

TABLE 1 | List of monoclonal antibodies.

Antibody	Clone	Dilution	Incubation time	Manufacturer	Host
Macrophage panel					
CD68	KP1	1:6,000	30 min at RT or overnight at 4°C	Dako	Mouse
CD86	BO63	1:200		Novus Biologicals	Mouse
CD105	SN6h	1:25		Dako	Mouse
CD163	5C6FAT	1:800		BMA Biomedicals	Mouse
CD206	15/2	1:200		Origene	Mouse
Neutrophil panel					
CD68	KP1	1:6,000	30 min at RT or overnight at 4°C	Dako	Mouse
CD15	I112R.1	1:2,000		Diagnostic BioSystems	Mouse
Histone H3	Polyclonal	1:2,000		Abcam	Rabbit
MPO	EPR20257	1:4,000		Abcam	Rabbit
NE	Polyclonal	1:400		Abcam	Rabbit
Lymphocyte panel					
CD3	F7.2.38	1:1,000	30 min at RT or overnight at 4°C	Dako	Mouse
CD4	4B12	1:500		Dako	Mouse
CD8	CD8/144B	1:500		Dako	Mouse
CD20	L26	1:600		Dako	Mouse
CD68	KP1	1:6000		Dako	Mouse

Monoclonal antibodies used in this study sorted by panel. Additional information: type of clone, dilution, incubation time, manufacturer, and host. MPO, myeloperoxidase; NE, neutrophil elastase; RT, room temperature.

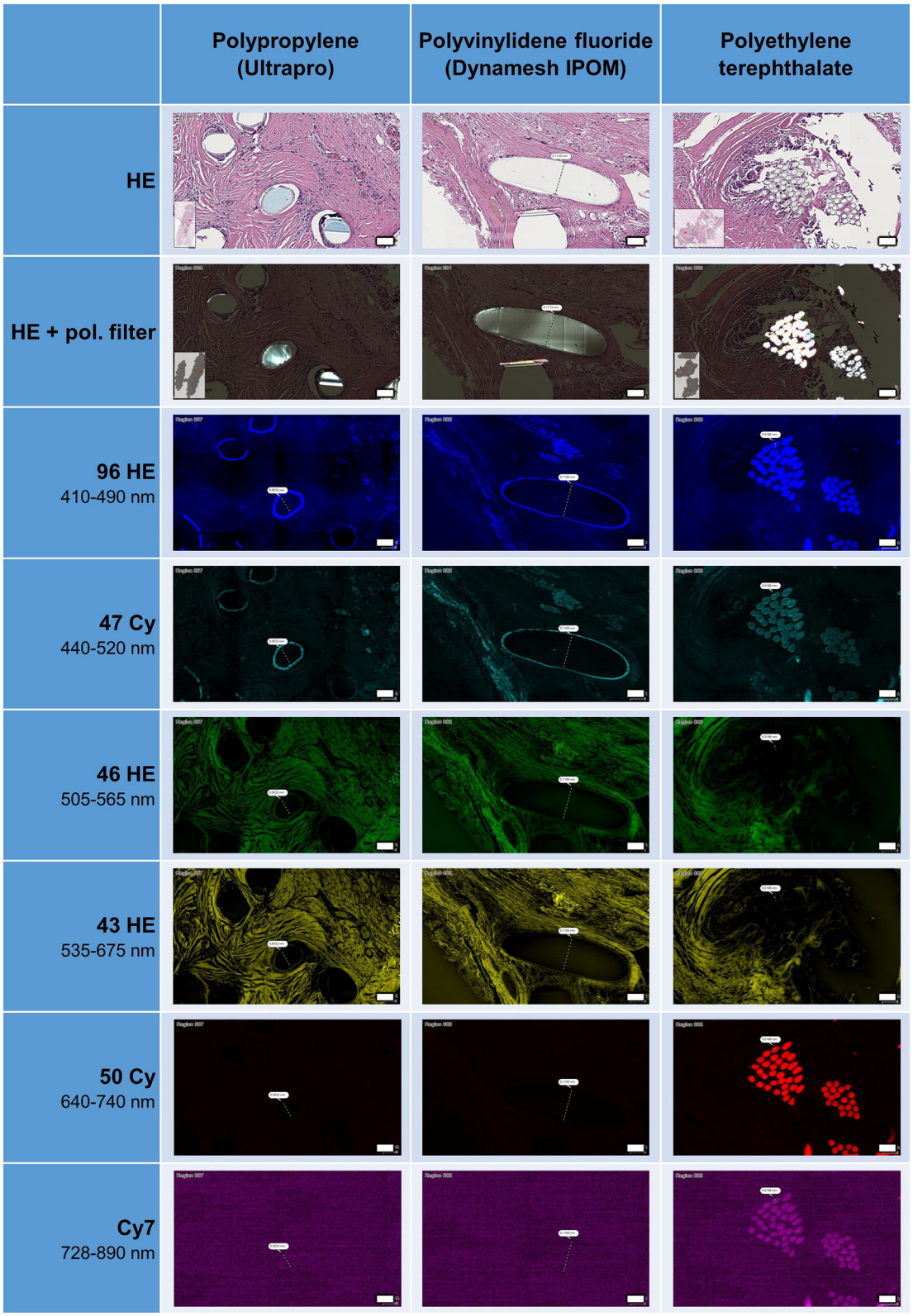

FIGURE 1 | Appearance of HE-stained meshes in bright field microscopy, with or without polarization filter, and with fluorescence microscopy. All polymers visible with pol. filter. Surface of PP and PVDF fibers visible as ring formation with autofluorescence at 410–520 nm, whereas polyester fibers visible at 410–520 and at 640–890 nm. Scale bars = 50 μm.

TABLE 2 | List of LED modules, filters with excitation and emission [wavelength/FWHM], and staining/fluorophore.

Marker	LED	ZEISS filter	Excitation	Emission	Staining/Fluorophore
Nuclear	UV DAPI	96 HE	390/40	450/40	DAPI
First	Violet	47 Cy	436/25	480/40	Opal™ 480
Second	Green Cy3	46 HE	500/25	535/30	Opal™ 520
Third	Yellow AF594	43 HE	550/25	605/70	Opal™ 570
Fourth	Red Cy5	50 Cy	640/30	690/50	Opal™ 650
Fifth	Far red	Cy 7E	708/75	809/81	Opal™ 780

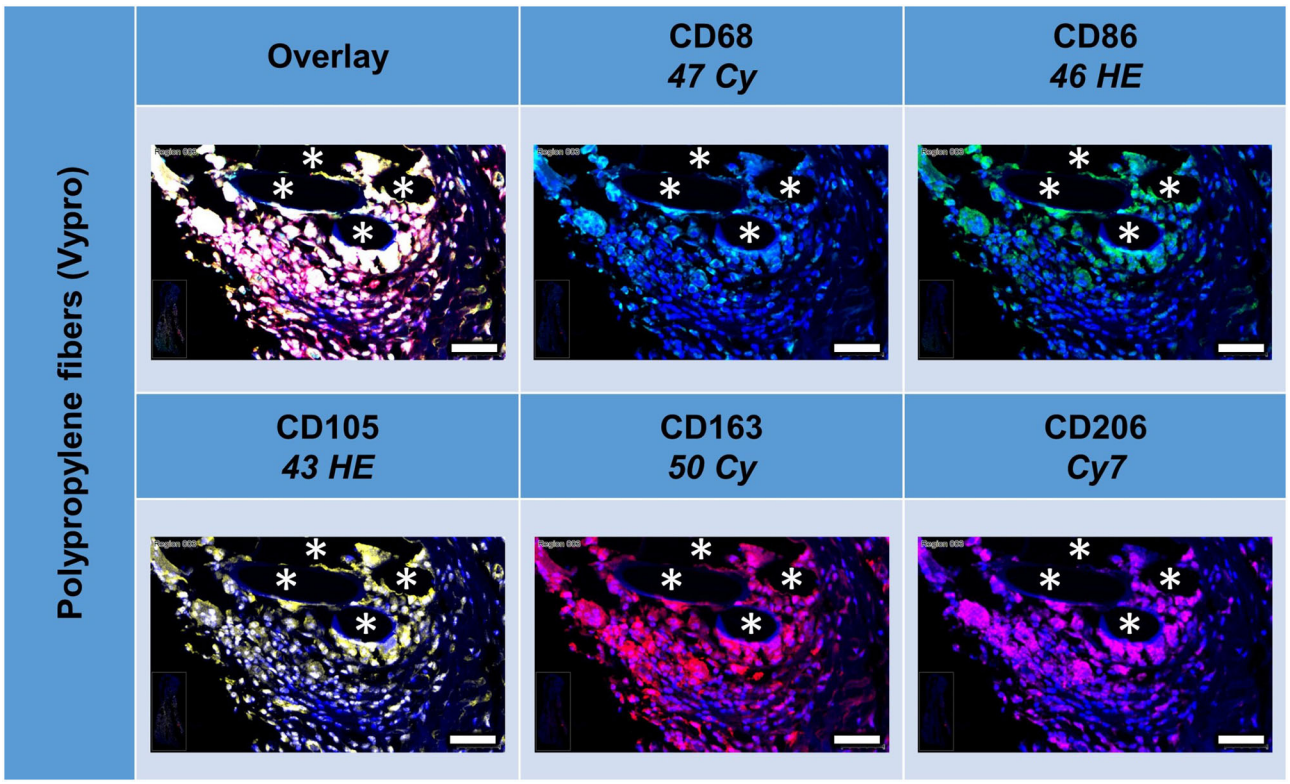

FIGURE 2 | Example of mesh-tissue section stained with macrophage panel. Labeling for nuclei with DAPI (blue), macrophages with CD68 (turquoise), M1 macrophages with CD86 (green), activated macrophages with CD105 (yellow), M2 macrophages with CD163 (red), and CD206 (magenta). Asterisks mark fiber locations, scale bars = 50 μm.

Prior to immunofluorescence staining, mesh samples were checked for the presence of mesh and FBGs by hematoxylin and eosin (H&E) with the addition of a polarization filter. By immunohistochemical staining with diaminobenzidine (DAB), we confirmed the functionality and dilution of the antibody markers. All mesh samples showed the typical foreign body reaction around the mesh fibers with an inner layer of inflammatory infiltrate, followed by an outer fibrotic layer. Most specimens showed a varying number of lymphocytes and FBGCs, and also small vessels at the mesh-tissue interface.

Immunofluorescence Staining

General

All steps were performed at room temperature. Serial 2-μm sections of each specimen were labeled with a first marker and subsequently with 4 other markers (**Table 1**). The "macrophage panel" includes CD68 (pan-macrophage), CD86 (M1), CD105 (activated macrophages), and also CD163 and CD206 both (M2). The "neutrophil panel" includes CD15 (neutrophils), histone H3, MPO, NE, and CD68. The "lymphocyte panel" includes CD3 (pan-T-lymphocyte), CD4 (T-helper cell), CD8 (cytotoxic T cell), CD20 (pan-B-lymphocyte), and CD68 (**Supplementary Figure 1** in **Supplementary Material 1**).

The order of the fluorophores or fluorescent dyes was always kept the same for all panels; Opal™ 480 was used first, followed by Opal™ 520, Opal™ 570, Opal™ 650, and finally Opal™ 780. All antibodies used were monoclonal and diluted with antibody diluent (with Background Reducing Components, Dako, Germany). Secondary antibodies were applied with ImmPRESS™ HRP (peroxidase) Polymer Detection Kit (Vector,

TABLE 3 | Comparison of cells located in the FBG and in the scar tissue by means of the macrophage panel.

Macrophage panel					FBG Mean (SD) $n = 72$	Scar Mean (SD) $n = 12$	*t*-test
CD68	**CD86**	**CD105**	**CD163**	**CD206**			
All "positive" cells for a given marker, independent of the other markers (n. d., not defined; pos., positive)							
pos.	n. d.	n. d.	n. d.	n. d.	405 (319)	475 (708)	0.778
n. d.	pos.	n. d.	n. d.	n. d.	418 (325)	266 (211)	*0.044
n. d.	n. d.	pos.	n. d.	n. d.	407 (429)	374 (680)	0.823
n. d.	n. d.	n. d.	pos.	n. d.	430 (397)	270 (325)	0.113
n. d.	n. d.	n. d.	n. d.	pos.	266 (260)	76 (55)	*0.000
All possible marker combinations (pos., positive; neg., negative)							
neg.	neg.	neg.	neg.	neg.	1,045 (500)	1,387 (895)	0.326
pos.	neg.	neg.	neg.	neg.	71 (89)	184 (308)	0.230
neg.	pos.	neg.	neg.	neg.	58 (99)	37 (41)	0.299
neg.	neg.	pos.	neg.	neg.	57 (109)	78 (176)	0.718
neg.	neg.	neg.	pos.	neg.	111 (149)	57 (68)	*0.033
neg.	neg.	neg.	neg.	pos.	43 (86)	18 (20)	0.053
pos.	pos.	neg.	neg.	neg.	69 (118)	57 (68)	0.745
pos.	neg.	pos.	neg.	neg.	17 (41)	43 (120)	0.465
pos.	neg.	neg.	pos.	neg.	10 (13)	8 (7)	0.367
pos.	neg.	neg.	neg.	pos.	5 (13)	2 (2)	0.194
neg.	pos.	pos.	neg.	neg.	14 (31)	9 (8)	0.278
neg.	pos.	neg.	pos.	neg.	6 (7)	7 (7)	0.658
neg.	pos.	neg.	neg.	pos.	10 (26)	2 (3)	*0.027
neg.	neg.	pos.	pos.	neg.	52 (101)	52 (127)	0.974
neg.	neg.	pos.	neg.	pos.	12 (36)	7 (11)	0.266
neg.	neg.	neg.	pos.	pos.	27 (60)	5 (5)	*0.004
pos.	pos.	pos.	neg.	neg.	54 (88)	52 (83)	0.949
pos.	pos.	neg.	pos.	neg.	18 (29)	11 (13)	0.197
pos.	pos.	neg.	neg.	pos.	11 (18)	2 (2)	*0.001
pos.	neg.	pos.	pos.	neg.	20 (65)	39 (118)	0.558
pos.	neg.	pos.	neg.	pos.	1 (3)	1 (2)	0.795
pos.	neg.	neg.	pos.	pos.	5 (10)	1 (1)	*0.001
neg.	pos.	pos.	pos.	neg.	17 (42)	9 (8)	0.194
neg.	pos.	pos.	neg.	pos.	8 (20)	2 (3)	*0.048
neg.	pos.	neg.	pos.	pos.	5 (16)	1 (2)	0.110
neg.	neg.	pos.	pos.	pos.	21 (47)	6 (6)	*0.017
pos.	pos.	pos.	pos.	neg.	39 (54)	50 (72)	0.668
pos.	pos.	pos.	neg.	pos.	22 (39)	4 (5)	*0.004
pos.	pos.	neg.	pos.	pos.	19 (34)	3 (4)	*0.001
pos.	neg.	pos.	pos.	pos.	6 (14)	2 (3)	0.129
neg.	pos.	pos.	pos.	pos.	25 (56)	4 (5)	*0.003
pos.	pos.	pos.	pos.	pos.	62 (81)	15 (13)	*0.000

Mean number of "positive" cells per 2,000 cells. For the FBG, six circular ROIs including mesh fibers were analyzed per sample (n = 12). Comparison with t-test between 280,760 cells located in the FBG and 6,445,165 cells in the whole sample (= scar). Statistically significant differences are marked with asterisks.

Laboratories, US). Fluorochromes were diluted with 1x Plus Amplification Diluent (PerkinElmer, US).

Protocol

Tissue sections with the explanted mesh devices were deparaffinized with xylol, rehydrated through graded alcohol and Milli-Q, before incubation in 3.5% formalin for 10 min. Sections were then placed in a cuvette filled with Milli-Q and pH6 citrate buffer (1:10) and treated with a Decloaking Chamber^{TM} (Biocare Medical, US) for 10 min at 110°C. Afterward, sections were washed with Milli-Q and TBST Tris (buffered saline with Tween 20, Dako) and cooled. Non-specific binding was blocked by incubation with antibody diluent for 10 min.

These steps were followed by incubation with the primary antibody of the first marker. After incubation, sections were rinsed in TBST Tris and incubated with the secondary antibody

for 20 min, before applying staining with the Opal™ 480 Reagent Pack (1:100, PerkinElmer) for 10 min. Sections were then washed with TBST Tris and placed in a cuvette filled with AR6 buffer (PerkinElmer) and Milli-Q (1:10). The cuvette was microwave treated for 3 min at 385 W reaching a maximal temperature of 92°C and 15 min at 120 W reaching a maximal temperature of 90°C, before being cooled with cold water. Sections were removed and rinsed with Milli-Q.

Afterward, the primary antibody of the second marker was applied after having blocked again with the antibody diluent for 10 min. Sections were rinsed in TBST Tris and incubated with the secondary antibody for 20 min, before applying staining with the Opal™ 520 reagent pack (1:100, PerkinElmer) for 10 min. Sections were then washed with TBST Tris and placed in a cuvette filled with AR6 buffer (PerkinElmer) and Milli-Q (1:10). The cuvette was microwave treated for 3 min at 385 W reaching a maximal temperature of 92°C and 15 min at 120 W reaching a maximal temperature of 90°C, before being cooled with cold water. Sections were removed and rinsed with Milli-Q.

Subsequent markers were applied the same way as the second marker. After the fifth staining cycle (application of the fifth marker), all tissue sections were mounted with VECTRASHIELD® HardSet™ Antifade Mounting Medium (Vector) with DAPI and coverslipped. The whole staining process for one panel took 3 days in total.

Analysis of the Fluorescence Images or Stainings

Fluorescence imaging was performed with an Axio Imager 2 microscope (20x, ZEISS, Germany) with an attached Colibri 7 light source (ZEISS, Germany) and the TissueFAXS PLUS system (TissueGnostics, Austria). The light source contains six LED modules and seven fluorescence channels, each producing monochromatic light of a different wavelength. LED-optimized filters and direct coupling increase sensitivity and ensure optimum excitation and emission spectra (**Table 2**, **Supplementary Material 2**).

Images were processed and quantitatively analyzed with StrataQuest Analysis Software (v7, TissueGnostics, Austria). Before applying the analysis app, the minimum and maximum ranges for each filter were set by automatically adjusting the saturation, and the mean minimum and maximum intensities of the slides were used for each marker in each panel.

DAPI images were used to detect and segment nuclei. Nuclei areas were used to measure the mean staining intensities for the five different markers (in six selected circular ROIs with an area of 1 mm^2). The ROIs were selected such that the mesh fibers were located in the center. We recorded the total number of cells with a mean intensity > 100, considered to be "positive." The number of "positive" cells was normalized to 2,000 cells (mean of number of cells within the ROIs, reflecting mainly the inflammatory infiltrate of the FBG) for each of the 32 possible combinations of the five markers. Then, the mean of 12 slides each with 6 ROIs was determined. The results of the total of 72 ROIs were compared to the analyses of the entire tissue samples, which were considered mainly as scar tissue.

With a cut-off value of 100 for the mean intensity in the nucleus area for the "positive" cells, the analyses yielded on average <5% "false-positive" cells (**Supplementary Material 3**).

RESULTS

Autofluorescence of HE-Stained Meshes

During the preparation and cutting process of the thin tissue sections (2 μm), most of the polymer fibers were removed, though some fibers remained in all samples (**Figure 1**). After HE staining, polymer fibers were slightly visible as milky clouds, whereas with the use of a polarization filter, all polymers were hyperintense and could be clearly distinguished from the hypointense surrounding tissues. When using the filters of the fluorescence microscopy, an intrinsic autofluorescence of the fibers became apparent. PP and PVDF showed a marked outer ring formation or "bark" at wavelength of 410–520 nm, in case of the PP with pronounced fragmentation. In contrast, the multifilament PES fibers demonstrated an intense autofluorescence of the entire fiber at both 410–520 nm and 640–890 nm. The illumination of the entire PES fibers is probably due to birefringence within the small (∼20 μm) individual fibers.

The frequent fragmentation of the "bark" seen for PP may represent the surface degradation of the fibers seen after incorporation in tissues (6). This fragmentation could also be clearly observed with the use of a polarization filter.

Multiplex Fluorescence Microscopy With Five Macrophage Cell Markers: CD68, CD86, CD105, CD163, and CD206

All five markers were detected within the 1 mm^2 ROIs around mesh fibers that marked the FBG, whereas their spatial heterogeneity confirmed their protein specificity (**Figure 2**). At first glance, cells in close vicinity to the fiber usually expressed not only a single marker, but often coexpressed multiple macrophage markers, which was confirmed by quantification using a mean nuclear intensity cut-off of 100 (**Table 3**).

Of the mean 2,000 cells of the ROIs, which included the majority of the FBG, more than 400 cells were either CD68+, CD86+, CD105+, or CD163+, whereas only 206 cells expressed CD206. Almost half of the cells ($n = 1{,}045$) did not express any of the five markers, whereas 341 showed only one marker, and 614 showed at least some coexpression, and 62 even coexpressed all five markers. Most of the 405 CD68+ cells coexpressed CD86+ ($n = 294$, ∼70%), half of them CD105+ ($n = 221$). Coexpression of CD68 and CD163 was seen in 179 cells and CD68 with CD206 in 131 cells.

Comparison of scar tissue vs. the FBG ROIs showed significant differences mainly for CD86+ ($p < 0.044$) and CD206+ ($p < 0.001$) cells, which were predominantly seen within the FBG. Cells coexpressing all five markers were mainly seen in the FBG (62 vs. 15, $p < 0.001$).

Depicting the linearly scaled scatter plots for the mean cellular intensities of two markers usually showed a homogenous cloud with a dense cluster marking the background and a continuous transition to the labeled cells without any clear

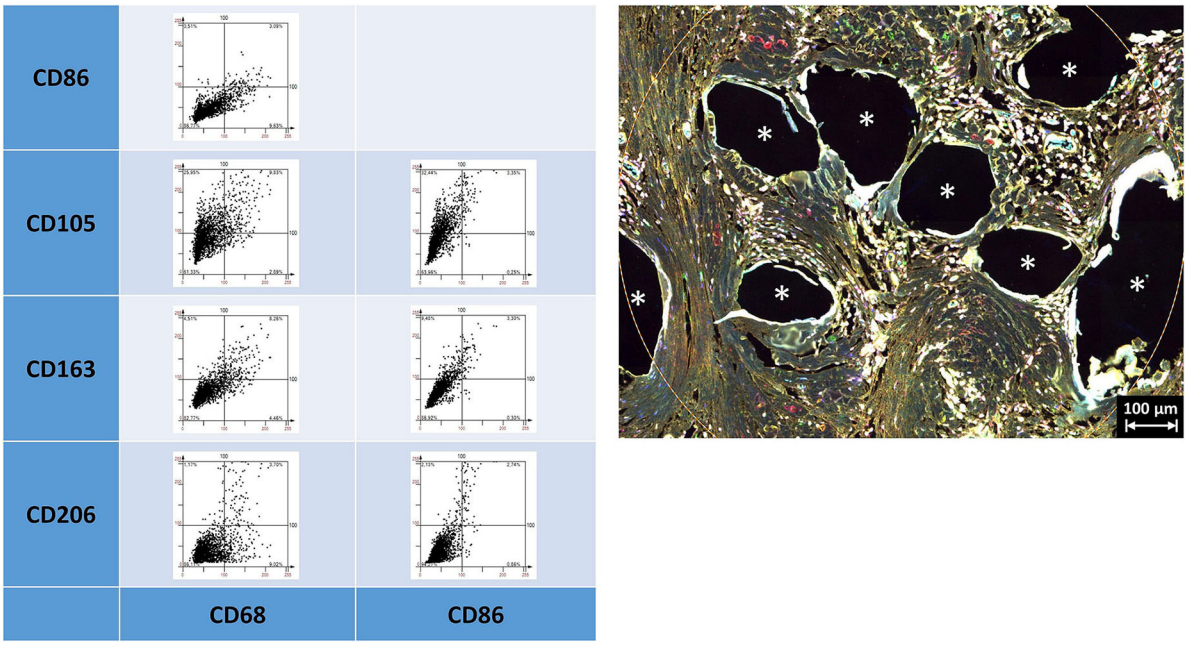

FIGURE 3 | Examples of linear scatter plots from macrophage panel. Scatter plots of mean cellular intensities of two markers in a 1 mm^2 ROI placed around fibers of a PP mesh plug. Lines in the scatter plots mark the cut-off value 100. Cytometric analysis was performed with StrataQuest 7. Asterisks mark fiber locations.

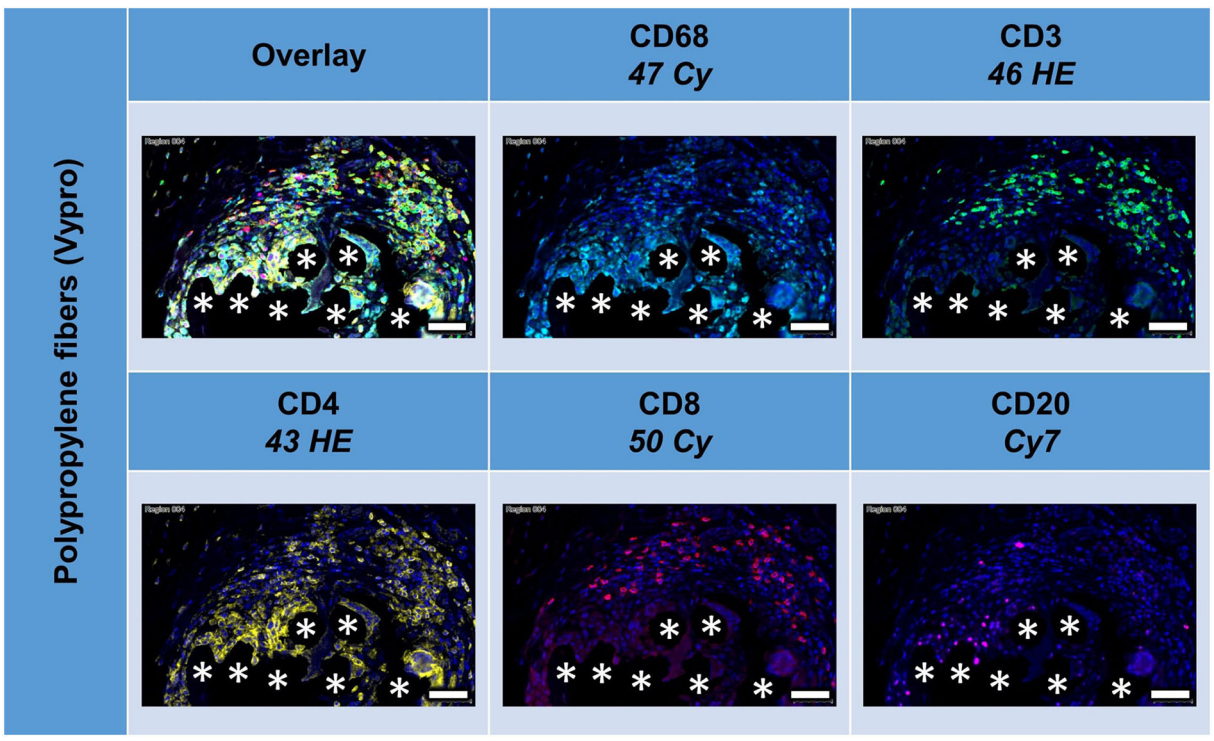

FIGURE 4 | Example of mesh-tissue section stained with lymphocyte panel. Labeling for nuclei with DAPI (blue), macrophages with CD68 (turquoise), T-lymphocytes with CD3 (green), T-helper cells with CD4 (yellow), cytotoxic T cells with CD8 (red), and B-lymphocytes with CD20 (magenta). Asterisks mark fiber locations, scale bars = 50 µm.

TABLE 4 | Comparison of cells located in the FBG and in the scar tissue by means of the lymphocyte panel.

Lymphocyte panel					FBG Mean (SD) $n = 72$	Scar Mean (SD) $n = 12$	t-test
CD68	CD3	CD4	CD8	CD20			
All "positive" cells for a given marker, independent of the other markers (n. d., not defined; pos., positive)							
pos.	n. d.	n. d.	n. d.	n. d.	360 (287)	183 (156)	*0.004
n. d.	pos.	n. d.	n. d.	n. d.	304 (288)	124 (101)	*0.000
n. d.	n. d.	pos.	n. d.	n. d.	345 (289)	169 (160)	*0.005
n. d.	n. d.	n. d.	pos.	n. d.	395 (399)	288 (217)	0.185
n. d.	n. d.	n. d.	n. d.	pos.	93 (193)	31 (38)	*0.015
All possible marker combinations (pos., positive; neg., negative)							
neg.	neg.	neg.	neg.	neg.	1,104 (523)	1,803 (1,445)	0.174
pos.	neg.	neg.	neg.	neg.	119 (111)	58 (57)	*0.008
neg.	pos.	neg.	neg.	neg.	48 (60)	21 (17)	*0.004
neg.	neg.	pos.	neg.	neg.	58 (101)	34 (43)	0.242
neg.	neg.	neg.	pos.	neg.	115 (144)	136 (137)	0.680
neg.	neg.	neg.	neg.	pos.	38 (85)	14 (17)	*0.031
pos.	pos.	neg.	neg.	neg.	12 (25)	2 (3)	*0.006
pos.	neg.	pos.	neg.	neg.	59 (88)	21 (25)	*0.006
pos.	neg.	neg.	pos.	neg.	39 (66)	40 (51)	0.986
pos.	neg.	neg.	neg.	pos.	1 (4)	0 (1)	0.072
neg.	pos.	pos.	neg.	neg.	32 (42)	18 (19)	0.070
neg.	pos.	neg.	pos.	neg.	45 (64)	20 (19)	*0.011
neg.	pos.	neg.	neg.	pos.	12 (32)	3 (5)	*0.045
neg.	neg.	pos.	pos.	neg.	25 (65)	13 (17)	0.145
neg.	neg.	pos.	neg.	pos.	3 (7)	1 (1)	*0.012
neg.	neg.	neg.	pos.	pos.	3 (12)	2 (3)	0.185
pos.	pos.	pos.	neg.	neg.	19 (30)	5 (5)	*0.003
pos.	pos.	neg.	pos.	neg.	20 (54)	3 (4)	*0.022
pos.	pos.	neg.	neg.	pos.	0 (1)	0 (0)	0.363
pos.	neg.	pos.	pos.	neg.	34 (55)	26 (37)	0.481
pos.	neg.	pos.	neg.	pos.	0 (1)	0 (0)	0.099
pos.	neg.	neg.	pos.	pos.	0 (1)	0 (0)	0.896
neg.	pos.	pos.	pos.	neg.	33 (55)	17 (22)	0.122
neg.	pos.	pos.	neg.	pos.	16 (34)	4 (7)	*0.015
neg.	pos.	neg.	pos.	pos.	6 (20)	2 (3)	0.105
neg.	neg.	pos.	pos.	pos.	2 (7)	0 (1)	0.075
pos.	pos.	pos.	pos.	neg.	60 (80)	25 (32)	*0.018
pos.	pos.	pos.	neg.	pos.	1 (1)	0 (1)	0.371
pos.	pos.	neg.	pos.	pos.	0 (0)	0 (0)	0.635
pos.	neg.	pos.	pos.	pos.	0 (1)	0 (0)	0.310
neg.	pos.	pos.	pos.	pos.	7 (25)	2 (4)	0.127
pos.	pos.	pos.	pos.	pos.	1 (4)	1 (3)	0.618

Mean number of "positive" cells per 2,000 cells. For the FBG, six circular ROIs including mesh fibers were analyzed per sample (n = 12). Comparison with t-test between 234,177 cells located in the FBG and 5,775,972 cells in the whole sample (= scar). Statistically significant differences are marked with asterisks.

subsets of cell clusters with distinct intensities (**Figure 3**). Just as little, a clear separation of "positive" cells could not be seen, for any of the five markers (**Supplementary Figures 1**, **2** in **Supplementary Material 4**). Noteworthy, the intensity of CD68 correlates with the intensity of CD86 in a linear way as a long oval cloud, and also with CD163, whereas the mean cellular intensities for CD68 and CD105 and also CD68 and CD206 were more distributed at higher intensities. Remarkably, also the intensities of CD86 correlate linearly with CD163 and CD206, which indicate the high plasticity and continuous spectrum of macrophages between the antiinflammatory (M1) and inflammatory (M2) states.

As already indicated by the previous work of Dievernich et al. using double stainings, only a minority of cells that just expressed a single marker can be assigned to a specific cell type (1). As we restricted the analyses just to the inflammatory infiltrate of the granuloma in this study, we did not look for spatial gradients. However, though the markers used were thought to separate the

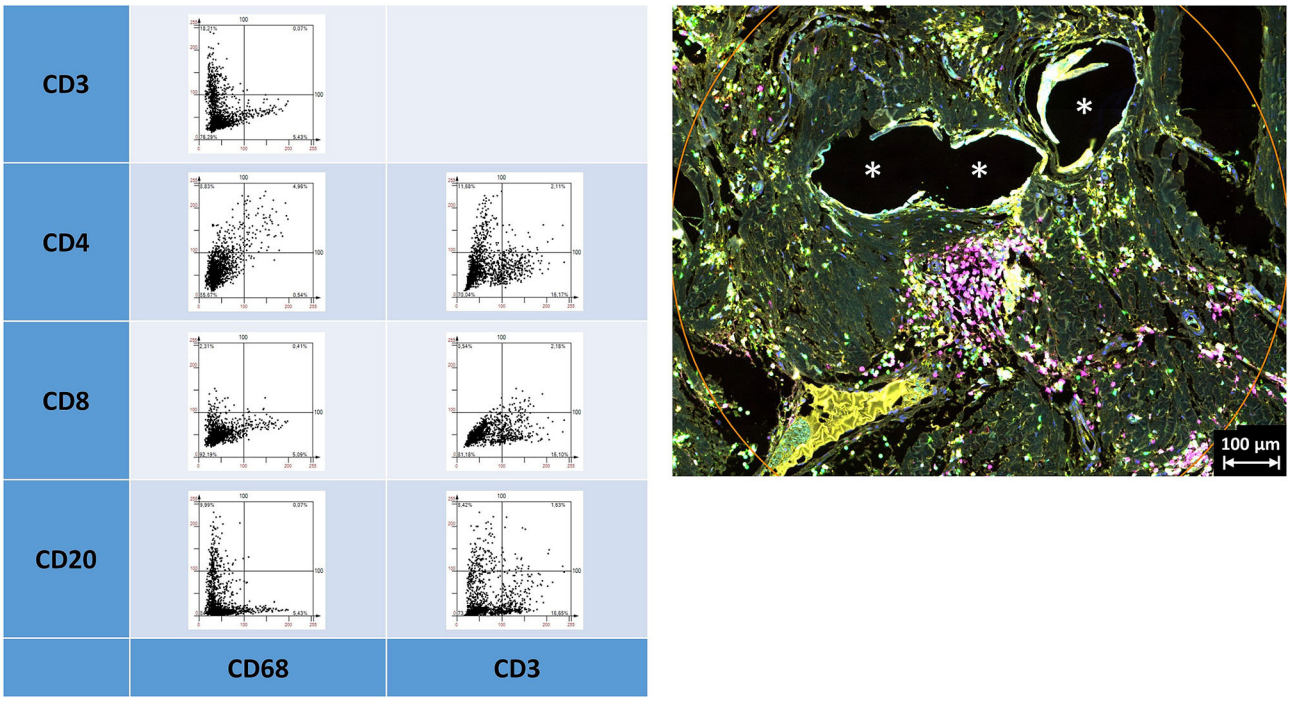

FIGURE 5 | Examples of linear scatter plots from lymphocyte panel. Scatter plots of mean cellular intensities of two markers in a 1 mm^2 ROI placed around PP mesh fibers. Lines in the scatter plot mark the cut-off value 100. Cytometric analysis was performed with StrataQuest 7. Asterisks mark fiber locations.

cells into distinct morphological or functional subgroups, the expression profiles of the cells within the FBG were found to be considerably more complex than expected with a high level of interference or coexpression.

Multiplex Fluorescence Microscopy With Four Lymphocyte Cell Markers: CD3, CD4, CD8, CD20, and CD68 as Reference

All lymphocyte markers were detected within the 1 mm^2 ROIs around mesh fibers that marked the FBG, but CD20+ cells were mainly seen in clusters outside the FBG (**Figure 4**). In close vicinity to the fibers, there were predominantly CD68+ cells and CD4+ cells, whereas in a distance of 10 to 20 µm, there were accumulations of CD3+ and CD8+ cells. Single CD20+ cells were distributed equally all over the FBG. Cells in close vicinity to the fiber usually express not only a single marker, but also often coexpressed multiple (**Table 4**).

Of the mean 2,000 cells of the sphere in the FBG, more than 300 cells were CD68+, CD3+, CD4+, or CD8+, and only CD20+ cells were markedly less with 93 cells. CD8+ cells were most common. A total of 148 cells were even "double-positive" for CD4 and CD8 (CD4+CD8+ cells). Half of the CD8+ cells costained for CD3, but only 25% of the CD4+ cells. Of 395 CD8+ cells, there are only 115 "single-positive" cells, 45 are CD8+CD3+, 39 are CD8+CD68+, and 20 are CD3+CD8+CD68+. Of 345 CD4+ cells, there are 58 exclusively positive for CD4, 32 are CD4+CD3+, 59 are CD4+CD68+, and 19 are CD3+CD4+CD68+. Altogether, among the CD4+ cells, in the mean per 2,000 cells, there were 93 that were CD68+ but not CD3+, 88 were CD3+ but not CD68+, and 81 were positive for both CD3 and CD68 (**Table 4**).

Comparing the scar area vs. ROIs within the FBG showed significant differences for CD68+ ($p < 0.01$), CD3+ ($p < 0.001$), CD4+ ($p < 0.01$), and CD20+ ($p = 0.015$) cells, which all were predominantly seen in the FBG, but no differences for CD8+ cells. Cells coexpressing all five markers were almost absent (**Table 4**).

Depicting the linearly scaled scatter plots for the intensities of two markers in the lymphocyte panel showed a clearer separation for CD68+ and CD3+, CD68+ and CD8+, and CD68+ and CD20+, and also CD3+ and CD4+ and CD3+ and CD20+ cells compared to the marker combinations of the macrophage panel, as indicated by an "L" configuration. However, coexpressing cells were also present (**Figure 5**). As for the macrophage marker, a clear separation of "positive" cells could not be seen.

Multiplex Fluorescence Microscopy With Four Neutrophil Cell Markers: CD15, Histone, MPO, and NE

All these markers were detected within the ROIs (**Figure 6**, **Table 5**). Whereas, histone usually appeared within the area of the nuclear mask, CD15, MPO, and NE were often found in the extranuclear area, too. CD15+ ($p = 0.010$) and histone+ ($p = 0.049$) cells were seen significantly more often in the FBG compared to the general scar tissue.

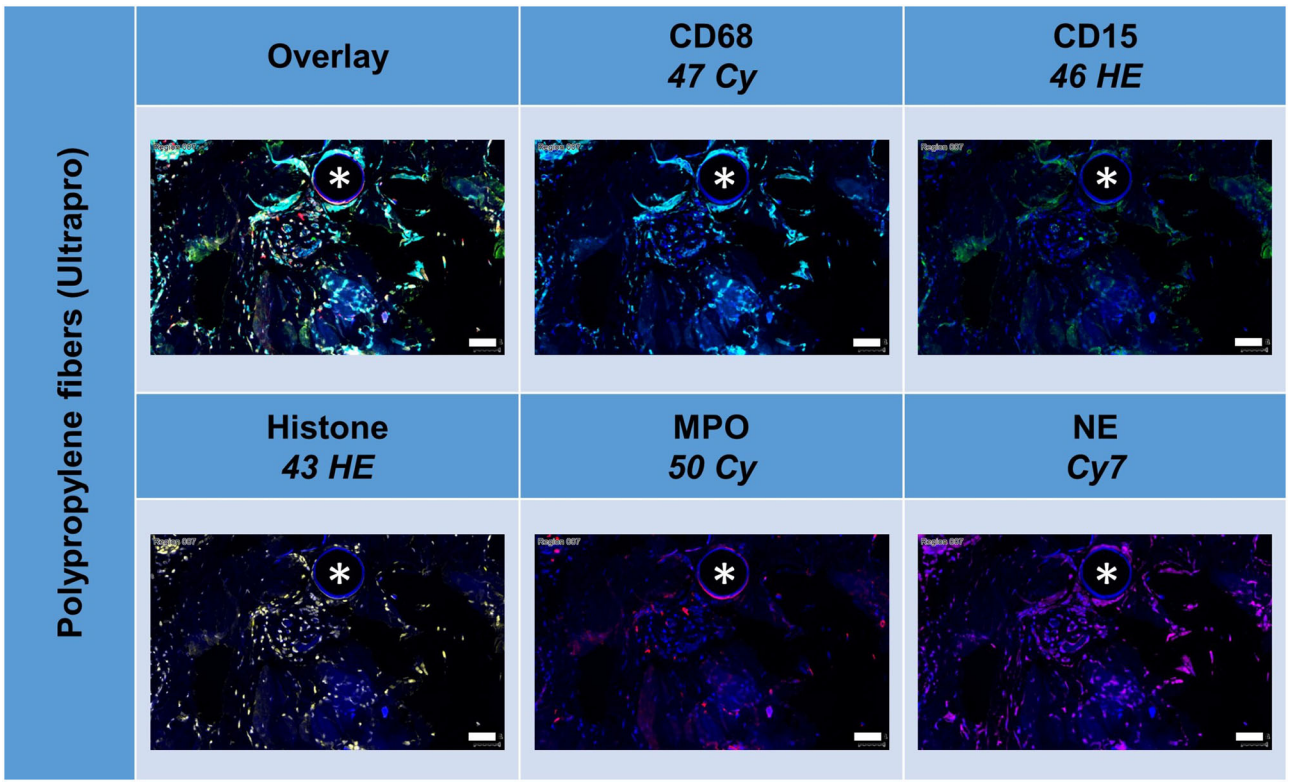

FIGURE 6 | Example of mesh-tissue section stained with neutrophil panel. Labeling for nuclei with DAPI (blue), macrophages with CD68 (turquoise), neutrophils with CD15 (green), histone (yellow), myeloperoxidase (MPO, red), and neutrophil elastase (NE, magenta). Asterisk marks a fiber location, scale bars = 50 μm.

The linearly scaled scatter plots usually revealed point clouds with a wide distribution of intensities rather than oval clouds with less variation in intensities (**Figure 7**). Many CD68+ cells showed coexpression of CD15, histone, MPO, and NE, and CD15+ cells were usually positive for histone, MPO, and NE, as expected.

Noteworthy, considerable extranuclear DAPI areas (EDA) were visible near the meshes (**Figure 8**). As DAPI is considered to bind specifically to DNA, these DAPI deposits can indicate the presence of neutrophil extracellular traps (NETs). Lowering the ranges for DAPI and excluding the area of the nuclear masks, EDAs could be identified, separated from the nuclear area, and the expression of the marker analyzed in the EDAs. Though the clinical relevance of neutrophils and NETs still is obscure, this study demonstrated their presence within the inflammatory infiltrate of the FBG and may be considered as the reason for long-term immunological problems of some patients (7).

Collaborative Network of Macrophages, Lymphocytes, and Neutrophils Within the FBG

Considering positive staining as intensities above mean + 2 SD, there were abundant CD68+ macrophages, CD3+ lymphocytes, and CD15+ neutrophils seen within the inflammatory infiltrate around PP fibers (**Figure 9**). Visualization revealed the spatial expression of the 13 markers used, and some of them coexpressed in similar cell clusters. Of the 4,560 possible correlations among the different panels of "positive" or "negative" markers, there were 898 significant Pearson's two-sided correlations ($p < 0.05$) reflecting the many functional linkages among the various markers. Since most markers showed, at least in some cells, that their expression occurred independently of the expression of other markers, higher correlations with $r > 0.6$ were rare ($n = 81$).

DISCUSSION

In comparison with previous studies with just two markers besides DAPI, the use of 5-marker multiplex immunofluorescence microscopy demonstrated the marked complexity of the biology within a FBG. The distinct spatial distribution of the markers within the entire tissue sample confirmed the high specificity of the antibody–protein binding. However, the complex and overlapping expression signature demonstrated that there was hardly any cell pattern that uniformly determined the presence of a specific subgroup or cell cluster with either identical origin or similar functionality.

The separation of M1 and M2 macrophages due to their mere staining with CD86 or CD163/CD206 appears to be incomplete to mirror the high heterogeneity of the macrophage response to the meshes. All the more so as the lymphocytic system obviously contributes to a similar extent and complexity. Additionally,

TABLE 5 | Comparison of cells located in the FBG and in the scar tissue by means of the neutrophil panel.

Neutrophil panel					FBG Mean (SD) $n = 72$	Scar Mean (SD) $n = 12$	*t*-test
CD68	**CD15**	**Histone**	**MPO**	**NE**			
All "positive" cells for a given marker, independent of the other markers (n. d., not defined; pos., positive)							
pos.	n. d.	n. d.	n. d.	n. d.	374 (272)	516 (499)	0.354
n. d.	pos.	n. d.	n. d.	n. d.	264 (323)	144 (86)	*0.010
n. d.	n. d.	pos.	n. d.	n. d.	250 (345)	135 (137)	*0.049
n. d.	n. d.	n. d.	pos.	n. d.	300 (347)	241 (249)	0.485
n. d.	n. d.	n. d.	n. d.	pos.	262 (315)	204 (175)	0.363
All possible marker combinations (pos., positive; neg., negative)							
neg.	neg.	neg.	neg.	neg.	1,242 (444)	2,069 (1,802)	0.141
pos.	neg.	neg.	neg.	neg.	111 (112)	290 (353)	0.109
neg.	pos.	neg.	neg.	neg.	48 (64)	24 (15)	*0.006
neg.	neg.	pos.	neg.	neg.	59 (107)	30 (37)	0.083
neg.	neg.	neg.	pos.	neg.	58 (80)	67 (91)	0.764
neg.	neg.	neg.	neg.	pos.	100 (178)	82 (88)	0.586
pos.	pos.	neg.	neg.	neg.	34 (53)	33 (39)	0.929
pos.	neg.	pos.	neg.	neg.	13 (22)	9 (12)	0.462
pos.	neg.	neg.	pos.	neg.	23 (31)	53 (111)	0.362
pos.	neg.	neg.	neg.	pos.	22 (39)	26 (32)	0.663
neg.	pos.	pos.	neg.	neg.	6 (9)	2 (3)	*0.010
neg.	pos.	neg.	pos.	neg.	35 (65)	15 (14)	*0.028
neg.	pos.	neg.	neg.	pos.	5 (9)	2 (3)	*0.028
neg.	neg.	pos.	pos.	neg.	15 (32)	6 (9)	0.052
neg.	neg.	pos.	neg.	pos.	31 (51)	20 (26)	0.285
neg.	neg.	neg.	pos.	pos.	5 (12)	5 (3)	0.898
pos.	pos.	pos.	neg.	neg.	8 (22)	3 (4)	0.118
pos.	pos.	neg.	pos.	neg.	39 (99)	24 (25)	0.282
pos.	pos.	neg.	neg.	pos.	5 (10)	3 (4)	0.262
pos.	neg.	pos.	pos.	neg.	17 (39)	8 (13)	0.131
pos.	neg.	pos.	neg.	pos.	10 (21)	11 (19)	0.854
pos.	neg.	neg.	pos.	pos.	10 (27)	13 (14)	0.551
neg.	pos.	pos.	pos.	neg.	8 (18)	4 (6)	0.099
neg.	pos.	pos.	neg.	pos.	2 (4)	1 (1)	0.055
neg.	pos.	neg.	pos.	pos.	3 (7)	2 (1)	0.098
neg.	neg.	pos.	pos.	pos.	5 (12)	3 (3)	0.222
pos.	pos.	pos.	pos.	neg.	23 (48)	9 (16)	0.054
pos.	pos.	pos.	neg.	pos.	4 (9)	2 (2)	0.062
pos.	pos.	neg.	pos.	pos.	11 (28)	7 (8)	0.373
pos.	neg.	pos.	pos.	pos.	15 (30)	13 (25)	0.757
neg.	pos.	pos.	pos.	pos.	3 (8)	1 (2)	0.216
pos.	pos.	pos.	pos.	pos.	31 (84)	12 (16)	0.096

Mean number of "positive" cells per 2,000 cells. For the FBG, six circular ROIs including mesh fibers were analyzed per sample (n = 12). Comparison with t-test between 304,998 cells located in the FBG and 6,471,629 cells in the whole sample (= scar). Statistically significant differences are marked with asterisks.

not least, the detection of EDAs around the mesh fibers with abundant expression of histone, MPO, and NE underlines the importance of the neutrophils and their formation of neutrophil extracellular traps, which may be responsible for the ongoing chronic inflammation and any possible autoimmune stress.

However, despite the high evidence for the present high level of coexpression, any attempt for quantification of immunohistochemistry has severe limitations:

The possible impact on functionality by the expression of proteins with variable intensities, which may be the consequence of different concentrations of the binding epitopes on the cells, is known, but hard to control (8). The poor quality of the tissue with, for example, long ischemia before fixation may reduce the binding sites further. Patient's biology and their immunological response may differ to an unknown extent. The surgical trauma and

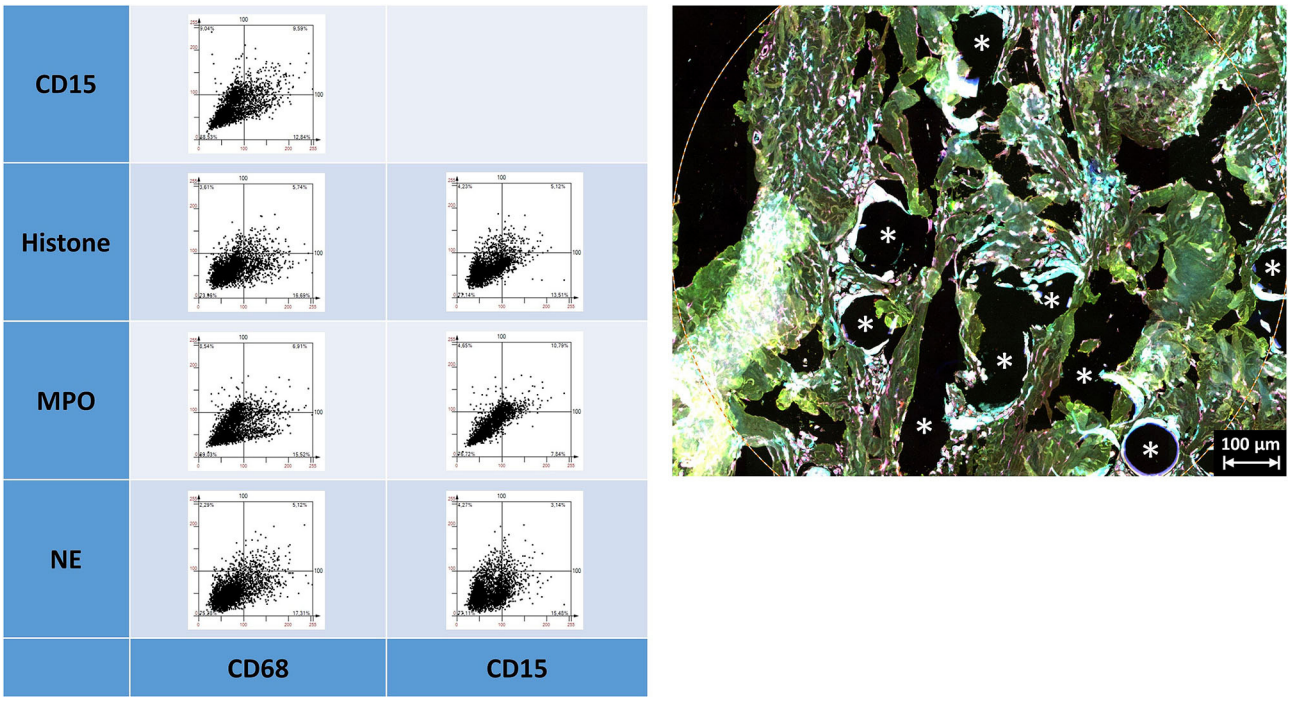

FIGURE 7 | Examples of linear scatter plots from neutrophil panel. Scatter plots of mean cellular intensities of two markers in a 1 mm^2 ROI placed around PP mesh fibers. The lines in the scatter plot mark the cut-off value 100. Cytometric analysis was performed with StrataQuest 7. Asterisks mark fiber locations.

wound infection may change the local tissue response to the mesh materials.

Quantification of multiplex staining results, of course, has lots of confounders, such as overlaying background signals, unspecific binding of the primary or secondary antibody, distinct affinity binding of the dye, variable number of binding sites in heterogeneous cells, and alteration of epitopes by ischemia or the fixation procedure. Some of them can be excluded by reasonable spatial staining pattern and using various controls. However, for the question at what staining intensity a cell should be considered "positive" there still is not an easy answer. Sometimes, the staining signal is relatively weak but distributed over most of the cell, whereas in other cases, a hyperintense signal emanates from only part of the cell, resulting in the same mean signal. Without additional analysis, it is impossible to define any as functional "negative" or "positive." Adjusting the intensity ranges using imaging tools can decrease or increase the image contrast, but it does not solve the problem. We decided to use the automatic ranges provided by TissueFAXS for the StrataQuest analyses and to use a fixed cut-off value of 100 to determine "positive" cells.

Any quantification needs to define a reliable cut-off to determine at what intensity a cell may be considered "positive" (9). The cut-off usually does not result from natural order with distinct intensities but always has to be fixed manually and arbitrarily (10). The intensity may be measured as mean or maximum in an eroded or dilated nuclear mask. The definition of reliable ROIs is essential to overcome the usual huge heterogeneity of the tissue samples, in particular, if the mesh fibers are removed during the cutting process. Using specific LED light sources in combination with bandpass filters ideally matched to their spectra and selected fluorescent dyes, any artificial overlap by interfering signals must be avoided. A mean intensity > 100 does not automatically reflect a "positive" cell for a maker. It has to be checked by visual control and backward gating whether the staining pattern is reasonable and in accordance with the published literature. Conversely, a mean intensity < 100 does not prove that the cell does not express the marker anyhow. However, a fixed cut-off value of 100 reduces the subjective impact of a manual gating and improves reproducibility.

This "high" cut-off value may exclude several cells that are only partially or overall "weakly" stained, but a lower cut-off would result in higher percentages without contradicting the fact that there are many coexpressions and complex marker patterns in cells of a FBG.

Despite the many limitations mentioned above in quantifying cells with "positive" staining, the present protocol provides tools to analyze the inflammatory response to meshes in a highly standardized, reproducible, reliable, and objective manner.

In regard to the many confounders with an impact on the cell response to meshes and in consideration of the limited information given by clinicians, this study cannot link its quantification of inflammatory cells with a specific clinical outcome. However, this protocol and the results for this mix of various materials may serve as a standard for future comparisons

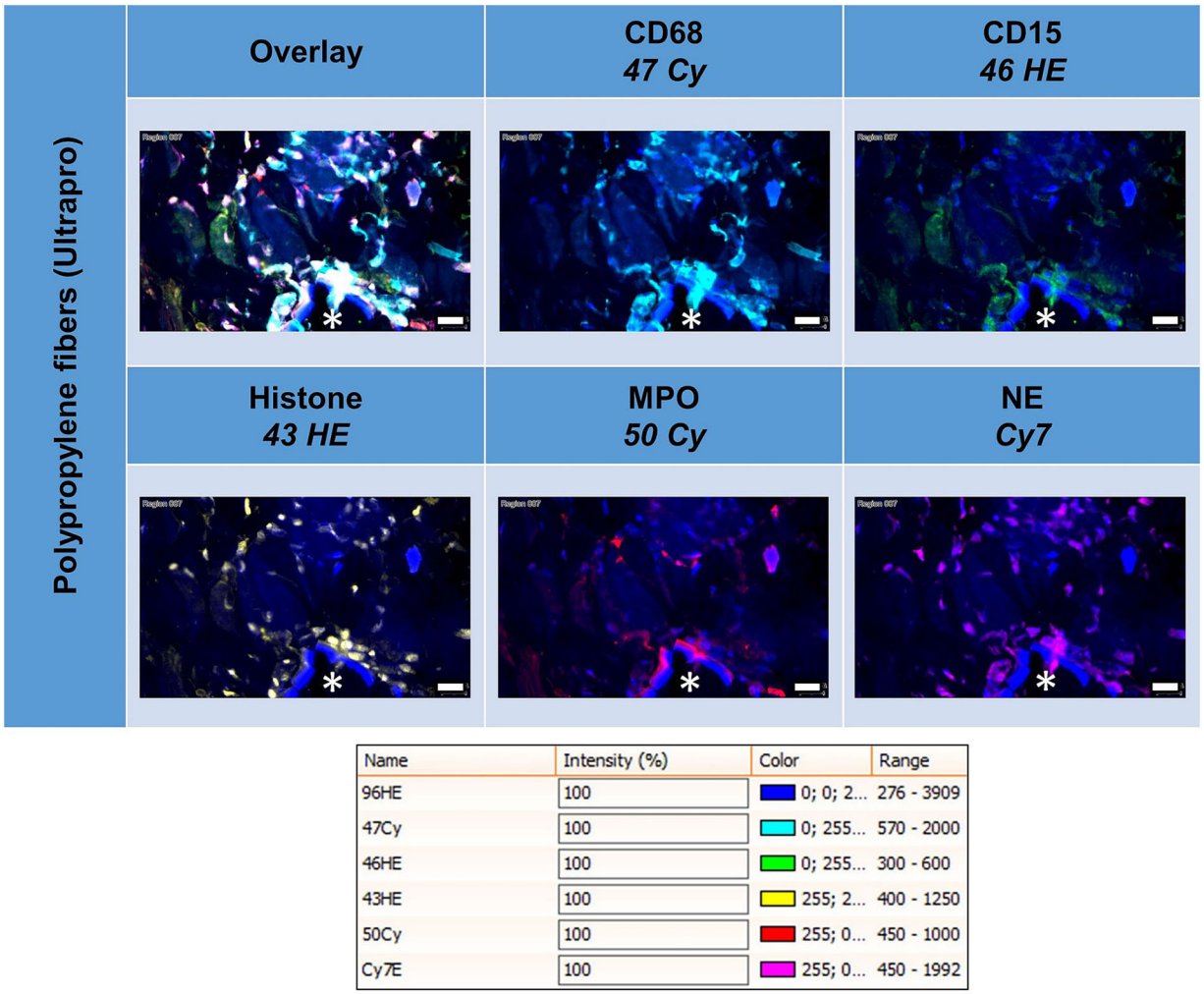

Name	Intensity (%)	Color	Range
96HE	100	0; 0; 2...	276 - 3909
47Cy	100	0; 255...	570 - 2000
46HE	100	0; 255...	300 - 600
43HE	100	255; 2...	400 - 1250
50Cy	100	255; 0...	450 - 1000
Cy7E	100	255; 0...	450 - 1992

FIGURE 8 | Tissue section of infected composite PP mesh labeled for nuclei with DAPI (blue), macrophages with CD68 (turquoise), neutrophils with CD15 (green), histone (yellow), myeloperoxidase (MPO, red), and neutrophil elastase (NE, magenta). EDAs indicate the presence of neutrophil extracellular traps (NETs). Asterisk marks a fiber location, scale bars = 50 μm.

to detect any gross violation from the standard and to identify high-risk materials.

CONCLUSION

The cells of the inflammatory infiltrate around mesh fibers showed a variable signature of macrophage, lymphocyte, and neutrophil markers in multiplex immunofluorescence microscopy. Instead of distinct subgroups of cells with clear marker profiles, we found comprehensive interference resulting in a blurred cloud of overlapping coexpression. A clear physiological threshold to separate "negative" and "positive" cells was not seen for any of the 13 markers, which, in contrast, all showed a continuous spectrum of intensities. In addition to the polarization filter in bright field microscopy, viewing polymer fibers with bandpass filters can help to analyze meshes and their degradation in tissue specimens.

The recent decades of research in the field of biomaterials and meshes, respectively, have been characterized by semi-quantitative analyses mainly focusing on macrophages, defined by immunohistochemistry usually with CD68 as the only marker. These results have been used to assess the biocompatibility and potential risks of the implants. However, these approaches obviously were not able to reflect the complexity of the foreign body reaction around the material and to provide data for reliable comparisons. In this study, we demonstrate that single marker approaches are not suitable to define specific subgroups of immunological cells in the FBG, which is possible with multiplex methods. Furthermore, by focusing on the mean intensities within the nuclear area, a precise quantification is feasible. The present data of a variety of different meshes thus provide a first standard for future comparisons. It still has to be shown by additional methods and/or targeted material

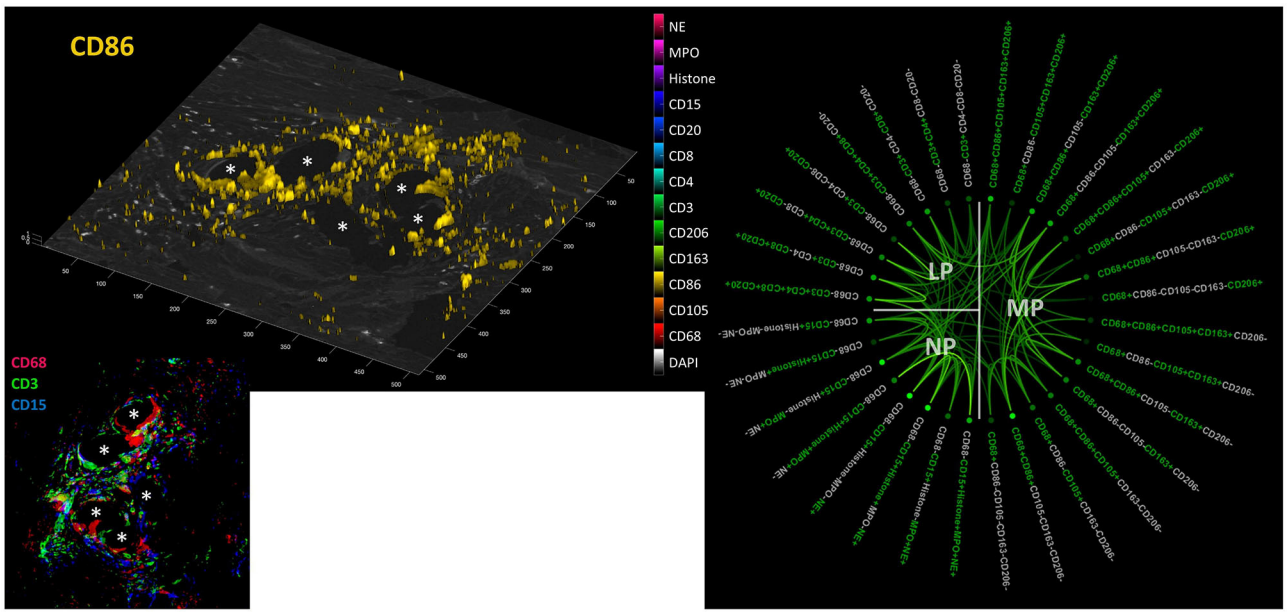

FIGURE 9 | Collaboration network in the FBG. **Left**: Example image from a video file (available as **Supplementary Material**) showing all "positive" cells (threshold = mean + 2 SD) for all 13 markers on a DAPI image; CD86 is shown here. **Inset**: CD68+ macrophages (red), CD3+ lymphocytes (green), and CD15+ neutrophils (blue) in the FBG of a PP mesh. Asterisks mark fiber locations. **Right**: Significant Pearson's correlations ($p < 0.05$) within and between macrophage (MP), lymphocyte (LP), and neutrophile (NP) panels. Marker colored green = positive and marker colored light gray = negative. The stronger the saturation of the depicted correlations between individual marker combinations, the higher is their correlation coefficient.

modifications, which of these marker profiles are relevant for the clinical outcome. This study clearly demonstrates that future analyses should be done with multiplex imaging to enable precision medicine.

DATA AVAILABILITY STATEMENT

The raw data supporting the conclusions of this article will be made available by the authors, without undue reservation.

ETHICS STATEMENT

The studies involving human participants were reviewed and approved by Ethic Committee of the University Hospital of the RWTH Aachen EK 239/19. The patients/participants provided their written informed consent to participate in this study.

AUTHOR CONTRIBUTIONS

UK performed the microscopic measurements. AD, JS, and UK together prepared the analysis and the manuscript. All authors contributed to the article and approved the submitted version.

FUNDING

The support by the Federal Ministry of Education and Research (FKZ 13GW0108B) enabled the acquisition of the Tissue Gnostics system.

SUPPLEMENTARY MATERIAL

The Supplementary Material for this article can be found online at: https://www.frontiersin.org/articles/10.3389/fmed.2022.777439/full#supplementary-material

REFERENCES

1. Dievernich A, Achenbach P, Davies L, Klinge U. Tissue remodeling macrophages morphologically dominate at the interface of polypropylene surgical meshes in the human abdomen. *Hernia.* (2020) 24:1175–89. doi: 10.1007/s10029-020-02315-2
2. Dievernich A, Achenbach P, Davies L, Klinge U. Characterization of innate and adaptive immune cells involved in the foreign body reaction to polypropylene meshes in the human abdomen. *Hernia.* (2021) 18:571–8. doi: 10.1007/s10029-021-02396-7
3. Rosales C. Neutrophil: a cell with many roles in inflammation or several cell types? *Front Physiol.* (2018) 9:113. doi: 10.3389/fphys.2018.00113
4. Mungenast F, Fernando A, Nica R, Boghiu B, Lungu B, Batra J, et al. Next-generation digital histopathology of the tumor microenvironment. *Genes.* (2021) 12:538. doi: 10.3390/genes12040538

5. Meshcheryakova A, Mungenast F, Ecker R, Mechtcheriakova D. Tissue image cytometry. In: *Imaging Modalities for Biological and Preclinical Research: A Compendium*, Vol. 1. IOP Publishing (2021). p. I.2.h-1–h-10. doi: 10.1088/978-0-7503-3059-6ch14
6. Iakovlev VV, Guelcher SA, Bendavid R. Degradation of polypropylene in vivo: A microscopic analysis of meshes explanted from patients. *J Biomed Mater Res B Appl Biomater.* (2017) 105:237–48. doi: 10.1002/jbm.b.33502
7. Tervaert JW. Autoinflammatory/autoimmunity syndrome induced by adjuvants (Shoenfeld's syndrome) in patients after a polypropylene mesh implantation. *Best Pract Res Clin Rheumatol.* (2018) 32:511–20. doi: 10.1016/j.berh.2019.01.003
8. Parra ER, Jiang M, Solis L, Mino B, Laberiano C, Hernandez S, et al. Procedural requirements and recommendations for multiplex immunofluorescence tyramide signal amplification assays to support translational oncology studies. *Cancers.* (2020) 12:255. doi: 10.3390/cancers12020255
9. Schiffer M. Going single but not solo with podocytes: potentials, limitations, and pitfalls of single-cell analysis. *Kidney Int.* (2017) 92:1038–41. doi: 10.1016/j.kint.2017.05.033
10. Klinge U, Dievernich A, Tolba R, Klosterhalfen B, Davies L. CD68+ macrophages as crucial components of the foreign body reaction demonstrate an unconventional pattern of functional markers quantified by analysis with double fluorescence staining. *J Biomed Mater Res B Appl Biomater.* (2020) 108:3134–46. doi: 10.1002/jbm.b.34639

Conflict of Interest: The authors declare that the research was conducted in the absence of any commercial or financial relationships that could be construed as a potential conflict of interest.

Publisher's Note: All claims expressed in this article are solely those of the authors and do not necessarily represent those of their affiliated organizations, or those of the publisher, the editors and the reviewers. Any product that may be evaluated in this article, or claim that may be made by its manufacturer, is not guaranteed or endorsed by the publisher.

frontiers | Frontiers in Medicine

TYPE Original Research
PUBLISHED 11 November 2022
DOI 10.3389/fmed.2022.978146

OPEN ACCESS

EDITED BY
Enrico Heffler,
Humanitas University, Italy

REVIEWED BY
Chen Li,
Northeastern University, China
Ghada Zamzmi,
National Institutes of Health (NIH), United States

*CORRESPONDENCE
Amirreza Mahbod
amirreza.mahbod@meduniwien.ac.at

SPECIALTY SECTION
This article was submitted to Precision Medicine, a section of the journal Frontiers in Medicine

RECEIVED 25 June 2022
ACCEPTED 28 October 2022
PUBLISHED 11 November 2022

CITATION
Mahbod A, Schaefer G, Dorffner G, Hatamikia S, Ecker R and Ellinger I (2022) A dual decoder U-Net-based model for nuclei instance segmentation in hematoxylin and eosin-stained histological images. *Front. Med.* 9:978146. doi: 10.3389/fmed.2022.978146

A dual decoder U-Net-based model for nuclei instance segmentation in hematoxylin and eosin-stained histological images

Amirreza Mahbod[1,2]*, Gerald Schaefer[3], Georg Dorffner[4], Sepideh Hatamikia[2,5], Rupert Ecker[6] and Isabella Ellinger[1]

[1]Institute for Pathophysiology and Allergy Research, Medical University of Vienna, Vienna, Austria, [2]Research Center for Medical Image Analysis and Artificial Intelligence, Department of Medicine, Danube Private University, Krems an der Donau, Austria, [3]Department of Computer Science, Loughborough University, Loughborough, United Kingdom, [4]Institute of Artificial Intelligence, Medical University of Vienna, Vienna, Austria, [5]Austrian Center for Medical Innovation and Technology, Wiener Neustadt, Austria, [6]Department of Research and Development, TissueGnostics GmbH, Vienna, Austria

Even in the era of precision medicine, with various molecular tests based on omics technologies available to improve the diagnosis process, microscopic analysis of images derived from stained tissue sections remains crucial for diagnostic and treatment decisions. Among other cellular features, both nuclei number and shape provide essential diagnostic information. With the advent of digital pathology and emerging computerized methods to analyze the digitized images, nuclei detection, their instance segmentation and classification can be performed automatically. These computerized methods support human experts and allow for faster and more objective image analysis. While methods ranging from conventional image processing techniques to machine learning-based algorithms have been proposed, supervised convolutional neural network (CNN)-based techniques have delivered the best results. In this paper, we propose a CNN-based dual decoder U-Net-based model to perform nuclei instance segmentation in hematoxylin and eosin (H&E)-stained histological images. While the encoder path of the model is developed to perform standard feature extraction, the two decoder heads are designed to predict the foreground and distance maps of all nuclei. The outputs of the two decoder branches are then merged through a watershed algorithm, followed by post-processing refinements to generate the final instance segmentation results. Moreover, to additionally perform nuclei classification, we develop an independent U-Net-based model to classify the nuclei predicted by the dual decoder model. When applied to three publicly available datasets, our method achieves excellent segmentation performance, leading to average panoptic quality values of 50.8%, 51.3%, and 62.1% for the CryoNuSeg, NuInsSeg, and MoNuSAC datasets, respectively. Moreover, our model is the top-ranked method in the MoNuSAC post-challenge leaderboard.

KEYWORDS

digital pathology, medical image analysis, nuclei segmentation, machine learning, deep learning

1. Introduction

Evaluation of images obtained from tissue sections stained with hematoxylin and eosin (H&E) has long been the gold standard method in medicine for disease diagnosis, cancer grading, and treatment decisions (1). While at some point it was predicted that molecular biology would replace traditional histopathology, even in the era of precision medicine, where an ever-growing list of molecular tests based on omics technologies is available to support precision oncology, microscopic analysis and interpretation of the information contained in H&E-stained tissue sections provides critical information for diagnostic and treatment decisions. It is time- and cost-efficient, and can be applied to small amounts of tissue, while rapid intra-operative tissue analysis based on H&E staining of cryosections remains indispensable to assist surgeons in deciding how to proceed with surgery. H&E-stained histological image analysis also provides valuable information for medical scientists studying the pathophysiology of diseases (2, 3).

Interpretation of H&E-stained images by experts such as pathologists, clinicians, or scientists is however the bottleneck of the common manual analysis as it is time-consuming and prone to inter-observer differences. With the advent of microscopy-based slide scanners that acquire and digitize histological images, computer-aided image analysis systems have been introduced to support human experts and to make the process faster and more objective (4). Computerized methods and in particular deep neural network (DNN)-based algorithms have been shown to be capable of providing diagnostic interpretation with similar accuracy to medical experts (5, 6), while computer-aided analysis can also enable the extraction of quantitative and complex qualitative features that are not recognized by human experts (7).

The nuclei are the most prominent cell organelles. Since they are present in almost all eukaryotic cells, their detection enables cell localization. Various intra- and extra-cellular factors determine the nuclear shape. This results in a physiologic variation of nucleus shapes that can be used to identify sub-populations of cells (8). Moreover, there are significant morphological alterations of nuclei in diseases. Cancer, for example, is known to alter nuclear parameters such as size and shape. These variations are thus an important piece of information contributing to tumor diagnosis and grading (9). Consequently, automated detection, segmentation and in some cases classification of nuclei are important processing steps of computer systems used in histological image analysis in the clinical and scientific context.

Various computer-assisted approaches have been proposed for nuclei instance segmentation, ranging from conventional image processing techniques to classical machine learning and advanced deep learning-based approaches (10–12). Image processing techniques such as adaptive thresholding or watershed segmentaion are still widely used for non-sophisticated images. Open-source software packages, such as ImageJ2 (13) or CellProfiler (14) have in-built image processing engines that can be used for microscopic image analysis, for example, for the segmentation of cell nuclei. However, for tissue samples where the nuclei are close together or even overlap or show considerable differences in intensity, such methods generally do not perform well (15, 16). For more complex images, machine learning, and in particular convolutional neural network (CNN)-based approaches, can be exploited (12). In the medical domain where access to fully annotated dataset is limited, more and more semi-supervised and unsupervised approaches are being used to deal with this issue (17, 18). However, supervised deep learning (DL) and specially CNN-based approaches still deliver the best performances in most cases. Supervised CNN algorithms have shown excellent detection, segmentation and classification performance for a range of medical image modalities such as COVID-19 detection in X-ray images (19), cervical cell classification or pollen grain classification in microscopic images (20–22) or foot ulcer segmentation in clinical images (23). CNN-based techniques for nuclei instance segmentation (and classification) can be broadly classified into two main categories, detection-based methods such as Mask R-CNN (24), and encoder-decoder-based approaches such as the U-Net model and its variants (25–27), while more recently, hybrid approaches have also been proposed to perform nuclei instance segmentation in H&E-stained histological images (28–30). Although these methods have shown significant improvement compared to other non-DL-based approaches, a robust and accurate model for the segmentation of nuclei of multiple cell types in different organs that generalizes well for different datasets is still challenging to achieve.

In this paper, we propose a novel architecture, consisting of one encoder and two decoders, to perform nuclei instance segmentation in H&E-stained histological images. While the encoder performs standard feature extraction, the decoders are designed to predict image foreground and distance maps of all nuclei. To verify robustness and generalisability of our segmentation model, we test it on three publicly available datasets and demonstrate it to achieve excellent instance segmentation performance. Moreover, to perform nuclei classification, we develop an independent U-Net-based model that classifies the objects detected by the dual decoder model. Applied on the CryoNuSeg (31) and NuInsSeg (32) datasets (both datasets for instance segmentation of cell nuclei) and the MoNuSAC dataset (16) (a dataset for instance segmentation and classification of cell nuclei), our method yields average panoptic quality (PQ) scores of 50.8%, 51.3%, and 62.1%, respectively. Furthermore, it is the top ranked entry in the MoNuSAC post-challenge leaderboard[1].

1 https://monusac-2020.grand-challenge.org/Results/.

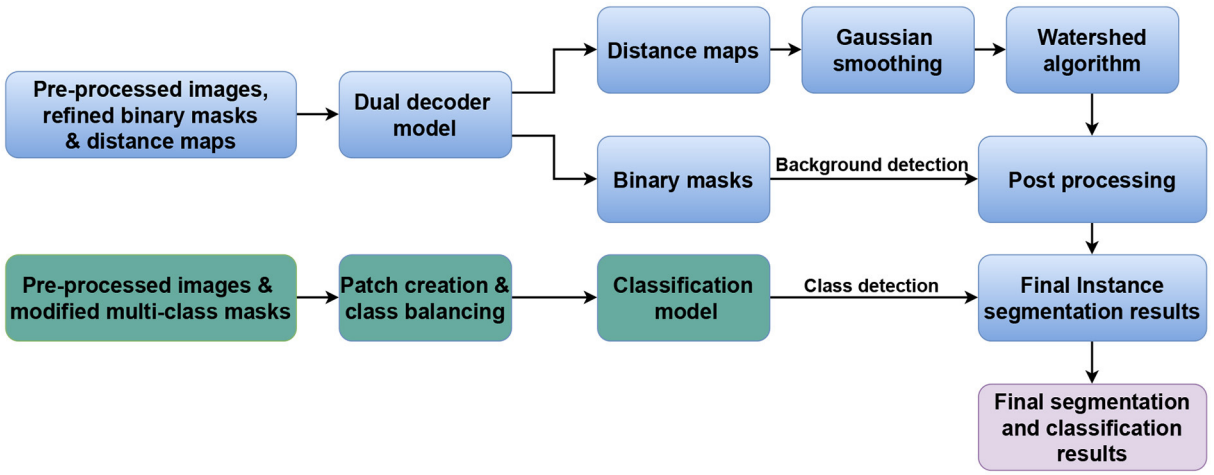

FIGURE 1
Generic workflow of the proposed method. The blue and green parts represent the nuclei instance segmentation and nuclei classification components, respectively.

2. Method

Our approach is inspired by our previous work on nuclei instance segmentation in H&E-stained histological images in Mahbod et al. (27). However, in contrast to there, where two separate models were designed to predict nuclei foreground and nuclei distance maps, a single model performs both tasks in our proposed approach. In addition, we also present an independent classification model to extend the workflow to also perform nuclei classification (if required). Figure 1 illustrates the generic workflow of our proposed model for performing nuclei instance segmentation (blue sections) and classification (green sections). In the following, we describe the details of the utilized datasets, our proposed model, and the experimental setup.

2.1. Datasets

We use four datasets of H&E-stained histological images, namely the CryoNuSeg (31), NuInsSeg, MoNuSeg (15), and MoNuSAC (16) datasets. Details on how we exploit these datasets in different experiments are given in Section 2.6.

CryoNuSeg, NuInsSeg, and MoNuSeg are manually annotated datasets for nuclei instance segmentation. The CryoNuSeg dataset contains 30 image patches of 512×512 pixels from 10 different human organs, NuInSeg comprises 667 image patches of the same size from 31 human and mouse organs, while MoNuSeg contains 44 images of size of $1,000 \times 1,000$ pixels from 9 human organs.

MoNuSAC is a manually annotated dataset for nuclei instance segmentation and classification and has 209 and 101 image patches in the training and test set, respectively. The images are of varying sizes, ranging from 82×35 to $1,422 \times 2,162$ pixels, and are derived from four human organs. Four nuclei classes are manually labeled, namely epithelial (21,752 nuclei), lymphocyte (23,460 nuclei), neutrophil (803 nuclei), and macrophage (894 nuclei).

Further details of the datasets can be found in Table 1 and the respective publications/repositories.

2.2. Pre-processing

Considering the dataset and the task (either nuclei instance segmentation or nuclei instance segmentation and classification), we apply the following pre-processing steps:

- **Intensity normalization**: we normalize the intensity values of the images in all datasets to the standard range of [0; 1] as normalization has shown to be an important step in training a CNN nuclei segmentation model (33).
- **Augmentation**: we apply various forms of morphological and color augmentations during the training phase including random horizontal/vertical flipping, random scaling and random contrast as well as brightness shifts.
- **Generating additional ground truth masks**: we create refined binary masks and elucidation distance maps from the provided manual binary annotations in all datasets to train the dual decoder segmentation model. To generate a refined binary masks, we remove the touching borders between the overlapping nuclei and then apply an erosion operation to obtain a better distinction between close

TABLE 1 Details of the utilized datasets.

	# patches	# nuclei	Magnification	# organs	Patch size	# classes	Source
CryoNuSeg	30	7,596	40×	10	512 × 512	-	TCGA
NuInsSeg	665	30,698	40×	31	512 × 512	-	IPA
MoNuSeg	44	28,846	40×	9	1,000 × 1,000	-	TCGA
MoNuSAC	310	46,909	40×	4	82 × 35 – 1422 × 2,162	4	TCGA

TCGA=The Cancer Genome Atlas; IPA= Institute for Pathophysiology and Allergy Research, Medical University of Vienna.

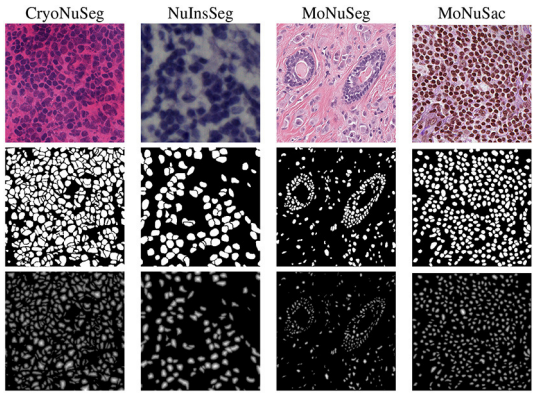

FIGURE 2
Image examples from the employed datasets (first row), the refined masks generated from ground truth annotations (second row), and the obtained distance maps (third row).

objects as suggested in Mahbod et al. (27). Examples of generated masks for each dataset are shown in Figure 2. For the MoNuSAC training data, we also create multi-class labeled masks to train the classification model. The generated refined binary and labeled masks are only used in the training phase, and for performance evaluation, the originally labeled masks are compared with the model's predictions.

2.3. Model

Our proposed method for nuclei instance segmentation is a dual decoder U-Net-based model. The generic architecture of the developed model is shown in Figure 3. The encoder part of the model has a similar architecture as the original U-Net model, with five convolution blocks, followed by max-pooling layers to extract deep features from the images. In contrast to the original U-Net architecture, we also add drop-out layers between convolutional layers as regularisers (with a rate of 0.1). The generated features in the encoder are then fed to the two decoder paths to predict nuclei foreground and nuclei elucidation distance maps, respectively. The architectures of these two decoders are identical except for the last layer. Both have five convolutional layers, which are equipped with drop-out layers similar to the encoder, and we use transposed convolutional layers in the decoders to up-sample the feature maps. The last activation functions in the first (distance map) and second (binary mask) decoders are linear and sigmoid activations, respectively. We use 3 × 3 convolutional kernels and ReLu activation layers in all other layers, both for encoder and decoder. The loss function of the distance map head is a mean squared error loss function, while the loss function of the binary mask head is a combination of Dice loss and binary cross-entropy loss. We merge the three losses, giving equal weight to each loss term. We utilize the Adam optimiser (34) and an initial learning rate of 0.001 to train the dual decoder model. We train the model for 120 epochs while dropping the learning rate by a factor of 0.1 after every 20 epochs. The model is trained from scratch after Xavier initialization (35) of the weights.

To obtain the final instance segmentation results, the outputs of the dual decoder models are merged as shown in Figure 1. We first calculate the average nucleus size from the semantic segmentation results (binary mask head), and then apply a Gaussian smoothing filter to the distance map predictions with the kernel size of the file derived from the average nucleus size. Finally, we identify the local maxima from the filtered predicted distance maps and use them as seed points for a marker-controlled watershed algorithm (36) to produce the labeled segmented masks.

To perform nuclei classification as required in the MoNuSAC challenge, we design an independent U-Net-based classification model to the workflow. The generic architecture of the developed classification model is shown in Figure 4. The encoder and decoder of the classification model are similar to the dual decoder model but with a unique decoder with a softmax activation in the last layer. Moreover, in contrast to the dual decoder model, here we generate four output masks, one for each nucleus class. We use a combination of categorical cross-entropy and Dice loss (with equal weights) as loss function, while the other parameters are identical to the dual decoder model. The output from the classification network is used to determine the nuclei classes of the predicted objects by the dual decoder model. We use a majority voting approach based on the output

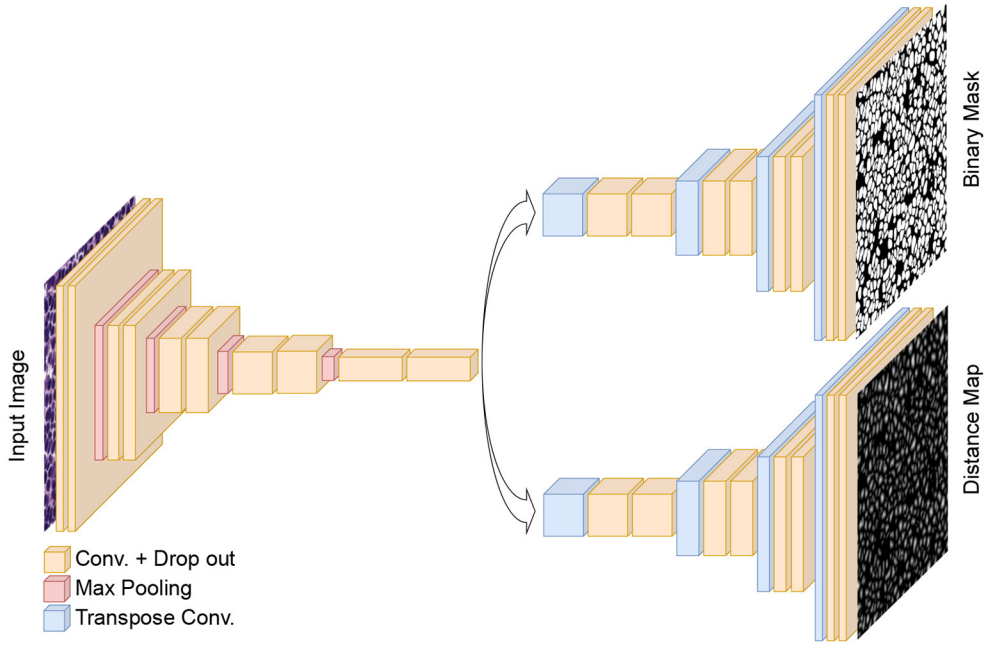

FIGURE 3
The architecture of the proposed dual decoder model for nuclei instance segmentation. The two decoders are designed to perform binary segmentation and distance map prediction, respectively. For simplicity, skip connections between the encoder and two decoders are not shown.

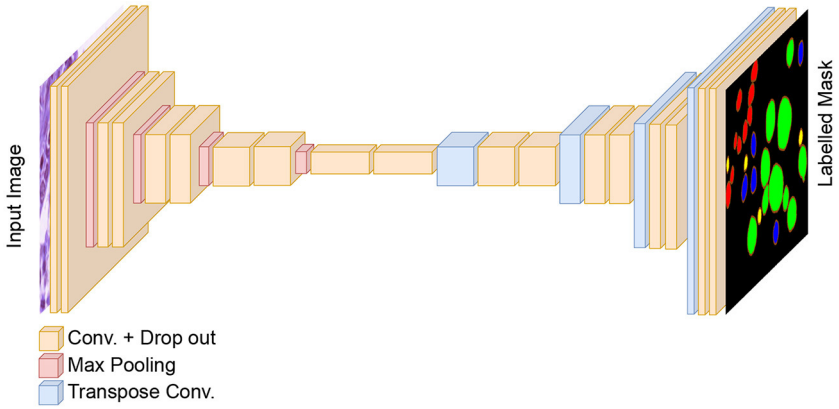

FIGURE 4
The architecture of the classification model for nuclei instance categorization. The different colors in the output represent the nuclei classes in the MoNuSAC dataset. For simplicity, skip connections between the encoder and two decoders are not shown.

of the classification model to choose the nucleus type for each object.

2.4. Post-processing

We remove tiny detected objects (with an area less than 30 pixels) from the segmentation masks during post-processing. Any holes inside detected nuclei are filled using morphological operations.

For the MoNuSAC experiments, we also remove the vague areas from the final instance segmentation and classification masks. The challenge organizers provide these vague areas for the entire test set images. We use a five-fold cross-validation model ensemble and test-time augmentation (TTA) for our finalized submission for the MoNuSAC post-challenge phase, as these methods have been shown to boost the segmentation performances in other studies (37) including our own (38). We use 90-degree rotated and horizontally flipped images for TTA.

2.5. Evaluation

To evaluate the results for the nuclei instance segmentation tasks (CryoNuSeg and NuInsSeg), we use Dice score, aggregate Jaccard Index (AJI), and the panoptic quality (PQ) score. While the Dice score characterizes the general semantic segmentation performance, AJI and PQ score also evaluate a model's ability to separate touching objects and thus quantify instance segmentation performance. A higher Dice score, higher AJI and higher PQ score indicate better performance; further details about the evaluation indices can be found in Graham et al. (39) and Kirillov et al. (40). We also perform statistical Wilcoxon signed-rank test method (37, 41) for each of the evaluation index to compare our model with other approaches.

For the combined nuclei instance segmentation and classification task (MoNuSAC), we use the average PQ score per nuclei class for evaluation. The MoNuSAC challenge organizers performed the evaluation based on the 101 test images of the challenge dataset. Further details about the submission process and multi-class mask format for evaluation can be found on the challenge website[2] and in Verma et al. (16).

2.6. Experimental setup

We conduct three experiments to evaluate the performance of our proposed method. In the first two experiments, we use the CryoNuSeg and NuInsSeg datasets, respectively, to evaluate nuclei instance segmentation performance. In the third experiment, we assess nuclei instance segmentation and classification performance using the MoNuSAC and MoNuSeg datasets with the MoNuSeg dataset only being used for training but not for evaluation purposes. We run our experiments with an identical setup to the one proposed in the reference studies (16, 31) to compare our results with other state-of-the-art algorithms.

For the CryoNuSeg experiment, we follow the 10-fold cross-validation (10CV) scheme proposed in the original study (31), for which the dataset (30 images) is divided into 10-folds (each containing three images) based on the organs. Then, in each CV fold, the images from nine organs are used for training, while the images from the remaining organ are used for testing. We use full-sized images of 512×512 pixels both for training and testing.

For the NuInsSeg experiment, we use a 5-fold cross-validation scheme as suggested in the NuInsSeg repository[3]. Full-sized images of 512×512 pixels are used for training and testing. We utilize an identical suggested random state to generate the folds.

For the MoNuSAC experiment, we use images of size 256×256 randomly cropped from the MoNuSeg dataset to pre-train the dual decoder model. Then, we utilize 256×256 cropped images from the MoNuSAC training set to fine-tune the model. Since some MoNuSAC images are smaller than 256×256 pixels, we use white pixel padding to create 256×256 pixel images. To train the classification model, we extract overlapping patches from the MoNuSAC training images.To address the class imbalance in the dataset, we extract more patches from the underrepresented classes, taking into account the number of nuclei in each class in the training set. In total, 14,862 patches are generated to train the classification model. To evaluate the performance, we use the test set of the MoNuSAC challenge. The test images are first padded (white pixel padding) to create square images and then resized to suitable image sizes (the closest size divisible by 32). We apply the inverse steps to the predicted results to have the final segmentation masks identical to the original MoNuSAC test image sizes. It should be noted that the evaluation in this experiment was performed directly by the challenge organizers.

All experiments are performed on a single workstation with an Intel Core i7-8700 3.20 GHz CPU, 32 GB of RAM and a TITIAN V NVIDIA GPU card with 12 GB of installed memory. Matlab software (version 2020a) is used to prepare the datasets and generate segmentation masks, while the Tensorflow (version 2.4) and Keras (version 2.4) deep learning frameworks are used for model training and testing.

3. Results and discussion

The nuclei instance segmentation results on the CryoNuSeg dataset are given in Table 2, which lists the Dice score, AJI and PQ score of our proposed model as well as of several other approaches. The comparative results are split into three sections.

The first section (first row) compares our method (row 8) with a standard image processing technique using the StrataQuest (SQ) software (version 7.1) [4]. We use SQ's pre-built image processing engines to derive the results. We use adaptive thresholding, local maxima detection, Watershed algorithm and morphological operations to derive the results. The results show that our model delivers a much better performance considering all three evaluation indices.

The second section (rows 2–4) is an ablation study. This section shows the performance of a single semantic segmentation U-Net (row 2), a single distance U-Net (row 3), and two independent models for semantic segmentation and distance map prediction (row 4) as suggested in Mahbod et al. (27). The results of the ablation study confirm the superior performance of our proposed dual decoder approach (row 8) compared to the sub-models for all three evaluation indices.

2 https://monusac-2020.grand-challenge.org/.

3 https://www.kaggle.com/datasets/ipateam/nuinsseg.

4 TissueGnostics GmbH https://tissuegnostics.com/products/contextual-image-analysis/strataquest.

TABLE 2 Nuclei instance segmentation results on CryoNuSeg dataset based on 10CV configuration from Mahbod et al. (31).

	Dice [%)]	AJI [%)]	PQ [%)]
Standard image processing	71.9 (*)	39.9 (*)	32.0 (*)
U-Net+Watershed (25, 36)	79.3 (*)	47.8 (*)	40.4 (*)
Distance U-Net+Watershed (27, 42)	74.7 (*)	48.6(*)	37.5 (*)
Two-stage U-Net (27)	80.3 (*)	52.5 (*)	47.7 (*)
Attention U-Net (43)	79.4 (*)	48.2 (*)	41.7 (*)
Residual attention U-Net (43, 44)	79.8 (*)	49.1 (*)	42.7 (*)
CellPose (45)	77.6 (*)	52.6	50.9
Proposed dual decoder U-Net	81.5	54.1	50.8

(*) signs for each evaluation index show statistical differences ($p < 0.05$) between our proposed method and other approaches.

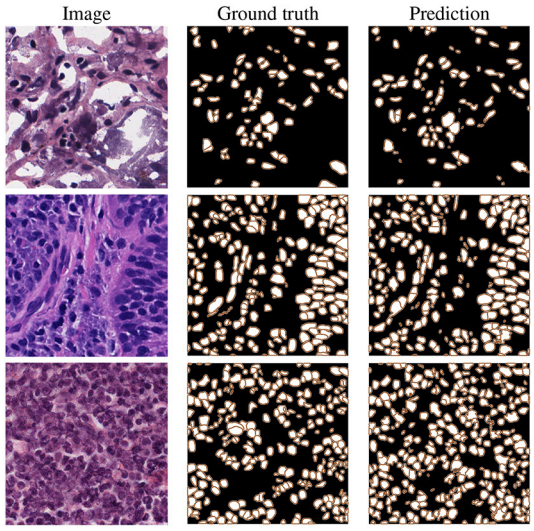

FIGURE 5
Example results on CryoNuSeg test images, selected from adrenal gland **(top)**, larynx **(middle)**, and lymph node **(bottom)** samples.

The third section (rows 5–7) compares the performance of our method (row 8) with other state-of-the-art DL-based algorithms. As is evident from the ablation study and reported results in the table, our proposed dual decoder U-Net-based model outperforms the other approaches based on the Dice score and AJI and delivers very competitive performance based on the PQ score.

It should be noted that for all reported results in the table (besides the standard image processing technique where a set of fixed empirically-driven parameters are used), we utilize the exact same 10CV folds suggested in Mahbod et al. (31). These results confirm our proposed algorithms' excellent semantic and instance segmentation performances. Examples of this performance are given in Figure 5, which shows nuclei instance segmentation results for some CryoNuSeg images.

We report the results of instance segmentation of our model and several others on the NuInsSeg dataset in Table 3, all based on identical 5CV folds as defined in the repository. Similar to the previous experiments for the CryoNuSeg dataset, we report the results in three sections for comparison to standard image processing technique (first row), ablation study (rows 2-4) and comparison to other deep learning- based approaches (rows 5-7). The results in the first two sections confirm the superior performance of our proposed method compared to standard image processing and sub-models derived from our dual decoder architecture.

As we can see in the third section, our proposed model (row 8) clearly achieves the best instance-based segmentation performance (i.e., the highest AJI and PQ score), while delivering slighlty inferior semantic segmentation performance based on the Dice score. In Figure 6, we show some examples of the automatic segmentations obtained from our approach.

The results in Tables 2, 3 also show that the majority of the DL-based results are superior in comparison to the applied standard image processing approach by a large margin,

TABLE 3 Nuclei instance segmentation results on NuInsSeg dataset based on the 5CV configuration from the repository.

	Dice [%)]	AJI [%)]	PQ [%)]
Standard Image processing	47.8 (*)	23.6 (*)	10.7 (*)
U-Net+Watershed (25, 36)	78.8	50.5 (*)	42.8 (*)
Distance U-Net+Watershed (27, 42)	74.1 (*)	50.3 (*)	41.0 (*)
Two-stage U-Net (27)	76.6 (*)	52.7 (*)	47.2 (*)
Attention U-Net (43)	80.5 (*)	45.7 (*)	36.4 (*)
Residual attention U-Net (43, 44)	81.4 (*)	46.2 (*)	36.9 (*)
CellPose (45)	74.7 (*)	52.8 (*)	48.0 (*)
Proposed dual decoder U-Net	79.4	55.9	51.3

(*) signs for each evaluation index show statistical differences ($p < 0.05$) between our proposed method and other approaches.

especially in Table 3 (minimum difference of 26.3%, 22.1%, and 25.7% for the Dice, AJI and PQ score, respectively).

The results obtained on the MoNuSAC dataset are given in Table 4. Since the results are directly provided by the challenge organizers and they only report results in terms of average PQ scores, we do so also in the table. It should be noted that the results are slightly different from the original report in Verma et al. (16) since the authors of Verma et al. (16) detected a bug in the evaluation code; the official updated results (identical to those in Table 4) are available in Verma et al. (46), while further details about the evaluation error can be found in Foucart et al. (47).

Our proposed method is top-ranked in the MoNuSAC post-challenge leaderboard and would be ranked second considering

both legacy and post-challenge phases. For nuclei class-dependent scores, our model achieves the second, second, fourth and second rank for the epithelial, lymphocyte, neutrophil, and macrophage class, respectively. While our method yields very competitive scores in comparison to the top-ranked approach, the results are not directly comparable since the latter used the PanNuke dataset of about 200,000 segmented nuclei (48), i.e., a vastly larger dataset, for pre-training. Samples results from the MoNuSAC experiment are shown in Figure 7.

In general, our results in Tables 2–4 show superior or at least very competitive nuclei instance segmentation performance of our model in comparison to other state-of-the-art methods. Multi-task learning in encoder-decoder-based architectures has become more popular in recent years. Works such as DDU-Net (49) for small-size road detection in high-resolution remote sensing images, ADU-Net (50) for rain and haze removal in natural images or two-stage and dual-decoder convolutional U-Net (51) ensembles for vessel and plaque segmentation in ultrasound images are examples of multi-task models for semantic segmentation or image reconstruction. In our study, we propose a novel dual-task model for a new application, i.e., nuclei instance segmentation in histological images.

While here we report results on datasets that mainly serve for development and benchmarking purposes, our final intention is to make use of our method in either clinical or research applications. Automatic nuclei segmentation and classification are essential tasks in digital pathology; they enable nuclei morphology analysis, cell type classification, as well as cancer detection and grading. Our model can add to the qualitative and quantitative analyses of cells in cancer-affected tissues whenever H&E-stained tissue sections are part of the diagnostic pipeline. For example, in the histopathologic examination of prostate tissue biopsies, nuclei segmentation is still a decisive factor for diagnosing and grading prostate

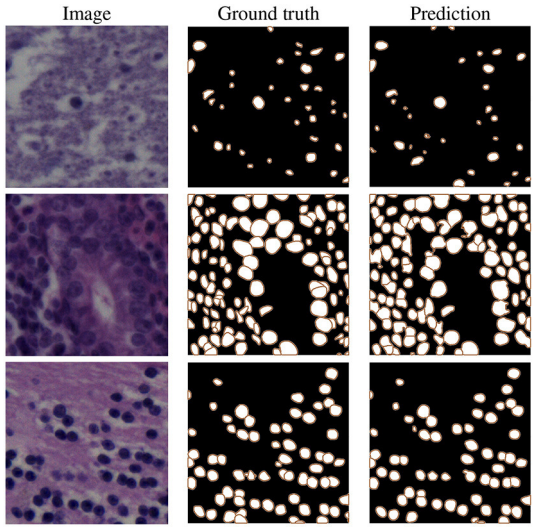

FIGURE 6
Example results on NuInsSeg test images, selected from human brain **(top)**, human cardia **(middle)**, and human cerebellum **(bottom)** samples.

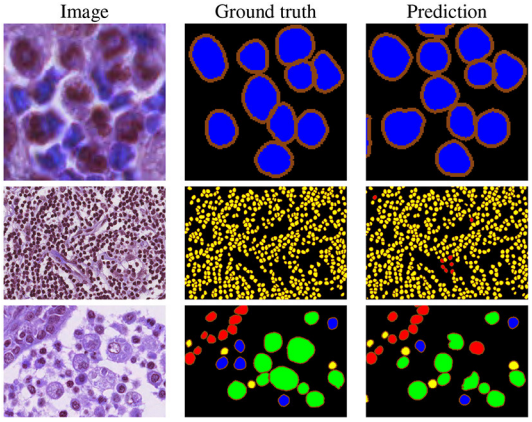

FIGURE 7
Example results on MoNuSAC images. The colors in the ground truth and segmentation masks represent the different nuclei types (red = epithelial, yellow = lymphocyte, blue = neutrophil, and green = macrophage).

TABLE 4 Nuclei instance segmentation and classification results on the MoNuSAC challenge test data in terms of average PQ scores for different nucleus classes.

Team	Epithilial cells	Lymphocytes	Macrophages	Neutrophils	Average	Rank
TIA-Lab	60.3	63.5	63.1	66.5	65.8	L1
SJTU-426	62.2	56.0	61.2	63.0	61.8	L2
IIAI	60.1	55.6	60.5	61.3	60.5	PL2
Sharif_hooshpardaz	55.2	54.5	50.2	60.0	58.2	PL3
IVG	56.7	45.8	51.2	60.0	55.3	L3
Proposed	61.0	57.1	55.4	65.2	62.1	PL1

In the rank column, L represents the legacy leaderboard, while PL refers to the post-challenge leaderboard.

cancer. A concentration of epithelial nuclei on the prostate gland's boundaries indicates an intact tissue structure (the tissue is thus benign). On the other hand, spreading of epithelial nuclei with irregular shapes across the stroma areas suggests that the biopsy sample is malignant (52, 53). Following the detection and segmentation of nuclei with our proposed model for instance segmentation, the classification component of our model could thus be trained to distinguish healthy and malignant nuclei shapes.

Previous work has suggested that the same trained algorithms often yield different performance metrics for tissues from different organs (54, 55). Thus, effective nuclei segmentation methods which can be generalized across various cell, tissue and organ types are required. Our model has demonstrated to perform very well on different datasets containing various organs generated by different laboratories or clinics. Another application scenario is pharmacological research, where imaging technologies have become essential tools for drug development. Here, our method could enable rapid and accurate evaluation of *in vivo* experiments, where the effect of certain drugs on cell number (i.e., nuclei number) or the shape and size of the nuclei should be tested, specifically in organs with a high density of nuclei. If, in this context, it is required to evaluate the effect of the drug on certain cell types, such as immune cells or cancer cells, further training of the classification component of our model might be required.

Last no least, some recent work, such as low-cost U-Net (56) and pruned models (57), introduce computationally less expensive models to reduce inference time and make the CNN-based algorithm more applicable in a real clinical setting, and we aim to extend our work in this direction in our future research.

4. Conclusions

Nuclei instance segmentation and classification are essential in analyzing H&E-stained whole slide histological images. In this paper, we have proposed a multi-task encoder-decoder-based model to identify, segment, and if additionally required classify nuclei in histological image patches. The proposed model is demonstrated to yield excellent performance on three benchmark datasets and shown to outperform other state-of-the-art approaches.

Data availability statement

The datasets presented in this study can be found in online repositories. The names of the repository/repositories and accession number(s) can be found below: https://github.com/masih4/dual_decoder_nuclei_segmentation.

Ethics statement

Ethical review and approval was not required for the study on human participants in accordance with the local legislation and institutional requirements. Written informed consent for participation was not required for this study in accordance with the National Legislation and the institutional requirements. Ethical review and approval was not required for the animal study because this study was conducted retrospectively using human and animal subject data made available through open access. Ethical approval was not required as confirmed by the license attached with the open access data.

Author contributions

AM and IE: conceptualization, methodology, and writing–review and editing. GD, RE, and IE: funding acquisition. AM: investigation. IE and SH: supervision. AM, GS, and SH: writing–original draft. All authors read and agreed to the published version of the manuscript.

Funding

This work was supported by the Austrian Research Promotion Agency (FFG), No. 872636.

Acknowledgments

The authors would like to thank TissueGnostics's Research and Development team for valuable inputs and suggestions. Moreover, we thank NVIDIA corporation for the generous GPU donation.

Conflict of interest

Author RE was employed by TissueGnostics GmbH.

The remaining authors declare that the research was conducted in the absence of any commercial or financial relationships that could be construed as a potential conflict of interest.

Publisher's note

References

1. Chan JKC. The wonderful colors of the hematoxylin-eosin stain in diagnostic surgical pathology. *Int J Surg Pathol*. (2014) 22:12–32. doi: 10.1177/1066896913517939

2. Djuric U, Zadeh G, Aldape K, Diamandis P. Precision histology: how deep learning is poised to revitalize histomorphology for personalized cancer care. *NPJ Prec Oncol*. (2017) 1:1–5. doi: 10.1038/s41698-017-0022-1

3. Angerilli V, Galuppini F, Pagni F, Fusco N, Malapelle U, Fassan M. The role of the pathologist in the next-generation ERA of tumor molecular characterization. *Diagnostics*. (2021) 11:339. doi: 10.3390/diagnostics11020339

4. Wu Y, Cheng M, Huang S, Pei Z, Zuo Y, Liu J, et al. Recent advances of deep learning for computational histopathology: principles and applications. *Cancers*. (2022) 14:1199. doi: 10.3390/cancers14051199

5. Esteva A, Kuprel B, Novoa RA, Ko J, Swetter SM, Blau HM, et al. Dermatologist-level classification of skin cancer with deep neural networks. *Nature*. (2017) 542:115–8. doi: 10.1038/nature21056

6. Zhang Z, Chen P, McGough M, Xing F, Wang C, Bui M, et al. Pathologist-level interpretable whole-slide cancer diagnosis with deep learning. *Nat Mach Intell*. (2019) 1:236. doi: 10.1038/s42256-019-0052-1

7. Dong F, Irshad H, Oh EY, Lerwill MF, Brachtel EF, Jones NC, et al. Computational pathology to discriminate benign from malignant intraductal proliferations of the breast. *PLoS ONE*. (2014) 9:e114885. doi: 10.1371/journal.pone.0114885

8. Skinner BM, Johnson EE. Nuclear morphologies: their diversity and functional relevance. *Chromosoma*. (2017) 126:195–12. doi: 10.1007/s00412-016-0614-5

9. Dey P. Cancer nucleus: morphology and beyond. *Diagn Cytopathol*. (2010) 38:382–90. doi: 10.1002/dc.21234

10. Kumar N, Verma R, Sharma S, Bhargava S, Vahadane A, Sethi A. A dataset and a technique for generalized nuclear segmentation for computational pathology. *IEEE Trans Med Imaging*. (2017) 36:1550–60. doi: 10.1109/TMI.2017.2677499

11. Hayakawa T, Prasath V, Kawanaka H, Aronow BJ, Tsuruoka S. Computational nuclei segmentation methods in digital pathology: a survey. *Arch Comput Methods Eng*. (2021) 28:1–13. doi: 10.1007/s11831-019-09366-4

12. Hollandi R, Moshkov N, Paavolainen L, Tasnadi E, Piccinini F, Horvath P. Nucleus segmentation: towards automated solutions. *Trends Cell Biol*. (2022) 32:295–310. doi: 10.1016/j.tcb.2021.12.004

13. Rueden CT, Schindelin J, Hiner MC, DeZonia BE, Walter AE, Arena ET, et al. ImageJ2: Imagej for the next generation of scientific image data. *BMC Bioinformatics*. (2017) 18:1–26. doi: 10.1186/s12859-017-1934-z

14. Carpenter AE, Jones TR, Lamprecht MR, Clarke C, Kang IH, Friman O, et al. CellProfiler: image analysis software for identifying and quantifying cell phenotypes. *Genome Biol*. (2006) 7:R100. doi: 10.1186/gb-2006-7-10-r100

15. Kumar N, Verma R, Anand D, Zhou Y, Onder OF, Tsougenis E, et al. A multi-organ nucleus segmentation challenge. *IEEE Trans Med Imaging*. (2020) 39:1380–91. doi: 10.1109/TMI.2019.2947628

16. Verma R, Kumar N, Patil A, Kurian NC, Rane S, Graham S, et al. MoNuSAC2020: A multi-organ nuclei segmentation and classification challenge. *IEEE Trans Med Imaging*. (2021) 40:3413–23. doi: 10.1109/TMI.2021.3085712

17. Alemi Koohbanani N, Jahanifar M, Zamani Tajadin N, Rajpoot N. NuClick: a deep learning framework for interactive segmentation of microscopic images. *Med Image Anal*. (2020) 65:101771. doi: 10.1016/j.media.2020.101771

18. Raza K, Singh NK. A tour of unsupervised deep learning for medical image analysis. *Curr Med Imaging*. (2021) 17:1059–77. doi: 10.2174/1573405617666210127154257

19. Rahaman MM, Li C, Yao Y, Kulwa F, Rahman MA, Wang Q, et al. Identification of COVID-19 samples from chest X-Ray images using deep learning: a comparison of transfer learning approaches. *J Xray Sci Technol*. (2020) 28:821–39. doi: 10.3233/XST-200715

20. Liu W, Li C, Xu N, Jiang T, Rahaman MM, Sun H, et al. CVM-Cervix: a hybrid cervical Pap-smear image classification framework using CNN, visual transformer and multilayer perceptron. *Pattern Recognit*. (2022) 130:108829. doi: 10.1016/j.patcog.2022.108829

21. Rahaman MM, Li C, Yao Y, Kulwa F, Wu X, Li X, et al. DeepCervix: A deep learning-based framework for the classification of cervical cells using hybrid deep feature fusion techniques. *Comput Biol Med*. (2021) 136:104649. doi: 10.1016/j.compbiomed.2021.104649

22. Mahbod A, Schaefer G, Ecker R, Ellinger I. Pollen grain microscopic image classification using an ensemble of fine-tuned deep convolutional neural networks. In: *International Conference on Pattern Recognition*. Springer (2021). p. 344–56.

23. Wang C, Mahbod A, Ellinger I, Galdran A, Gopalakrishnan S, Niezgoda J, et al. FUSeg: the foot ulcer segmentation challenge. *arXiv preprint arXiv:220100414*. (2022). doi: 10.48550/arXiv.2201.00414

24. Johnson JW. Adapting mask-RCNN for automatic nucleus segmentation. *arXiv preprint arXiv:180500500*. (2018) doi: 10.1007/978-3-030-17798-0_32

25. Ronneberger O, Fischer P, Brox T. U-Net: convolutional networks for biomedical image segmentation. In: *International Conference on Medical Image Computing and Computer-Assisted Intervention*. Munich (2015). p. 234–41. doi: 10.1007/978-3-319-24574-4_28

26. Zeng Z, Xie W, Zhang Y, Lu Y. RIC-Unet: an improved neural network based on Unet for nuclei segmentation in histology images. *IEEE Access*. (2019) 7:21420–8. doi: 10.1109/ACCESS.2019.2896920

27. Mahbod A, Schaefer G, Ellinger I, Ecker R, Smedby Ö, Wang C. A two-stage U-Net algorithm for segmentation of nuclei in H&E-stained tissues. In: *European Congress on Digital Pathology*. Warwick (2019). p. 75–82. doi: 10.1007/978-3-030-23937-4_9

28. Vuola AO, Akram SU, Kannala J. Mask-RCNN and U-Net ensembled for nuclei segmentation. In: *International Symposium on Biomedical Imaging*. Venice (2019). p. 208–12. doi: 10.1109/ISBI.2019.8759574

29. Bancher B, Mahbod A, Ellinger I, Ecker R, Dorffner G. Improving mask R-CNN for nuclei instance segmentation in hematoxylin & eosin-stained histological images. In: *MICCAI Workshop on Computational Pathology. vol. 156*. Strasbourg (2021). p. 20–35. Available online at: https://proceedings.mlr.press/v156/bancher21a.html

30. Xu Z, Sobhani F, Moro CF, Zhang Q. US-Net for robust and efficient nuclei instance segmentation. In: *International Symposium on Biomedical Imaging*. Venice (2019). p. 44–7. doi: 10.1109/ISBI.2019.8759530

31. Mahbod A, Schaefer G, Bancher B, Löw C, Dorffner G, Ecker R, et al. CryoNuSeg: a dataset for nuclei instance segmentation of cryosectioned H&E-stained histological images. *Comput Biol Med*. (2021) 132:104349. doi: 10.1016/j.compbiomed.2021.104349

32. Mahbod A. *NuInsSeg A Fully Annotated Dataset for Nuclei Instance Segmentation in H&E-Stained Images*. (2022). Available online at: https://www.kaggle.com/datasets/ipateam/nuinsseg (accessed November 2, 2022).

33. Mahbod A, Schaefer G, Löw C, Dorffner G, Ecker R, Ellinger I. Investigating the impact of the Bit depth of fluorescence-stained images on the performance of deep learning-based nuclei instance segmentation. *Diagnostics*. (2021) 11:967. doi: 10.3390/diagnostics11060967

34. Kingma DP, Ba J. Adam: a method for stochastic optimization. In: *International Conference on Learning Representations*. California (2015). Available online at: https://dblp.org/rec/journals/corr/KingmaB14.html

35. Glorot X, Bengio Y. Understanding the difficulty of training deep feedforward neural networks. In: *International Conference on Artificial Intelligence and Statistics*. Sardinia (2010). p. 249–56. Available online at: https://proceedings.mlr.press/v9/glorot10a/glorot10a.pdf

36. Yang X, Li H, Zhou X. Nuclei segmentation using marker-controlled watershed, tracking using mean-shift, and Kalman filter in time-lapse microscopy. *IEEE Trans Circ Syst I Regul Pap*. (2006) 53:2405–14. doi: 10.1109/TCSI.2006.884469

37. Moshkov N, Mathe B, Kertesz-Farkas A, Hollandi R, Horvath P. Test-time augmentation for deep learning-based cell segmentation on microscopy images. *Sci Rep*. (2020) 10:1–7. doi: 10.1038/s41598-020-61808-3

38. Mahbod A, Ecker R, Ellinger I. Automatic foot Ulcer segmentation using an ensemble of convolutional neural networks. *arXiv preprint arXiv:210901408*. (2021).

39. Graham S, Vu QD, Raza SEA, Azam A, Tsang YW, Kwak JT, et al. Hover-Net: simultaneous segmentation and classification of nuclei in multi-tissue histology images. *Med Image Anal*. (2019) 58:101563. doi: 10.1016/j.media.2019.101563

40. Kirillov A, He K, Girshick R, Rother C, Dollar P. Panoptic Segmentation. In: *Conference on Computer Vision and Pattern Recognition*. California (2019). p. 9404–13. Available online at: https://openaccess.thecvf.com/content_CVPR_2019/html/Kirillov_Panoptic_Segmentation_CVPR_2019_paper.html

41. Gibbons JD, Chakraborti S. *Nonparametric Statistical Inference: Revised and Expanded*. Alabama: CRC Press (2014). Available online at: http://www.ru.ac.bd/stat/wp-content/uploads/sites/25/2019/03/501_13_Gibbons_Nonparametric_statistical_inference.pdf

42. Naylor P, Laé M, Reyal F, Walter T. Segmentation of nuclei in histopathology images by deep regression of the distance map. *IEEE Trans Med Imaging*. (2019) 38:448–59. doi: 10.1109/TMI.2018.2865709

43. Oktay O, Schlemper J, Folgoc LL, Lee M, Heinrich M, Misawa K, et al. Attention U-Net: learning where to look for the pancreas. *arXiv preprint arXiv:180403999*. (2018). doi: 10.48550/arXiv.1804.03999

44. He K, Zhang X, Ren S, Sun J. Deep residual learning for image recognition. In: *Conference on Computer Vision and Pattern Recognition*. Las Vegas, NV (2016). p. 770–8. doi: 10.1109/CVPR.2016.90

45. Stringer C, Wang T, Michaelos M, Pachitariu M. Cellpose: a generalist algorithm for cellular segmentation. *Nat Methods*. (2021) 18:100–6. doi: 10.1038/s41592-020-01018-x

46. Verma R, Kumar N, Patil A, Kurian NC, Rane S, Sethi A. MoNuSAC2020: A multi-organ nuclei segmentation and classification challenge. *IEEE Trans Med Imaging*. (2022) 41:1000–3. doi: 10.1109/TMI.2022.3157048

47. Foucart A, Debeir O, Decaestecker C. Comments on "MoNuSAC2020: a multi-organ nuclei segmentation and classification challenge". *IEEE Trans Med Imaging*. (2022) 41:997–9. doi: 10.1109/TMI.2022.3156023

48. Gamper J, Koohbanani NA, Graham S, Jahanifar M, Khurram SA, Azam A, et al. PanNuke dataset extension, insights and baselines. *arXiv preprint arXiv:200310778*. (2020). doi: 10.48550/arXiv.2003.10778

49. Wang Y, Peng Y, Li W, Alexandropoulos GC, Yu J, Ge D, et al. DDU-Net: dual-decoder-U-Net for road extraction using high-resolution remote sensing images. *IEEE Trans Geosci Remote Sens*. (2022) 60:1–12. doi: 10.1109/TGRS.2022.3197546

50. Feng Y, Hu Y, Fang P, Yang Y, Liu S, Chen S. Asymmetric dual-decoder U-net for joint rain and haze removal. *arXiv preprint arXiv:220606803*. (2022). doi: 10.48550/arXiv.2206.06803

51. Xie M, Li Y, Xue Y, Huntress L, Beckerman W, Rahimi SA, et al. Two-stage and dual-decoder convolutional U-Net ensembles for reliable vessel and plaque segmentation in carotid ultrasound images. In: *IEEE International Conference on Machine Learning and Applications*. Miami, FL: IEEE (2020). p. 1376–81.

52. Ren J, Sadimin E, Foran DJ, Qi X. Computer aided analysis of prostate histopathology images to support a refined Gleason grading system. In: *Medical Imaging 2017: Image Processing. Vol. 10133*. Florida, FL: SPIE (2017). p. 101331V. doi: 10.1117/12.2253887

53. Ali T, Masood K, Irfan M, Draz U, Nagra AA, Asif M, et al. Multistage segmentation of prostate cancer tissues using sample entropy texture analysis. *Entropy*. (2020) 22:1370. doi: 10.3390/e22121370

54. Kang Q, Lao Q, Fevens T. Nuclei segmentation in histopathological images using two-stage learning. In: *Medical Image Computing and Computer Assisted Intervention*. Shenzhen: Springer International Publishing (2019). p. 703–11. doi: 10.1007/978-3-030-32239-7_78

55. Cui Y, Zhang G, Liu Z, Xiong Z, Hu J. A deep learning algorithm for one-step contour aware nuclei segmentation of histopathology images. *Med Biol Eng Comput*. (2019) 57:2027–43. doi: 10.1007/s11517-019-02008-8

56. Zhang J, Li C, Kosov S, Grzegorzek M, Shirahama K, Jiang T, et al. LCU-Net: a novel low-cost U-Net for environmental microorganism image segmentation. *Pattern Recognit*. (2021) 115:107885. doi: 10.1016/j.patcog.2021.107885

57. Mahbod A, Entezari R, Ellinger I, Saukh O. Deep neural network pruning for nuclei instance segmentation in hematoxylin and eosin-stained histological images. In: *Applications of Medical Artificial Intelligence*. Cham: Springer (2022). p. 108–17. doi: 10.1007/978-3-031-17721-7_12

frontiers | Frontiers in Oncology

TYPE Brief Research Report
PUBLISHED 12 April 2023
DOI 10.3389/fonc.2023.1151255

OPEN ACCESS

EDITED BY
Rupert Ecker,
TissueGnostics GmbH, Austria

REVIEWED BY
Jung Sun Yoo,
Hong Kong Polytechnic University,
Hong Kong SAR, China
Gudrun Elisabeth Koehl,
University Hospital Regensburg,
Germany

*CORRESPONDENCE
Emmanuel M. Gabriel
Gabriel.Emmanuel@mayo.edu

SPECIALTY SECTION
This article was submitted to Surgical Oncology, a section of the journal Frontiers in Oncology

RECEIVED 27 January 2023
ACCEPTED 30 March 2023
PUBLISHED 12 April 2023

CITATION
Gabriel EM, Sukniam K, Popp K and Bagaria SP (2023) Human intravital microscopy in the study of sarcomas: an early trial of feasibility.
Front. Oncol. 13:1151255.
doi: 10.3389/fonc.2023.1151255

Human intravital microscopy in the study of sarcomas: an early trial of feasibility

Emmanuel M. Gabriel[1]*, Kulkaew Sukniam[2], Kyle Popp[3] and Sanjay P. Bagaria[1]

[1]Department of General Surgery, Division of Surgical Oncology, Mayo Clinic, Jacksonville, FL, United States, [2]Department of General Surgery, Philadelphia College of Osteopathic Medicine, Suwanee, GA, United States, [3]Florida State University, Tallahassee, FL, United States

Sarcomas comprise a vast and heterogenous group of rare tumors. Because of their diversity, it is challenging to study sarcomas as a whole with regard to their biological and molecular characteristics. This diverse set of tumors may also possess differences related to their tumor-associated vasculature, which in turn may impact the ability to deliver systemic therapies (e.g., chemotherapy, targeted therapies, and immunotherapy). Consequently, response to systemic treatment may also be variable as these depend on the ability of the therapy to reach the tumor target *via* the tumor-associated vasculature. There is a paucity of data regarding sarcoma-related tumor vessels, likely in part to the rarity and heterogeneity of this cancer as well as the previously limited ability to image tumor-associated vessels in real time. Our group has previously utilized confocal fluorescent imaging technology to observe and characterize tumor-associated vessels in real time during surgical resection of tumors, including cutaneous melanoma and carcinomatosis implants derived from gastrointestinal, gynecological, or primary peritoneal (e.g., mesothelioma) tumors. Our prior studies have demonstrated the feasibility of real-time, human intravital microscopy in the study of these tumor types, leading to early but important new data regarding tumor vessel characteristics and their potential implications on drug delivery and efficacy. In this brief report, we present our latest descriptive findings in a cohort of patients with sarcoma who underwent surgical resection and real-time, intravital microscopy of their tumors. Overall, intravital imaging was feasible during the surgical resection of large sarcomas.

Clinical trial registrations: ClinicalTrials.gov, identifier NCT03517852; ClinicalTrials.gov, identifier NCT03823144.

KEYWORDS

sarcoma, vessels, imaging, intravital, clinical trial

Introduction

Sarcomas comprise a vast, heterogeneously diverse group of malignancies that afflict connective tissues of the body, including bone, nerve, and soft tissue. There are over 80 defined sarcomas, each with specific therapeutic approaches that are often multidisciplinary and require a high level of expertise to provide the most optimal outcome (1, 2). Despite the diversity of this group of tumors, even the most common types of sarcomas are relatively rare compared to other cancers (such as cutaneous tumors or breast cancer). This leads to inherent difficulty in investigating the underlying molecular biology and biodiversity of this group of tumors, and likely contributes to the limited sarcoma treatment options compared to other cancers, resulting in high rates of tumor recurrence or disease progression (3). Similar to these challenges, the tumor-associated vasculature of sarcomas has largely been unstudied. While certain sarcomas by their nature are intrinsically vascular (namely angiosarcomas), the extent of vascularity for many of the more common sarcomas (such as gastrointestinal stromal tumors or GISTs, liposarcomas, and leiomyosarcomas) are undefined.

Our group has utilized innovative technologies to study tumor-associated vessels in real time among patients undergoing surgical resection (4). These investigations were initially performed in patients undergoing wide local excision of cutaneous melanoma (5). In this first trial of its kind, real-time, intravital fluorescence microscopy was successfully performed to identify, characterize, and quantify melanoma-associated vessels, revealing drastic differences in human tumor-associated vessels as compared with normal (control) vessels. We have since broadened our study of tumor-associated vessels by using human intravital microscopy to examine the tumor vessels in patients with peritoneal carcinomatosis (6). In this recent clinical trial, further differences in tumor vessel density and functionality were identified, whereby patients who had received neoadjuvant systemic therapies and experienced partial response qualitatively had lower proportions of non-functional tumor-associated vessels and higher proportions of functional, normal vessels compared to patients who had stable or progressive disease. Other groups have also started to investigate tumor-associated vessels in other cancer settings in humans, including esophagogastric, colorectal, and bladder cancers (7–10). These differences are important to recognize and define because systemic drug delivery is highly dependent on the tumor vasculature (11–13). Our group and others have shown that manipulation or optimization of blood flow through tumor-associated vessels at the time of drug delivery can improve tumor responses in animal cancer models (14–17). However, little is known about these interventions on sarcoma-associated vessels. Therefore, to increase the understanding of sarcoma tumor-associated vessels, we analyzed a cohort of 10 sarcoma patients who underwent surgical resection and real-time, intraoperative tumor vessel imaging. Our main objective was to determine the feasibility of intravital microscopy (IVM) in the observation of sarcoma-related tumor vessels. Herein, we present a descriptive analysis of our results.

Patients and methods

Patient selection

Patients were enrolled in single center, nonrandomized clinical trials at Mayo Clinic in Jacksonville, Florida, USA. These trials included Intravital Microscopy (IVM) in Patients with Peritoneal Carcinomatosis (ClinicalTrials.gov identifier: NCT03517852) and Intravital Microscopy in Human Solid Tumors (ClinicalTrials.gov identifier: NCT03823144) (6, 8). Both trials received IRB approval from the Mayo Clinic (IRB #17-009823 and IRB #18-010370, respectively). The protocols for these trials, and the inclusion and exclusion criteria had previously been reported and are available through nct.gov (6, 8). Briefly, patients underwent informed consent for participation and received a fluorescein skin prick test to evaluate the low risk of an allergic reaction to the fluorescein dye used to enhance the intravital in-human observations of blood vessels. Recorded information included demographic data (age, sex, body-mass index, race, history of smoking, history of diabetes, prior abdominal surgery), sarcoma-specific data (tumor histology and subtype, grade, primary versus recurrent diagnosis, size of the primary tumor with the longest dimension reported), and treatment-related variables (receipt and type of neoadjuvant and/or adjuvant chemotherapy or other systemic therapy; receipt of neoadjuvant radiotherapy, radiographic response to neoadjuvant therapy as measured by standard RECIST criteria, surgical approach, and complications from surgery including cytoreduction surgery with or without hyperthermic intraperitoneal chemotherapy, or CRS-HIPEC, when applicable).

Intravital microscopic observations in patients

The technique for real-time human intravital microscopy had also been previously described by our group (6, 8). Briefly, we utilized the ultra-high definition (UHD) probe-based confocal laser endomicroscopy device (Gastroflex, Cellvizio System, Mauna Kea Technologies, Paris, France). Sarcoma-associated vessels were observed at 100x magnification. Videos were obtained in a proprietary format video files (.mkt) for *post hoc* data analysis. Offline quantification of vessel characteristics was performed using the Mauna Kea Technologies IC-Viewer (Mauna Kea Technologies, Paris, France). All images/videos were stored on a password-protected institutional hard drive for later analysis.

Prior to surgical resection, tumor vessel observations were performed on two separate sarcoma-bearing areas and two separate non-tumor bearing control areas. The tumor areas and control areas were separated by a distance of at least 10 centimeters (cm). We selected the tumor areas based on the highest amount of gross tumor burden that was visualized, which was up to the surgeon's discretion at the time of the resection. Common gross characteristics of abnormal tissue included color (often white or gray compared to yellow normal tissue), texture (often firm compared to soft), and infiltration into normal organs or

structures. Observations occurred either through open or minimally invasive (laparoscopic or robotic) approaches. Prior to the observation, the surgeon instructed the anesthesiologist to administer 1 ml of fluorescein (AK-Fluor® fluorescein, 10% at 100 mg/mL) intravenously followed by a 10 ml saline flush. During the fluorescein administration, the Gastroflex probe was positioned over the first predetermined sarcoma field to be ready for observation once the recording was initiated. After 10-15 seconds of administering the fluorescein, the dye could be visualized within functional tumor vessels. Each predetermined area was observed for 60-90 seconds, for a total of about 4-6 minutes for the entire patient observation. Within each area, multiple fields were observed over an area of approximately 2 square cm during each observation period. In order to facilitate stabilization of the HIVM observations, respirations were temporarily restricted by the anesthesiologist for a maximum of approximately 30 seconds per observed area. By approximately 5-6 minutes after the fluorescein administration, the dye (which has a molecular weight of 332.31 g/mol) extravasated into the background stroma, which in turn increased the fluorescent signal of the surrounding stromal tissue as compared to any functional vessels (normal or tumor-associated) present within the field of view. Similar to our prior study in peritoneal carcinomatosis, the observation for a given patient was completed when fluorescein was noted to have extravasated out of tumor/control vessels into the surrounding background tissue (6).

Characterization of the tumor vessels and the measured parameters had previously been described by our group (5, 6, 9). Briefly, we characterized the following tumor vessel characteristics during the intraoperative observations: (1) vessel identification per high power field, (2) vessel density, (3) fluorescein uptake as a measure of tumor vessel functionality (dye uptake) or non-functionality (lack of dye uptake), and (4) blood flow velocity. Vessel density (for both functional and non-functional) was calculated by dividing the number of vessels by the number of fields of observation per area (control or tumor). The percentage of non-functional vessels per area (tumor or control) was calculated by dividing the number of non-functional vessels by the total number of vessels observed (# non-functional vessels/# non-functional vessels + # functional vessels) times 100. IC-Viewer software was used to measure vessel diameter (d) at the vessel's largest width as well as vessel length prior to any branching points. Blood flow velocity (v) was evaluated by determining the time that distinct features (e.g., a prominent red blood cell or clump of red blood cells) in an observed vessel would take to travel a known distance. Velocity was calculated by dividing the measured distance by the time taken to travel that distance, and then averaging these values for at least 3 points per vessel. No velocities were calculated for non-functional vessels as by definition, these vessels did not support any blood flow.

Statistical analyses

Demographic and clinical characteristics were summarized using the mean and standard deviation (std) for continuous variables, and using frequencies for categorical variables. Vessel characteristics (diameter, density, and velocity) were summarized using mean and std. The two-sided, paired t test was used to make comparisons between the control and treatment groups. Progression-free (PFS) and disease-specific survival (DSS) were summarized using standard Kaplan-Meier methods. All analyses were conducted in SAS v9.4 (Cary, NC) at a significance level of 0.05. As this was a study of IVM feasibility, the statistical analysis was limited to descriptive statistics. Correlative analyses of vessel characteristics with outcomes (response to neoadjuvant chemotherapy, PFS, or DSS) were not performed.

Results

Patient demographics, tumor-specific characteristics, and treatment outcomes

Between January 1, 2018 and December 31, 2022, we enrolled 10 patients with sarcoma as part of our clinical trials (NCT03517852 Intravital Microscopy in Patients with Peritoneal Carcinomatosis and NCT03823144 Intravital Microscopy in Human Solid Tumors). Patient and tumor-specific characteristics are shown in Table 1. Most patients had retroperitoneal liposarcomas (5 total, 2 well-differentiated and 3 dedifferentiated). Half of the tumors (5/10) were high grade, and 4 were recurrences. Only 2 patients received neoadjuvant systemic chemotherapy (including doxorubicin/ifosfamide/mesna and doxorubicin/olaratumab), but 4 patients received neoadjuvant radiation (55-60 Grey). Of these patients, there were no partial responses, and 3 patients had stable disease with 1 patient having disease progression. One patient received multiple rounds of adjuvant chemotherapy (including gemcitabine/docetaxel, doxorubicin/olaratumab, and pazopanib). One patient also required liver ablation for a metastasis. Two patients had died at the time of our analysis. The individual progression-free and disease-specific survivals are reported in Table 1. The median follow-up was 2.5 years. Unlike our most recent study in peritoneal carcinomatosis, correlations of tumor vessel characteristics and response to neoadjuvant treatment or survival outcomes were not calculated due to the small cohort of sarcoma patients.

HIVM vessel characteristics

Table 2 shows the vessel characteristics obtained from the in-human intravital observations. Similar numbers of tumor and control fields were observed within our patient cohort ($p = 0.22$). Statistically significant differences between the tumor and control fields were observed for some blood vessel characteristics. Similar to our previous study in peritoneal carcinomatosis, tumor-associated areas were observed to have a higher density of non-functional vessels ($p < 0.0018$) and a higher proportion of non-functional vessels compared to non-tumor control areas ($p < 0.0032$) (6). Similarly, the mean blood flow velocity of functional vessels within tumor areas was significantly slower than the mean velocity of functional vessels within non-tumor areas ($p < 0.0001$), which was

10.3389/fonc.2023.1151255

TABLE 1 Patient, tumor, and treatment-related variables.

Variable		N (#)
Age (years)	mean (std)	62.1 (10.8)
Sex	female	3
	male	7
Body mass index (BMI)	mean (std)	30.5 (2.6)
Race	Asian	1
	White	9
Smoking history	current	0
	former	1
	never	9
Diabetes	no	8
	yes	2
Histology	retroperitoneal liposarcoma	5
	gastrointestinal stromal tumor	2
	uterine leiomyosarcoma	1
	pleomorphic sarcoma	1
	leiomyosarcoma	1
Grade	low/well-differentiated	4
	intermediate	1
	high/dedifferentiated	5
Recurrence	no	4
	yes	6
Tumor size (longest dimension, cm)	mean (std)	8.8 (5.5)
Previous abdominal surgery	no	4
	yes	6
Surgical approach	open	8
	laparoscopic/robotic	2
Neoadjuvant therapy	no	8
	yes	2
Neoadjuvant radiotherapy	no	6
	yes	4
Adjuvant chemotherapy	no	9
	yes	1
RECIST response (N = 4)	partial response	0
	stable disease	3
	progressive disease	1
Survival (median months, 95% CI)	progression-free	2.6 (2.5, 2.7)
	disease-specific	2.9 (2.8, 3.0)

also the case with the tumor-associated vessels in patients with carcinomatosis.

Conversely, there were no statistically significant differences between the density of functional vessels ($p = 0.92$), the diameter of functional vessels ($p = 0.35$) within control and tumor areas, or the vessel length among either functional ($p = 0.78$) or non-functional ($p = 0.67$) vessels within control and tumor areas. Some of these findings were different from our study in peritoneal carcinomatosis, where there were statistically significant differences among these parameters. Specifically, there was a lower density of functional vessels associated with carcinomatosis, and the average diameter of functional vessels was smaller in tumor areas compared with the diameter of functional vessels in control areas (6). In our prior study in patients with peritoneal carcinomatosis, the mean diameter of non-functional vessels was similar between the tumor and non-tumor areas ($p = 0.15$). However, in this study of patients with sarcoma, there was a statistically significant difference in the diameter of non-functional vessels, whereby non-functional tumor vessels were larger than non-functional control vessels. Table 3 summarizes the differences between vessel characteristics in our current study with sarcoma and our previous study in patients with peritoneal carcinomatosis (NCT03517852 Intravital Microscopy in Patients with Peritoneal Carcinomatosis).

Representative examples of real-time images of sarcoma and non-tumor vessels among individual patients are shown in Figure 1 (scale bar = 20 μm). Observations from well-differentiated (A) and dedifferentiated (B) retroperitoneal liposarcomas, gastrointestinal tumors (C), and leiomyosarcomas (D) are depicted for both control and sarcoma areas. The outlines of individual adipocytes could be visualized within the normal fatty area controls in the liposarcoma panels (A and B). Individual red blood cells could also be observed within a given functional blood vessel. Part E demonstrates an example of how blood flow velocity was observed and estimated by tracking a distinct cluster of red blood cells traveling through a functional blood vessel in a visualized normal (control) area for a patient with a dedifferentiated liposarcoma. Similar to our previous clinical trials in melanoma and peritoneal carcinomatosis, aberrant and non-functional sarcoma-associated vessels could be observed using our intravital microscope. There was a high proportion of non-functional vessels observed in tumor areas, with several panels demonstrating the juxtaposition of functional and non-functional vessels within the same field of view. Arrows highlight qualitative differences between normal and sarcoma-associated vessels.

Discussion

To our knowledge and extensive review of the literature, this was the first in-human study of sarcoma-associated vessels in real time. When comparing sarcoma-associated vessels to normal control vessels, we expectedly demonstrated that tumor areas had on average a higher density and proportion of non-functional vessels compared to control areas. This was observed in our previous trials in melanoma and peritoneal carcinomatosis (5, 6). However, unlike our previous studies, in this trial we demonstrated differences among other vessel characteristics, specifically among

TABLE 2 Comparison of tumor and non-tumor (control) vessel characteristics during intravital microscopic observations.

Variable		Sarcoma Cohort (N = 10)	
		Mean (Std, Range)	P value
Number of observed fields	Control	6.67 (1.94, 3-12)	0.22
	Tumor	8.20 (2.96, 4-10)	
Density of functional vessels	Control	2.12 (0.88)	0.92
	Tumor	2.17 (1.22)	
Density of non-functional vessels	Control	0.11 (0.17)	0.0018
	Tumor	1.02 (0.72)	
% Non-functional vessels	Control	4.59 (7.68)	0.0032
	Tumor	35.69 (26.18)	
Diameter of functional vessels (μm)	Control	23.35 (12.5)	0.35
	Tumor	18.05 (11.36)	
Diameter of non-functional vessels (μm)	Control	14.11 (3.27)	0.034
	Tumor	21.34 (8.86)	
Length of functional vessels (μm)	Control	187.55 (52.64)	0.78
	Tumor	166.72 (68.72)	
Length of non-functional vessels (μm)	Control	148.83 (78.41)	0.67
	Tumor	160.29 (49.65)	
Velocity of functional vessels (μm/s)	Control	430.49 (49.74)	<0.0001
	Tumor	286.77 (44.45)	

the density of functional vessels, the diameter of functional vessels, and the diameter of non-functional vessels (Table 3). Interestingly, these differences are consistent with the increasing body of knowledge that supports a vascular heterogeneity among tumor types. Indeed, there is considerable tumor vessel heterogeneity (in addition to tumor genetic and molecular heterogeneity) that exists between tumor types. While most of this data has been reported in animal models, there are some clinical studies that describe tumor vessel heterogeneity. For example, Mezheyeuski et al. showed in pathologic stage II/III colon cancer specimens (312 patients) that increased vessel density was associated with increased response to chemotherapy (18). Also pertaining to colorectal cancer, Herrera et al. showed that tumor-associated vessels may influence the interaction between stromal fibroblasts and circulating effector T cells, potentially optimizing immune crosstalk and anti-tumor responses (19). Using preclinical models of melanoma, our own group has demonstrated that drug delivery can depend on intra-arterial or intravenous delivery, and that blood flow through tumor-associated vessels can be optimized to enhance systemic treatment delivery, which in turn improves therapeutic responses (16, 17). Our ongoing translational studies seek to develop methods of dynamic tumor vessel control with the end goal of optimizing tumor blood flow at the time of systemic drug delivery. These include experiments with fluorescently-labeled effector T cells, fluorescently-labeled liposomal nanoparticle formulations of sustained-released targeted therapies, and chemotherapies that display intrinsic autofluorescence (e.g., doxorubicin), each of which are combined with dynamic tumor vessel control. Furthermore, other groups have shown that modulation of tumor vessels through targeted nanoparticle technology can normalize blood flow through neurologic tumors, leading to increased drug delivery with the same goal of improving treatment response (20, 21).

These findings from neurologic cancers, gastrointestinal cancers, and cutaneous malignancies are imperative to more comprehensively understand and investigate because tumor-associated vessel heterogeneity (with regard to structure and functionality) may impact drug delivery and therefore affect multidisciplinary treatment efficacy (22–25). It has been increasingly shown that the most successful chemotherapeutic agents and targeted inhibitors require adequate distribution to the tumor *via* the circulation, or else they are rendered ineffective (14, 26–29). Even cell-based onco-immunotherapeutics, such as adoptive cell transfer and CAR T cells, are similarly dependent upon accessing the tumor *via* the vasculature, and better outcomes have been directly correlated to immune cell infiltration of the tumor (30–32). A considerable amount of study has focused on elucidating the properties of tumor vessels and overcoming limitations to therapy that involve these heterogeneously organized and functional vessels (33–37). Therefore, our trial

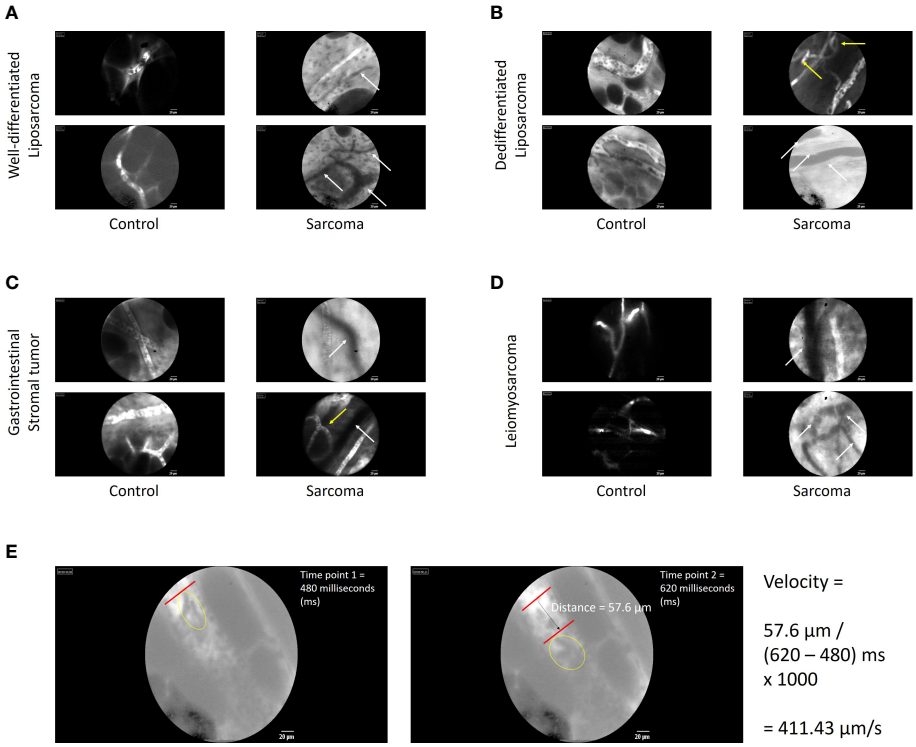

FIGURE 1
Images of tumor and non-tumor vessels among individual patients with sarcoma. Observations of sarcoma-associated vessels from well-differentiated **(A)** and dedifferentiated **(B)** retroperitoneal liposarcomas, gastrointestinal tumors **(C)**, and leiomyosarcomas **(D)** are depicted for both control and sarcoma areas. Similar to our previous clinical trials in melanoma and peritoneal carcinomatosis, aberrant and non-functional sarcoma-associated vessels could be observed using our intravital microscope. Arrows highlight qualitative differences between normal and sarcoma-associated vessels. White arrows highlight nonfunctional vessels (absence of fluorescent dye uptake). Yellow arrows indicate aberrant loop or branch patterns. **(E)** Example calculation of how blood flow velocity was observed and estimated by tracking a distinct cluster of red blood cells traveling through a functional blood vessel in a visualized normal (control) area for a patient with a dedifferentiated liposarcoma. The left frame shows the cluster of interest (within yellow oval) at first time point. The right frame shows the same cluster traveling a measurable distance with the blood vessel. The velocity calculation is shown to derive velocity in µm/s.

provides the initial step in characterizing vessel heterogeneity among patients with sarcoma, which are often refractory to radiation and systemic treatments.

Key to our IVM trial was the use of the Gastroflex fluorescent microscope. IVM provides several advantages over conventional imaging techniques, such as ultrasound, computerized tomography (CT) scan, or magnetic resonance imaging (MRI). Whereas these more conventional imaging techniques provide a more global view of these often large sarcomas, they cannot provide imaging resolution at the capillary level in the way that IVM can (as shown in Figure 1) (9). IVM can also provide longer real-time imaging at the time of surgery, where differences in blood pressure or blood flow can be analyzed. However, currently IVM is mostly limited to imaging of surface malignancies. In our current report,

TABLE 3 Comparison of vessel characteristics between sarcoma (current trial) and peritoneal carcinomatosis (previous trial NCT03517852 Intravital Microscopy in Patients with Peritoneal Carcinomatosis).

Variable	Sarcoma	Peritoneal Carcinomatosis
	control versus tumor	
Number of observed fields	No difference	No difference
Density of functional vessels	No difference	Control > tumor
Density of non-functional vessels	Tumor > control	Tumor > control
% Non-functional vessels	Tumor > control	Tumor > control
Diameter of functional vessels (µm)	No difference	Control > tumor
Diameter of non-functional vessels (µm)	Tumor > control	No difference
Velocity of functional vessels (µm/s)	Control > tumor	Control > tumor

only the surface of the sarcomas could be observed and imaged. More conventional techniques (US, CT, MRI) can better characterize the inner portions of the tumor, which often display heterogeneous characteristics compared to the superficial tumor areas. For example, the tumor surface tends to be the most active in terms of replication and growth as the tumor expands outwards and display increased enhancement on contrasted imaging modalities, whereas the core of the tumor tends to become more necrotic as the vasculature cannot support the deeper tumor tissues and so may display decreased internal enhancement. Thus, there are limitations to using IVM to analyze parenchymal tumors, unless they are exposed during surgical resection. Indeed, at this time IVM may be very useful for surface malignancies such as cutaneous cancers as our group previously demonstrated (5). In addition, during resection of larger sarcomas (greater than 10 cm), we were limited in observing the most grossly abnormal tumor areas. While observations of the entire sarcoma could be performed during the course of the surgery, this would have significantly prolonged operative times and exposure to anesthesia, which may have increased the undue risks for patients. Therefore, while we assume that there would be similarities to the tumor vasculature along different surface areas of the sarcoma, additional sarcoma-related vessel heterogeneity may exist that could not be characterized by our approach.

We recognize that there are other limitations in our analysis, similar to our previous studies (5, 6). Our cohort of sarcoma patients was small and only one-third of the patients in our previous trial of peritoneal carcinomatosis. Consequently, this brief research report focuses mainly on the feasibility of IVM in the study of sarcomas and only provides a descriptive analysis of the results. In addition, there was considerable diversity among the tumor histologies within our sarcoma patient cohort. Therefore, this trial was not sufficiently powered to analyze any associations between tumor-associated vessel characteristics and outcomes, namely response to neoadjuvant therapies and survival (PFS and DSS). However, our continuation of NCT03823144 Intravital Microscopy in Human Solid Tumors will likely address this limitation of statistical power with a larger cohort of patients. In fact, to date we have enrolled 30 patients with ovarian tumors who have received neoadjuvant chemotherapy. Our future investigation will evaluate tumor vessel characteristics with response to neoadjuvant chemotherapy and survival outcomes.

In conclusion, despite the acknowledged limitations, this analysis represents the first in-human study of sarcoma-associated vessels in real time. While similarities were identified among sarcoma-associated vessels and peritoneal carcinomatosis-associated vessels from our previous trial, there were also significant differences providing new, direct real-time evidence to support the existence of vascular heterogeneity for different tumors and the feasibility to observe these differences during the course of surgical resection. Further study with a larger cohort of patients with a single type of cancer will potentially correlate tumor-associated vessels with treatment outcomes and help tailor individualized anti-cancer therapy.

Data availability statement

The raw data supporting the conclusions of this article will be made available by the authors, without undue reservation.

Ethics statement

The studies involving human participants were reviewed and approved by Mayo Clinic IRB. The patients/participants provided their written informed consent to participate in this study.

Author contributions

EG and SB developed the concept, protocol, and IRB approval. EG and SB enrolled patients. EG analyzed the data. KS and KP organized the data and edited the manuscript. Each author drafted and approved the final version.

Funding

This work was supported by CTSA Grant Number KL2 TR002379 from the National Center for Advancing Translational Science (NCATS) (to EG).

Conflict of interest

The authors declare that the research was conducted in the absence of any commercial or financial relationships that could be construed as a potential conflict of interest.

Publisher's note

Author disclaimer

The publication contents are solely the responsibility of the authors and do not necessarily represent the official views of the NIH.

References

1. Bagaria SP, Neville M, Gray RJ, Gabriel E, Ashman JB, Attia S, et al. The volume-outcome relationship in retroperitoneal soft tissue sarcoma: Evidence of improved short- and long-term outcomes at high-volume institutions. *Sarcoma* (2018) 2018:3056562. doi: 10.1155/2018/3056562

2. Bagaria SP, Swallow C, Suraweera H, Raut CP, Fairweather M, Cananzi F, et al. Morbidity and outcomes after distal pancreatectomy for primary retroperitoneal sarcoma: An analysis by the trans-Atlantic Australasian retroperitoneal sarcoma working group. *Ann Surg Oncol* (2021) 28(11):6882–9. doi: 10.1245/s10434-021-09739-9

3. Bagaria SP, Gabriel E, Mann GN. Multiply recurrent retroperitoneal liposarcoma. *J Surg Oncol* (2018) 117(1):62–8. doi: 10.1002/jso.24929

4. Jain RK, Munn LL, Fukumura D. Dissecting tumour pathophysiology using intravital microscopy. *Nat Rev Cancer* (2002) 2(4):266–76. doi: 10.1038/nrc778

5. Fisher DT, Muhitch JB, Kim M, Doyen KC, Bogner PN, Evans SS, et al. Intraoperative intravital microscopy permits the study of human tumour vessels. *Nat Commun* (2016) 7:10684. doi: 10.1038/ncomms10684

6. Gabriel EM, Kim M, Fisher DT, Mangum C, Attwood K, Ji W, et al. A pilot trial of intravital microscopy in the study of the tumor vasculature of patients with peritoneal carcinomatosis. *Sci Rep* (2021) 11(1):4946. doi: 10.1038/s41598-021-84430-3

7. Nussbaum S, Shoukry M, Ashary MA, Kasbi AA, Baksh M, Gabriel E. Advanced tumor imaging approaches in human tumors. *Cancers (Basel)* (2022) 14(6):1549. doi: 10.3390/cancers14061549

8. Trumbull DA, Lemini R, Bagaria SP, Elli EF, Colibaseanu DT, Wallace MB, et al. Intravital microscopy (IVM) in human solid tumors: Novel protocol to examine tumor-associated vessels. *JMIR Res Protoc* (2020) 9(10):e15677. doi: 10.2196/15677

9. Gabriel EM, Fisher DT, Evans S, Takabe K, Skitzki JJ. Intravital microscopy in the study of the tumor microenvironment: from bench to human application. *Oncotarget* (2018) 9(28):20165–78. doi: 10.18632/oncotarget.24957

10. Fukumura D, Duda DG, Munn LL, Jain RK. Tumor microvasculature and microenvironment: Novel insights through intravital imaging in pre-clinical models. *Microcirculation* (2010) 17(3):206–25. doi: 10.1111/j.1549-8719.2010.00029.x

11. Nagy JA, Chang SH, Dvorak AM, Dvorak HF. Why are tumour blood vessels abnormal and why is it important to know? *Br J Cancer* (2009) 100(6):865–9. doi: 10.1038/sj.bjc.6604929

12. Nagy JA, Chang SH, Shih SC, Dvorak AM, Dvorak HF. Heterogeneity of the tumor vasculature. *Semin Thromb hemostasis* (2010) 36(3):321–31. doi: 10.1055/s-0030-1253454

13. Abdollahi A, Folkman J. Evading tumor evasion: current concepts and perspectives of anti-angiogenic cancer therapyDrug resistance updates: Reviews and commentaries in antimicrobial and anticancer chemotherapy. *Drug Resist Updat.* (2010) 13(1-2):16–28. doi: 10.1016/j.drup.2009.12.001

14. Jain RK. Normalizing tumor microenvironment to treat cancer: bench to bedside to biomarkers. *J Clin Oncol* (2013) 31(17):2205–18. doi: 10.1200/jco.2012.46.3653

15. Morikawa S, Baluk P, Kaidoh T, Haskell A, Jain RK, McDonald DM. Abnormalities in pericytes on blood vessels and endothelial sprouts in tumors. *Am J Pathol* (2002) 160(3):985–1000. doi: 10.1016/s0002-9440(10)64920-6

16. Visioni A, Kim M, Wilfong C, Blum A, Powers C, Fisher D, et al. Intra-arterial versus intravenous adoptive cell therapy in a mouse tumor model. *J immunotherapy (Hagerstown Md: 1997)* (2018) 41(7):313–8. doi: 10.1097/cji.0000000000000235

17. Gabriel EM, Kim M, Fisher DT, Powers C, Attwood K, Bagaria SP, et al. Dynamic control of tumor vasculature improves antitumor responses in a regional model of melanoma. *Sci Rep* (2020) 10(1):13245. doi: 10.1038/s41598-020-70233-5

18. Mezheyeuski A, Hrynchyk I, Herrera M, Karlberg M, Osterman E, Ragnhammar P, et al. Stroma-normalised vessel density predicts benefit from adjuvant fluorouracil-based chemotherapy in patients with stage II/III colon cancer. *Br J cancer* (2019) 121 (4):303–11. doi: 10.1038/s41416-019-0519-1

19. Herrera M, Mezheyeuski A, Villabona L, Corvigno S, Strell C, Klein C, et al. Prognostic Interact between FAP+ Fibroblasts CD8a+ T Cells Colon Cancer. *Cancers (Basel)* (2020) 12(11):3238. doi: 10.3390/cancers12113238

20. Jiang W, Huang Y, An Y, Kim BY. Remodeling tumor vasculature to enhance delivery of intermediate-sized nanoparticles. *ACS nano* (2015) 9(9):8689–96. doi: 10.1021/acsnano.5b02028

21. Du S, Xiong H, Xu C, Lu Y, Yao J. Attempts to strengthen and simplify the tumor vascular normalization strategy using tumor vessel normalization promoting nanomedicines. *Biomaterials science* (2019) 7(3):1147–60. doi: 10.1039/c8bm01350k

22. Shahab D, Gabriel E, Attwood K, Ma WW, Francescutti V, Nurkin S, et al. Adjuvant chemotherapy is associated with improved overall survival in locally advanced rectal cancer after achievement of a pathologic complete response to chemoradiation. *Clin Colorectal Cancer* (2017) 16(4):300–7. doi: 10.1016/j.clcc.2017.03.005

23. Deng L, Groman A, Jiang C, Perimbeti S, Gabriel E, Kukar M, et al. Association of preoperative chemosensitivity with postoperative survival in patients with resected gastric adenocarcinoma. *JAMA network Open* (2021) 4(11):e2135340. doi: 10.1001/jamanetworkopen.2021.35340

24. Trumbull DA, Lemini R, Díaz Vico T, Jorgensen MS, Attwood K, Ji W, et al. Prognostic significance of complete pathologic response obtained with chemotherapy versus chemoradiotherapy in gastric cancer. *Ann Surg Oncol* (2021) 28(2):766–73. doi: 10.1245/s10434-020-08921-9

25. Gabriel E, Attwood K, Du W, Tuttle R, Alnaji RM, Nurkin S, et al. Association between clinically staged node-negative esophageal adenocarcinoma and overall survival benefit from neoadjuvant chemoradiation. *JAMA surgery* (2016) 151(3):234–45. doi: 10.1001/jamasurg.2015.4068

26. Chauhan VP, Martin JD, Liu H, Lacorre DA, Jain SR, Kozin SV, et al. Angiotensin inhibition enhances drug delivery and potentiates chemotherapy by decompressing tumour blood vessels. *Nat Commun* (2013) 4:2516. doi: 10.1038/ncomms3516

27. Katsuta E, Qi Q, Peng X, Hochwald SN, Yan L, Takabe K. Pancreatic adenocarcinomas with mature blood vessels have better overall survival. *Sci Rep* (2019) 9(1):1310. doi: 10.1038/s41598-018-37909-5

28. Colby AH, Liu R, Schulz MD, Padera RF, Colson YL, Grinstaff MW. Two-step delivery: Exploiting the partition coefficient concept to increase intratumoral paclitaxel concentrations *In vivo* using responsive nanoparticles. *Sci Rep* (2016) 6:18720. doi: 10.1038/srep18720

29. Mangala LS, Wang H, Jiang D, Wu SY, Somasunderam A, Volk DE, et al. Improving vascular maturation using noncoding RNAs increases antitumor effect of chemotherapy. *JCI Insight* (2016) 1(17):e87754. doi: 10.1172/jci.insight.87754

30. Fisher DT, Chen Q, Skitzki JJ, Muhitch JB, Zhou L, Appenheimer MM, et al. IL-6 trans-signaling licenses mouse and human tumor microvascular gateways for trafficking of cytotoxic T cells. *J Clin Invest* (2011) 121(10):3846–59. doi: 10.1172/JCI44952

31. Mikucki ME, Fisher DT, Matsuzaki J, Skitzki JJ, Gaulin NB, Muhitch JB, et al. Non-redundant requirement for CXCR3 signalling during tumoricidal T-cell trafficking across tumour vascular checkpoints. *Nat Commun* (2015) 6:7458. doi: 10.1038/ncomms8458

32. Ribas A, Comin-Anduix B, Economou JS, Donahue TR, de la Rocha P, Morris LF, et al. Intratumoral immune cell infiltrates, FoxP3, and indoleamine 2,3-dioxygenase in patients with melanoma undergoing CTLA4 blockade. *Clin Cancer Res* (2009) 15 (1):390–9. doi: 10.1158/1078-0432.ccr-08-0783

33. Zheng X, Fang Z, Liu X, Deng S, Zhou P, Wang X, et al. Increased vessel perfusion predicts the efficacy of immune checkpoint blockade. *J Clin Invest* (2018) 128 (5):2104–15. doi: 10.1172/jci96582

34. He B, Ganss R. Modulation of the vascular-immune environment in metastatic cancer. *Cancers (Basel)* (2021) 13(4):810. doi: 10.3390/cancers13040810

35. Munn LL, Jain RK. Vascular regulation of antitumor immunity. *Sci (New York NY)* (2019) 365(6453):544–5. doi: 10.1126/science.aaw7875

36. Sprowls SA, Arsiwala TA, Bumgarner JR, Shah N, Lateef SS, Kielkowski BN, et al. Improving CNS delivery to brain metastases by blood-tumor barrier disruption. *Trends cancer* (2019) 5(8):495–505. doi: 10.1016/j.trecan.2019.06.003

37. Mohammad AS, Adkins CE, Shah N, Aljammal R, Griffith JIG, Tallman RM, et al. Permeability changes and effect of chemotherapy in brain adjacent to tumor in an experimental model of metastatic brain tumor from breast cancer. *BMC cancer* (2018) 18(1):1225. doi: 10.1186/s12885-018-5115-x

frontiers | Frontiers in Medicine

TYPE Original Research
PUBLISHED 17 April 2023
DOI 10.3389/fmed.2023.1064242

OPEN ACCESS

EDITED BY
Rupert Ecker,
TissueGnostics GmbH, Austria

REVIEWED BY
Florian Schueder,
Yale University, United States
Shawn C. Owen,
The University of Utah, United States

*CORRESPONDENCE
John C. Williams
✉ jcwilliams@coh.org
Tijana Jovanovic-Talisman
✉ ttalisman@coh.org

†These authors share first authorship

SPECIALTY SECTION
This article was submitted to Precision Medicine, a section of the journal Frontiers in Medicine

RECEIVED 08 October 2022
ACCEPTED 30 March 2023
PUBLISHED 17 April 2023

CITATION
Wakefield DL, Golfetto O, Jorand R, Biswas S, Meyer K, Avery KN, Zer C, Cacao EE, Tobin SJ, Talisman IJ, Williams JC and Jovanovic-Talisman T (2023) Using quantitative single molecule localization microscopy to optimize multivalent HER2-targeting ligands. *Front. Med.* 10:1064242. doi: 10.3389/fmed.2023.1064242

Using quantitative single molecule localization microscopy to optimize multivalent HER2-targeting ligands

Devin L. Wakefield†, Ottavia Golfetto†, Raphael Jorand†, Sunetra Biswas, Kassondra Meyer, Kendra N. Avery, Cindy Zer, Eliedonna E. Cacao, Steven J. Tobin, Ian J. Talisman, John C. Williams* and Tijana Jovanovic-Talisman*

Department of Cancer Biology and Molecular Medicine, Beckman Research Institute, Duarte, CA, United States

Introduction: The progression-free survival of patients with HER2-positive metastatic breast cancer is significantly extended by a combination of two monoclonal antibodies, trastuzumab and pertuzumab, which target independent epitopes of the extracellular domain of HER2. The improved efficacy of the combination over individual antibody therapies targeting HER2 is still being investigated, and several molecular mechanisms may be in play: the combination downregulates HER2, improves antibody-dependent cell mediated cytotoxicity, and/or affects the organization of surface-expressed antigens, which may attenuate downstream signaling.

Methods: By combining protein engineering and quantitative single molecule localization microscopy (qSMLM), here we both assessed and optimized clustering of HER2 in cultured breast cancer cells.

Results: We detected marked changes to the cellular membrane organization of HER2 when cells were treated with therapeutic antibodies. When we compared untreated samples to four treatment scenarios, we observed the following HER2 membrane features: (1) the monovalent Fab domain of trastuzumab did not significantly affect HER2 clustering; (2) individual therapy with either trastuzumab or (3) pertuzumab produced significantly higher levels of HER2 clustering; (4) a combination of trastuzumab plus pertuzumab produced the highest level of HER2 clustering. To further enhance this last effect, we created multivalent ligands using meditope technology. Treatment with a tetravalent meditope ligand combined with meditope-enabled trastuzumab resulted in pronounced HER2 clustering. Moreover, compared to pertuzumab plus trastuzumab, at early time points this meditope-based combination was more effective at inhibiting epidermal growth factor (EGF) dependent activation of several downstream protein kinases.

Discussion: Collectively, mAbs and multivalent ligands can efficiently alter the organization and activation of the HER2 receptors. We expect this approach could be used in the future to develop new therapeutics.

KEYWORDS

HER2, meditope, valency, single molecule localization microscopy, trastuzumab, pertuzumab

1. Introduction

Roughly 20% of breast cancers exhibit overexpression and/or gene amplification of human epidermal growth factor receptor 2 (HER2). These cases are typically associated with aggressive disease and poor outcomes (1–6). The patient outcomes have been significantly improved by therapeutic monoclonal antibodies (mAbs) targeting HER2 (7–13). The first mAb therapy against HER2 to be approved by the U.S. Food and Drug Administration (FDA) was trastuzumab; it binds close to the transmembrane domain of HER2, on an extracellular region (domain IV), and it may inhibit HER2 homodimerization (14). At least four mechanisms of action have been suggested for trastuzumab: it induces internalization and degradation of HER2, activates antibody-dependent cellular cytotoxicity (ADCC), prevents shedding of the HER2 extracellular domain, and/or inhibits downstream signaling (15–17). While trastuzumab may benefit patients through one or more of these effects, a significant challenge in the clinic has been both intrinsic and acquired resistance (15, 18). Understanding the manifestation of these mechanisms is critical to guide alternative treatment strategies.

The combination of mAbs have been suggested as an approach to improve clinical outcomes in several cancers (13, 19, 20). In fact, patients with HER2-positive breast cancer benefited when they received a combination of trastuzumab and pertuzumab plus chemotherapy (10–13, 21). Pertuzumab binds to the extracellular domain II (the dimerization domain) of HER2 and inhibits its heterodimerization with other HER family members (22, 23). Pertuzumab may prevent HER2/HER3 heterodimerization, activate ADCC, and inhibit downstream signaling (9, 17, 22, 23). When pertuzumab was combined with trastuzumab, the density of HER2 on the plasma membrane was reduced (24, 25). The enhanced efficacy of trastuzumab plus pertuzumab may also be associated with two additional effects: an increase in ADCC (17) and inhibition of both homo- and hetero-dimerization of HER2, which subsequently attenuates the HER2 signaling cascade (26–28). Local differences in HER2 membrane patterning in different cell types (29–33) also point toward functional differences, which are likely relevant to the therapeutic response. Details that would shed light on these mechanisms remain poorly understood at the molecular level, and accordingly, our group and others have been studying how therapeutic agents affect HER2 molecular organization as a means to gain additional insight to ultimately improve clinical outcomes.

To this end, we have developed methods for quantitative single molecule localization microscopy (qSMLM). This approach is designed to count detected receptors, report on the spatial patterns of these receptors, and define their regional heterogeneity. In our prior study, we observed significant changes in HER2 spatial organization when cultured cells were treated with the chemotherapeutic agent paclitaxel and targeted inhibitor afatinib (31). We have also extended HER2 single molecule localization microscopy (SMLM) imaging to patient specimens (32). Importantly, in cultured cell lines and pre-treatment patient biopsies, we observed that HER2 density and clustering appear to correlate with therapy sensitivity/response (33). Herein, we have applied qSMLM to study in more detail how HER2 patterning is affected by different antibody-based agents, either alone or in combination. In addition to studying clinical therapies, we probed a set of pre-clinical reagents known as meditopes. These small, peptide-based molecules bind to a unique site within the Fab arm of the clinically relevant antibody cetuximab (that targets epidermal growth factor receptor, EGFR). This site has also been engineered into other mAbs which we have named meditope-enabled mAbs (memAbs) (34). MemAbs retain their affinity, selectivity, and function (35–38). Importantly, this technology allows us to add unique functionality to mAbs, including "non-covalent crosslinking" through multivalent meditopes. Here, we observe that the valency of meditope-based reagents modulates the spatial patterns and activity of HER2 in the presence of a trastuzumab memAb. These results indicate that reagent valency may be exploited to develop novel antibody-based therapeutics.

2. Materials and methods

2.1. Coverslip preparation

Twenty-five-millimeter #1.5 coverslips (Warner Instruments) were cleaned and coated with fibronectin-like engineered protein [25 μg/ml in phosphate buffer saline (PBS), pH 7.4, Sigma] as described before (32).

2.2. Cell culture

MDA-MB-468 and SK-BR-3 cells (originally obtained from the American Type Culture Collection, ATCC) were cultured in Phenol Red-free Dulbecco's Modified Eagle Medium (DMEM) supplemented with 10% fetal bovine serum, 1 mM sodium pyruvate, 100 units/ml penicillin, 100 units/ml streptomycin, and 2 mM L-alanyl-L-glutamine. MDA-MB-453 cells (also from ATCC) were cultured in DMEM-F12 media supplemented with 10% fetal bovine serum, 0.5 mM sodium pyruvate 100 units/ml penicillin and 100 units/ml streptomycin. BT-474 cells were cultured as described previously (32).

2.3. HER2-paGFP plasmid construct

A perbB2-EGFP pcDNA3.1(+) plasmid was purchased from Adgene (plasmid # 39321). This plasmid was used for iterative site directed mutagenesis to mutate the EGFP coding region into paGFP. The following primer pairs were used for iterative site directed mutagenesis to alter five amino acids in the EGFP coding region of the plasmid:

Primer pair 1

5' CCCACCCTCGTGACCACCTTTAGTTACGGCGTGCAG TGCTTC 3'

5' GAAGCACTGCACGCCGTAACTAAAGGTGGTCACGAG GGTGGG 3'

Primer pair 2

5' GAACGGCATCAAGGCGAACTTCAAGATCC 3'

5' GGATCTTGAAGTTCGCCTTGATGCCGTTC 3'

Primer pair 3

5' GACAACCACTACCTGAGCCATCAGTCCAAACTGAG CAAAG 3'

5' CTTTGCTCAGTTTGGACTGATGGCTCAGGTAGTGG TTGTC 3'

After each round of site directed mutagenesis, the DNA was transformed into BP5alpha competent cells (Biopioneer) and plated on LB/ampicillin agar plates at 37°C. Single colonies were selected from the plate and amplified in 10 ml LB culture to purify plasmid DNA to be used for the next round of site directed mutagenesis. After the final round of SDM was complete, the plasmid was sent for Sanger sequencing at the City of Hope Integrative Genomics Core.

2.4. Antibodies, antibody fragments, and fluorescent dye conjugation

Pertuzumab and trastuzumab (Genetech) were clinical grade. Trastuzumab memAb I83E (referred to here as trastuzumab memAb, or TmemAb) and wild type trastuzumab (for ADCC experiments) were prepared similarly as described before (34).

The Fc used for control studies was obtained from a papain digest of clinical trastuzumab. The Fc was purified by application of the papain digest material to first a protein L column (GE, 5 ml) with collection of the flow through. The flow through material was concentrated and further purified by gel filtration chromatography (GE, superdex 10/300 GL). The fractions were concentrated and stored at −80°C.

Fab trastuzumab was generated through the digestion of the clinical trastuzumab with immobilized papain (Pierce) and purified by reverse purification with protein A (GE Healthcare) and SEC on a HiLoad 16/600 pg Superdex 75 column (GE Healthcare).

MemAbs were labeled with Alexa Fluor 647 (AF647) dyes presenting an N-hydroxysuccinidimidyl ester (NHS) group for protein conjugation. A solution with 4–6 x excess of dye dissolved in dimethyl sulfoxide was mixed with a solution of 1 mg/ml of TmemAb in PBS, pH 7.4, and 0.02 M $NaHCO_3$. The conjugation reaction solution was placed on a rotator for 30 min at room temperature and quenched with 1.5 M hydroxylamine (pH 8.5) for 10 min. Unconjugated dye was removed by passing the solution through a size exclusion chromatography column (Bio-Rad, Hercules, CA, USA) while any potential aggregates were removed by passing labeled Ab through a 300-kDa concentrator. Measurements from a NanoDrop 1000 (Thermo) were used to calculate (with respect to the dye correction factor) the final concentration and degree of labeling for each fluorescent antibody. Approximately one dye per antibody (degree of labeling ∼1) was obtained in all cases for antibodies labeled with AF647. These conditions are desired as an increased degree of labeling has been reported to decrease affinity for trastuzumab (39).

2.5. M2Fc and M4Fc

M2Fc contains the meditope sequence fused to the N-terminus of the Fc using a flexible 37 amino acid sequence (**Supplementary methods**). For the M4Fc moiety, the meditope sequence is placed at both N and C-termini using flexible 39 and 30 amino acid linkers respectively (**Supplementary methods**). Each were produced in insect cells. Specifically, baculovirus encoding each were produced in TNI insect cells according to the manufacturer's protocol by transfecting M2Fc or M4Fc expression vectors and propagating the virus three times (Expression Systems). TNI cells were seeded in ESF921 media at a density of 1e6 cells/ml and allowed to grow overnight. The following day, high titer baculovirus containing the M2Fc or M4Fc expression vectors was added to the TNI cells at a MOI of 50 and the cells were allowed to produce protein. After three days, cells were separated from the media by centrifugation and media containing M2Fc or M4Fc was placed over a protein A column for purification. M2Fc or M4Fc in PBS was further purified using fast protein liquid chromatography.

2.6. Antibody dependent cell-mediated cytotoxicity (ADCC) assay

Antibody dependent cell-mediated cytotoxicity assays were conducted using a luciferase reporter-based core kit according to manufacturer instructions (G7010, Promega). SK-BR-3 cells were used as the target cell line and seeded at 5,000 cells per well in a 96-well white, tissue-culture treated plate in DMEM with 10% FBS one day prior to conducting the ADCC assay. The next day, media was replaced with 4% low IgG serum in RPMI media, according to kit protocol. Dilutions of listed antibodies were made at 1:2 starting at 1 nM antibody in the presence or absence of 10 nM M4Fc and added to cells along with the effector cells provided. Antibodies at 1 nM, with or without M4Fc, were also added to wells containing no target or effector cells as a negative control. Cells were incubated at 37°C for 6 h prior to adding luciferase substrate. Luminescence was measured on a Synergy 4 multi-mode microplate reader (BioTek) with a 0.5 s integration time. Each experiment was repeated at least three times with three technical replicates per experiment.

2.7. Transfection and antibody treatment of cells for imaging

MDA-MB-468 cells were transiently transfected 48 h after plating on coverslips using Jet Prime (PolyPlus) according to the manufacturer's instructions. For steady-state measurements, cells were washed with PBS at 37°C and fixed with 4% (w/v) paraformaldehyde and 0.2% (w/v) glutaraldehyde (EMS, Cat# 157-8 and 16019, respectively, Hatfield, MA, USA) in PBS for 30 min at room temperature; fixation was quenched with 25 mM glycine for 10 min as described before (32).

For Ab/Ab fragment treatments, 24 h after HER2-paGFP transfection, MDA-MB-468 cells were washed with media and treated with: 20 nM Fab trastuzumab, 10 nM trastuzumab, 10 nM pertuzumab, or 10 nM trastuzumab combined with 10 nM pertuzumab in media for 10 min. Cells were washed again with warm media and fixed/quenched as described above. For multivalent meditope treatment, MDA-MB-468 cells transfected with HER2-paGFP were first incubated with meditope-enabled trastuzumab memAb for 10 min. After a quick warm media wash, cells were incubated with 10 nM Fc, 10 nM M2Fc, 20 nM M2Fc, or 10 nM M4Fc in media for indicated times and fixed. To assess the effect of multivalent meditopes on endogenous HER2, BT-474 cells

were incubated with 10 nM TmemAb-AF647, alone or premixed with 10 nM multivalent meditope (i.e., M2Fc and its variants or M4Fc), for 10 min at 37°C and subsequently fixed as described above. Alternatively, cells were stained with 10 nM TmemAb-AF647 postfixation as indicated. All incubations were performed at 37°C in the cell culture incubator.

About 0.1 μm TetraSpeck beads (Life Technologies) served as fiducial markers in all experiments to correct any lateral drift as described before (40). Coverslips in Attofluor cell chambers (Life Technologies) were imaged immediately after preparation in PBS (to detect paGFP using photoactivated localization microscopy, PALM) or direct stochastic optical reconstruction microscopy (dSTORM) imaging buffer (41) (to detect AF647, using dSTORM).

2.8. Optical setup, image acquisition, and data analysis

PALM and dSTORM imaging were performed using a 3D N-STORM super-resolution microscope system (32). Data was acquired using NIS Elements 4.3 software and ANDOR Solis 4.23. Images of 256 × 256 pixels (27 μm × 27 μm for PALM and 41 μm × 41 μm for dSTORM) were collected with a frame rate of 100 ms (PALM) and 10 ms (dSTORM). paGFP, which is a monomeric optical highlighter protein with good signal to noise ratio, was activated and excited with a 488 nm laser with power values ranging from 1.5 to 2 mW (measured out of the optical fiber) and a 505/15 emission filter. paGFP molecules were imaged until the signal was completely exhausted—typically 15,000–25,000 frames were acquired. For fluorescently labeled trastuzumab memAb (TmemAb-AF647), dSTORM imaging was performed similarly as before (32), with a laser power of 120 mW (measured out of the optical fiber) and acquiring 20,000–40,000 frames until the AF647 signal was exhausted. Additionally, NIS-Elements software was used with the following identification settings to capture positive signal and produce localization data for analysis: 700 as the minimum number of photons/localization, 200 nm minimum localization width, 400 nm maximum localization width, 300 nm initial fit width, 1.3 maximum axial ratio, and 1 pixel maximum displacement.

We characterized the blinking behavior of paGFP and TmemAb-AF647. As described previously (31, 32), the average number of localizations was approximately 5 for paGFP, whereas the average number of localizations for TmemAb-AF647 was approximately 3. These values represent the average number of localizations (discrete appearances α) of the fluorescent probe for a given set of imaging conditions and particular optical setup (31, 40, 42). We have demonstrated that robust molecular counting can be obtained using this approach (31, 32).

Pair correlation (PC) analysis and k-means-like clustering analysis were performed using MATLAB (The Mathworks, Inc., Natick, MA, USA) on 10–18 μm^2 regions of interest (ROIs) as described previously (31, 32, 40, 42, 43). To briefly summarize key steps in the analysis, images of cells were first binarized using localization xy-coordinate centers obtained from NIS-elements. Localizations corresponding to noise (precision values outside the 98th percentile) were removed from these images. Individual ROIs were placed across the cells and the total number of localizations from within these regions was divided by a constant value (α, respective to the specific fluorophore) to obtain detected densities in terms of the number of molecules. Auto-correlation functions were computed using fast Fourier transforms to obtain the number of molecules per cluster and cluster radius (40, 42). Subsequently, localization precision and the cluster radius from PC analysis were directed into a k-means-like clustering algorithm (32, 43) to determine the fraction of clustered receptors. This calculation groups detected localizations via thresholds for spatial parameters (PC cluster radius and average localization precision) and a temporal parameter (maximum fluorophore dark time). Molecules were counted as part of a cluster (more than two receptors) if these spatiotemporal requirements are met; otherwise, molecules were counted as unclustered. All codes for this analysis workflow have been provided previously (32, 42) and the described approach was validated using Monte Carlo simulations (32).

The calculation for all *p*-values was performed in Excel using the Student's *t*-test with a one-tailed distribution and heteroscedastic two-sample unequal variance type.

2.9. Drug treatment for Western blot assays

Cells were treated with PBS as vehicle control, 10 μM afatinib (LC LABS) for the indicated times. For multivalent meditope treatment, cells were treated with 10 nM trastuzumab memAb for 10 min, washed with warm media briefly and subsequently treated with either 10 nM Fc, 10 nM M2Fc, or 10 nM M4Fc for the indicated times. For parenteral antibody treatment, cells were treated with 10 nM trastuzumab and 10 nM pertuzumab in combination for the indicated times. The meditope treated and parental antibody treated cells were then washed briefly with warm media and treated with or without 10 ng/ml EGF (Genscript). All drug incubations were performed at 37°C in a cell culture incubator. To test for HER2-paGFP transfection activity, cells were treated with 10 ng/ml EGF for 30 min.

2.10. Kinetic studies

Cells were treated with multivalent meditopes as described above for the indicated times. Cells were lysed for immunoblotting with phospho-Akt, total Akt, phospho-HER2, total HER2, phospho-Erk1/2, total Erk1/2, phospho-EGFR, and total EGFR. Blots were imaged and quantified using the Image Lab software (Biorad). Akt, Erk1/2, and EGFR phosphorylation at each time point was quantified and normalized by calculating the ratio of pAkt over total Akt, pErk1/2 over total Erk1/2, and pEGFR over total EGFR, respectively, in each lane. The relative phosphorylation was normalized to the maximum response by control Fc at each time point. The experiment was repeated five times independently to calculate an average normalized relative phosphorylation.

2.11. Western blot

To prepare protein extracts for immunoblotting, cells were pelleted by centrifugation and washed two times using ice-cold PBS.

The pellets were subsequently resuspended in lysis buffer (150 mM sodium chloride, 50 mM Tris, pH 8.0, 1% NP-40, Protease and Phosphatase Inhibitor Mini Tablets, Pierce) and rotated at 4°C for 30 min to lyse the cells. The cells were then centrifuged for 20 min at 10,000 rpm at 4°C. The supernatant consisting of the protein lysate was stored at −80°C. SDS-polyacrylamide gel electrophoresis and western blotting procedures were carried out using the treated cell lysates as per standard protocols. Primary antibodies used included anti-phospho-EGFR (Tyr 1068) (rabbit monoclonal, Cell Signaling), anti-EGFR (rabbit monoclonal, Abcam), anti- phospho-HER2 (tyr877) (rabbit monoclonal, Abcam) anti-HER2 (rabbit monoclonal, Abcam), anti-phospho-Akt (S473) (rabbit polyclonal, Abcam), anti-Akt (rabbit polyclonal, Abcam), anti-phospho-Erk1/2 (Thr202/Tyr204) (rabbit monoclonal, Cell Signaling); anti-Erk1/2 (rabbit polyclonal, Abcam); and anti-β-actin (mouse monoclonal, Cell signaling). Proteins were detected with Pierce ECL detection reagents (Pierce). The blots were imaged on a Biorad Chemidoc imager.

3. Results

3.1. Evaluation of a functional HER2-paGFP construct

In SMLM, target molecules of interest are detected via fluorescent reporters. Since one of our objectives was to use qSMLM to map the membrane organization of HER2 in breast cancer cells, we genetically tagged HER2 with photoactivatable green fluorescent protein (HER2-paGFP) and expressed this construct in MDA-MB-468 cells. This breast cancer cell line has a very low expression level of HER2 (32) and high expression of EGFR (44) and is considered HER2 negative. We then compared levels of HER2-paGFP expressed in MDA-MB-468 cells to native HER2 found in HER2 overexpressing SK-BR-3 breast cancer cells. According to our results from Western blot analysis (**Supplementary Figure 1**), the amount of expressed HER2-paGFP in MDA-MB-468 cells was comparable to endogenous HER2 in SK-BR-3 cells. In addition, both cell lines were exposed (for 0, 5, 30 min) to one of two treatments: either epidermal growth factor (EGF) or a combination of EGF + afatinib. EGF is a ligand for EGFR and has been shown to stimulate growth and differentiation, activate HER2, and promote phosphorylation of receptor tyrosine kinases. Conversely, afatinib is an irreversible inhibitor of both EGFR and HER2. During the treatments, we followed the phosphorylation status of five protein kinases involved in HER2 signaling: HER2, EGFR, protein kinase B (Akt), and extracellular signal-regulated kinases 1 and 2 (Erk1/2). Treating both cell lines with 10 ng/ml EGF led to the phosphorylation of all four kinases. Phosphorylation was reduced when both cell lines were additionally treated with 10 μ M afatinib.

We next assessed how the phosphorylation of EGFR (Y1068) was affected by HER2-paGFP expression. Using Western blot analysis (**Supplementary Figure 2**), we probed the phosphorylation of EGFR when 10 ng/ml EGF was applied to the following cells: SK-BR-3, MDA-MB-468, MDA-MB-468 expressing HER2-paGFP, and MDA-MB-453 cells. MDA-MB-453 breast cancer cells do not express significant amounts of EGFR and HER2. As expected, MDA-MB-453 cells did not show EGFR phosphorylation following EGF treatment. Treatment of the other three cell lines with EGF showed increased phosphorylation of EGFR. This increase was more pronounced in MDA-MB-468 expressing HER2-paGFP than in MDA-MD-468 cells, which have minimal endogenous HER2. Altogether, results in **Supplementary Figures 1**, **2** suggest that the HER2-paGFP construct is functional.

3.2. Therapeutic antibodies affect clustering of HER2

Using qSMLM, we assessed the distribution of HER2-paGFP in cultured MDA-MD-468 cells. As shown in **Figure 1**, HER2 was imaged both in the steady state and upon the following four treatments: Fab trastuzumab, trastuzumab, pertuzumab, and the combination of trastuzumab + pertuzumab. While some degree of HER2 clustering was observed in both the steady state and upon treatment with Fab trastuzumab, an increase in clustering was evident for all mAb treatments (**Figure 1A**). We assessed the imaging data using analysis algorithms to define the distribution of detected HER2 molecules per cluster (**Figure 1B**), the distribution of HER2 cluster radii (**Figure 1C**), and the fraction of clustered HER2 molecules (**Figure 1D**). The detected HER2 densities are shown in **Supplementary Figure 3A** and corresponding localization precision distributions are shown in **Supplementary Figure 4A**. Individual mAb treatments, trastuzumab or pertuzumab, resulted in an increased frequency of larger clusters with radii > 80 nm (**Figure 1C**, in gray). Trastuzumab + pertuzumab treatment produced the highest frequency of larger clusters (>80 nm radii) that contained > 8 HER2 molecules (**Figures 1B, C**, in gray). Additionally, the fraction of clustered HER2 molecules increased when breast cancer cells were treated with trastuzumab, pertuzumab, or a combination of trastuzumab + pertuzumab. Overall, the combination of trastuzumab + pertuzumab led to the most pronounced increase in HER2 clustering.

3.3. Clustering of HER2 increases upon treatment with multivalent reagents

Meditopes are cyclic 12-mer peptides that bind tightly (∼400 nM) to a unique site within the Fab arm of cetuximab (34). Previously, we demonstrated that this meditope-binding site is absent in human mAbs but can be readily grafted onto them; we termed the constructs meditope-enabled Abs (memAbs). We have demonstrated that the presence of the meditope does not affect antigen binding of memAbs (35–38). Here, we used the technology, in concert with qSMLM, to determine how the clustering of HER2 was affected by the valency. To this end, we fused the meditope sequence to either the N-termini or both the N- and C-termini of an IgG1 Fc (CH_2-CH_3) domain. We used this approach to generate two multivalent meditopes: Fc-divalent meditope (M2Fc) and Fc-tetravalent meditope (M4Fc).

Using qSMLM, we identified how the clustering of HER2-paGFP in MDA-MB-468 cells was affected by trastuzumab memAb (TmemAb) in combination with one of the following

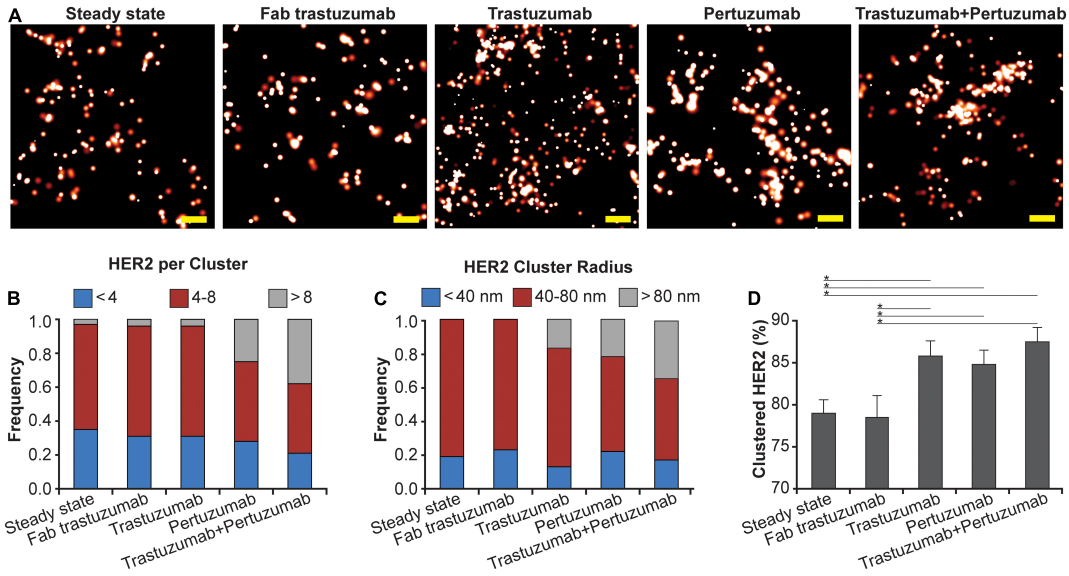

FIGURE 1
Effect of mAbs on HER2 nanoscale organization. **(A)** SMLM images of HER2-paGFP within a region from MDA-MB-468 cells in steady state and upon mAb/Fab treatment. An example for steady state HER2 is shown on the left, and examples for the organization of HER2 upon 10-min treatment with 20 nM Fab trastuzumab, 10 nM trastuzumab, 10 nM pertuzumab, and co-treatment with 10 nM trastuzumab and 10 nM pertuzumab are shown from left to right. All treatments were performed at 37°C. Scale bars: 200 nm. Standard PALM image analysis was employed (68) and localizations were grouped using a maximum blinking time of 5 s for paGFP and group radius of three times the maximum localization precision. **(B)** Distribution of detected HER2-paGFP molecules per cluster in steady state and upon mAb treatment. **(C)** Distribution of cluster radius of HER2-paGFP in steady state and upon mAb treatment. **(D)** Fraction of clustered HER2-paGFP molecules with SEM; *denotes p value ≤ 0.05. Quantitative analysis **(B–D)** was based on the following cell and region of interest (ROI) statistics: steady state (12 cells, 26 ROI), Fab trastuzumab (12 cells, 26 ROI), trastuzumab (13 cells, 30 ROI), pertuzumab (13 cells, 36 ROI), and co-treatment with trastuzumab and pertuzumab (12 cells, 29 ROI). ROIs for analysis were 10-18 μm^2. While Fab trastuzumab had minimal effect on the HER2 distribution, mAbs and mAb combination induced significant clustering.

ligands: Fc domain (monovalent control), M2Fc (divalent meditope ligand), and M4Fc (tetravalent meditope ligand). Treatments were assessed at 3 and 10 min by qSMLM (Figure 2A and Supplementary Figure 5). The detected HER2 densities are shown in Supplementary Figure 3B and the associated localization precision distributions are shown in Supplementary Figure 4B. We assessed the imaging data upon each treatment using the same analysis as the therapeutic antibodies to obtain quantitative information on the distribution of detected HER2 per cluster (Figure 2B), the distribution of HER2 cluster radii (Figure 2C), and the fraction of clustered HER2 (Figure 2D). While some HER2 clustering was observed for all treatments at 3 min, it was most pronounced for tetravalent meditope M4Fc combined with TmemAb. This combination produced the highest frequency of larger-sized clusters (>80 nm radii) occupied with >8 HER2 molecules (Figures 2B, C in gray), and the highest fraction of clustered HER2 (Figure 2D). While still present at 10 min, the magnitude of HER2 clustering was reduced across all treatments.

3.4. Endogenous HER2 in BT-474 breast cancer cells shows a high degree of clustering upon treatment with multivalent reagents

In addition to mapping the nanoscale organization of HER2-paGFP, where HER2 is covalently attached to the fluorescent reporter, we assessed the organization of endogenous HER2 in breast cancer BT-474 cells. To this end, TmemAb was covalently labeled with a suitable fluorescent reporter, Alexa Fluor 647 (AF647), for qSMLM. For steady state, cells were first fixed and subsequently stained with TmemAb-AF647 postfixation (PF). To assess the effects of multivalent ligands, live cells were first incubated with reagents and subsequently fixed. In the latter scenario, we tested the following six treatments: (1) TmemAb-AF647 alone; (2–5) TmemAb-AF647 + one of four M2Fc ligands; and (6) TmemAb-AF647 + M4Fc. In all cases, TmemAb-AF647 was administered at a 10 nM concentration. In the case of M2Fc, the length of the meditope linker was varied (c10, c20, c30, and c37) to probe the impact of meditope geometry on HER2 clustering.

SMLM images in Figure 3A illustrate that M2Fc and M4Fc induce an increase in HER2 clustering in combination with the TmemAb. Figure 3B summarizes the average detected molecular density of HER2 (as detected with TmemAb-AF647) and the corresponding localization precision distributions are provided in Supplementary Figure 4C. The p values for the HER2 densities are given in Supplementary Table 1. The highest HER2 densities were detected when TmemAb-AF647 was paired with either M2Fc (c37) or M4Fc (Figure 3B). According to studies in different cell lines, the normal function of HER2 may be influenced by local differences in HER2 spatial arrangement on the cell membrane: monomers, dimers, and clusters (29–33). We thus analyzed the imaging data to determine nanoscale organization of endogenous HER2 upon multivalent ligand treatment, Figures 3C, D. We identified the fraction of TmemAb-bound HER2 as either an isolated receptor (monomer), a cluster of two receptors, or a cluster

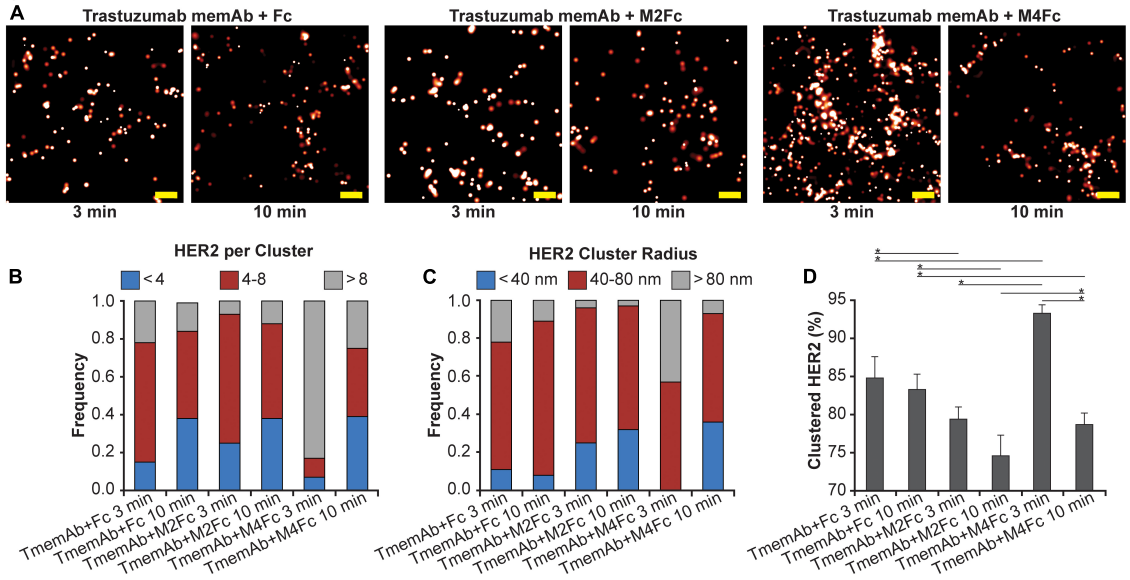

FIGURE 2
Effect of multivalent meditope-based ligands on HER2 nanoscale organization. **(A)** SMLM images of HER2-paGFP from a region on MDA-MB-468 cells upon treatment with trastuzumab memAb (TmemAb) in combination with Fc or Fc-multivalent meditiope constructs. Image pairs from left to right show HER2 upon treatment with 10 nM TmemAb for 10 min and subsequent incubation for either: 3 or 10 min with Fc; Fc-divalent meditope (M2Fc); or Fc-tetravalent meditope (M4Fc). All treatments were performed at 37°C and cells were briefly washed with warm media before treatment with Fc or Fc-meditope constructs. Scale bars: 200 nm. Standard PALM image analysis was employed (68) and localizations were grouped using a maximum blinking time of 5 s for paGFP and a group radius of three times the maximum localization precision. **(B)** Distribution of detected HER2-paGFP molecules per cluster upon treatment with TmemAb in combination with Fc or Fc-multivalent meditiope treatment. **(C)** Distribution of cluster radius of HER2-paGFP upon treatment with TmemAb in combination with Fc or Fc-multivalent meditiope treatment. **(D)** Fraction of clustered HER2-paGFP molecules with SEM; *denotes p value ≤ 0.05. Quantitative analysis **(B–D)** was based on the following cell and region of interest (ROI) statistics: TmemAb and Fc treatment for 3 min (12 cells, 27 ROI), TmemAb and Fc treatment for 10 min (12 cells, 26 ROI), TmemAb and M2Fc treatment for 3 min (12 cells, 28 ROI), TmemAb and M2Fc treatment for 10 min (14 cells, 34 ROI), TmemAb and M4Fc treatment for 3 min (12 cells, 30 regions), TmemAb and M4Fc treatment for 10 min (12 cells, 28 ROI). ROIs for analysis were 10–18 μm^2. Treatment with M4Fc for 3 min had a significant clustering effect on the HER2 distribution.

with more than two receptors; the p values for the fraction of clustered HER2 are given in Supplementary Table 2. Based on the analysis (Figure 3C), HER2 monomers were most abundant when TmemAb-AF647 was used alone (PF or in live cells) and lower frequencies of HER2 monomers were observed when TmemAb-AF647 was combined with multivalent meditopes. By far the highest percentage of clustered HER2 was observed for the tetravalent meditope (Figure 3D).

3.5. Combination of memAbs and multivalent meditopes significantly reduces receptor tyrosine kinase phosphorylation at early time points

Given these findings, we were interested in identifying how multivalent treatments affected downstream HER2 signaling pathways. For example, data suggests HER receptors may be highly expressed in a trastuzumab resistant setting (45–52) and may associate into signaling platforms to activate pathways and compensate for trastuzumab-induced inhibition (45, 52). We thus tested how exposing MDA-MB-468 cells that express HER2-paGFP to different treatments affected the phosphorylation of HER2, EGFR, Akt, and Erk1/2. Western blot analysis was used to identify the impact of four different treatments: (1) TmemAb + Fc; (2) TmemAb + M2Fc; (3) TmemAb + M4Fc; and (4) trastuzumab + pertuzumab. After the treatments were administered for the indicated times (Figure 4A), cells were incubated for an additional 30 min at 37°C either in the presence or absence of EGF. Images of the Western blots are shown in Figure 4A. The relative phosphorylation of Akt, HER2, and EGFR was calculated as a ratio (pReceptor divided by total Receptor) and normalized to the maximum response by Fc (Figure 4B). Remarkably, both TmemAb + M2Fc and TmemAb + M4Fc effectively blocked EGFR, HER2, and Akt phosphorylation at 10 min. Compared to the control (TmemAb + Fc), phosphorylation of EGFR, HER2, and Akt was attenuated with TmemAb and multivalent meditope ligands at 30 min; the effect was more pronounced with M4Fc. Compared to the control, phosphorylation of EGFR, HER2, and Akt was attenuated with trastuzumab + pertuzumab at 10 and 30 min, but to a lower extent.

3.6. Treatment with TmemAb + tetravalent meditope activates antibody dependent cellular cytotoxicity

One mechanism promoted by trastuzumab, which may lead to improved clinical outcomes, is ADCC (15, 16). Similarly,

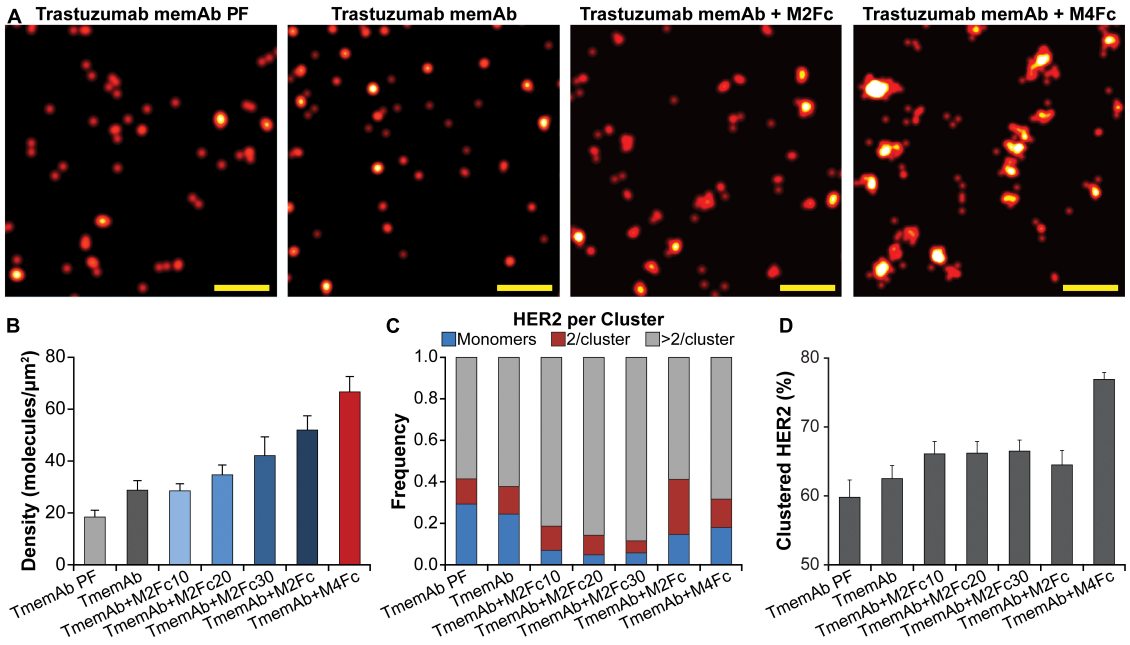

FIGURE 3
Trastuzumab memAb and multivalent meditopes induce HER2 reorganization. **(A)** SMLM images of AF647 labeled trastuzumab memAb (TmemAb) targeting HER2 on BT-474 cells. Live cells were incubated with 10 nM TmemAb-AF647, alone or premixed with 10 nM multivalent meditope (i.e., M2Fc and its variants or M4Fc), for 10 min at 37°C and subsequently fixed. Alternatively, cells were stained with 10 nM TmemAb-AF647 postfixation (PF). Scale bars: 200 nm. **(B)** Average molecular density of HER2 detected with TmemAb; the p values are provided in **Supplementary Table 1**. **(C)** Fraction of TmemAb-bound HER2 identified as an isolated receptor (blue), within a cluster of two receptors (red), or as part of a cluster with more than two receptors (gray). **(D)** Percentage of clustered proteins within a given ROI; the p values are provided in **Supplementary Table 2**. Quantitative analysis **(B–D)** used the following cell and region of interest (ROI; 18 μm^2) statistics: TmemAb PF (14 cells, 29 ROI), TmemAb (14 cells, 34 ROI), TmemAb + M2Fc10 (16 cells, 40 ROI), TmemAb + M2Fc20 (17 cells, 39 ROI), TmemAb + M2Fc30 (15 cells, 35 ROI), TmemAb + M2Fc (23 cells, 43 ROI), and TmemAb + M4Fc (24 cells, 57 ROI).

pertuzumab has been shown to activate ADCC and the enhanced efficacy of the antibody combination treatment has been explained, in part, by this mode of action (9, 17). Since clustering and phosphorylation were significantly increased by the tetravalent meditope, we were interested in measuring how it affected ADCC. To this end, SK-BR-3 cells were exposed for 6 h at 37°C to one of four treatments: (1) trastuzumab; (2) trastuzumab + M4Fc; (3) TmemAb; (4) TmemAb + M4Fc. The concentration of M4Fc was held at 10 nM while we assessed different concentrations of the Abs. Consistently across the various concentrations (**Figure 5**), the highest levels of ADCC activity were observed when cells were treated with TmemAb + M4Fc. A control experiment (**Supplementary Figure 6**) was performed, which demonstrated that ADCC activity was negligible without target or effector cells. Overall, these results suggest that the multivalent meditope, in combination with meditope-enabled trastuzumab, enhances ADCC activity.

4. Discussion

While the precise mechanism of mAb combinations is still being investigated, trastuzumab plus pertuzumab combined with chemotherapy is now part of the clinician's armamentarium to treat HER2-positive breast cancer. Multiple mechanisms have been presented to explain its clinical utility, including its ability to block (homo- and hetero-) HER2 dimerization, increase ADCC, and/or attenuate the HER2 signaling cascade (9, 17, 26–28). Recent studies have demonstrated additional effects of HER2 associated with receptor nanoscale organization. For example, high expression levels of HER2 on breast cancer cells appear to drive individual receptors into detectable molecular clusters and potentially altering interactions with adjacent cells (30). Large HER2 clusters also appear to be more resistant to internalization when activated (53–57). Of interest, abnormal trafficking into intracellular compartments appears to be a common theme for cell surface receptors involved in tumor development (58, 59). Indeed, HER2 has been detected within nanometer sized cholesterol-enriched plasma membrane domains (60–62) that support rapid signaling. Additionally, membrane HER2 nanoscale clustering is sensitive to treatment with targeted or chemotherapeutic agents (31) and may be associated with therapy response in HER2-positive breast cancer (33). These studies suggest there is a potential link between important physiological events, such as the membrane residency time of HER2, and local differences in the membrane organization of HER2. Given that the propagation of signals *in vitro* occurs on minute time scales (**Supplementary Figures 1**, **2**), we probed the molecular dynamics of HER2 membrane organization at early time points. We show that mAb(s)/memAb-ligand treatments affect cell surface receptor clustering; the observed effects were dependent on ligand valency. Moreover, these treatments also affected downstream processes,

10.3389/fmed.2023.1064242

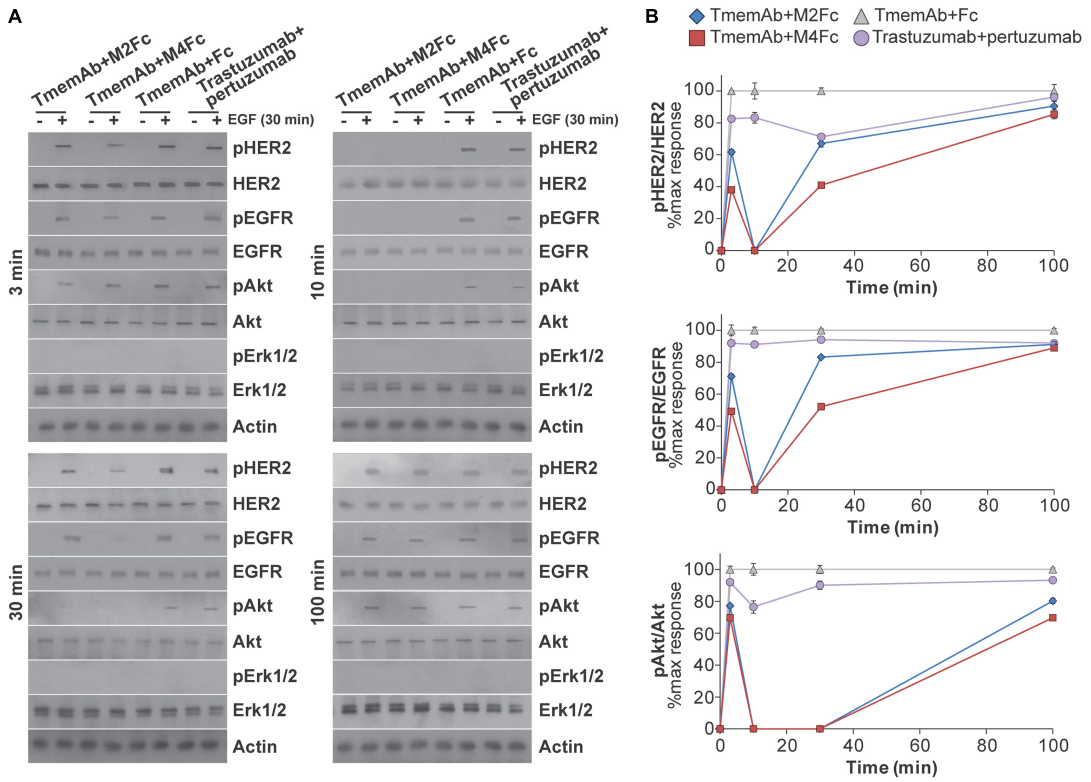

FIGURE 4
Effects of multivalent meditopes on cell signaling pathways upon EGF stimulation of HER2-paGFP transfected MDA-MB-468 cells. Cells were treated with 10 nM trastuzumab memAb for 10 min, followed by either 10 nM Fc, M2Fc, M4Fc or Fc for indicated times. Cells were incubated for additional 30 min without or with addition of 10 ng/ml EGF. Alternatively, cells were co-treated with 10 nM trastuzumab and 10 nM pertuzumab for indicated periods of time. After brief wash with warm media, cells were incubated for additional 30 min without or with addition of 10 ng/ml EGF. All treatments were performed at 37°C; cells were briefly washed with warm media before and after treatment with Fc or Fc-meditope constructs. **(A)** Phosphorylation of EGFR(Y1068), HER2(Y877), and downstream signaling targets Akt(S473) and Erk1/2(p42/44 T202/Y204) was determined using Western blot analysis for cells treated as described above. **(B)** Relative phosphorylation of Akt, HER2, and EGFR for cells treated as described above was calculated as the ratio of pAkt over total Akt, pHER2 over total HER2 or pEGFR over total EGFR and normalized to the maximum response by Fc at the indicated time points. Results are representative of 5 independent experiments. Colors show Fc treatment in gray, M2Fc treatment in blue, M4Fc in red, and combined parental trastuzumab and pertuzumab in purple. M4Fc has the highest inhibition of EGF mediated phosphorylation.

including phosphorylation in HER2 signaling pathways, at notably short timeframes.

To understand the effects of mAb and memAb therapies on HER2 molecular organization, we combined meditope technology, which allows us to control the valency of the treatment, with qSMLM. These technologies enabled us to report on the effect of valency on molecular density and organization of HER2. Because SMLM imaging requires a fluorescent reporter, we applied both PALM (detecting HER2 genetically tagged with optical highlighter protein, in this case, paGFP) and dSTORM (detecting HER2 tagged with an affinity reagent that contains a fluorescent dye, in this case, AF647) to comprehensively assess HER2 clustering. HER2-paGFP was transiently overexpressed in MDA-MB-468 breast cancer cells (very low levels of endogenous HER2). Having established the functionality of the construct (Supplementary Figure 1, 2), we set out to map how the membrane organization of HER2-paGFP was affected by either clinical therapies or our meditope reagents. For the therapeutic antibodies, the images show that the most extensive clustering of HER2 (Figure 1) was produced when cells were treated with a combination of pertuzumab + trastuzumab. For the meditope reagents, the most significant clustering of HER2 (Figure 2) was observed when cells were treated with TmemAb plus the M4Fc. Similar results were obtained when we used fluorescently labeled trastuzumab to detect native HER2 in BT-474 breast cancer cells (Figure 3A): by far the highest fraction of clustered HER2 was observed for the tetravalent meditope (Figure 3D). Of note, trastuzumab can likely bind both sterically accessible dimeric HER2 and monomeric HER2 (63). However, trastuzumab cannot bind—and thus detect—HER2 that is sterically hindered (e.g., with heavily glycosylated proteins) or HER2 that lacks an extracellular trastuzumab binding domain. Accordingly, using fluorescently labeled trastuzumab we have previously reported (33) differences in HER2 clustering in cell lines that have a different expression of large, glycosylated proteins (e.g., JIMT-1 cells vs. SK-BR-3 cells). Thus, trastuzumab can sensitively detect changes in HER2 clustering at different receptor densities and local membrane environments.

In the canonical mode of signaling, cell surface dimerization of HER receptors leads to interaction between their intracellular kinase domains, transphosphorylation of tyrosine residues in the C-terminal ends, and initiation of signals that are transduced to the nucleus via different pathways including mitogen-activated protein kinases (MAPKs), phosphoinositide-3-kinase (PI3K)/Akt, and phospholipase C gamma (PLCgamma) pathways. Interestingly,

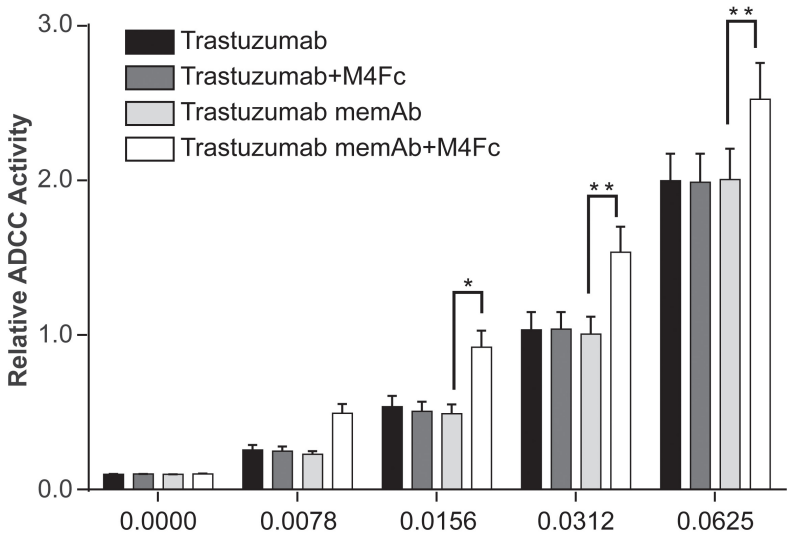

FIGURE 5
Effects of M4Fc on ADCC in SK-BR-3 cells. ADCC activity was measured in SK-BR-3 cells treated with increasing doses of trastuzumab or trastuzumab memAb in the presence or absence of 10 nM M4Fc for 6 h. Data was compiled from three experiments and analyzed using a 2-way ANOVA (*$p < 0.05$; **$p < 0.01$). Data is normalized to the untreated (0 nM antibody) cell signal. Treatment with M4Fc in the presence of trastuzumab memAb shows higher levels of ADCC activity.

activated HER2 can resist significant endocytosis (54). While trastuzumab-induced receptor downregulation is a slow process, it can affect the remodeling of the plasma membrane at early time points (preceding endocytosis) (64). Given that mAb treatment (with or without multivalent ligands) can quickly alter HER2 nanoscale organization, we next probed if these biologics can also affect the propagation of signals. We show that changes to HER2 organization at early time points are accompanied by changes in physiological function. The multivalent meditopes (complexed with TmemAb) that show the most pronounced HER2 clustering also exhibited the highest inhibition of EGF-mediated phosphorylation (**Figure 4**). Additionally, tetravalent meditope/TmemAb enhanced ADCC (**Figure 5**).

In addition to canonical signaling, HER fragments can signal directly. Such fragments are typically generated by the action of alpha and gamma secretases. For example, previous work has shown gene transcription to be regulated by a nuclear carboxy-terminal fragment comprising the cytoplasmic domain of HER4 (65, 66) and HER2 (67). Importantly, a fragment of the intracellular domain of HER2, termed 611-CTF (carboxy terminal fragment), can constitutively homodimerize and regulate MET, EPHA2, matrix metalloproteinase 1, interleukin 11, angiopoietin-like 4, and different integrins, promoting mammary tumor growth and metastasis. Future experiments are needed to explore if the membrane nanoscale organization of HER receptors is associated with fragment generation and activity.

Altogether, our results suggest that high valent treatments, achieved either through a combination of clinical Abs or meditope technology, have the capacity to arrange HER2 on the membrane of breast cancer cells, may abrogate elements of the HER2 signaling cascade, and may ultimately lead to the elimination of breast cancer cells. This study as well as others highlight the role of valency on receptor dynamics and geography. The multivalent ligand approach may be a general strategy for manipulating receptor clustering applicable to many unique targets (e.g., PD-L1, CD38, CD19). Beyond increasing the valency, this approach also vitiates the need to identify additional mAbs to non-overlapping epitopes. However, the consequences of massive clustering will be unique for each system and need to be assessed. Critically, this study also suggests that qSMLM can provide valuable information and guide the effort to design multivalent biologics (e.g., bispecific and biparatropic mAbs) for therapeutic intent.

Data availability statement

The raw data supporting the conclusions of this article will be made available by the authors, without undue reservation.

Author contributions

DLW, OG, RJ, SB, JCW, and TJ-T conceived and designed the experiments and developed experimental/computational techniques. DLW, OG, RJ, SB, KM, KNA, CZ, SJT, EEC, JCW, and TJ-T carried out the experiments and analyzed the data. DLW, OG, RJ, SB, KM, KNA, SJT, IJT, JCW, and TJ-T wrote the manuscript. All authors contributed to the article and approved the submitted version.

Funding

This work was supported by NCI R21-CA174608 grant (Williams/Talisman), W. M. Keck Medical Foundation grant (Williams/Talisman/Horne/Park), STOP Cancer Foundation (Talisman), and Beckman Research Institute of the City of Hope.

Research reported in this publication included work performed in the Drug Discovery and Structural Biology Core supported by the National Cancer Institute of the National Institutes of Health under award number P30CA33572.

Conflict of interest

JCW is a Founder and Shareholder of Meditope Biosciences, Inc. In addition, we note that KNA, CZ, and JCW are declared to be inventors on patents U.S. Patent No. 8,658,774.

The remaining authors declare that the research was conducted in the absence of any commercial or financial relationships that could be construed as a potential conflict of interest.

Publisher's note

All claims expressed in this article are solely those of the authors and do not necessarily represent those of their affiliated organizations, or those of the publisher, the editors and the reviewers. Any product that may be evaluated in this article, or claim that may be made by its manufacturer, is not guaranteed or endorsed by the publisher.

Author disclaimer

The content is solely the responsibility of the authors and does not necessarily represent the official views of the National Institutes of Health.

Supplementary material

The Supplementary Material for this article can be found online at: https://www.frontiersin.org/articles/10.3389/fmed.2023.1064242/full#supplementary-material

References

1. Paik S, Hazan R, Fisher E, Sass R, Fisher B, Redmond C, et al. Pathologic findings from the national surgical adjuvant breast and bowel project: prognostic significance of ErbB-2 protein overexpression in primary breast cancer. *J Clin Oncol.* (1990) 8:103–12. doi: 10.1200/jco.1990.8.1.103

2. Sjogren S, Inganas M, Lindgren A, Holmberg L, Bergh J. Prognostic and predictive value of C-ErbB-2 overexpression in primary breast cancer, alone and in combination with other prognostic markers. *J Clin Oncol.* (1998) 16:462–9. doi: 10.1200/jco.1998.16.2.462

3. Slamon D, Clark G, Wong S, Levin W, Ullrich A, McGuire W. Human breast cancer: correlation of relapse and survival with amplification of the HER-2/neu oncogene. *Science.* (1987) 235:177–82.

4. Press M, Pike M, Chazin V, Hung G, Udove J, Markowicz M, et al. Her-2/neu expression in node-negative breast cancer: direct tissue quantitation by computerized image analysis and association of overexpression with increased risk of recurrent disease. *Cancer Res.* (1993) 53:4960–70.

5. Seshadri R, Firgaira F, Horsfall D, McCaul K, Setlur V, Kitchen P. Clinical significance of HER-2/neu oncogene amplification in primary breast cancer. The south Australian breast cancer study group. *J Clin Oncol.* (1993) 11:1936–42. doi: 10.1200/jco.1993.11.10.1936

6. Stern H. Improving treatment of HER2-positive cancers: opportunities and challenges. *Sci Transl Med.* (2012) 4:127rv2. doi: 10.1126/scitranslmed.3001539

7. Vogel C, Cobleigh M, Tripathy D, Gutheil J, Harris L, Fehrenbacher L, et al. Efficacy and safety of trastuzumab as a single agent in first-line treatment of Her2-overexpressing metastatic breast cancer. *J Clin Oncol.* (2002) 20:719–26. doi: 10.1200/jco.2002.20.3.719

8. Slamon D, Leyland-Jones B, Shak S, Fuchs H, Paton V, Bajamonde A, et al. Use of chemotherapy plus a monoclonal antibody against HER2 for metastatic breast cancer that overexpresses HER2. *N Engl J Med.* (2001) 344:783–92. doi: 10.1056/nejm200103153441101

9. Kreutzfeldt J, Rozeboom B, Dey N, De P. The trastuzumab era: current and upcoming targeted HER2+ breast cancer therapies. *Am J Cancer Res.* (2020) 10:1045–67.

10. Swain S, Baselga J, Kim S, Ro J, Semiglazov V, Campone M, et al. Pertuzumab, trastuzumab, and docetaxel in HER2-positive metastatic breast cancer. *N Engl J Med.* (2015) 372:724–34. doi: 10.1056/NEJMoa1413513

11. von Minckwitz G, Procter M, de Azambuja E, Zardavas D, Benyunes M, Viale G, et al. Adjuvant pertuzumab and trastuzumab in early HER2-positive breast cancer. *N Engl J Med.* (2017) 377:122–31. doi: 10.1056/NEJMoa1703643

12. Clark A, Yau C, Wolf D, Petricoin E, van 't Veer L, Yee D, et al. Neoadjuvant T-Dm1/pertuzumab and paclitaxel/trastuzumab/pertuzumab for HER2$^{(+)}$ breast cancer in the adaptively randomized I-Spy2 trial. *Nat Commun.* (2021) 12:6428. doi: 10.1038/s41467-021-26019-y

13. Baselga J, Cortes J, Kim S, Im S, Hegg R, Im Y, et al. Pertuzumab plus trastuzumab plus docetaxel for metastatic breast cancer. *N Engl J Med.* (2012) 366:109–19. doi: 10.1056/NEJMoa1113216

14. Ghosh R, Narasanna A, Wang S, Liu S, Chakrabarty A, Balko J, et al. Trastuzumab has preferential activity against breast cancers driven by HER2 homodimers. *Cancer Res.* (2011) 71:1871–82. doi: 10.1158/0008-5472.can-10-1872

15. Vu T, Claret F. Trastuzumab: updated mechanisms of action and resistance in breast cancer. *Front Oncol.* (2012) 2:62. doi: 10.3389/fonc.2012.00062

16. Hudis C. Trastuzumab–mechanism of action and use in clinical practice. *N Engl J Med.* (2007) 357:39–51. doi: 10.1056/NEJMra043186

17. Mandó P, Rivero S, Rizzo M, Pinkasz M, Levy E. Targeting Adcc: a different approach to HER2 breast cancer in the immunotherapy era. *Breast.* (2021) 60:15–25. doi: 10.1016/j.breast.2021.08.007

18. Nahta R, Yu D, Hung M, Hortobagyi G, Esteva F. Mechanisms of disease: understanding resistance to HER2-targeted therapy in human breast cancer. *Nat Clin Pract Oncol.* (2006) 3:269–80. doi: 10.1038/ncponc0509

19. Mancini M, Gaborit N, Lindzen M, Salame T, Dall'Ora M, Sevilla-Sharon M, et al. Combining three antibodies nullifies feedback-mediated resistance to erlotinib in lung cancer. *Sci Signal.* (2015) 8:ra53. doi: 10.1126/scisignal.aaa0725

20. Francis D, Huang S, Armstrong E, Werner L, Hullett C, Li C, et al. Pan-her inhibitor augments radiation response in human lung and head and neck cancer models. *Clin Cancer Res.* (2016) 22:633–43. doi: 10.1158/1078-0432.CCR-15-1664

21. Chen S, Liang Y, Feng Z, Wang M. Efficacy and safety of HER2 inhibitors in combination with or without pertuzumab for HER2-positive breast cancer: a systematic review and meta-analysis. *BMC Cancer.* (2019) 19:973. doi: 10.1186/s12885-019-6132-0

22. Nami B, Maadi H, Wang Z. The effects of pertuzumab and its combination with trastuzumab on HER2 homodimerization and phosphorylation. *Cancers.* (2019) 11:375.

23. Sak M, Szymanska M, Bertelsen V, Hasmann M, Madshus I, Stang E. Pertuzumab counteracts the inhibitory effect of ErbB2 on degradation of Erbb3. *Carcinogenesis.* (2013) 34:2031–8. doi: 10.1093/carcin/bgt173

24. Bon G, Pizzuti L, Laquintana V, Loria R, Porru M, Marchiò C, et al. Loss of HER2 and decreased T-Dm1 efficacy in HER2 positive advanced breast cancer treated with dual HER2 blockade: the sepher study. *J Exp Clin Cancer Res.* (2020) 39:279. doi: 10.1186/s13046-020-01797-3

25. Nahta R, Hung M, Esteva F. The HER-2-targeting antibodies trastuzumab and pertuzumab synergistically inhibit the survival of breast cancer cells. *Cancer Res.* (2004) 64:2343–6. doi: 10.1158/0008-5472.can-03-3856

26. Scheuer W, Friess T, Burtscher H, Bossenmaier B, Endl J, Hasmann M. Strongly enhanced antitumor activity of trastuzumab and pertuzumab combination treatment

on HER2-positive human xenograft tumor models. *Cancer Res.* (2009) 69:9330–6. doi: 10.1158/0008-5472.Can-08-4597

27. Metzger-Filho O, Winer E, Krop I. Pertuzumab: optimizing HER2 blockade. *Clin Cancer Res.* (2013) 19:5552–6. doi: 10.1158/1078-0432.Ccr-13-0518

28. Cai Z, Zhang G, Zhou Z, Bembas K, Drebin J, Greene M, et al. Differential binding patterns of monoclonal antibody 2c4 to the Erbb3-P185her2/Neu and the Egfr-P185her2/Neu complexes. *Oncogene.* (2008) 27:3870–4. doi: 10.1038/onc.2008.13

29. Peckys D, Korf U, de Jonge N. Local variations of HER2 dimerization in breast cancer cells discovered by correlative fluorescence and liquid electron microscopy. *Sci Adv.* (2015) 1:e1500165. doi: 10.1126/sciadv.1500165

30. Chung I, Reichelt M, Shao L, Akita R, Koeppen H, Rangell L, et al. High cell-surface density of HER2 deforms cell membranes. *Nat Commun.* (2016) 7:12742. doi: 10.1038/ncomms12742

31. Golfetto O, Wakefield D, Cacao E, Avery K, Kenyon V, Jorand R, et al. A platform to enhance quantitative single molecule localization microscopy. *J Am Chem Soc.* (2018) 140:12785–97. doi: 10.1021/jacs.8b04939

32. Tobin S, Wakefield D, Liu X, Jones V, Schmolze D, Jovanovic-Talisman T. Single molecule localization microscopy coupled with touch preparation for the quantification of trastuzumab-bound HER2. *Sci Rep.* (2018) 11:15154. doi: 10.1038/s41598-018-33225-0

33. Maddox A, Brehove M, Eliato K, Saftics A, Romano E, Press M, et al. Molecular assessment of HER2 to identify signatures associated with therapy response in HER2-positive breast cancer. *Cancers.* (2022) 14:2795. doi: 10.3390/cancers14112795

34. Donaldson J, Zer C, Avery K, Bzymek K, Horne D, Williams J. Identification and grafting of a unique peptide-binding site in the fab framework of monoclonal antibodies. *Proc Natl Acad Sci USA.* (2013) 110:17456–61. doi: 10.1073/pnas.1307309110

35. King J, Ma Y, Kuo Y, Bzymek K, Goodstein L, Meyer K, et al. Template-catalyzed, disulfide conjugation of monoclonal antibodies using a natural amino acid tag. *Bioconjug Chem.* (2018) 29:2074–81. doi: 10.1021/acs.bioconjchem.8b00284

36. Bzymek K, Puckett J, Zer C, Xie J, Ma Y, King J, et al. Mechanically interlocked functionalization of monoclonal antibodies. *Nat Commun.* (2018) 9:1580. doi: 10.1038/s41467-018-03976-5

37. Kuo Y, Kuo C, Jenkins K, Hung A, Chang W, Park M, et al. Antibody-based redirection of universal fabrack-CAR T cells selectively kill antigen bearing tumor cells. *J Immunother Cancer.* (2022) 10:e003752. doi: 10.1136/jitc-2021-003752

38. Avery K, Zer C, Bzymek K, Williams J. Development of a high affinity, non-covalent biologic to add functionality to fabs. *Sci Rep.* (2015) 5:7817. doi: 10.1038/srep07817

39. Chen L, Wang L, Shion H, Yu C, Yu Y, Zhu L, et al. In-depth structural characterization of Kadcyla® (ado-trastuzumab emtansine) and its biosimilar candidate. *MABs.* (2016) 8:1210–23. doi: 10.1080/19420862.2016.1204502

40. Sengupta P, Jovanovic-Talisman T, Skoko D, Renz M, Veatch S, Lippincott-Schwartz J. Probing protein heterogeneity in the plasma membrane using palm and pair correlation analysis. *Nat Methods.* (2011) 8:969–75. doi: 10.1038/nmeth.1704

41. Dempsey G, Vaughan J, Chen K, Bates M, Zhuang X. Evaluation of fluorophores for optimal performance in localization-based super-resolution imaging. *Nat Methods.* (2011) 8:1027–36. doi: 10.1038/nmeth.1768

42. Sengupta P, Jovanovic-Talisman T, Lippincott-Schwartz J. Quantifying spatial organization in point-localization superresolution images using pair correlation analysis. *Nat Protoc.* (2013) 8:345–54. doi: 10.1038/nprot.2013.005

43. Rogacki M, Golfetto O, Tobin S, Li T, Biswas S, Jorand R, et al. Dynamic lateral organization of opioid receptors (kappa, muwt and mun40d) in the plasma membrane at the nanoscale level. *Traffic.* (2018) 19:690–709. doi: 10.1111/tra.12582

44. Subik K, Lee J, Baxter L, Strzepek T, Costello D, Crowley P, et al. The expression patterns of ER, PR, HER2, CK5/6, EGFR, Ki-67 and AR by immunohistochemical analysis in breast cancer cell lines. *Breast Cancer (Auckl).* (2010) 4:35–41.

45. Ritter C, Perez-Torres M, Rinehart C, Guix M, Dugger T, Engelman J, et al. Human breast cancer cells selected for resistance to trastuzumab in vivo overexpress epidermal growth factor receptor and ErbB ligands and remain dependent on the ErbB receptor network. *Clin Cancer Res.* (2007) 13:4909–19. doi: 10.1158/1078-0432.ccr-07-0701

46. Lee H, Seo A, Kim E, Jang M, Kim Y, Kim J, et al. Prognostic and predictive values of Egfr overexpression and Egfr copy number alteration in HER2-positive breast cancer. *Br J Cancer.* (2015) 112:103–11. doi: 10.1038/bjc.2014.556

47. Cheng H, Ballman K, Vassilakopoulou M, Dueck A, Reinholz M, Tenner K, et al. EGFR expression is associated with decreased benefit from trastuzumab in the ncctg N9831 (alliance) trial. *Br J Cancer.* (2014) 111:1065–71. doi: 10.1038/bjc.2014.442

48. Luque-Cabal M, Garcia-Teijido P, Fernandez-Perez Y, Sanchez-Lorenzo L, Palacio-Vazquez I. Mechanisms behind the resistance to trastuzumab in HER2-amplified breast cancer and strategies to overcome it. *Clin Med Insights Oncol.* (2016) 10(Suppl. 1):21–30. doi: 10.4137/cmo.s34537

49. Oliveras-Ferraros C, Vazquez-Martin A, Martin-Castillo B, Perez-Martinez M, Cufi S, Del Barco S, et al. Pathway-focused proteomic signatures in HER2-overexpressing breast cancer with a basal-like phenotype: new insights into de novo resistance to trastuzumab (herceptin). *Int J Oncol.* (2010) 37:669–78. doi: 10.3892/ijo_00000716

50. Alexander P, Chen R, Gong C, Yuan L, Jasper J, Ding Y, et al. Distinct receptor tyrosine kinase subsets mediate anti-HER2 drug resistance in breast cancer. *J Biol Chem.* (2017) 292:748–59. doi: 10.1074/jbc.M116.754960

51. Weitsman G, Barber P, Nguyen L, Lawler K, Patel G, Woodman N, et al. HER2-HER3 dimer quantification by flim-fret predicts breast cancer metastatic relapse independently of HER2 IHC status. *Oncotarget.* (2016) 7:51012–26. doi: 10.18632/oncotarget.9963

52. Lee-Hoeflich S, Crocker L, Yao E, Pham T, Munroe X, Hoeflich K, et al. A central role for HER3 in HER2-amplified breast cancer: implications for targeted therapy. *Cancer Res.* (2008) 68:5878–87. doi: 10.1158/0008-5472.can-08-0380

53. Jeong J, Kim W, Kim L, VanHouten J, Wysolmerski J. HER2 signaling regulates HER2 localization and membrane retention. *PLoS One.* (2017) 12:e0174849. doi: 10.1371/journal.pone.0174849

54. Bertelsen V, Stang E. The mysterious ways of ErbB2/HER2 trafficking. *Membranes (Basel).* (2014) 4:424–46. doi: 10.3390/membranes4030424

55. Hommelgaard A, Lerdrup M, van Deurs B. Association with membrane protrusions makes ErbB2 an internalization-resistant receptor. *Mol Biol Cell.* (2004) 15:1557–67. doi: 10.1091/mbc.e03-08-0596

56. Stüber J, Richter C, Bellón J, Schwill M, König I, Schuler B, et al. Apoptosis-inducing anti-HER2 agents operate through oligomerization-induced receptor immobilization. *Commun Biol.* (2021) 4:762. doi: 10.1038/s42003-021-02253-4

57. Kast F, Schwill M, Stüber J, Pfundstein S, Nagy-Davidescu G, Rodríguez J, et al. Engineering an anti-HER2 biparatopic antibody with a multimodal mechanism of action. *Nat Commun.* (2021) 12:3790. doi: 10.1038/s41467-021-23948-6

58. Mosesson Y, Mills G, Yarden Y. Derailed endocytosis: an emerging feature of cancer. *Nat Rev Cancer.* (2008) 8:835–50. doi: 10.1038/nrc2521

59. Sorkin A, Goh L. Endocytosis and intracellular trafficking of ErbBs. *Exp Cell Res.* (2009) 315:683–96.

60. Bourseau-Guilmain E, Menard J, Lindqvist E, Indira Chandran V, Christianson H, Cerezo Magana M, et al. hypoxia regulates global membrane protein endocytosis through caveolin-1 in cancer cells. *Nat Commun.* (2016) 7:11371. doi: 10.1038/ncomms11371

61. Shatz M, Liscovitch M. Caveolin-1: a tumor-promoting role in human cancer. *Int J Radiat Biol.* (2008) 84:177–89. doi: 10.1080/09553000701745293

62. Gueguinou M, Gambade A, Felix R, Chantome A, Fourbon Y, Bougnoux P, et al. Lipid rafts, Kca/ClCa/Ca2+ channel complexes and EGFR signaling: novel targets to reduce tumor development by lipids? *Biochim Biophys Acta.* (2015) 1848:2603–20. doi: 10.1016/j.bbamem.2014.10.036

63. Zhao J, Mohan N, Nussinov R, Ma B, Wu W. Trastuzumab blocks the receiver function of HER2 leading to the population shifts of Her2-containing homodimers and heterodimers. *Antibodies (Basel).* (2021) 10:7. doi: 10.3390/antib10010007

64. Wymant J, Sayers E, Muir D, Jones A. Strategic trastuzumab mediated crosslinking driving concomitant HER2 and HER3 endocytosis and degradation in breast cancer. *J Cancer.* (2020) 11:3288–302. doi: 10.7150/jca.32470

65. Linggi B, Carpenter G. ErbB-4 S80 intracellular domain abrogates ETO2-dependent transcriptional repression. *J Biol Chem.* (2006) 281:25373–80. doi: 10.1074/jbc.M603998200

66. Vidal G, Naresh A, Marrero L, Jones F. Presenilin-dependent gamma-secretase processing regulates multiple ErbB4/HER4 activities. *J Biol Chem.* (2005) 280:19777–83. doi: 10.1074/jbc.M412457200

67. Pedersen K, Angelini P, Laos S, Bach-Faig A, Cunningham M, Ferrer-Ramón C, et al. A naturally occurring HER2 carboxy-terminal fragment promotes mammary tumor growth and metastasis. *Mol Cell Biol.* (2009) 29:3319–31. doi: 10.1128/mcb.01803-08

68. Betzig E, Patterson G, Sougrat R, Lindwasser O, Olenych S, Bonifacino J, et al. Imaging intracellular fluorescent proteins at nanometer resolution. *Science.* (2006) 313:1642–5. doi: 10.1126/science.1127344

frontiers | Frontiers in Medicine

TYPE Original Research
PUBLISHED 28 April 2023
DOI 10.3389/fmed.2023.1166758

OPEN ACCESS

EDITED BY
Felicitas Mungenast,
TissueGnostics GmbH, Austria

REVIEWED BY
Shweta Singh,
National Cancer Institute at Frederick (NIH), United States
Tamar Tak,
Leiden University Medical Center (LUMC), Netherlands

*CORRESPONDENCE
Anna Rita Migliaccio
✉ a.migliaccio@unicampus.it;
✉ amigliaccio@altius.org

†These authors share senior authorship

RECEIVED 15 February 2023
ACCEPTED 11 April 2023
PUBLISHED 28 April 2023

CITATION
Mazzarini M, Arciprete F, Picconi O, Valeri M, Verachi P, Martelli F, Migliaccio AR, Falchi M and Zingariello M (2023) Single cell analysis of the localization of the hematopoietic stem cells within the bone marrow architecture identifies niche-specific proliferation dynamics. *Front. Med.* 10:1166758. doi: 10.3389/fmed.2023.1166758

Single cell analysis of the localization of the hematopoietic stem cells within the bone marrow architecture identifies niche-specific proliferation dynamics

Maria Mazzarini[1,2], Francesca Arciprete[3], Orietta Picconi[4], Mauro Valeri[5], Paola Verachi[1], Fabrizio Martelli[6], Anna Rita Migliaccio[2,3]*, Mario Falchi[4†] and Maria Zingariello[2†]

[1]Department of Biomedical and Neuromotor Sciences, University of Bologna, Bologna, Italy, [2]Altius Institute for Biomedical Sciences, Seattle, WA, United States, [3]Unit of Microscopic and Ultrastructural Anatomy, University Campus Bio-Medico, Rome, Italy, [4]National Center for HIV/AIDS Research, Istituto Superiore di Sanità, Rome, Italy, [5]Center for Animal Experimentation and Well-Being, Istituto Superiore di Sanità, Rome, Italy, [6]National Center for Preclinical and Clinical Research and Evaluation of Pharmaceutical Drugs, Istituto Superiore di Sanità, Rome, Italy

Introduction: Hematopoietic stem cells (HSC) reside in the bone marrow (BM) in specialized niches which provide support for their self-replication and differentiation into the blood cells. Recently, numerous studies using sophisticated molecular and microscopic technology have provided snap-shots information on the identity of the BM niches in mice. In adults, HSC are localized around arterioles and sinusoids/venules whereas in juvenile mice they are in close to the osteoblasts. However, although it is well recognized that in mice the nature of the hematopoietic niche change with age or after exposure to inflammatory insults, much work remains to be done to identify changes occurring under these conditions. The dynamic changes occurring in niche/HSC interactions as HSC enter into cycle are also poorly defined.

Methods: We exploit mice harboring the *hCD34tTA/Tet-O-H2BGFP* transgene to establish the feasibility to assess interactions of the HSC with their niche as they cycle. In this model, *H2BGFP* expression is driven by the TET trans-activator under the control of the human *CD34* promoter which in mice is active only in the HSC. Since Doxycycline inhibits TET, HSC exposed to this drug no longer express *H2BGFP* and loose half of their label every division allowing establishing the dynamics of their first 1-3 divisions. To this aim, we first validated user-friendly confocal microscopy methods to determine HSC divisions by hemi-decrement changes in levels of GFP expression. We then tracked the interaction occurring in old mice between the HSC and their niche during the first HSC divisions.

Results: We determined that in old mice, most of the HSC are located around vessels, both arterioles which sustain quiescence and self-replication, and venules/sinusoids, which sustain differentiation. After just 1 week of exposure to Doxycycline, great numbers of the HSC around the venules lost most of their GFP label, indicating that they had cycled. By contrast, the few HSC surrounding the arterioles retained maximal levels of GFP expression, indicating that they are either dormant or cycle at very low rates.

Conclusion: These results reveal that in old mice, HSC cycle very dynamically and are biased toward interactions with the niche that instructs them to differentiate.

KEYWORDS

hematopoietic stem cells, GFP reporter, quantitative microscopy, microenvironment, aging, adipocytes

1 Introduction

Recent studies, using a combination of mouse models, expression profiling and sophisticated multicolor confocal microscopy coupled with high power computer technologies, have demonstrated that under steady-state conditions the hematopoietic stem cells (HSC) are localized in areas of the bone marrow (BM) microenvironment defined as the HSC niche (1–5). The BM contains several niches, each one of them representing a unique cellular configuration that regulates specific aspects of the HSC fate. The most studied of the BM niches are the endosteal and the vascular niche. The endosteal niche consists of osteoclasts, osteoblasts and mesenchymal cells and is supposed to retain HSC into quiescence and to assure that they undergo self-renewal upon division. The vascular niche is composed by the endothelial cells surrounding the vessels and by pericytes surrounding the sinusoids and regulates the differentiation and mobilization of the HSC. The niche may affect HSC fate directly, by secreting factors such as stem cell factor (SCF) and C-X-C motif chemokine ligand 12 (CXCL12), necessary for their survival and proliferation, and indirectly, by recruiting cells such as megakaryocytes, macrophages and other stromal cells, which are responsible to secrete factors, such as platelet factor 4 (PF-4, also known as CXCL4) and Transforming Growth Factor-β (TGF-β) that induce HSC into quiescence allowing them to retain stemness (6).

In adult mice and under steady state conditions, the majority of HSC are located near the vascular niche, in particular around the arterioles (7). However, the location of HSC withing the BM architecture changes with age and under conditions of inflammation. In juvenile mice (3-weeks of age) HSC are found in high numbers near stromal cells expressing CXCL12 or associated with the osteoblast niche of the bone. By contrast, studies in old (>8-months old) mice, have identified profound changes in the localization of the HSC within the BM architecture, although the identity of the niche in these old mice has not been well characterized as yet (8–11). Experimentally induced inflammation, such as treatment with the pro-inflammatory cytokine interferon-γ, greatly reduces the interaction of the HSC with the arteriole niche, reducing their self-renewal potential, while increasing their interaction with the perisinusoidal niche, favoring differentiation and exhaustion (7, 12–14).

All these studies have two caveats: (1) they are all conducted on mice with the same genetic background (C57Bl6) and therefore they do not reflect the variability of the human population and (2) they provide snapshots of HSC fate in the mouse BM but say little on the dynamics of HSC location as they cycle. To study the cycling of the HSC, the Moore laboratory has developed the *hCD34tTA/TET-O-H2BGFP* transgenic mouse model (15–17). The *hCD34tTA* gene encodes a tet-Transactivator (tTA), which is suppressed by doxycycline (Doxy), under the control of the human CD34 promoter. The human CD34 promoter is active only in the HSC, restraining the expression of tTA to the HSC (16). *TET-O-H2B-GFP* encodes a H2B-GFP fusion gene under the control of the TetO element activated by tTA which is expressed only in the HSC. Therefore, in double *hCD34tTA/TET-O-H2BGFP* transgenic mice only the HSC are labeled by GFP. When mice are treated with Doxy, HSC lose half of their label following each division. It takes approximately 4 divisions for the HSC to lose their label. By flow cytometry, the HSC, identified by the SLAM phenotype (18, 19), may be divided based on hemi-decrements of GFP intensity into four populations: G0, which express maximal GFP levels and never divided, and cells which divided 1, 2, 3, and 4 times expressing, respectively, half (GFP1), a quarter (GFP2), an eighth (GFP3) or none (GFP4) of the maximal GFP level. Using this model, the Moore laboratory has demonstrated the feasibility to study the dynamics of the HSC proliferation in young mice under steady state conditions and after stimulation with G-SCF (20–23). By tracking the cumulative division history of the HSC throughout life, the Moore laboratory has also identified a slow-cycling HSC population that contains all the long-term repopulation activity of the HSC (15). This population undergoes four self-renewal divisions which last progressively longer time and then enters in a state of dormancy which is retained for the rest of the life of the mice. The niche which sustains the "dormant" and "cycling" HSC in these old mice has not been identified as yet.

Since the *hCD34tTA/TET-O-H2BGFP* transgenic mice express autofluorescence signals only in the bones (Dr. Moore personal communication), we decided to exploit the power of confocal microscopy to validate these mice as a model to track the HSC localization within the BM architecture as they divide. Given the limited information available on the identity of the niche which sustains the "dormant" and the "cycling" HSC in old mice discussed above (15), these studies were performed in *hCD34tTA/TET-O-H2BGFP* mice >11-months old. In addition, since TGF-β is one of the factors which retain the HSC into quiescence (24), the *hCD34tTA/TET-O-H2BGFP* mutation was brought in the CD1 background which express a baseline pro-inflammatory signature (25) that includes high levels of TGF-β. Th CD1 model allow assessing the number of HSC in proliferation under physiologically high TGF-β levels similar to that found in some of the elder population (26).

2 Materials and methods

2.1 Mice

Transgenic mice were bred in the animal facility of Istituto Superiore di Sanità as described (27, 28). The original *huCD34tTA and TetO-H2BGFP* single transgenic mice were provided by Dr. Katery Moore (15–17). The single mutant mice were bread with wild type CD1 mice to create double *huCD34tTA/TetO-H2BGFP* transgenic mice in the animal facility of Istituto Superiore di Sanità according to standard genetic protocols (15–17) and backcrossed for at least 10 generation before being included in this study. All the mice used in these experiments were genotyped by PCR at birth as a control that they carried the double mutation. *huCD34tTA/TetO-H2BGFP* mice (6 females, 11–15 months of age) were divided into two groups, one received tap water *ad libidum*, and the other one received tap water supplemented with Doxy (0.5 mg/mL; Clontech laboratories, Mountain View, CA, USA). After 1-week, the mice in both groups were sacrificed under humane conditions (cervical dislocation previous general anesthesia with an overdose of gaseous isoflurane 4%, Aesica Queenborough Ltd, Queenborough, UK) and their femur harvested for analyses. Selected experiments were performed with 2-months old *huCD34tTA/TetO-H2BGFP* female

mice ($n = 3$). All the experiments included single *TetO-H2BGFP* transgenic mice as control for possible leakage of the expression of the transgene. The experiments were performed according to the protocols D9997.121 approved by the Italian Ministry of Health on September 2nd 2021, and according to the European Directive 86/609/EEC.

2.2 Flow cytometry determinations

Mononuclear BM cells were incubated with a cocktail of antibodies containing APC-CD117, APC-Cy7-Sca1, PE-Cy7-CD150, biotin-labeled CD48, and biotin-labeled anti-lineage antibodies. After 30 min of incubation on ice, cells were washed and stained with streptavidin-PE-Cy5, and cell fluorescence analyzed with the Gallios FACS analyzer (Beckman Coulter, Brea, CA, USA). The enriched HSC population was defined as LSK (Lin–/CD48–/c-kit+/Sca-1+), while long-term repopulating HSC were defined by the SLAM phenotype (Lin–/CD48–/c-kit+/Sca-1+/CD150+) as previously described (18, 19). All the antibodies were purchased from BD-Pharmingen (San Diego, CA, USA). Dead cells were excluded by Sytox Blue staining (0.002 mM, Molecular Probes, Eugene, OR, USA). Results were analyzed with the Kaluza analysis version 2.1 (Beckman Coulter, Cassina de Pecchi, Italy). Hemi-decrements of the GFP levels expressed by the SLAM were used to divide them into four classes of proliferation as described by Qiu et al. (20). Briefly, cells expressing the maximal level of GFP were defined G0 because did not underwent DNA replication events; cells expressing half of the maximal level were defined G1 because underwent 1 DNA replication cycle; cells expressing a quarter of the maximal level were defined G2 because underwent 2 DNA replication; cells expressing an eighth of the maximal level were defined G3 because underwent 3 DNA replication and, finally cells with barely detected levels of GFP, G4 because they underwent at least 4 DNA replication events. The hemi-decrements described in the paper were determined by hand because of the challenges to properly divide into classes of descendent fluorescence with the FlowJo program (FlowJo™ v10.8, FlowJo LLC, Ashland, Oregon, USA) the signal from the rare SLAM cells (data not shown).

2.3 Histology and confocal microscopy determinations

Femurs were fixed in formaldehyde (10%, *v*/*v* with neutral buffer), incubated for 1 h + 4°C with BM biopsy decalcifying solution (EDTA 10%) and included in paraffin. Sections (3 μm) were stained with hematoxylin–eosin (Hematoxylin Cat. #01HEMH2500, Eosin cat#01EOY101000, Histo-Line Laboratories, Milan, Italy). Slides were observed and images acquired with the NanoZoomer 2.0-RS microscope (Hanamatsu Photonic K.K., Hamamatsu City, Japan,), using the NDP.view2 software for NanoZoomer (Hanamatsu Photonic K.K). Sequential sections were stained with DAPI (D9542-5MG, Sigma Aldrich) and analyzed with the confocal microscope Zeiss LSM 900 (Carl Zeiss GmbH, Jena, Germany) in Airyscan mode. Excitation lights were generated by a 405 nm Laser for DAPI and with an argon ion 488 nm laser for GFP. Optical thickness varied from 0.50 μm for the 10x objective to 0.20 μm for the 63x objective. All images were captured under the same conditions and were process and analyzed with the Zen Blue (3.2) software (Carl Zeiss GmbH, November 2021) and the ImageJ (version 1.53t) software (National Institutes of Health http://imagej.nih.gov/ij, accessed on 23 November 2018). Three-dimensional reconstructions were obtained by the full set of stack images, 15 images for the 20× objective and 34 images for 63× objective using the Zen Blue software. Nuclei were counterstained with Hoechst 33342, trihydrochloride and trihydrate (Invitrogen), and the samples mounted with Fluor-shield histology mounting medium (Catalog F6182-10MG, Sigma-Aldrich). In selected experiments, the sections were stained with the CD150 antibody (rabbit polyclonal, anti-SLAM/CD150 antibody-N-terminal, cat. no. ab156288, Abcam, Cambridge, UK) coupled with the Alexa Fluor 568-conjugated goat anti-rabbit antibody (Invitrogen, Waltham, MA, USA), as control of the specificity of the GFP label, while endothelial cells were positively identified by staining the sections with the rabbit anti von Willebran factor (vWF) antibody directly conjugated with ALEXAFLUO (Cat. no. ab9378, Abcam, Cambridge, UK).

2.4 Single cell quantification of GFP intensity

Images were captured at 8 bit and processed with the Fiji software (ImageJ version 1.53t). The intensity of the GFP signal in the nucleus was measured as described in Supplementary Figure 1. Briefly, (1) color channels are split in 3 single components: Red, Green and Blue. (2) In the Blue channel, it is applied a threshold (60 as lower limit and 255 as highest limit) for selecting the area stained with DAPI (Blue component of the original image) which corresponds to the nucleus. Superimposed or strictly packed nuclei have been resolved applying a binary process called "watershed" that separates adjacent nuclei. (3) Applying this criterium, the number and areas for each single nucleus present in the image is determined. (4) The resulting image is converted into a mask that excluded all pixels outside the holes created by the recognition of the single nuclei. This mask is superimposed to the signal from the Green channel of the same image which contains information on the GFP signal. (5) This process generates an image containing the GFP information (as gray levels) only related to the areas where the nuclei are located. All pixels outside the nuclei are set to zero. For each single nucleus it was then determined the minimum, maximal and Mean value of the gray signal. This process allows to determine for each image the number of nuclei present and the Mean, minimal and maximal level of GFP signal (in arbitrary unit) contained in each nucleus.

2.5 Statistical analysis

GFP levels were measured as Mean value by confocal microscopy and as total fluorescence (GFP-A) by flow cytometry. The overall GFP values between untreated and Doxy-treated mice were compared by T Student's Test. Differences in GFP

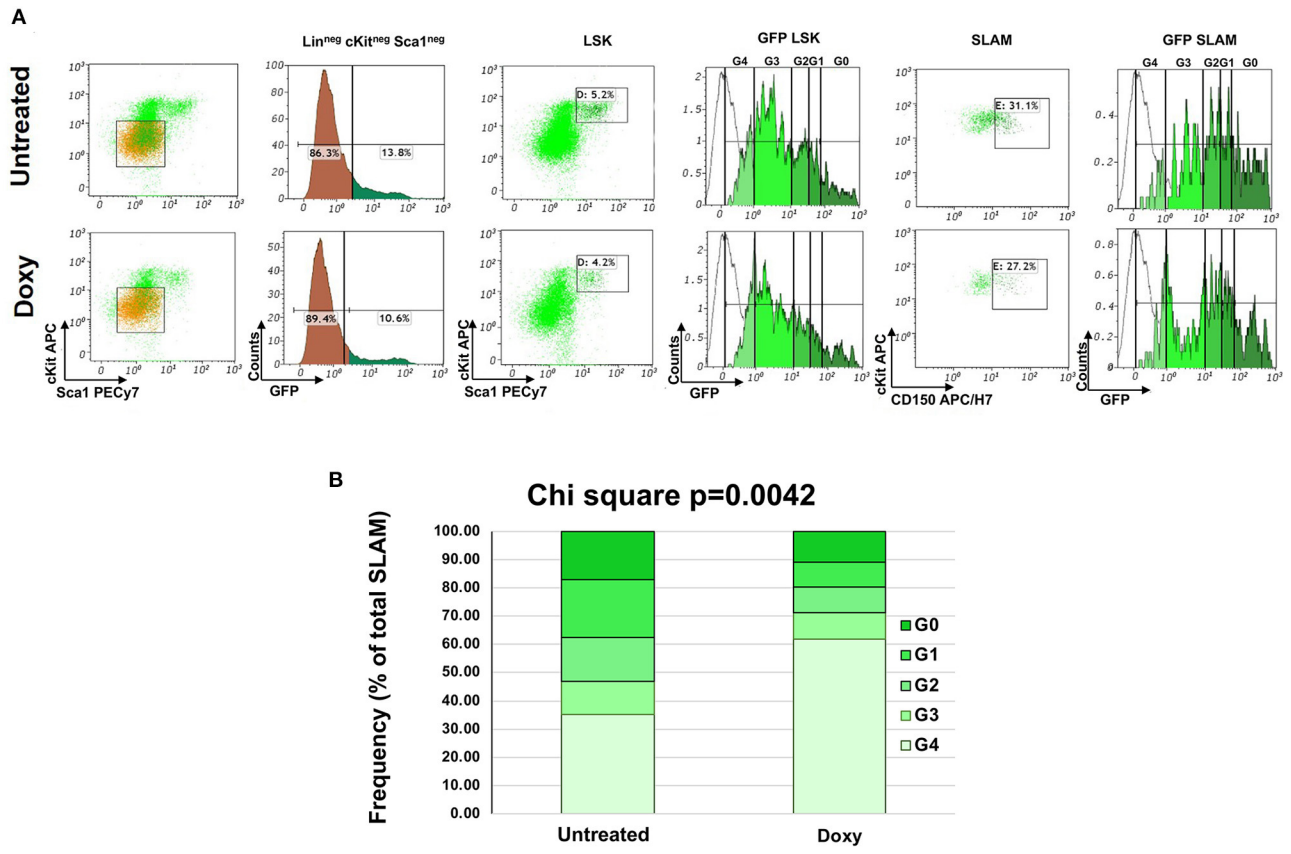

FIGURE 1
FACS analyses of the hemi-decrement changes in GFP expression occurring in the HSC of the BM after 1 week of exposure to Doxy. **(A)** Representative FACS analyses of Lin-neg BM cells from double mutant mice (15-months old males) either untreated or exposed to Doxy for one week. The levels of GFP expressed by the Lin-neg cells are also presented as control. The levels of GFP expressed by the LSK and SLAM cells are divided into the G0, G1, G2. G3 and G4 gates, as reported (20). The gating used to define the LSK and SLAM populations are also indicated. The white lines indicate the levels of GFP expressed by the BM cells from a single *TetO-H2BGFP* transgenic mouse, used as negative control. The total number of events analyzed is 10,000 per sample which correspond to 500 LSK cells (5% of 10,000 events) and 155 SLAM cells (31% of 500 cells) for the untreated group and to 420 LSK cells (4.2% of 10,000 events) and 114 SLAM cells (27.2% of 500 cells) for the Doxy group. **(B)** Percentage of cells in the various GFP classes over the total frequency of SLAM cells in the BM of untreated or Doxy treated-mice. Data are presented as mean of those observed in three mice per group. The distribution of the cells among the classes in the two groups is statistically significant by Chi-Square test. The statistical analyses of the differences within each class is reported in Supplementary Figure 2.

values among untreated and Doxy-treated mice were analyzed by One-way Analysis of variance (ANOVA) and the Tukey-Kramer Adjustment for Multiple Comparisons. Confocal microscopy evaluation of GFP levels in single cells were grouped in classes by two different methods: (1) Levels were grouped in 3 classes according to cumulative percent or (2) grouped in four classes according to the maximum value of GFP intensity registered; the first cut off is represented by half the maximum value of GFP intensity, the second cut off is half the value of the first cut off, and the third cut off correspond to half the value of the second cut off. Chi Square Test was used to compare proportions of the categories of these two grouping classes in untreated vs. Doxy-treated mice and within the bone marrow architecture. Mann-Whitney Test was used to compare fluorescence intensity classes by FACS determination because the data do not show normal distribution. *P*-values for this test were showed both two-tailed and 1-tailed, under the assumption that we expected one group of mice to be better than the other one. All the statistical analysis was performed with the SAS® version 9.4 (SAS Institute Inc. 100 SAS, Campus Drive Cary, NC, USA).

3 Results

3.1 Tracking HSC cycling by flow cytometry

The Moore laboratory has pioneered the use of untreated and Doxy-treated *huCD34tTA-TetO-H2BGFP* mice to track the cycling of HSC by flow cytometry during the lifespan of mice of C57Bl6 background (15). In preliminary experiments, we tracked the cycling of the HSC in old *huCD34tTA-TetO-H2BGFP* mice harboring the mutation in the CD1 background which, by contrast with C57Bl mice, express a pro-inflammatory phenotype at baseline (26). In these experiments, 15-months old *huCD34tTA-TetO-H2BGFP* mice were exposed to Doxy in their drinking water for only 1 week and the frequency of LSK and SLAM cells, as well

TABLE 1 Comparison of the levels of cKIT and CD150 (as mean fluorescent intensity, MFI) expressed by the LSK and SLAM cells divided for fluorescence classes presented in Figure 1.

	LSK			SLAM		
	Untreated ($n = 3$)	Doxy ($n = 5$)	*P*-value (*t*-test)	Untreated ($n = 3$)	Doxy ($n = 5$)	*P*-value (*t*-test)
cKIT (CD117) MFI						
G0	26.5 ± 1.4	25.8 ± 4.0	0.5354	24.0 ± 2.2	24.9 ± 3.9	0.7738
G1	28.7 ± 3.5	25.9 ± 1.5	0.1192	28.9 ± 2.5	24.4 ± 2.9	0.0087
G2	32.8 ± 4.2	28.0 ± 2.0	0.0480	36.6 ± 6.8	28.6 ± 2.4	0.0300
G3	30.2 ± 5.0	27.0 ± 3.1	0.2688	29.9 ± 18.2	29.8 ± 5.1	0.9915
G4	24.6 ± 1.9	24.1 ± 3.8	0.8158	18.1 ± 5.5	23.2 ± 3.0	0.1092
CD150 MFI						
G0	n.a.	n.a.		28.4 ± 3.3	47.8 ± 9.6	0.0128
G1	n.a.	n.a.		26.5 ± 3.0	41.2 ± 6.9	0.0101
G2	n.a.	n.a.		22.1 ± 4.2	38.2 ± 11.3	0.0537
G3	n.a.	n.a.		20.5 ± 5.2	35.3 ± 12.3	0.0875
G4	n.a.	n.a.		26.5 ± 10.4	35.6 ± 12.9	0.3268

n, number of mice in the experimental group; n.a., not applicable.

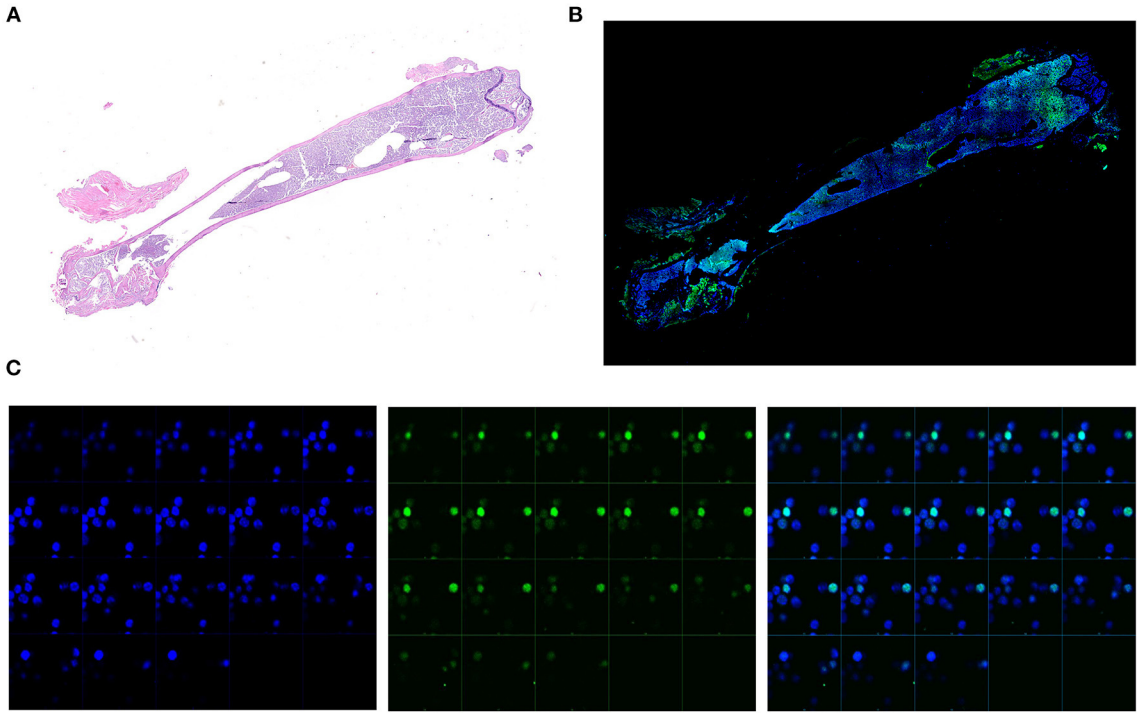

FIGURE 2
Representative analyses of the GFP levels expressed by the single cells from the BM of an untreated double mutant female mouse (11-months old). **(A)** Reconstruction of the whole femur from the representative double mutant mouse stained by Hematoxylin/Eosin. Scanning was performed with a resolution equivalent to that of a x40 objective. **(B)** Reconstruction of the whole femur from the same representative double mutant mouse shown in A stained with DAPI by confocal microscopy. The original images were acquired at x200 magnification. Blu = DAPI, Green = GFP. **(C)** Zeta stacking (each photogram a different focal plane) at X400 magnification of images collected by confocal microscopy in order to confirm the nuclear colocalization of both the DAPI and the GFP signal. Two representative GFP positive cells are shown. Images are presented as individual DAPI (left panels) and GFP (central panels) and as merged (right panels) signals.

as the expression of the GFP in these cells, were evaluated by flow cytometry (Figure 1). Treatment with Doxy did not alter the frequency of LSK or SLAM cells which were equivalent in the two groups (LSK: 5.4 ± 0.5 vs. 5.1 ± 1.6% of total Lin^{neg} cells; SLAM: 34.5 ± 4.4 vs. 32.15.4 ± 7.2 of the LSK, respectively). GFP was expressed almost exclusively by the LSK and SLAM. Very few

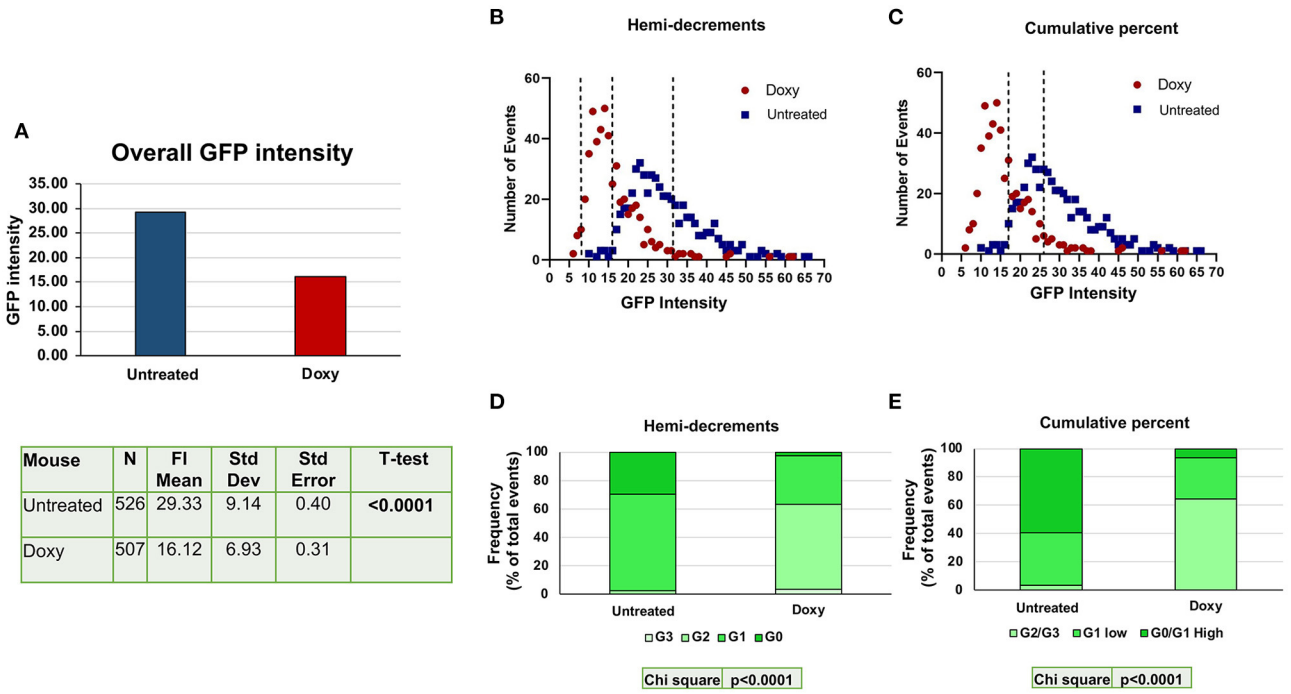

Mouse	N	FI Mean	Std Dev	Std Error	T-test
Untreated	526	29.33	9.14	0.40	<0.0001
Doxy	507	16.12	6.93	0.31	

FIGURE 3
Doxy reduces the levels of GFP expressed by the single cells detected by confocal microscopy in the femur sections from untreated or Doxy-treated mice. **(A)** Comparison between the overall GFP levels expressed by single cells from the BM sections of the untreated (blue) and Doxy-treated (red) mice (two mice per group), as indicated. All the GFPpos cells present in one section were considered. The data are reported with statistical analyses in a table format below the graph. **(B)** Distribution of the GFP levels expressed by individual cells (each dot a different cell) from the femur of untreated (blue dots) and Doxy-treated (red dots) mice, as indicated. In this case, the GFP levels are divided into four classes by hemi-decrement analyses of the maximal levels of GFP intensity determined. **(C)** The same distribution of the GFP levels shown in B but divided into 3 classes according to the cumulative percentage of the values distribution. The total number of events presented in **(B, C)** is 1,033 (526 for untreated and 507 for the Doxy-treated group). **(D, E)** Frequency of the cells in the various GFP classes over the total frequency of SLAM cells observed in the BM of either untreated or treated-mice. Data are presented as mean of those observed with two mice per group. Both in **(D, E)**, differences in cell distribution among the classes in the two groups are statistically significant by Chi-Square test.

(~10%) of the Lin^{neg} cells contained GFP. In a previous study, we identified that the $Lin^{neg}cKit^{neg}Sca1^{neg}$ cells that express GFP are larger than the other cells, contain the GFP signal mostly in their cytoplasm and express F40/80, suggesting that they are macrophages that have phagocytized HSC (26). By contrast, robust numbers of LSK and SLAM expressed GFP at a level which spanned over 4 logs, supporting the knowledge that expression of *TetO-H2BGFP* is switched off in the progeny generated by the first differentiative division of the HSC and that its content decreases by half with every cell division thereafter (20). Treatment with Doxy for only 1 week induced significant changes in the distribution of the SLAM among the various classes of fluorescence intensity with an enrichment in the frequency of SLAM expressing barely detectable levels of GFP (Figure 1). In depth analyses of the differences in the distribution of the SLAM in the various classes of GFP intensity indicates a statistically significant reduction in the frequency of SLAM in the G1 and G2 classes and a statistically increase in that of SLAM in G4 after Doxy treatment by 1-tailed Mann-Whitmey analyses (Supplementary Figure 2).

The levels of cKIT and CD150 expressed by SLAM in the untreated and Doxy group according to their fluorescence classification was also determined (Table 1). There is no difference in the level of expression of these two antigens among the classes within the same experimental group. However, the G1 and G2 cells from the untreated group expressed levels of cKIT significantly greater than those of the corresponding cells from the Doxy group, while the G0 and G1 cells of this group express levels of CD150 significantly lower than those expressed by the corresponding cells in the Doxy group. The physiological significance of these differences is presently unclear.

These results indicate that the SLAM in the BM of old mice expressing constitutively higher levels of TGF-β are a dynamic cell population with few of the very positive cells entering in cycle but with as many as 12–7% of the intermediate positive cells entering cycle over a 1-week period.

3.2 Tracking HSC cycling by confocal microscopy

To investigate the distribution of GFP positive cells within the BM architecture, we first confirmed that great numbers of small cells expressing robust levels of GFP signal in their nucleus were detectable by confocal microscopy (Figures 2A, B). By contrast, GFP positive cells were not detectable in the femur from a single *TetO-H2BGFP* mouse, used as negative control (Supplementary Figure 3). Sequential Z stacking images

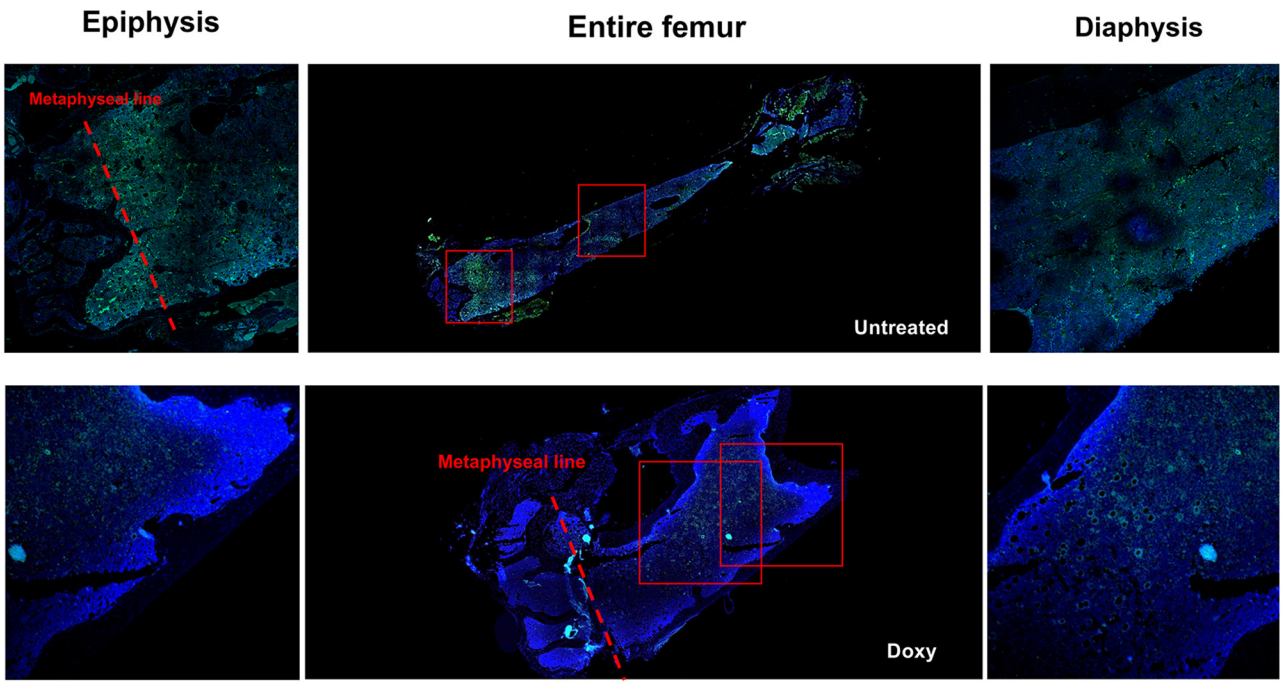

FIGURE 4
Both in untreated and in Doxy-treated mice, GFP positive cells are localized in all the areas of a femur (both in the epiphysis and in the diaphysis). Reconstruction of the femur from a representative untreated and Doxy-treated mutant mouse **(middle panels)** and detail of the epiphysis **(left panels)** and of the diaphysis **(right panels)** of the same femur obtained by confocal microscopy. The Dapi and GFP signals are merged. The rectangles in the middle panels indicate the areas shown at greater magnification in the panels on the side. Original magnification x100 and x200 for the entire femurs and their detail, respectively.

indicated that the green GFP signal was co-localized with DAPI, confirming that GFP was localized in the nucleus of these cells (Figure 2C).

Using the criteria defined in Supplementary Figure 1, the levels of GFP detected in the nucleus of single cells from the BM of untreated and Doxy-treated double mutant mice were determined (>500 cells per group) (Figure 3). Overall, the levels of GFP intensity expressed by the single cells from the Doxy-treated mice was significantly lower than that expressed by the untreated mice (Figure 3A). As observed by flow cytometry, the levels of GFP determined by confocal microscopy in the single cells from both groups did not have a normal distribution and showed a peak at 23 and 14 arbitrary units, respectively. Since the GFP is expressed in the nuclei only of the HSC and of their immediate progeny, we used GFP staining and small size as criteria to recognize HSC and their immediate progeny. We divided the cells according to their GFP intensity by two statistical methods: the first method was similar to that used by flow cytometry and divided the cells into four classes based on hemy-decrements of GFP intensity (Figure 3B). These classes are basically similar to the G0 (never divided); G1 (divided once), G2 (divided twice) and G3 (divided three times) recognized by flowcytometry. It is worthy of attention that, since the confocal analysis used in this study did not include a positive marker for HSC identification, it does not allow to identify the progeny of the fourth division of HSC (G4, that express barely detectable levels of GFP by flow cytometry). The second method divides the cells into cumulative percentage of their intensity score in three classes which partially overlap with those identifies by hemi-decrements. In both cases, the difference in the distribution of the individual cells among the classes of GFP intensities from the untreated and the Doxy-treated mice is highly significant ($p < 0.0001$ by Chi square) (Figures 3D, E). Also by confocal microscopy, the greater differences between untreated and Doxy-treated cells were represented by a decrease in the frequency of cells expressing the highest levels and increases in the cells expressing intermediate levels of GFP.

3.3 The most positive GFP+ cells are localized around vessels

By confocal microscopy analysis, the cells expressing GFP were distributed along the entire femur (Figure 4). Both in the untreated and in the Doxy-treated mice, the GFP positive cells were more frequent in the epiphysis below the metaphyseal line and in the medulla. They were localized either around optical empty spaces, or in their proximity (within 20 μm) although some GFP positive cells was also observed within the BM parenchyma. Observations at greater magnification, indicated that the empty spaces which were lined by strongly GFP positive cells had the structure of small vessels (Figure 5A). Given the thickness of the sections (3 μm) and the fact that we have not made 3D BM reconstructions by combining images collected from multiple consecutive sections, the distinction between cells located near vessels and within the parenchyma may be artificial.

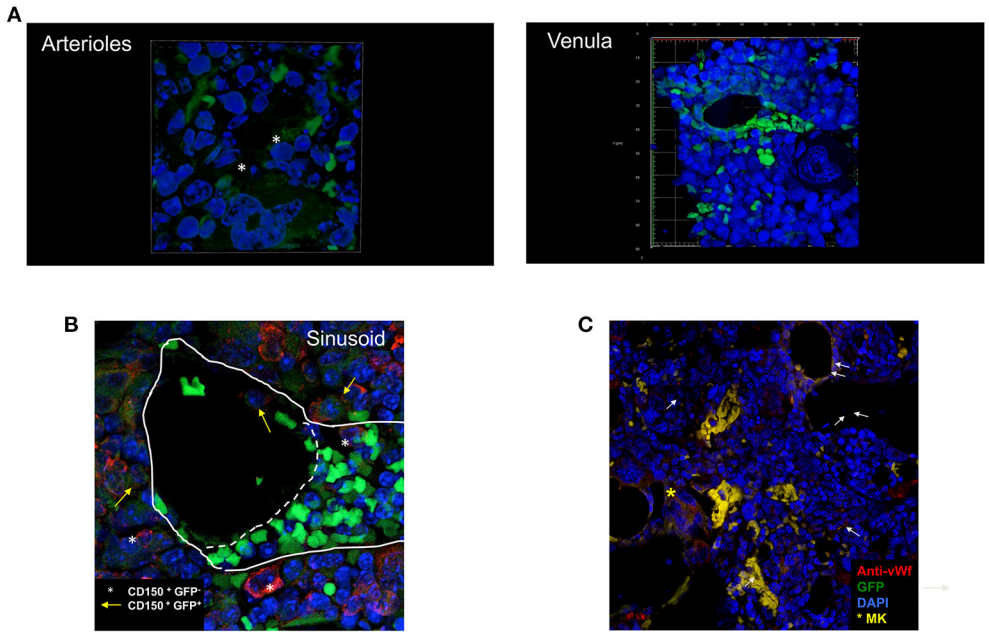

FIGURE 5
Cells expressing high levels of GFP are often found located around vessels. **(A)** 3D reconstruction of an arteriole (top panel) and of a venula (bottom panel) surrounded by small GFP positive cells. **(B)** Confocal microscopy observation of a representative BM section stained with the von Willebrand (vWF) antibody. The arrows indicate representative GFP pos cells localized around the vessels which are lined by vWF positive cells. To be noted the presence of a vessel surrounded by vWF positive endothelial cells which does not contain GFP-positive cells (symbol) but associated with a megakaryocyte in the process to release platelets (the large cells with multi-lobated nucleus positive for vWF indicated by the asterisk). **(C)** Confocal microscopy observation of a representative BM section stained with the CD150 antibody showing that all the GFPpos cells around the vessel are also CD150pos (yellow arrows) while there are same CD150pos which are not labeled by GFP (asterisks). The image shows the anastomosis between two venules, one cut transversally and another one cut longitudinally. This anastomosis identifies the two vessels as sinusoids. The straight line indicates the localization of the basal lamina while the dotted line indicates the junction between the two vessels. The small green cells in the vessel cut longitudinally are red blood cells. To be noted the GFPposCD150+ cells located in the lumen of the vessel cut transversally and the GFPnegCD150pos cells located near the transversal vessel that appears in cytodieresis. Original magnification x600 (arterioles and venula) and x200 in all the other panels.

By morphology, we identified two types of vessels: arterioles, circular areas well delimitated by a lumen wall composed by elongated cells with endothelial-like morphology and surrounded by a thick layer of cells, probably representing muscle cells, and venules, elliptic/collapsed spaces surrounded by a thin layer of elongated cells. In most of the cases, the morphology does not allow us to discriminate whether these elliptic structures are represented by veins or sinusoids. The morphological hypothesis that these structures are vessels was confirmed by determining that they were lined by cells that reacted with a von Willebrand Factor (vWF) antibody, a marker for endothelial cells (Figure 5C).

To confirm that the GFP labeled cells surrounding the vessels are HSC, we performed a pilot experiment in which the BM sections were stained with the CD150 antibody (the SLAM marker used in flow cytometry) (Figure 5B). This experiment confirmed that all the GFP labeled cells express CD150, and are therefore HSC, and identified a CD150pos cell population which is not labeled by GFP and that may represent the G4 Class identified by flow cytometry.

Single cell analyses of the levels of GFP expression according to location confirmed that, overall, the cells expressing GFP were mostly located around vessels which were surrounded by almost 50% of all the GFP+ cells detected in a femur section (518 vs. 237 + 238 cells, respectively, Figures 6A, B). It also indicated that 30% (by hemi-decrements) or 70% (by cumulative percentage) of the cells with the highest levels of GFP expression were located near vessels ($p < 0.0001$ in both cases) (Figures 6C–E). As expected, in old mice, very few GFP labeled cells were present near the endosteum of the trabecular bone (Supplementary Figure 4).

To start investigated the effects of age on the frequency and localization of GFP+ cells, a preliminary experiment was performed to analyze the distribution of GFPpos cells within the bone marrow architecture of young (2–3-months old) mice (Supplementary Figure 5). The frequency of GFP+ cells in the BM of these young mice was much lower than that detected in the BM of old mice (compare the frequency of GFP+ events in Figure 4; Supplementary Figure 5). In addition, the GFP+ cells were localized both near the endosteum of the bone and the vessels.

These results confirm that in old mice the endothelial cells surrounding the vessels are an important niche for the most primitive HSC.

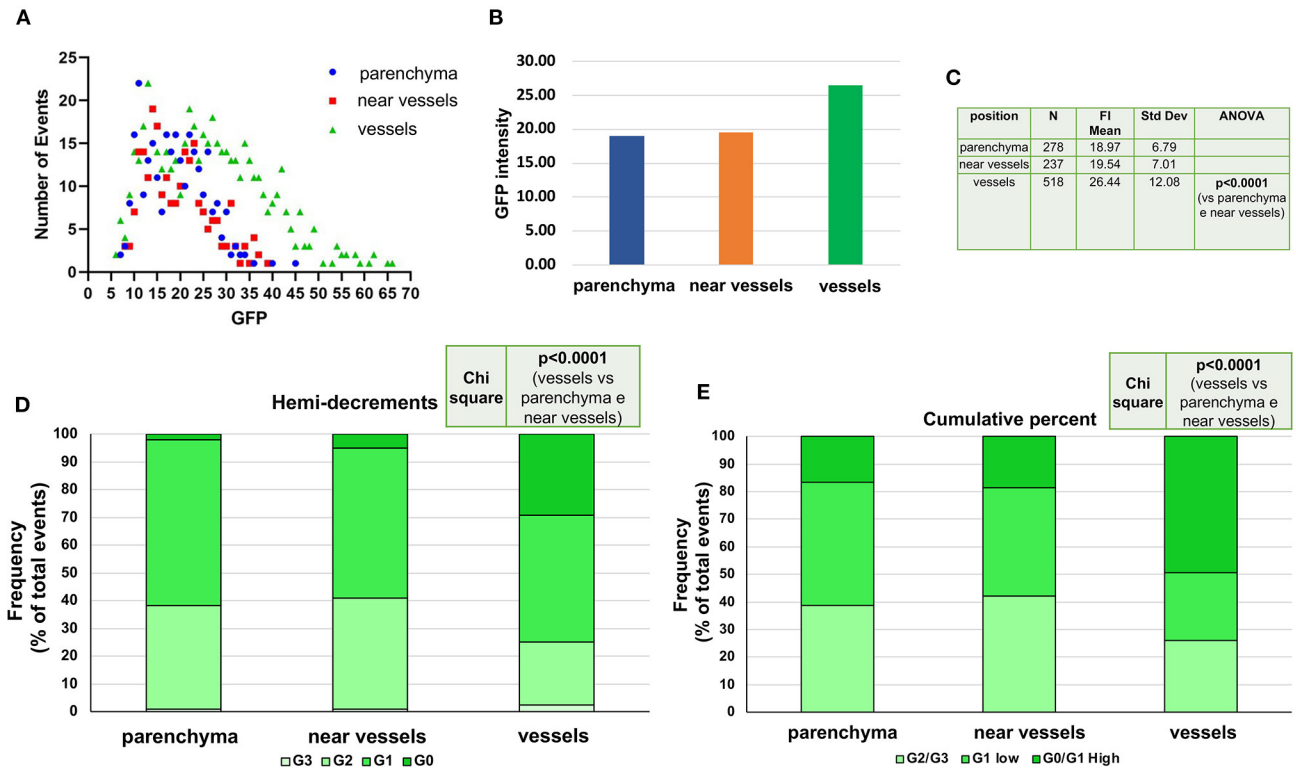

FIGURE 6
The cells expressing the highest levels of GFP are localized in proximity of the vessels. **(A)** Distribution of the levels of GFP expressed by single cells (each symbol a different cell) according to their localization. GFP positive cells were divided into cells surrounding vessels, in close proximity (within 20 ?m) of a vessel or within the BM parenchyma, as indicated. The cell localization was determined by the Image J program and by the control software of acquisition ZenBlue. **(B)** Overall GFP intensity expressed by the cells according to their location. **(C)** Number and GFP content [Mean (+/-SD)] of the single GFP+ cells analyzed for each localization. The p value was analyzed by ANOVA. **(D, E)** Distribution of single cells expressing different levels of GFP fluorescence intensity divided by either the hemi-decrement or the cumulative percent criteria (the same criteria as in Figure 3). In both analyses, Chi-Square test shows statistically significant difference in the localization of the GFP positive cells, with the cells expressing the highest levels localized around vessels.

3.4 Doxy-treatment spares the GFP label expressed by cells surrounding the arterioles

In untreated mice, the strongest GFP positive cells were observed surrounding vessels with the morphology of both arterioles and venules (Figure 7A). One week of Doxy treatment reduced the levels of GFP expressed by the cells located in all the areas of the femur (Figures 7B, C). The greatest reductions, however, were observed in the levels of GFP expressed by the cells surrounding the vessels (50% overall reduction from 32.5 vs. 16.9 fluorescence intensity, before and after Doxy, respectively). Morphological analyses indicates that the fluorescence intensity is either lost or retained by all the cells surrounding a specific vessel (Figure 7A). In the Doxy-treated group, the cells that retain the highest levels of GFP appear co-localized all around vessels with the morphology of arterioles.

4 Discussion

The double *huCD34tTA-TetO-H2BGFP* mutant mouse has provided important information on the dynamics of HSC cycling over time (15, 21, 23). These studies have identified that 60% of HSC from young (12-weeks old) C57Bl mice remain quiescent over a period of 12 weeks (20). In this model, HSC are supposed to be retained into quiescence by the high levels of expression of genes of the TGF-β pathway. Treatment with factors, like G-CSF, which induce HSC mobilization, does not reduce the number of quiescent HSC, suggesting that in these mice HSC have greater affinity for the niche that retain them quiescent (23). With age, HSC enter into a state of dormancy which is retained for the rest of the life of a mouse (15). Whether the niche which sustains the "dormant" HSC in old mice is similar from that that sustain "cycling" HSC in young mice has not been clarified as yet.

Other studies, using multi-color confocal microscopy and expression profiling, have identified that in adult mice HSC are preferably located near vessels and are retained into quiescence by the niche which surrounds the arterioles while they are induced in proliferation by that surrounding the venules (1, 2, 4, 6, 29, 30). Since in old mice the HSC which remain quiescent are a minority, most of the HSC should be associated with a niche still poorly identified that sustain their proliferation, causing the HSC exhaustion which results in the anemia and thrombocytopenia observed in old mice.

A

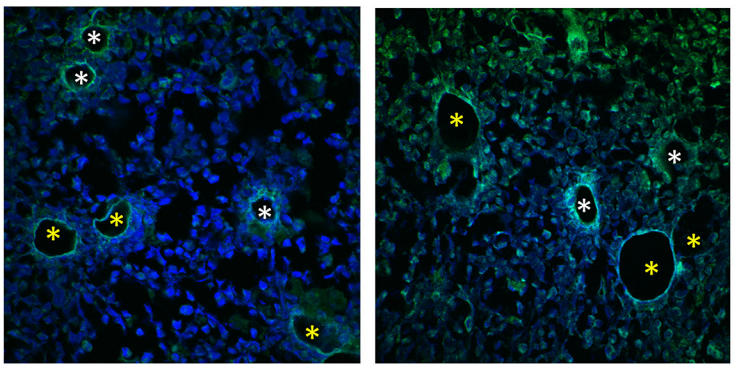

B

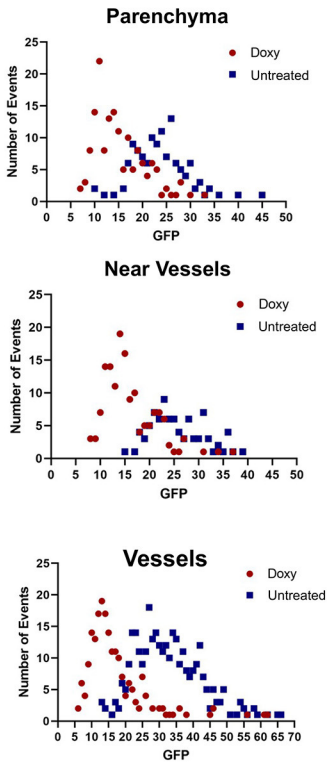

C

Untreated	N	FI Mean	Std Dev	post-hoc analysis	Doxy	N	FI Mean	Std Dev
parenchyma	124	23.7	5.4	**<0.0001**	parenchyma	154	15.2	5.2
near vessels	87	25.7	5.4	**<0.0001**	near vessels	150	15.9	5.1
vessels	315	32.5	9.7	**<0.0001**	vessels	203	16.9	8.9

FIGURE 7
Treatment with Doxy specifically reduces the GFP levels expressed by cells surrounding venules. **(A)** Confocal microscopy analyses of the femur from representative untreated and Doxy-treated mice stained with DAPI and GFP. The images indicate that in untreated mice cells expressing high levels of GFP surround both arterioles (white asterisks) and venules (yellow asterisks) while in the Doxy-treated animal high GFP expression is retained only by cells surrounding the arterioles. **(B)** Distribution of the GFP fluorescence intensity expressed by single cells from the BM of untreated (blue dots) or Doxy-treated (red dots) mice (two mice per group) according to their localization within the BM architecture (each symbol a different cell). **(C)** Number of single cells analyzed and Mean (+/−SD) of the levels of GFP expressed by the single cells from the BM of untreated or Doxy-treated mice according to their localization. The *p*-values were calculated by ANOVA with a *post-hoc* analysis.

The study presented here couples the power provided by the double *huCD34tTA-TetO-H2BGFP* mutant mouse with that of confocal microscopy to study the association of the HSC with their niche as they cycle in old mice with the spontaneous pro-inflammatory profiling provided by the CD1 background (28). In fact, compared to mice of other strains, such as C57Bl mice, the pro-inflammatory profile of the bone marrow from CD1 mice includes increased bioavailability of TGF-β, a factor known to induce HSC into quiescence promoting their self-replication (24).

A first set of experiments validated information on HSC cycling obtained in our model by comparing the levels of GFP intensity observed in the SLAM by flow cytometry with that obtained by measuring the nuclear levels of GFP in cells with a small size (a morphological criteria for HSC identification) by confocal microscopy. The fact that GFP signaling was barely observed in the BM of single *TetO-H2BGFP* mutant mouse with both methods, provided evidence for the specificity of our determinations. A significant difference between determinations of the cycling status of the HSC by flow cytometry and by confocal microscopy is that, by flow cytometry HSC are independently recognized by the SLAM marker while by the confocal microscopy assessment used in this paper GFP is both a marker for the HSC and for their cycling state. For this reason, HSC that divided more than four times, i.e., expressing barely detectable levels of GFP, can be identified by flow but not by the confocal microscopy method used in this manuscript. With this caveat, there was a good correlation between the HSC which never divided (quiescent HSC) and those that underwent 1, 2, and 3 divisions over one 1-week period determined with the two methods. In fact, with both methods, only a minority (10 vs. 5–10%) of the cells remained quiescent over a 1-week period while most of them (60% in both cases) underwent 1–3 cell divisions. These results indicate that in old mice HSC are a very dynamic populations and undergo numerous divisions over just 1 week time.

Single cell analyses of the distribution of the labeled HSC within the BM microenvironment indicated that most of the labeled HSC were located near vessels. It also indicated that the cells surrounding the vessels were those expressing the highest GFP intensity. This last result indicates that the HSC near the vessels are either quiescent or had divided at most once. After Doxy, the majority of the GFP labeled cells were still located near vessels. However, there was no longer difference between the intensity of GFP expressed by the HSC near the venules and those present in the BM parenchyma, indicating that in just 1-week period the HSC around the vessels had cycled few times. Interestingly, the arterioles were the vessels which were surrounded by the few HSC which

retained label after Doxy, suggesting that this niche supports either HSC which are quiescent or that enter in cycle at a rate lower than once a week. It is also possible that this niche sustains the dormant HSC identified by the Moore laboratory to be uniquely present in old mice (15). Since, because of the pro-inflammatory environment provided by the CD1 background, the levels of TGF-β are similarly high around the arterioles and the venules, it is possible that the arterioles produce additional factors, still to be identify, which retain HSC into a quiescent/dormant state (7). This hypothesis is supported by the observation that all the cells surrounding a specific arteriole retain label. However, further confocal microscopy studies, outside the purpose of this paper, which will compare the location of the labeled HSC using age, sex and time of Doxy treatment as independent variables, are necessary to clarify whether in old mice the HSC around the arterioles are quiescent or dormant. The rigor of these new studies will be greatly increased by including the CD150 marker to positively identify the HSC.

In conclusion, our results indicate that aged HSC are actively cycling and are mostly associated with venules, confirming that these cells are biased for interacting with the niche that instructs them to differentiate (4, 7, 30). The very few old HSC that retain label are located around the arterioles, providing morphological evidence that this niche may represent the niche that sustain the dormant HSC present in old mice.

Data availability statement

The original contributions presented in the study are included in the article/Supplementary material, further inquiries can be directed to AM, amigliaccio@altius.org.

Ethics statement

The experiments were performed according to the protocols D9997.121 approved by the Italian Ministry of Health on September 2nd 2021, and according to the European Directive 86/609/EEC.

Author contributions

MM and FA performed all the experiments. OP performed the statistical analyses of the data. PV, FM, and MV maintained the mouse colony, treated the mice, and performed flow cytometry determinations. ARM, MF, and MZ designed the study, interpreted the data, and wrote the manuscript. All authors read the manuscript, concur with its content, contributed to the article, and approved the submitted version.

Funding

This study was supported by grants from the National Cancer Institute (P01-CA108671) and Associazione Italiana Ricerca Cancro (AIRC, IG23525).

Acknowledgments

Dr. Katery Moore is gratefully acknowledged for providing the single huCD34tTA and TetO-H2BGFP mutant mice. Dr. Bernitz is thanked for providing training and for supervising the determination of GFP hemi-decrements by flowcytometry. Dr. Gisella Gaspari and Dr. Giorgio Vivacqua, lecturer, Department of Neuroscience, University of Cambridge, Cambridge, UK, are acknowledged for editorial assistance. Mrs. Yvan Gilardi, Enrico Cardarelli, and Andrea Giovannelli of the Animal Facility of Istituto Superiore di Sanità are gratefully acknowledged for their careful surveying of the wellbeing of the mice and compliance of the experiments with the approved Animal Protocol.

Conflict of interest

The authors declare that the research was conducted in the absence of any commercial or financial relationships that could be construed as a potential conflict of interest.

Publisher's note

Supplementary material

The Supplementary Material for this article can be found online at: https://www.frontiersin.org/articles/10.3389/fmed.2023.1166758/full#supplementary-material

SUPPLEMENTARY FIGURE 1
Graphic representation of the method developed to quantify the levels of GFP in the nucleus of single cells in the BM from the double mutant mice. **(A)** Workflow describing the process of quantification of the GFP intensity in single cells from the femur of the mice. The first step is the reconstruction of the image of the entire femur by slide scanner for H&E or by stitching the individual images acquired by confocal microscopy stained with DAPI. In both cases images have the same resolution as that acquired by a 20X objective. The second step consists in the examination of the green signals released by the GFP acquired by confocal microscopy. The third step is the quantification of the GFP intensity in the single cells by ImageJ (see Material & Methods for further detail of this quantification). **(B)** Visualization of the sequential steps described in A including representative images. Images are acquired with a 40x objective. The first step is to split color channels and analyze the Blue component converting them in a 8 bit, 255 gray levels image. Same threshold values have been adopted for all images. The resulting image is then used as mask to contour of the objects of interest in the Green component image in which the gray levels have been measured.

SUPPLEMENTARY FIGURE 2
Doxy significantly decreases the frequency of GFP positive SLAM in the G1 and G2 group and increases those present in the G4 group detected by flow cytometry. Data are presented as median (plus min and max) of those

observed with three mice per group. Statistical analyses was performed by Mann-Whitney and by Mann-Whitney (1-tailed) tests.

SUPPLEMENTARY FIGURE 3
GFP is not detected by confocal microscopy in the BM from mice arboring only the *TetOH2BGFP* transgene. **(A)** Reconstruction of the whole femur from a representative single *TetOH2BGFP* transgenic mouse stained either by Hematoxylin/Eosin **(A)** or analyzed by confocal microscopy for DAPI and GFP. Original magnification x200.

SUPPLEMENTARY FIGURE 4
GFP labels cells are seldomly found close to the endosteum of the trabecular bone. Bright field **(on the left)** and GFP/Hoechst staining **(on the right)** of a section of the trabecular bone from a representative 15-months *huCD34tTA/TetO-H2BGFP* transgenic male mouse. The dotted line in the left panel indicates the area occupied by the trabecular bone. Original magnification x600.

SUPPLEMENTARY FIGURE 5
Distribution of the GFP label cells within the bone architecture of a young (2–3-months old) *huCD34tTA/TetO-H2BGFP* transgenic male mouse. **(A)** Reconstruction of the whole femur from a 2-months double mutant mouse stained by Hematoxylin/Eosin. Scanning was performed with a resolution equivalent to that of a 20x objective. **(B)** Reconstruction of the whole femur from the same representative double mutant mouse shown in A stained with DAPI by confocal microscopy. **(C)** Large magnifications of the areas of the epiphysis, diaphysis and trabecular bones indicated in **(B)** showing the detail of the localization of the GFP labeled cells within the bone architecture. Results are representative of those observed with three individual mice. Original magnification x40 and x200 for the entire femur and its details, respectively.

References

1. Gao X, Xu C, Asada N, Frenette PS. The hematopoietic stem cell niche: from embryo to adult. Development (Cambridge) (2018) 145:dev.139691. doi: 10.1242/dev.139691

2. Baccin C, Al-Sabah J, Velten L, Helbling PM, Grünschläger F, Hernández-Malmierca P, et al. Combined single-cell and spatial transcriptomics reveal the molecular, cellular and spatial bone marrow niche organization. *Nat Cell Biol.* (2020) 22:38–48. doi: 10.1038/s41556-019-0439-6

3. Coutu DL, Kokkaliaris KD, Kunz L, Schroeder T. Three-dimensional map of nonhematopoietic bone and bone-marrow cells and molecules. *Nat Biotechnol.* (2017) 35:1202–10. doi: 10.1038/nbt.4006

4. Psaila B, Lyden D, Roberts I. Megakaryocytes, malignancy and bone marrow vascular niches. *J Thromb Haemost.* (2012) 10:177–88. doi: 10.1111/j.1538-7836.2011.04571.x

5. He N, Zhang L, Cui J, Li Z. Bone marrow vascular niche: home for hematopoietic stem cells. *Bone Marrow Res.* (2014) 2014:1–8. doi: 10.1155/2014/128436

6. Wei Q, Frenette PS. Niches for hematopoietic stem cells and their progeny. *Immunity.* (2018) 48:632–48. doi: 10.1016/j.immuni.2018.03.024

7. Kunisaki Y, Bruns I, Scheiermann C, Ahmed J, Pinho S, Zhang D, et al. Arteriolar niches maintain haematopoietic stem cell quiescence. *Nature.* (2013) 502:637–43. doi: 10.1038/nature12612

8. Arranz L, Sánchez-Aguilera A, Martín-Pérez D, Isern J, Langa X, Tzankov A, et al. Neuropathy of haematopoietic stem cell niche is essential for myeloproliferative neoplasms. *Nature.* (2014) 512:78–81. doi: 10.1038/nature13383

9. Young K, Borikar S, Bell R, Kuffler L, Philip V, Trowbridge JJ. Progressive alterations in multipotent hematopoietic progenitors underlie lymphoid cell loss in aging. *J Exp Med.* (2016) 213:2259–67. doi: 10.1084/jem.20160168

10. Ho YH, del Toro R, Rivera-Torres J, Rak J, Korn C, García-García A, et al. Remodeling of bone marrow hematopoietic stem cell niches promotes myeloid cell expansion during premature or physiological aging. *Cell Stem Cell.* (2019) 25:407–18.e6. doi: 10.1016/j.stem.2019.06.007

11. Kokkaliaris KD, Kunz L, Cabezas-Wallscheid N, Christodoulou C, Renders S, Camargo F, et al. Adult blood stem cell localization reflects the abundance of reported bone marrow niche cell types and their combinations. *Blood.* (2020) 136:2296–307. doi: 10.1182/blood.2020006574

12. Ho NPY, Takizawa H. Inflammation regulates haematopoietic stem cells and their niche. *Int J Mol Sci.* (2022) 23:1125. doi: 10.3390/ijms23031125

13. Bogeska R, Mikecin AM, Kaschutnig P, Fawaz M, Büchler-Schäff M, Le D, et al. Inflammatory exposure drives long-lived impairment of hematopoietic stem cell self-renewal activity and accelerated aging. *Cell Stem Cell.* (2022) 29:1273–84.e8. doi: 10.1016/j.stem.2022.06.012

14. Mitroulis I, Kalafati L, Bornhäuser M, Hajishengallis G, Chavakis T. Regulation of the Bone Marrow Niche by Inflammation. *Front Immunol.* (2020) 11:1540. doi: 10.3389/fimmu.2020.01540

15. Bernitz JM, Kim HS, MacArthur B, Sieburg H, Moore K. Hematopoietic stem cells count and remember self-renewal divisions. *Cell.* (2016) 167:1296–309.e10. doi: 10.1016/j.cell.2016.10.022

16. Radomska HS, Gonzalez DA, Okuno Y, Iwasaki H, Nagy A, Akashi K, et al. Transgenic targeting with regulatory elements of the human CD34 gene. *Blood.* (2002) 100:4410–9. doi: 10.1182/blood-2002-02-0355

17. Wilson A, Laurenti E, Oser G, van der Wath RC, Blanco-Bose W, Jaworski M, et al. Hematopoietic stem cells reversibly switch from dormancy to self-renewal during homeostasis and repair. *Cell.* (2008) 135:1118–29. doi: 10.1016/j.cell.2008.10.048

18. Kiel MJ, Yilmaz ÖH, Iwashita T, Yilmaz OH, Terhorst C, Morrison SJ, et al. family receptors distinguish hematopoietic stem and progenitor cells and reveal endothelial niches for stem cells. *Cell.* (2005) 121:1109–21. doi: 10.1016/j.cell.2005.05.026

19. Oguro H, Ding L, Morrison SJ. SLAM family markers resolve functionally distinct subpopulations of hematopoietic stem cells and multipotent progenitors. *Cell Stem Cell.* (2013) 13:102–16. doi: 10.1016/j.stem.2013.05.014

20. Qiu J, Papatsenko D, Niu X, Schaniel C, Moore K. Divisional history and hematopoietic stem cell function during homeostasis. *Stem Cell Rep.* (2014) 2:473–90. doi: 10.1016/j.stemcr.2014.01.016

21. Schaniel C, Moore KA. *Genetic Models to Study Quiescent Stem Cells and Their Niches. Annals of the New York Academy of Sciences.* Blackwell Publishing Inc. (2009). p. 26–35. doi: 10.1111/j.1749-6632.2009.04608.x

22. Kanda T, Sullivan KF, Wahl GM. Histone–GFP fusion protein enables sensitive analysis of chromosome dynamics in living mammalian cells. *Curr Biol.* (1998) 8:377–85. doi: 10.1016/S0960-9822(98)70156-3

23. Bernitz JM, Daniel MG, Fstkchyan YS, Moore K. Granulocyte colony-stimulating factor mobilizes dormant hematopoietic stem cells without proliferation in mice. *Blood.* (2017) 129:1901–12. doi: 10.1182/blood-2016-11-752923

24. Blank U, Karlsson S. TGF-β signaling in the control of hematopoietic stem cells. *Blood.* (2015) 125:3542–50. doi: 10.1182/blood-2014-12-618090

25. Brayton CF, Treuting PM, Ward JM. Pathobiology of aging mice and GEM. *Vet Pathol.* (2012) 49:85–105. doi: 10.1177/0300985811430696

26. Zingariello M, Verachi P, Gobbo F, Martelli F, Falchi M, Mazzarini M, et al. Resident self-tissue of proinflammatory cytokines rather than their systemic levels correlates with development of myelofibrosis in gata1low mice. *Biomolecules.* (2022) 12:234. doi: 10.3390/biom12020234

27. Vannucchi AM, Bianchi L, Cellai C, Paoletti F, Rana RA, Lorenzini R, et al. Development of myelofibrosis in mice genetically impaired for GATA-1 expression (GATA-1low mice). *Blood.* (2002) 100:1123–32. doi: 10.1182/blood-2002-06-1913

28. Martelli F, Ghinassi B, Panetta B, Alfani E, Gatta V, Pancrazzi A, et al. Variegation of the phenotype induced by the Gata1low mutation in mice of different genetic backgrounds. *Blood.* (2005) 106:4102–13. doi: 10.1182/blood-2005-03-1060

29. Lee GY, Jeong SY, Lee HR, Oh IH. Age-related differences in the bone marrow stem cell niche generate specialized microenvironments for the distinct regulation of normal hematopoietic and leukemia stem cells. *Sci Rep.* (2019) 9:1007. doi: 10.1038/s41598-018-36999-5

30. Boulais PE, Frenette PS. Making sense of hematopoietic stem cell niches. *Blood.* (2015) 125:2621–9. doi: 10.1182/blood-2014-09-570192

frontiers | Frontiers in Medicine

TYPE Opinion
PUBLISHED 01 June 2023
DOI 10.3389/fmed.2023.1155057

OPEN ACCESS

EDITED BY
Quan Nguyen,
The University of Queensland, Australia

REVIEWED BY
Camelia Quek,
Melanoma Institute Australia, Australia

*CORRESPONDENCE
Uwe Ritter
✉ uwe.ritter@ukr.de

RECEIVED 31 January 2023
ACCEPTED 25 April 2023
PUBLISHED 01 June 2023

CITATION
Ritter U (2023) *In situ* veritas: combining omics and multiplex imaging can facilitate the detection and characterization of cell-cell interactions in tissues. *Front. Med.* 10:1155057. doi: 10.3389/fmed.2023.1155057

In situ veritas: combining omics and multiplex imaging can facilitate the detection and characterization of cell-cell interactions in tissues

Uwe Ritter[1,2]*

[1]Chair for Immunology, University of Regensburg, Regensburg, Germany, [2]Department for Immunology, Leibniz Institute for Immunotherapy (LIT), Regensburg, Germany

KEYWORDS

proteomics, RNA-seq, spatial transcriptomics, multiplex imaging, physically interacting cells, dendritic cells, T cells

Immunity—The consequence of coordinated cellular interactions

In 1898, microscopic examinations were used to study changes in lymphoid tissues and cell distribution in pathological settings (1). More than 100 years after these first discoveries, the complexity of lymphoid organ composition and the existence of distinct immune-cell subpopulations with a diverse set of functions has been described.

For the adaptive immune system to function efficiently, complex series of spatial and temporal interactions between specialized immune cells must take place. This has been a field of vigorous interest, exemplified by the fact that nearly 100.000 papers have been published dealing with the keywords "interaction" and "immune cells" (PubMed search March 2023). Understanding cell-cell communication—resulting in immunological pathways—is being supported by a range of sophisticated analysis pipelines, ranging from *in vitro* and *ex vivo* single-cell sequencing analysis to genic analysis of immunological alterations. In this context, it is commonly accepted that cells can communicate through juxtacrine and paracrine processes (2). Signal transmission and reception between neighboring cells is fundamentally involved in the regulation of immunological processes, ranging from tissue homeostasis to defense mechanisms against tumour cells or pathogens. However, the final decryption of immunological programs responsible for coordinated and dynamic immunological adaption is multi-factorial and remains challenging.

Exploring the unknown below the surface of tissues—From single cell omics to spatial transcriptomics

Flow-cytometric analysis represents a central pilar of immunophenotyping (3). Based on this technique, it could be shown that immune cells sense and release many molecular mediators capable of modifying immune cell development, phenotype, and function. However, the limited availability of fluorescently labeled antibodies imposes limitations

on the detection of different epitopes. Consequently, other approaches such as single-cell RNA sequencing (scRNA-seq) have been established, allowing an upscaling of the analytic dimensions (4). What was previously impossible becomes routine. Transcriptomic datasets in combination with computational analytic pipelines can match raw data with cell clusters of interest and identify biomarkers involved in the developmental trajectory of immune cells (5–7). While these sequencing approaches improve our ability to analyse different cell populations in a variety of contexts, some limitations remain (5). Especially the enzymatic digestion of tissues is critical, as mediators released during tissue processing for single-cell analysis can result in cell activation or death (6). Consequently, rare cell populations can be lost and valuable information about cell-cell interactions and the transcriptome are overlooked. Most importantly, single-cell preparations abolish the spatial context of the cell populations and information about cell-cell interactions become inaccessible (2). Spatial transcriptomics (ST) (7, 8) address these shortcomings by detecting and localizing mRNA transcripts within tissues (2) and became "Method of the Year" in 2021 (9).

In contrast to early *in situ* hybridization techniques which only detect a single transcript (10), ST can detect a broad range of genes expressed within defined detection spots, containing barcoded poly-T oligonucleotides capable of trapping their complementary tissue mRNA. However, the resolution of detection spots can range from two to 55 microns [2 μm: High-definition spatial transcriptomics (11), 10 μm Slide-seq, Slide-seq v2 (12, 13); 55 μm: Visium spatial gene Expression (7)], leading to considerable uncertainty regarding the precise cell assignment of any identified mRNA. These relatively large spot areas represent therefore a major limitation (14) to this technique, since it is challenging to assign the generated RNAseq data to a distinct "cell type" within a sampled portion of tissue. Furthermore, even with a tissue thickness of less than seven microns, the processed tissue-sample still represents a three-dimensional cell layer (15, 16) containing cells stacked on top of each other, which causes a further inaccuracy of cellular specificity. Consequently, the genetic information of adjacent contaminating cells is easily trapped within the measured spot (14). These issues can be limited by integrating additional gene expression profiles from scRNA-seq or other single-cell genomic approaches and subsequent predictions of location specific cell-type proportions. This complex procedure also called "deconvolution" (2) requires the application of certain algorithms [e.g. SPOTlight (17), SpatialDWLS (18), stereoscope (19), robust cell-type decomposition (14)]. After cell-type scoring, a scRNA-seq-based assignment can be calculated to predict the RNA localization. This process is called "mapping" and can be achieved by the integration of suitable algorithms, such as Harmony (20), LIGER (21), or Seurat Integration (22).

Due to the occurrence of mismatched data sets, the current integrating computational models used for deconvolution and subsequent mapping are reaching their limits. Therefore, it remains difficult to precisely determine the spatial context of cell subsets (2). The essential aspects are summarized below: First, pre-sequencing issues are caused by the fact that classical sc-RNAseq data show a tendency towards a higher sequencing depth compared to most ST-methods (2, 16). Second, a preparation of single cells from tissues can also induce artificial stress responses, that do not take place in intact tissues (23). Third, a loss of cell subsets during the enzymatic preparation of tissues can further induce mismatches and problems during deconvolution steps (24, 25). Fourth, it is possible that "clustering capture spots" may uncover cell subsets only captured by spatial barcoding (2). Thus, a precise decryption of cell-cell interactions by ST still remains an ambitious goal.

Decrypting cellular communications *in situ*—Pushing the limits of *in situ* resolution by combining multimodal workflows

It is widely accepted that tissue-resident cells are continuously involved in short-range (<200 μm) communication (2). This is of crucial importance for the maintenance of organ architecture and coordination of immune responses. Some monospecific receptor-ligand-interactions have already been decoded, highlighting distinct immunological programs (26–28). However, the mode of action by which cellular phenotype adoption takes place, especially within a given temporal microenvironment, is still not fully understood. In line with this challenging question, different *in situ* approaches have been established to uncover cell-cell communication. A combination of multiplexed ion beam imaging (MIBI) and ST has been used to evaluate receptor-ligand proximity or ligand-receptor-target co-expression. Based on these computed data and appropriate algorithms, it is feasible to determine distinct multi-cellular areas of communicating and non-communicating cell subsets within tissues (8). The achieved resolution of the techniques used in "marker-mapping" and creating immunological landscapes is promising [Slide-seq 10 μm; ST 50–100 μm; MIBI 800×800 μm (12, 29)]. Most recently, a bead-based method produced high-definition ST with resolutions nearly comparable to the size of individual cells (11). Therefore, an integration of different *ex vivo* and *in situ* techniques might be suitable to push the limits in contextualized modeling of spatial cellular communication (30) in the near future. However, *in silico* generated landscapes still remain constructed based on computed models of cell type specifications (29). This reconstruction of "highly probable signaling networks" is often based on scRNA-seq data, without exact pairing transcriptomic quantification with probability-based protein identification (30). Models capable of indexing both transcriptomes and epitopes by sequencing, such as CITE-seq, already exist (31) and will help to combine RNA-data and protein abundance in a contextual manner. However, as Alexander F. Schier has already asked: … *"Is "landscapes" even the proper analogy for multidimensional phenotypic complexity? Addressing these questions requires the multiplex in vivo measuring of dozens of transcripts over time and at single-cell resolution — a Holy Grail technology that is not yet available"*… (29).

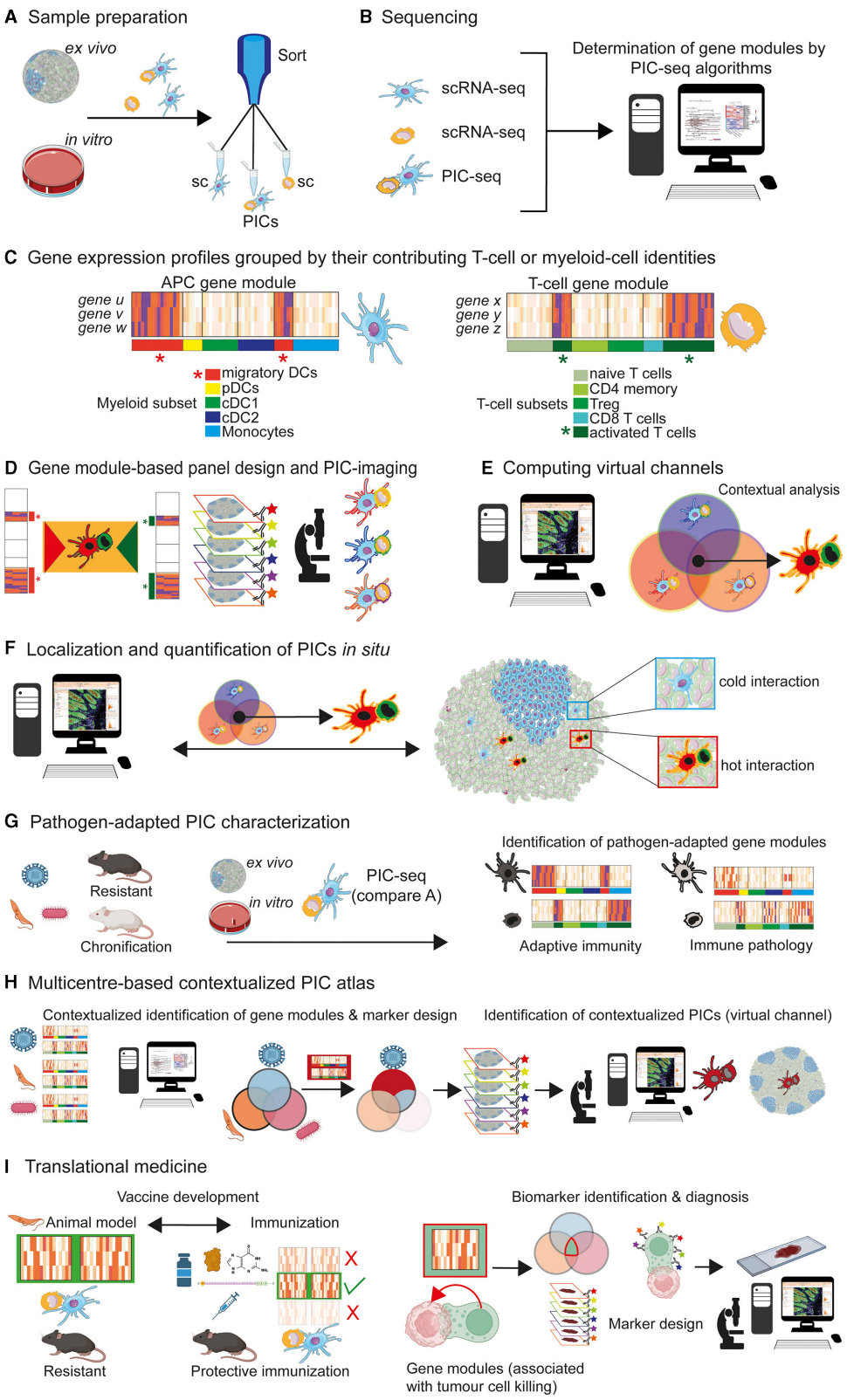

FIGURE 1
PIC characterization and implementation for contextual multiplex imaging. **(A)** *Ex vivo* and *in vitro* cultures, exposed to antigens, can be used for sorting single cells (sc; T cells or DCs) and physical interacting cells (PIC) [For further reading, see Giladi et al. (32)]. **(B)** Implementation of scRNA-seq and PIC-seq algorithms for subsequent characterization of gene modules (exemplary for T cells and DCs). **(C)** Grouped by their contributing myeloid or T-cell subset identities, it is possible to assign distinct gene modules to PICs: e.g., *genes u, v, w* to DC subsets and *genes x, y, z* to T-cell subsets [For further reading, see Giladi et al. (32)]. The putative gene expression profiles of PIC-contributing cell subsets are depicted. Specific "APC gene modules" of migratory DCs (red star) and "T-cell gene modules" of activated T cells (green star) can be generated [For further reading, see Giladi et al. (32)]. **(D)** Gene modules assigning specific cellular phenotypes can be used for panel designs and multiplex imaging. PICs consisting of migratory

(Continued)

FIGURE 1 (Continued)
DCs and activated T cells can be computed (orange insert). A contextualized detection of "migratory DCs" physically interacting with "activated T cells" becomes possible (highlighted by distinct DC and T cell shapes and colors). **(E)** Based on the phenotype of cells that contribute to PICs, a virtual channel (orange contour) can be generated by imaging software tools, capable of contextualized image analysis *in situ*. PICs (orange contour) consisting of "migratory DCs (red shape)" and "activated T cells (green shape)" can be computed. **(F)** Visualization and further characterization of PICs of interest (orange contour). It is feasible to dissect "cold" cell interactions (blue insert; non-reactive cells) from "hot" cell interactions (red insert; reactive cells) resulting in T-cell activation. **(G)** Different pathogens (viruses, protozoan, bacteria etc.) and models must be considered for the generation of context-adapted gene modules. This would allow a detailed characterization of gene modules of PICs in a pathogen-specific manner. A contextualized generation of PIC-associated gene modules will permit the decryption of two central immunological categories: beneficial adaptive immune responses, resulting in protective host defense mechanisms against pathogens and immunopathological process, associated with chronic diseases. **(H)** Multicentre data acquisition and storage (PIC atlas) for the long-term generation of contextualized gene models and subsequent marker design. This concept will allow an allocation of certain immunological attributes to PICs, in a contextualized manner. A spatial detection of PICs contributing to disease chronification or successful immunity would become possible. **(I)** Conceivable applications of the PIC-seq concept in translational medicine are depicted. Left side: vaccination development. Based on experimental models and definition of gene modules (green box), it is possible to define PICs that are contributing to protective immunity against pathogens. This protective gene signatures can be compared with gene modules of PICs that occur after immunization with different vaccine protocols. Such an approach might be useful for the selection of most promising (green check) and inefficient (red cross) vaccine formulation. Right side: biomarker identification in tumour immunology. Physical interactions among tumour and immune cells are supposed to play crucial roles in immune modulation, progression and response to treatments (46). Thus, contextualized analysis of tumour-immune communications would improve the understanding of the tumour-immune interface. Comparable to the described immune cell interactions [compare **(A–H)**] a biocomputational analysis of gene modules, associated with physically interacting immune and tumour cells, might help to identify biomarkers, involved in protective tumour-immune interactions. The integration of those biomarker in high precision imaging, would lead to massive improvements of contextual resolutions regarding tumour cell/effector cell interactions. This feature will help to correlate microenvironmental neoplasia with molecular modifications—aspects that are crucial for the evaluation of tumour progression and therapy controls.

Computed cell-cell communication networks—First steps in decrypting physically interacting cells *in situ*

Unbiased mapping of omics to a spatial context opens a new dimension in the field of immunology (29). Given the ST-limitations described above and the multidimensionality of cell-interactions, a precise characterization of single cells *in situ* still seems to be a distant goal. To understand the immunological relevance of physically interacting cells [PICs, (32)] *in situ*, a combination of existing sequencing methods and data sets might be promising. Given the broad spectrum of cell-cell communication during homeostasis and pathological conditions, it is impossible to present one conceptual workflow of data processing, covering all cell subsets and immunological responses. Thus, I would like to address this aspect of "PIC-decryption" based on dendritic cell (DC)/T-cell interactions.

Initiation of adaptive immunity by DCs involves a cascade of fine-tuned bidirectional processes (33). We and others have been able to identify that certain subsets of DCs are mandatory for adaptive T-cell responses against pathogens (34, 35). In this context, the formation of immunological synapses between DCs and T cells is crucial for T-cell polarization (36–38). Although DC/T-cell interactions are of high clinical relevance, current genomics and imaging tools for their detection and precise *in situ* characterization are still limited, possibly due to the fact that PICs must be analyzed *in situ* on a cell-by-cell basis. There is one general problem: Within lymphoid organs, all cells are close neighbors due to the density of the tissues.

One must realize that proximity alone is not sufficient to induce cell activation or differentiation. Thus, a robust detection-signature, capable of highlighting PICs like DC/T-cell interactions by multiplex imaging systems, would be of tremendous importance for the field to understand early events in adaptive immunity (32). PICs isolated from tissues, are already under investigation (32, 39, 40). The pipeline of PIC-transcriptome analysis [abbreviated as PIC-seq (32)] is encouraging (41). One strength of this PIC-seq-concept lies in the combination of transcriptome data from *ex vivo* isolated PIC-complexes and respective single-cell data (32). If transcriptional profiles of PICs are sufficiently different, a good deconvolution is possible and PIC-seq data can be generated (42). To further calculate the transcriptional profiles of PICs, other pipelines and algorithms, such as the Giotto workflow (43), SpaOTsc algorithm (44), or CSOmap (45) might be also be implemented.

Using PIC-seq and a dermal infection model with *Nippostrongylus brasiliensis* (Nb), it could be shown that PICs consisting of dermal-derived DCs that present Nb-antigens to T cells, upregulate distinct transcriptional profiles—also called gene modules (32). In case of Nb-infection, this DC-specific gene module is composed of chemokines (Ccl22 and Ccl17) and co-stimulatory genes CD40, Ebi3, and Dll4 (32). The T cell-specific gene modules of PICs seem to be more complex, due to the heterogeneity of T cells that interact with DCs (32). However, co-culture experiments revealed that T cells that interact with antigen-presenting DCs show a reduced Th-precursor program (Klf2, Sell) associated with an induction of interferon type-I response (Stat1, Irf7), and metabolic programs (Myc and Npm1), as well as an upregulation of cytokines, chemokine receptors and effector genes (Tigit, Il22, Cxcr6, Pdcd1, and Tnfrsf9) (32). Based on these data, it can be concluded that DCs, which physically interact with T cells (Figures 1A–C), express distinct PIC-associated gene modules (32). Consequently, it is possible to design gene module-derived staining panels, allowing a refined identification of DC/T-cell interactions by multiplex imaging and tissue image cytometry (47) (Figures 1D–F).

From PIC-associated gene modules to functionality: antibody-based multiplex imaging might represent a powerful tool for the characterization of PICs in translational clinical research

Focusing on physically interacting DC/T cells, Gialdi and colleagues could demonstrate that PICs are associated with a distinct expression of gene modules, under defined experimental conditions (32) (Figures 1A–E). This aspect represents a major limitation of the PIC-approach. Based on the huge antigen repertoire of pathogens and the corresponding heterogeneity of adaptive immunity, a context-adapted generation of gene modules is of crucial importance to avoid restrictive and oversimplified conditions. This approach is also necessary to ensure the determination of pathogen-adapted gene modules, expressed by PICs of interest (Figure 1G). Referring to the complexity of possible DC/T-cell interactions, a multicentre global database might represent a mandatory prerequisite for the identification of contextualized gene modules (Figure 1H). In line with the integration of high-dimensional data sets, an acceptable point of data reduction can be achieved, allowing the compilation of gene module-based antibody panels, useful for the spatial characterization of PICs, in a context-dependent manner (Figure 1H). This strategy might be further integrated into the new discipline of spatiotemporal molecular medicine, which aims to decrypt pathological processes within a spatial context (48, 49). A variety of applications in the field of basic research and translational medicine are conceivable. Two aspects are of particular importance in translational medicine: identification of potent vaccination strategies and biomarker identification in the field of tumour immunology (Figure 1I).

Conclusion

It is quite clear that antigen-specific immunity represents more than the sum of its parts. Based on the multimodal incorporation of single-cell omics, ST, PIC-seq, and other cutting-edge technologies, deep-learning reconstruction of gene-regulatory and cellular networks *in situ* will become possible soon. This will be of central importance to understand the cellular crosstalk in tissues and for the decryption of complex immune responses within pathological tissues at a so far unknown level.

Author contributions

Conceptualization, investigation, and writing—original draft: UR.

Funding

This study was supported by the Bavarian Research Network (bayresq.net; Bavarian State Ministry for Science and the Arts, UR).

Acknowledgments

Many thanks to Russell Ulbrich of ScientiaLux LLC (www.scientialux.com) Worcester Massachusetts, United States of America, for critical reading and readability improvement of the manuscript. Lisa Schmidleithner (Department for Immunology, LIT—Leibniz Institute for Immunotherapy—Universitätsklinikum Regensburg Franz-Josef-Strauß-Allee 11, 93053 Regensburg) for critical reading of the manuscript and sharing BioRender icons created with BioRender.com. Graphic abstract illustration credits from Servier Medical Art (https://smart.servier.com/), reproduced under Creative Commons License attribution 3.0 Unported License.

Conflict of interest

The author declares that the research was conducted in the absence of any commercial or financial relationships that could be construed as a potential conflict of interest.

Publisher's note

References

1. Montgomery DWV. Report of a case of epithelioma of the skin of the face, with unusual course of infection of lymph-nodes. *Ann Surg.* (1898) 27:193–8.

2. Longo SK, Guo MG Ji AL, Khavari PA. Integrating single-cell and spatial transcriptomics to elucidate intercellular tissue dynamics. *Nat Rev Genet.* (2021) 22:627–44. doi: 10.1038/s41576-021-00370-8

3. Nolan JP. The evolution of spectral flow cytometry. *Cytometry A.* (2022). doi: 10.1002/cyto.a.24566

4. Tang F, Barbacioru C, Wang Y, Nordman E, Lee C, Xu N, et al. Mrna-Seq whole-transcriptome analysis of a single cell. *Nat Methods.* (2009) 6:377–82. doi: 10.1038/nmeth.1315

5. Chen G, Ning B, Shi T. Single-Cell Rna-Seq technologies and related computational data analysis. *Front Genet.* (2019) 10:317. doi: 10.3389/fgene.2019.00317

6. Merad M, Sathe P, Helft J, Miller J, Mortha A. The dendritic cell lineage: ontogeny and function of dendritic cells and their subsets in the steady state and the inflamed setting. *Annu Rev Immunol.* (2013) 31:563–604. doi: 10.1146/annurev-immunol-020711-074950

7. Stahl PL, Salmen F, Vickovic S, Lundmark A, Navarro JF, Magnusson J, et al. Visualization and analysis of gene expression in tissue sections by spatial transcriptomics. *Science.* (2016) 353:78–82. doi: 10.1126/science.aaf2403

8. Ji AL, Rubin AJ, Thrane K, Jiang S, Reynolds DL, Meyers RM, et al. Multimodal analysis of composition and spatial architecture in human squamous cell carcinoma. *Cell.* (2020) 182:497–514 e22. doi: 10.1016/j.cell.2020.05.039

9. Marx V. Method of the year: spatially resolved transcriptomics. *Nat Methods.* (2021) 18:9–14. doi: 10.1038/s41592-020-01033-y

10. Ritter U, Moll H, Laskay T, Brocker E, Velazco O, Becker I, et al. Differential expression of chemokines in patients with localized and diffuse cutaneous american leishmaniasis. *J Infect Dis.* (1996) 173:699–709. doi: 10.1093/infdis/173.3.699

11. Vickovic S, Eraslan G, Salmen F, Klughammer J, Stenbeck L, Schapiro D, et al. High-definition spatial transcriptomics for in situ tissue profiling. *Nat Methods.* (2019) 16:987–90. doi: 10.1038/s41592-019-0548-y

12. Rodriques SG, Stickels RR, Goeva A, Martin CA, Murray E, Vanderburg CR, et al. Slide-Seq: a scalable technology for measuring genome-wide expression at high spatial resolution. *Science.* (2019) 363:1463–7. doi: 10.1126/science.aaw1219

13. Stickels RR, Murray E, Kumar P, Li J, Marshall JL, Di Bella DJ, et al. Highly sensitive spatial transcriptomics at near-cellular resolution with slide-Seqv2. *Nat Biotechnol.* (2021) 39:313–9. doi: 10.1038/s41587-020-0739-1

14. Cable DM, Murray E, Zou LS, Goeva A, Macosko EZ, Chen F, et al. Robust decomposition of cell type mixtures in spatial transcriptomics. *Nat Biotechnol.* (2022) 40:517–26. doi: 10.1038/s41587-021-00830-w

15. Halpern KB, Shenhav R, Matcovitch-Natan O, Toth B, Lemze D, Golan M, et al. Single-cell spatial reconstruction reveals global division of labour in the mammalian liver. *Nature.* (2017) 542:352–6. doi: 10.1038/nature21065

16. Lohoff T, Ghazanfar S, Missarova A, Koulena N, Pierson N, Griffiths JA, et al. Integration of spatial and single-cell transcriptomic data elucidates mouse organogenesis. *Nat Biotechnol.* (2022) 40:74–85. doi: 10.1038/s41587-021-01006-2

17. Elosua-Bayes M, Nieto P, Mereu E, Gut I, Heyn H. Spotlight: seeded nmf regression to deconvolute spatial transcriptomics spots with single-cell transcriptomes. *Nucleic Acids Res.* (2021) 49:e50. doi: 10.1093/nar/gkab043

18. Dong R, Yuan GC. Spatialdwls: accurate deconvolution of spatial transcriptomic data. *Genome Biol.* (2021) 22:145. doi: 10.1186/s13059-021-02362-7

19. Andersson A, Bergenstrahle J, Asp M, Bergenstrahle L, Jurek A, Fernandez Navarro J, et al. Single-cell and spatial transcriptomics enables probabilistic inference of cell type topography. *Commun Biol.* (2020) 3:565. doi: 10.1038/s42003-020-01247-y

20. Korsunsky I, Millard N, Fan J, Slowikowski K, Zhang F, Wei K, et al. Fast, sensitive and accurate integration of single-cell data with harmony. *Nat Methods.* (2019) 16:1289–96. doi: 10.1038/s41592-019-0619-0

21. Welch JD, Kozareva V, Ferreira A, Vanderburg C, Martin C, Macosko EZ. Single-cell multi-omic integration compares and contrasts features of brain cell identity. *Cell.* (2019) 177:1873–87 e17. doi: 10.1016/j.cell.2019.05.006

22. Stuart T, Butler A, Hoffman P, Hafemeister C, Papalexi E, Mauck WM, et al. Comprehensive integration of single-cell data. *Cell.* (2019) 177:1888-902 e21. doi: 10.1016/j.cell.2019.05.031

23. Femino AM, Fay FS, Fogarty K, Singer RH. Visualization of single rna transcripts *in situ*. *Science.* (1998) 280:585–90. doi: 10.1126/science.280.5363.585

24. Moffitt JR, Bambah-Mukku D, Eichhorn SW, Vaughn E, Shekhar K, Perez JD, et al. Molecular, spatial, and functional single-cell profiling of the hypothalamic preoptic region. *Science.* (2018) 362. doi: 10.1126/science.aau5324

25. Ji AL, Rubin AJ, Thrane K, Jiang S, Reynolds DL, Meyers RM, et al. Multimodal analysis of composition and spatial architecture in human squamous cell carcinoma. *Cell.* (2020) 182:1661–2. doi: 10.1016/j.cell.2020.08.043

26. Forster R, Davalos-Misslitz AC, Rot A. Ccr7 and its ligands: balancing immunity and tolerance. *Nat Rev Immunol.* (2008) 8:362–71. doi: 10.1038/nri2297

27. Vinuesa CG, Cook MC. The molecular basis of lymphoid architecture and B Cell responses: implications for immunodeficiency and immunopathology. *Curr Mol Med.* (2001) 1:689–725. doi: 10.2174/1566524013363276

28. Cook MC, Korner H, Riminton DS, Lemckert FA, Hasbold J, Amesbury M, et al. Generation of splenic follicular structure and B cell movement in tumour necrosis factor-deficient mice. *J Exp Med.* (1998) 188:1503–10. doi: 10.1084/jem.188.8.1503

29. Schier AF. Single-cell biology: beyond the sum of its parts. *Nat Methods.* (2020) 17:17–20. doi: 10.1038/s41592-019-0693-3

30. Efremova M, Teichmann SA. computational methods for single-cell omics across modalities. *Nat Methods.* (2020) 17:14–7. doi: 10.1038/s41592-019-0692-4

31. Brombacher E, Hackenberg M, Kreutz C, Binder H, Treppner M. The performance of deep generative models for learning joint embeddings of single-cell multi-omics data. *Front Mol Biosci.* (2022) 9:962644. doi: 10.3389/fmolb.2022.962644

32. Giladi A, Cohen M, Medaglia C, Baran Y, Li B, Zada M, et al. Dissecting cellular crosstalk by sequencing physically interacting cells. *Nat Biotechnol.* (2020) 38:629–37. doi: 10.1038/s41587-020-0442-2

33. Hespel C, Moser M. Role of inflammatory dendritic cells in innate and adaptive immunity. *Eur J Immunol.* (2012) 42:2535–43. doi: 10.1002/eji.201242480

34. Brewig N, Kissenpfennig A, Malissen B, Veit A, Bickert T, Fleischer B, et al. Priming of Cd8+ and Cd4+ T cells in experimental leishmaniasis is initiated by different dendritic cell subtypes. *J Immunol.* (2009) 182:774–83. doi: 10.4049/jimmunol.182.2.774

35. Ritter U, Osterloh A, A. New view on cutaneous dendritic cell subsets in experimental leishmaniasis. *Med Microbiol Immunol.* (2007) 196:51–9. doi: 10.1007/s00430-006-0023-0

36. Cassioli C, Baldari CT. Lymphocyte polarization during immune synapse assembly: centrosomal actin joins the game. *Front Immunol.* (2022) 13:830835. doi: 10.3389/fimmu.2022.830835

37. Rodriguez-Fernandez JL, Criado-Garcia O. The actin cytoskeleton at the immunological synapse of dendritic cells. *Front Cell Dev Biol.* (2021) 9:679500. doi: 10.3389/fcell.2021.679500

38. Castro-Sanchez P, Aguilar-Sopena O, Alegre-Gomez S, Ramirez-Munoz R, Roda-Navarro P. Regulation of Cd4(+) T cell signaling and immunological synapse by protein tyrosine phosphatases: molecular mechanisms in autoimmunity. *Front Immunol.* (2019) 10:1447. doi: 10.3389/fimmu.2019.01447

39. Zimara N, Florian C, Schmid M, Malissen B, Kissenpfennig A, Mannel DN, et al. Langerhans cells promote early germinal center formation in response to leishmania-derived cutaneous antigens. *Eur J Immunol.* (2014) 44:2955–67. doi: 10.1002/eji.201344263

40. Bendall SC. Diamonds in the doublets. *Nat Biotechnol.* (2020) 38:559–61. doi: 10.1038/s41587-020-0511-6

41. Qian X, Harris KD, Hauling T, Nicoloutsopoulos D, Munoz-Manchado AB, Skene N, et al. Probabilistic cell typing enables fine mapping of closely related cell types *in situ*. *Nat Methods.* (2020) 17:101–6. doi: 10.1038/s41592-019-0631-4

42. Koch L. Transcriptional profiling of physically interacting cells. *Nat Rev Genet.* (2020) 21:275. doi: 10.1038/s41576-020-0229-9

43. Dries R, Zhu Q, Dong R, Eng CL Li H, Liu K, et al. Giotto: A Toolbox for integrative analysis and visualization of spatial expression data. *Genome Biol.* (2021) 22:78. doi: 10.1186/s13059-021-02286-2

44. Cang Z, Nie Q. Inferring spatial and signaling relationships between cells from single cell transcriptomic data. *Nat Commun.* (2020) 11:2084. doi: 10.1038/s41467-020-15968-5

45. Arnol D, Schapiro D, Bodenmiller B, Saez-Rodriguez J, Stegle O. Modeling cell-cell interactions from spatial molecular data with spatial variance component analysis. *Cell Rep.* (2019) 29:202–11e6. doi: 10.1016/j.celrep.2019.08.077

46. Biswas A, Ghaddar B, Riedlinger G, De S. Inference on spatial heterogeneity in tumour microenvironment using spatial transcriptomics data. *Comput Syst Oncol.* (2022) 2:3. doi: 10.1002/cso2.1043

47. Meshcheryakova A, Mungenast F, Ecker R, Mechtcheriakova D. Tissue Image Cytometry. (2021). In: *Imaging Modalities for Biological and Preclinical Research: A Compendium, Volume 1*. IOP Publishing. doi: 10.1088/978-0-7503-3059-6ch14

48. Wang X, Fan J. Spatiotemporal molecular medicine: a new era of clinical and translational medicine. *Clin Transl Med.* (2021) 11:e294. doi: 10.1002/ctm2.294

49. Wang T, Peng Q, Liu B, Liu Y, Wang Y. Disease module identification based on representation learning of complex networks integrated from gwas, eqtl summaries, and human interactome. *Front Bioeng Biotechnol.* (2020) 8:418. doi: 10.3389/fbioe.2020.00418

frontiers | Frontiers in Immunology

TYPE Methods
PUBLISHED 08 June 2023
DOI 10.3389/fimmu.2023.1021638

OPEN ACCESS

EDITED BY
Rupert Ecker,
TissueGnostics GmbH, Austria

REVIEWED BY
Jin Jiaqi,
Harbin Medical University, China
Diana Mechtcheriakova,
Medical University of Vienna, Austria

*CORRESPONDENCE
Michał Aleksander Ciach
m.ciach@mimuw.edu.pl
Anna Gambin
aniag@mimuw.edu.pl

†These authors have contributed equally to this work and share first authorship

RECEIVED 17 August 2022
ACCEPTED 24 April 2023
PUBLISHED 08 June 2023

CITATION
Ciach MA, Bokota G, Manda-Handzlik A, Kuźmicka W, Demkow U and Gambin A (2023) Trapalyzer: a computer program for quantitative analyses in fluorescent live-imaging studies of neutrophil extracellular trap formation.
Front. Immunol. 14:1021638.
doi: 10.3389/fimmu.2023.1021638

Trapalyzer: a computer program for quantitative analyses in fluorescent live-imaging studies of neutrophil extracellular trap formation

Michał Aleksander Ciach[1*†], Grzegorz Bokota[1,2†], Aneta Manda-Handzlik[3†], Weronika Kuźmicka[3], Urszula Demkow[3] and Anna Gambin[1*]

[1]Faculty of Mathematics, Informatics and Mechanics, University of Warsaw, Warsaw, Poland, [2]Centre of New Technologies, University of Warsaw, Warsaw, Poland, [3]Department of Laboratory Diagnostics and Clinical Immunology of Developmental Age, Medical University of Warsaw, Warsaw, Poland

Neutrophil extracellular traps (NETs), pathogen-ensnaring structures formed by neutrophils by expelling their DNA into the environment, are believed to play an important role in immunity and autoimmune diseases. In recent years, a growing attention has been put into developing software tools to quantify NETs in fluorescent microscopy images. However, current solutions require large, manually-prepared training data sets, are difficult to use for users without background in computer science, or have limited capabilities. To overcome these problems, we developed Trapalyzer, a computer program for automatic quantification of NETs. Trapalyzer analyzes fluorescent microscopy images of samples double-stained with a cell-permeable and a cell-impermeable dye, such as the popular combination of Hoechst 33342 and SYTOX™ Green. The program is designed with emphasis on software ergonomy and accompanied with step-by-step tutorials to make its use easy and intuitive. The installation and configuration of the software takes less than half an hour for an untrained user. In addition to NETs, Trapalyzer detects, classifies and counts neutrophils at different stages of NET formation, allowing for gaining a greater insight into this process. It is the first tool that makes this possible without large training data sets. At the same time, it attains a precision of classification on par with state-of-the-art machine learning algorithms. As an example application, we show how to use Trapalyzer to study NET release in a neutrophil-bacteria co-culture. Here, after configuration, Trapalyzer processed 121 images and detected and classified 16 000 ROIs in approximately three minutes on a personal computer. The software and usage tutorials are available at https://github.com/Czaki/Trapalyzer.

KEYWORDS

neutrophil, neutrophil extracellular traps, fluorescent microscopy, digital image processing, image annotation, SYTOX™ green, chromatin, quantification

1 Introduction

Neutrophils are the most abundant group of white blood cells in humans. They are often described as the organism's "frontline soldiers", responsible for fighting pathogens during the initial stages of infection (1, 2). One of their fighting strategies is the formation of Neutrophil Extracellular Traps (NETs), web-like structures formed from the cells' DNA, which ensnare and putatively kill microbes (3, 4). NETs help to fight infections, but may also harm the host by damaging surrounding tissues and promoting inflammation (5). Research shows that excessive or insufficient formation of NETs plays a role in a number of diseases, including periodontitis, thrombosis, and arthritis (6, 7). A better understanding of the dynamics of NET formation may lead to improved diagnostics and treatment of those diseases. This requires both qualitative studies of the biology of this process as well as quantitative studies of its rates in different conditions.

1.1 The biology of NET formation

NET formation induced by either ionomycin or the presence of *Candida albicans* has recently been studied on a cellular level by the means of high-resolution time-lapse microscopy (8). The authors have observed that this process progresses through a sequence of stages, shown schematically in Figure 1. The onset of NET formation is marked by the disassembly of the actin cytoskeleton and the formation of plasma membrane microvesicles containing cytosolic components. Next, the neutrophils' chromatin gradually decondenses, with its fluorescent staining becoming spatially homogeneous. During and after chromatin decondensation, the nucleus loses its characteristic lobulation and becomes partially or fully rounded. After some time, a rapid disruption of the nuclear envelope causes a release of the DNA into the cytoplasm. Simultaneously, the plasma membrane gradually increases its permeability, causing membrane-impermeable markers to enter the cell. Finally, the plasma membrane ruptures, releasing the genetic material to the environment.

1.2 Methods and technical challenges of computer-assisted NET quantification

In recent years, there has been a growing interest in developing computational methods of NET quantification to make it more replicable and objective, while at the same time less laborsome and time-consuming (9). A number of computer programs for NET quantification has been released, either based on machine learning algorithms, including convolutional neural networks and support vector machines (10–12), or digital image processing techniques, including image thresholding and classification of regions of interest (ROIs) based on features such as area or circularity (13–15). Modern machine learning-based methods are capable of quantifying not only NETs, but also cells at certain stages of NET formation, giving a greater insight into the dynamics of this process (12).

However, the complex nature of NET formation poses a substantial difficulty in developing software tools to analyze it. Furthermore, there are numerous experimental methods of NET quantification (7, 16, 17), and each experimental method not only requires a different computational approach, but also determines which stages of NET formation can be quantified. For example, microvesicle shedding is visible using high-resolution differential interference contrast microscopy, but not in fluorescent microscopic images of stained DNA. It is a challenging task to pinpoint distinct cell morphologies that can be rigorously quantified, provide their mathematical characterization, and use it to develop an algorithm for an automatic image annotation.

As a consequence, the currently available software solutions have a number of drawbacks which limit their usability. Computer programs based on machine learning require laborious manual preparations of large training data sets and are often difficult to use for users without a computer science background. Some of those programs annotate ROIs only using bounding boxes instead of a pixel-wise detection. This allows for a simple counting of NETs and cells, but not for more detailed analyses of their shapes and areas. On the other hand, the currently available tools based on digital image processing, which are free from many of those limitations, quantify NETs, but not the numbers of neutrophils at different stages of NET formation. One of the reasons for this situation is that they are arguably more difficult to develop. While machine learning algorithms, given a manually annotated data set, are able to figure out the crucial steps of image annotation by themselves, tools based on digital image processing techniques need an explicit, human-designed algorithm for this task. Developing such an algorithm requires an in-depth expert knowledge of the analyzed process and dedicated studies on how to mathematically describe and distinguish different cell morphologies.

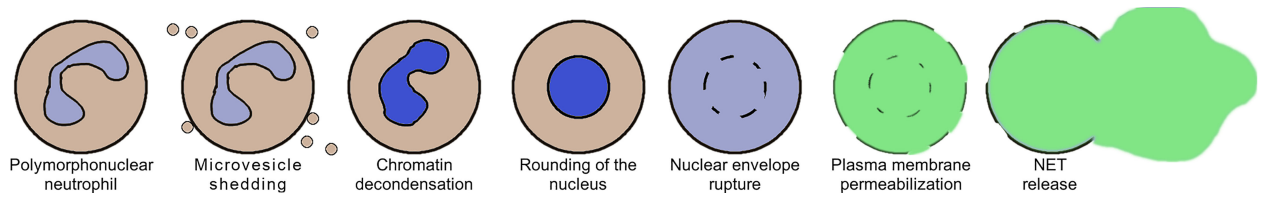

FIGURE 1
A schematic representation of the selected stages of Neutrophil Extracellular Trap (NET) formation, based on (8).

1.3 Trapalyzer: a new computer program to analyze the dynamics and rates of NET formation

In this work, we present Trapalyzer (Figure 2), a computer program for the analysis and annotation of fluorescent microscopy images of neutrophils and NETs double-stained with a cell-permeable and a cell-impermeable fluorescent DNA dye, such as a combination of Hoechst 33342 and SYTOX™ Green. Our software extends the capabilities of the currently available tools by quantifying more stages of NET formation without the need for large training data sets. This has been made possible by extensive studies of fluorescent microscopy images by an interdisciplinary team composed of clinical scientists, statisticians, and computer scientists, which have resulted in a small set of ROI features that characterize the stages, and a scoring system that uses those features to classify cells. To make NET quantification more reliable and robust, the program also detects artifacts in the green channel which can be caused e.g. by background signal or autofluorescence (18). Trapalyzer is freely available as a plug-in for the PartSeg software (19). It can be easily combined with other PartSeg's features, such as image pre-processing and feature extraction, which further increase the software's usability.

1.4 High-throughput computational analysis of thousands of cells with a user-friendly software

Trapalyzer offers two modes of analysis: an interactive session and a batch processing mode. The interactive session allows the user to set the program's parameters and visualize the annotation, while the batch processing mode can be used to process multiple images in a single run and save the results in a convenient Excel spreadsheet. The user can specify the information to be computed, both image-wise (such as the number of neutrophils at a given stage of NET formation, the percent of image area covered by NETs, or the quality of annotation) and ROI-wise (such as the area of each ROI, its bounding box, or assigned class). Since Trapalyzer detects ROIs on a pixel-wise basis instead of simple bounding boxes only, it can also calculate multiple different features describing their morphologies.

Trapalyzer is designed with an emphasis on software ergonomy and ease of use. The plug-in requires no installation other than downloading and placing in the PartSeg's directory and is accompanied with easy to follow tutorials available on the project's website. The tutorials guide the users through a step-by-step procedure to tune the program's parameters and configure its output. This allows the users to easily learn how to use the software and apply it to their own experiments even if they have no background in computer science, giving Trapalyzer the potential to be routinely used in laboratories researching diverse aspects of NET formation.

1.5 Quantitative analyses of NET formation in different experimental conditions

We validate our approach on a publicly available benchmark data set of neutrophils stimulated with peroxynitrite published in (12) and show that it attains a similar performance to convolutional

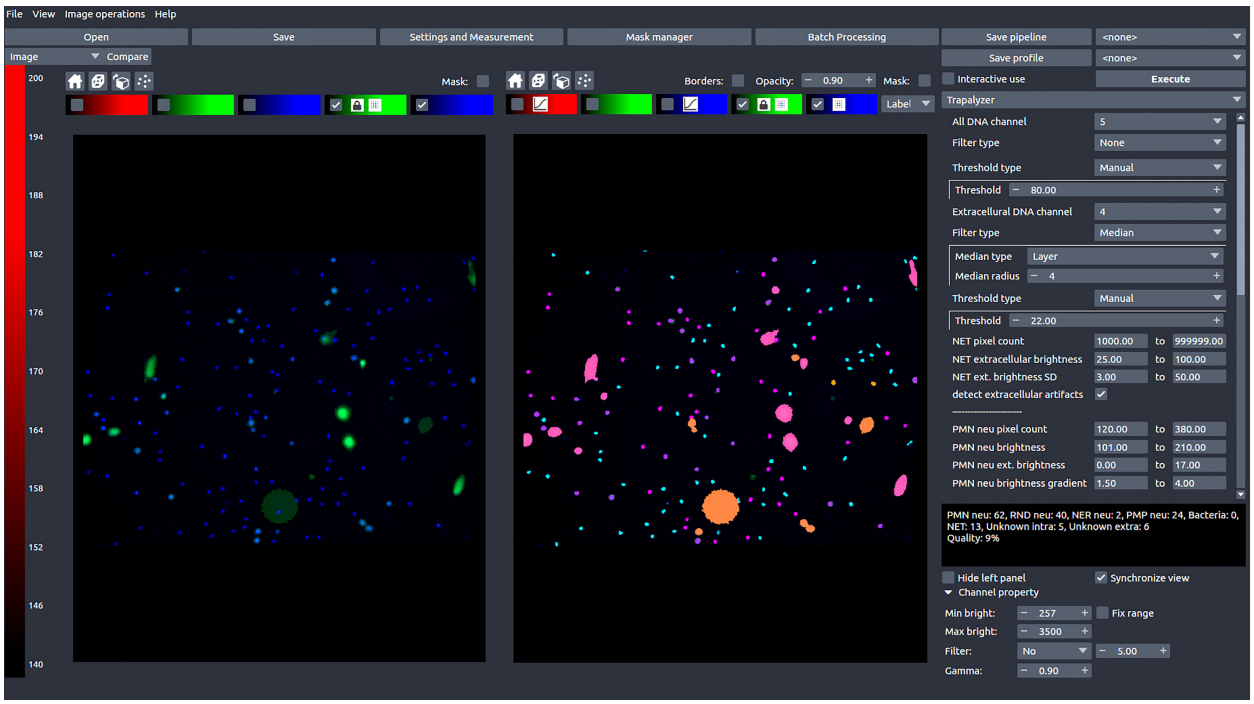

FIGURE 2
A screen shot of Trapalyzer running in an interactive session of PartSeg. The left window shows a fluorescence microscopy image taken as a part of our neutrophil killing assay with a double staining with SYTOX™ Green and Hoechst 33342 DNA dyes. The right window shows the image annotated by Trapalyzer.

neural networks using just a fraction of the training data set. We then show how Trapalyzer can be applied to an experiment on the dynamics of neutrophil-*E. coli* bacteria interactions, where we study the cells' progression through the stages of NET formation. The results of this experiment agree with observations made for individual cells by other authors (8).

2 Methods

To establish the quantifiable classes of ROIs for NET formation studies, we have performed a neutrophil killing assay of *Escherichia coli* bacteria. To verify our conclusions and to assess the performance of our approach we have downloaded a benchmark set of images in which neutrophils were incubated without bacteria and NET formation was induced by various chemical stimuli.

2.1 Reagents

Roswell Park Memorial Institute (RPMI) 1640 medium, HEPES, SYTOX™ Green, and Hoechst 33342 were purchased from Thermo Fisher Scientific (Waltham, USA). LB broth was purchased from Sigma Aldrich (St Louis, MO, USA).

2.2 Preparation of blood neutrophils

Neutrophils were obtained from peripheral blood of one healthy blood donor. Blood sample was purchased at Local Blood Donation Centre and according to local regulations, the blood donor enabled blood donation center to sell their blood samples for scientific purposes and the consent of bioethical committee was not required. Blood was collected into a citrate tube and processed within 2 hours from collection. Neutrophils were isolated using density gradient centrifugation followed by polyvinyl alcohol sedimentation, exactly as described in (20). Isolated neutrophils were suspended in RPMI 1640 medium with 10 mM HEPES (RH).

2.3 Preparation of bacteria

Escherichia coli (American Type Culture Collection(ATCC) 25922 strain) were grown overnight in LB broth with shaking. In the morning, an aliquot of bacterial culture was taken, diluted 100 x in a fresh LB medium and grown for subsequent 2-3 hours. Subsequently, bacterial cultures were washed and resuspended in RH medium.

2.4 Co-culture of neutrophils with bacteria

Neutrophils were seeded into the wells of 48-well plates at the density of 2×10^4 cells/well and allowed to settle for 30 minutes at 37°C, 5% CO2. Subsequently, *E. coli* was added into the appropriate wells at the multiplicity of infection of 4 or 1 (*E.coli*: neutrophil). Neutrophils incubated without bacteria were used as a control group. A technical duplicate for each condition was prepared. For each intended timepoint (t=0, 60, 90, 120, 180 minutes), a separate 48 well plate was prepared. The plates were centrifuged for 5 minutes at 250 g to allow the contact of bacteria with neutrophils. The plates were incubated at 37°C, 5% CO2 for a specified time and then the samples were stained with SYTOX™ Green (100 nM) and Hoechst 33342 (1.25 µM for 10 minutes. Four images of each well were taken with Leica DMi8 fluorescent microscope equipped with a 10× magnification objective (Leica, Wetzlar, Germany). Overall, 120 images have been obtained.

2.5 Benchmark data set

A benchmark data set of images of neutrophils and NETs stained with SYTOX™ Green and Hoechst 33342, published in (12), was downloaded from https://github.com/krzysztoffiok/CNN-based-image-analysis-for-detection-and-quantification-of-neutrophil-extracellular-traps on May 19, 2019. For evaluation of Trapalyzer's accuracy, we have selected the validation set in file large_validation_set.zip, subdirectory xml_pascal_voc_format/images/oryg. The validation set consists of 57 images. Manual annotations of the images were accessed in subdirectory xml_pascal_voc_format/annotations/oryg. Annotations in xml files were handled using the lxml library of the Python 3 programming language. For tuning of Trapalyzer's parameters, additional 10 images were selected from the file original_uncompressed_images_with_pascalvoc_annotations.zip, rescaled to match the dimentions of the validation set images and converted to the TIFF format using the convert program from the ImageMagick suite.

3 Results

3.1 Quantifiable stages of NET formation

In order to pinpoint the stages of NET formation that are suitable for quantification using an automated algorithm, we first analyzed manually a set microscopic images of a neutrophil-*E. coli* co-culture.

3.1.1 Stages of NET formation identified with high-resolution time-lapse microscopy can be observed in low-resolution fluorescent microscopy

Most of the cells in the images taken at t=0 min exhibited a typical appearance of unstimulated, polymorphonuclear neutrophils, without detectable signal in the extracellular channel (Figure 3A). In images taken between t=60 and t=120 min, we have observed cells which were visibly brighter and highly circular (Figure 3B). This morphology most likely corresponded to cells with a rounded nucleus. Individual cells exhibited this morphology in t=0 min as well. We have also observed ROIs with larger areas, lower brightness, and cloud-like appearance, with no signal in the

extracellular channel (Figure 3C). We assume that this morphology corresponded to cells with a ruptured nuclear envelope. We did not observe such cells in t=0 min. In images taken after t=60 min, and mostly in the later stages of the experiment, we have observed cells with cloudy appearance and detectable signal in the extracellular channel (Figure 3D). This morphology corresponded to cells with a permeabilized plasma membrane. The intensity of signal in the extracellular channel varied highly for those cells, indicating a gradual permeabilization, in agreement with (8). Throughout the experiment, we have also observed ROIs with significantly larger areas than individual cells, with intense signal in the extracellular channel and detectable signal in the total DNA channel (Figure 3E). This morphology corresponded to NETs.

3.1.2 Not all stages of NET formation are suitable for an automatic quantification

Unstimulated neutrophils, cells with rounded nuclei, cells with ruptured nuclear envelopes and cells with permeabilized plasma membranes have distinct morphologies in fluorescent microscopy images, making them suitable for automatic detection by a software tool. On the other hand, neutrophils inbetween those stages, in particular neutrophils undergoing chromatin decondensation and nuclear rounding, are more difficult to classify. The stage of chromatin decondensation (between the onset of NET formation and nuclear rounding) does not seem to have a clear delineation from its surrounding stages with simple qualitative features. As such, this stage does not seem to be a good candidate for a separate class in an automatic classification scheme, at least in fluorescent microscopy images of double-stained DNA. Accordingly, we have decided against distinguishing cells with decondensed chromatin as a separate class of objects. As a consequence, such ROIs were automatically classified as either unstimulated cells or cells with rounded nuclei, depending on the advancement of the NET formation process.

3.1.3 Clumps of bacteria are an important class of ROIs in neutrophil killing assays

Starting from t=120 min, we observed clumps of bacteria, both in the total DNA channel and in the visible light (Figure 4). In fluorescent light, they appeared as highly amorphous, low-brightness objects without well-defined edges. With the exponential growth of bacteria, those clumps become prevalent in t = 180 min, motivating the decision to include them as yet another class of ROIs.

3.1.4 Handling artifacts in the extracellular channel can further improve the precision of NET area quantification

At the boundaries of NETs, where the chromatin density is low, the fluorescent signal tends to be low as well, making the

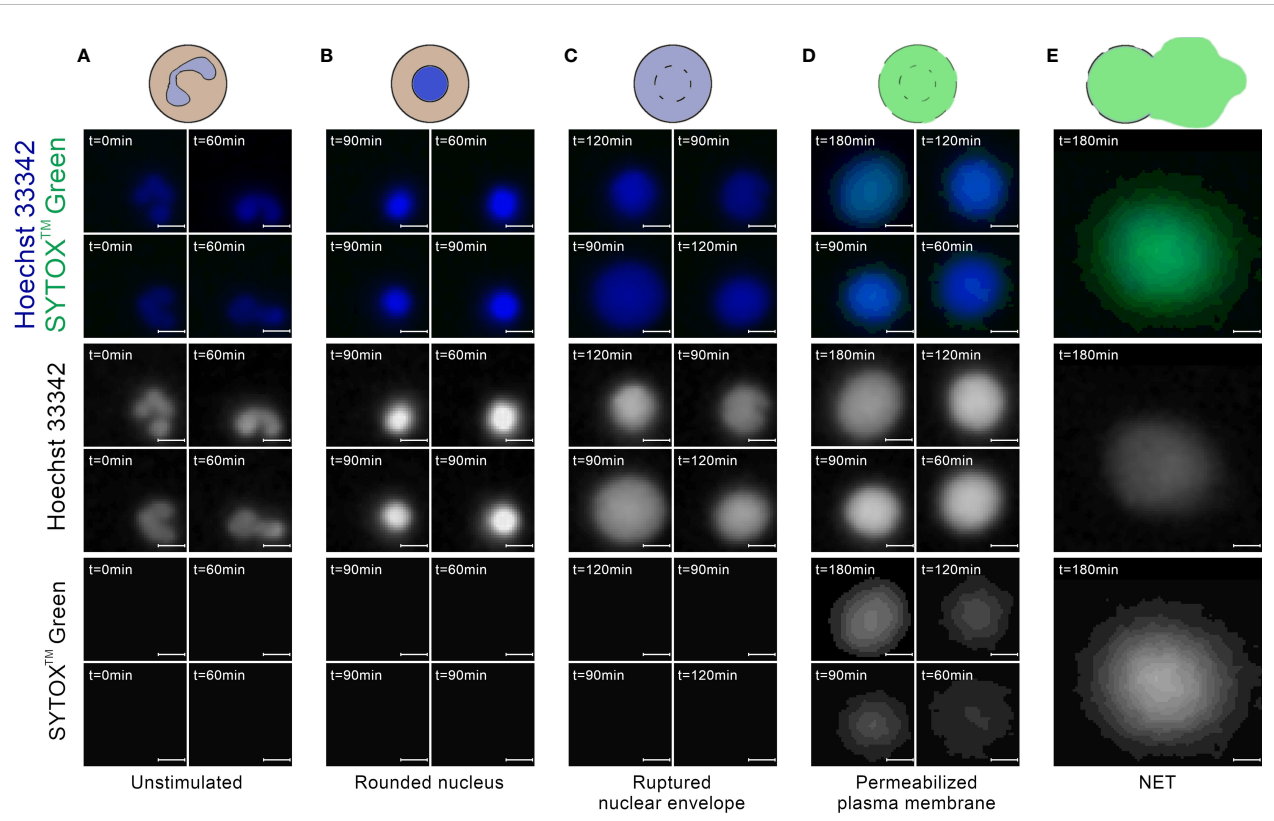

FIGURE 3
Neutrophils at different stages of NET formation visible in fluorescent microscopy with SYTOX™ Green/Hoechst 33342 double staining. The source images were taken as a part of the neutrophil *E coli* co-culture study. **(A)** Polymorphonuclear (unstimulated) neutrophils; **(B)** Neutrophils with rounded nucleus; **(C)** Neutrophils with ruptured nuclear envelope; **(D)** Neutrophils with permeabilized plasma membrane; **(E)** An example of a neutrophil extracellular trap. Scale bar = 10μm, microscope magnification 100x.

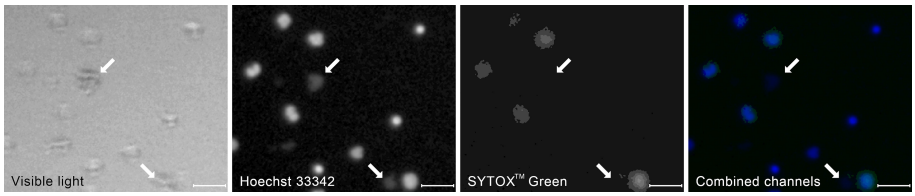

FIGURE 4
A typical appearance of a clumps of bacterial cells (arrows) in the visible and the fluorescent light compared to the appearance of neutrophil cells at different stages of NET formation. The contrast of the fluorescent images has been enhanced to better visualize the bacteria. The image was taken as a part of the neutrophil-E. coli co-culture study at t=90 min with multiplicity of infection equal 4. Scale bar = 50 µm, magnification 100x. Combined channels: Hoechst 33342 in blue, SYTOX™ Green in green as in Figure 3.

classification difficult even for human experts (10). Although the low-intensity regions of NETs can be highlighted by increasing the brightness and contrast of the image in the pre-processing stage, the brightness of some regions of NETs can be roughly similar to the background level. On the other hand, the background brightness level itself can be slightly uneven due to e.g. varying plastic density, plastic autofluorescence, or proximity to the edge of the well. As a consequence, increasing the image brightness can result in the appearance of artifacts that can be mistaken for NETs by automatic classifiers (Figure 5). When we increased the brightness to capture all the detectable NET regions, we have observed such artifacts in approximately 15% of our images. Therefore, if NETs are to be labeled precisely and reliably in a pixel-wise manner, a NET quantification algorithm should be able to detect and signal potential artifacts in the extracellular channel. On the other hand, if the precise determination of NET boundaries is not needed, the image brightness can simply be adjusted so that artifacts do not jeopardize the analysis. In this case, detection of artifacts may be unnecessary and, accordingly, Trapalyzer allows the user to disable this feature.

Additionally, we have observed individual artifacts in the green channel (with no detectble signal in the Hoechst 33342 channel) with the size of one to a few neutrophil cells. These artifacts may have been caused by out-of-focus cells with permeabilized plasma membrane or a slight contamination with pollen grains. However, since such objects jointly constituted less than 0.1% of ROIs in all images, they did not pose a risk of biasing the results of automatic classification and could be safely ignored.

3.2 ROI features at different stages

Based on the results presented in (8) and our analysis of fluorescent microscopy images, we consider seven classes of ROIs: unstimulated neutrophils; cells with decondensed chromatin and rounded nuclei; cells with ruptured nuclear envelopes; cells with permeabilized plasma membranes; neutrophil extracellular traps; clumps of bacteria; and artifacts in the extracellular channel. After fixing the set of ROIs that could potentially be quantified in fluorescent microscopy images of double-stained DNA, we looked for a minimal set of features that could be used to distinguish them.

3.2.1 Stages of NET formation have characteristic values of three ROI features

Polymorphonuclear neutrophils could be distinguished from other classes by a relatively small size and average brightness on the total DNA channel and the lack of signal inthe extracellular DNA channel. Neutrophils with rounded nuclei could be distinguished

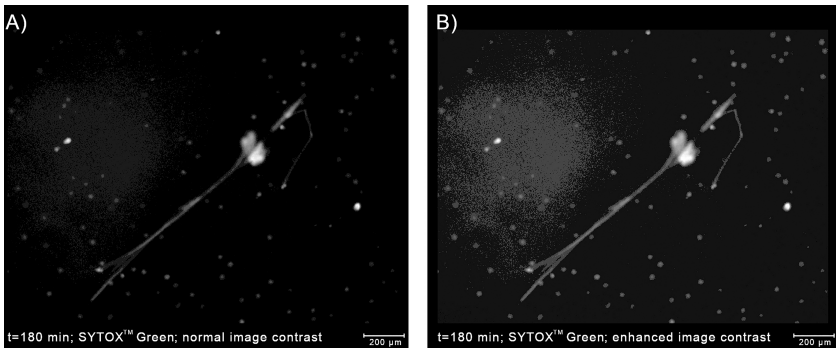

FIGURE 5
Detecting artifacts in the extracellular channel can improve the accuracy of the determination of the boundaries of NETs. **(A)** An example of a NET with low-brightness regions caused by low chromatin density. Using only the high-brightness regions would underestimate the area occupied by the NET. **(B)** Enhancing the image contrast highlights the NET boundaries, but also reveals a slightly uneven background brightness. Without a proper implementation in the classification algorithm, background regions with a higher brightness can be a source of errors. The image was taken as a part of the neutrophil-*E. coli* co-culture study at t=180 min with multiplicity of infection equal 1.

from other ROIs by particularly high values of average brightness in the total DNA channel. Neutrophils with ruptured nuclear envelopes typically had larger areas than both previous classes. In some cases, they had similar areas to neutrophils with rounded nuclei, but could be distinguished from this class by lower average brightness. Neutrophils with permeabilized plasma membrane covered the same range of areas and brightness in the total DNA channel as the three previous classes. However, they could be easily distinguished from other cells as the only ones with detectable signal in the extracellular DNA channel.

3.2.2 Standard deviation of extracellular signal separates artifacts in the extracellular channel from NETs

Large areas and intense signal in the extracellular DNA channel distinguished NETs from cells, but not from artifacts in the extracellular channel caused e.g. by uneven background brightness. However, due to differences in chromatin density, the brightness of NETs was spatially non-homogeneous, while for the artifacts it was mostly uniform, especially after applying a median filter. This was effectively captured by setting a threshold for the standard deviation of brightness of NETs in the extracellular DNA channel. Notably, with this approach, any ROI that does not conform to the characterization of a NET is classified as an artifact, regardless of its physical origin.

We did not observe an increase in classification accuracy when we additionally included an upper threshold for ROI circularity of NETs, as proposed by other authors (14). On the contrary, NETs can be highly circular in shape (Figure 3), especially when formed in the absence of bacteria (12).

3.2.3 Laplacian of Gaussian values characterize clumps of bacteria

The most defining feature of bacterial clumps was the low, highly non-homogeneous signal in the total DNA channel. However, the standard deviation of brightness failed to distinguish them from other classes of ROIs. Another characteristic feature was the lack of well-defined borders, which was effectively captured by small values of the average Laplacian of Gaussian (LoG) of the total DNA channel.

Five features distinguish eight classes of ROIs. The progression of NET formation, the observed morphologies of different stages in fluorescent microscopy images, and the mathematical features that characterize them motivate the classification of ROIs into the following classes:

- *PMN neutrophils*, polymorphonuclear, unstimulated neutrophils, with a moderate cell size and brightness, and a lack of signal on the extracellular DNA channel;
- *RND neutrophils*, cells with decondensed chromatin and rounded nucleus, with higher brightness than PMN neutrophils;
- *RUP neutrophils*, neutrophils with ruptured nuclear envelope, with larger cell sizes than RND neutrophils and possibly lower brightness than PMN neutrophils;
- *PER neutrophils*, neutrophils with a permeabilized plasma membrane, with detectable signal on the extracellular DNA channel;
- *NETs*, Neutrophil Extracellular Traps, with an intense signal on the extracellular DNA channel, low to no signal on the total DNA channel, and noticeable standard deviation of the brightness;
- *Groups of bacteria*, with low brightness and LoG values in the total DNA channel, and possibly moderate signal on the extracellular DNA channel due to possible co-localization with NET fragments;
- *Artifacts in the extracellular channel*, With a moderate, mostly homogeneous signal in the green channel;
- *Unclassified ROIs*, on the intracellular channel, not matching any of the previous classes. This class includes any potential artifacts in the intracellular channel.

Note that the set of features is smaller than the set of classes thanks to a combinatorial approach to class characterization.

3.3 Classification workflow

The processing of a single fluorescent image with two channels (an extracellular DNA channel and a total DNA channel) is represented schematically in Figure 6. In the pre-processing stage, the user may decide to use one of a number of filters provided by PartSeg (including the Gaussian and the median filter) on any or both channels. In the subsequent ROI detection stage, segmentation is performed on both channels by simple thresholding and detecting connected components. The brightness thresholds for both channels can be adjusted by the user during an interactive session of PartSeg to obtain a segmentation that matches a manual annotation.

In the first classification stage, Trapalyzer classifies ROIs on the extracellular DNA channel. Small ROIs on the extracellular channel, which typically correspond to neutrophils with a permeabilized plasma membrane, are not processed at this stage. If an ROI has a sufficient size and its average brightness and standard deviation are within user-defined ranges, it is classified as a NET. Otherwise, it is flagged as an "extracellular unknown" class, corresponding e.g. to artifacts caused by autofluorescence, uneven brightness, or atypical NETs that require manual inspection.

In the second classification stage, Trapalyzer classifies ROIs in the total DNA channel. For each class, Trapalyzer computes a score that measures whether a given ROI matches its user-defined characterization. The general idea behind the class score is to ensure that all of the ROI features are within appropriate ranges for this class, with an error margin that allows some flexibility when defining the ranges.

Formally, let x are the value of a particular feature (e.g. brightness) of a given ROI, and let $[l,u]$ are the acceptable interval for this feature for a given class of ROIs (e.g. RUP neutrophils). For a single feature, we define a partial score function $S(x;l,u,s)$ where the s parameter controls the extent of the error margins. The idea behind the partial score function is that $S(x;l,u,s)$ equals 1 if $x \in [l,u]$

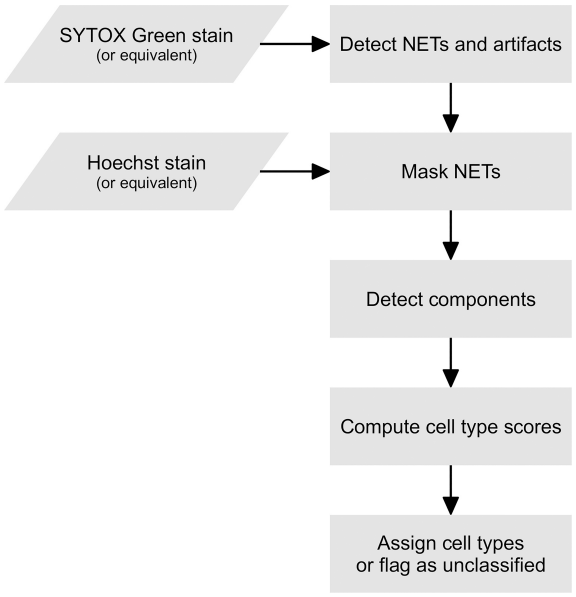

FIGURE 6
A flowchart of Trapalyzer.

and falls smoothly to 0 is x becomes distant from the interval $[l,u]$ with the decrease rate controlled by s. Formally, we want S to be equal to 0 either when $x \leq l - sl\frac{u-l}{u+l} = l - \Delta_l(s)$ or $x \geq u + su\frac{u-l}{u+l} = u + \Delta_u(s)$. This way, the left and right error margins for the characteristic range, $\Delta_l(s)$ and $\Delta_u(s)$, adjust to the interval length and its boundary values. Because of this, a single value of the error margin parameter s can be set for all features regardless of their units and typical values.

The properties described above are satisfied by the following function, where $l_0 = l - \Delta_l$ and $u_0 = u + \Delta_u$ define the range in which we want S to have a non-zero value:

$$S(x;\ l,u,s) = \begin{cases} 1 & \text{if} \quad x \in [l,u] \\ \frac{1}{2} + \frac{1}{2}\sin\left(\pi\frac{x-l+\Delta_l}{\Delta_l} - \frac{\pi}{2}\right) & \text{if} \quad x \in [l_0,l] \\ \frac{1}{2} + \frac{1}{2}\sin\left(\pi\frac{x-u+\Delta_u}{\Delta_u} - \frac{\pi}{2}\right) & \text{if} \quad x \in [u,u_0] \\ 0 & \text{otherwise} \end{cases}$$

To obtain a final score for a given class, we multiply the partial scores for all the features of the analyzed ROI. This ensures that an ROI fully matches a class when all the features are within or sufficiently close to their acceptable ranges.

An ROI is determined as belonging to a given class if the score for this class is sufficiently high (by default above 0.8), and the scores for all the other classes are sufficiently low (by default below 0.4). The upper threshold for the scores of "competing" classes ensures that an ROI is classified unambiguously. If an ROI does not reach a sufficiently high score for any class, or reaches a high score for more than one class, it is flagged as an unknown class that requires a manual inspection.

During the second classification stage, we mask the regions occupied by NETs and artifacts in the extracellular channel and ignore ROIs in those regions. This is because, if a neutrophil lies within such a region, it is either difficult or impossible to accurately distinguish whether or not it has a permeabilized plasma membrane, and classification would therefore be unreliable. On the other hand, the number of such ROIs is typically small compared to the overall number of ROIs, and ignoring them had a relatively small influence on the overall performance of the software.

After both classification stages are completed, Trapalyzer evaluates the quality of image annotation. We define the quality score as $Q = 100 \cdot (1 - U/S)\,\%$, where U denotes the area covered by unclassified ROIs and S denotes the area covered by all detected ROIs. We use the areas of ROIs instead of their numbers to make the score robust to small artifacts that otherwise do not interfere with the analysis.

3.4 Validation on a benchmark data set

In order to assess Trapalyzer's accuracy, we have compared it to previously reported results achieved with convolutional neural networks (CNNs) on a publicly available benchmark data set (12). To match the original study, we have restricted the classification to four classes: PMN, RUP and PER neutrophils and NETs (the RUP neutrophils were referred to as *decondensed* in the original work).

First, we tuned the parameters on 10 images selected from a training data set. Then, we used Trapalyzer's batch processing mode to analyze a full validation data set of 57 images containing 1083 manually annotated objects. We compared the resulting annotation with the manual one provided with the data set. We used an Intersection over Union (IoU) threshold of 0.10, meaning that we match objects if the overlap of their bounding boxes is at least 10% of their joint area. The IoU value was based on previous results in NET quantification (10, 12). In case of more than two ROIs with overlapping bounding boxes, the pair with the highest IoU was selected as a match.

3.4.1 Consistent image acquisition conditions are crucial for automated image analysis

The results of Trapalyzer annotation are shown in Table 1, and an example annotation is shown in Figure 7A. On average, 11.90% of ROIs were unclassified in each image, with two images exceeding 50% due to atypically low brightness of cells, likely caused by a low exposure time.

3.4.2 Simple classification workflow achieves precision on par with convolutional neural networks

Over all ROI classes, Trapalyzer achieved an average precision of 95%, higher than 91% reported for the CNN classifier trained on 188 images. Precision varied slightly between classes, with the highest equal 100% for RUP neutrophils, and the lowest equal 89% for PER neutrophils, caused by annotating some NETs as neutrophils with permeabilized plasma membrane. Separating NETs from PER neutrophils is difficult due to the gradual nature

TABLE 1 The results of an analysis of a publicly available benchmark data set of 57 fluorescent microscopic images.

		Ground truth (manual annotation)						
		NET	PMN neu	RUP neu	PER neu	Unmatched	Total predicted	Precision
Trapalyzer	NET	**223**	1	0	5	2	231	0.97
	PMN neu	0	**365**	3	0	14	382	0.96
	RUP neu	0	0	**34**	0	0	34	1.00
	PER neu	16	0	4	**200**	5	225	0.89
	Unknown	1	31	37	4	59	132	N/A
	Unmatched	66	2	0	11	0	79	N/A
	True total	306	399	78	220	80		Avg=0.95
	Recall	0.73	0.91	0.44	0.91	N/A	Avg=0.75	

N/A, Not Applicable.
Shaded values: NETs and neutrophil cells. Values in bold: correctly classified ROIs.

of chromatin release into the extracellular environment, so mismatches between the manual and automatic annotation are to be expected.

3.4.3 Trapalyzer avoids uncertain classifications

We have achieved an average recall of 75%, lower than 93% reported for the CNN. However, the recall varied greatly between classes, from 44% for RUP neutrophils up to 91% for PMN and PER neutrophils. Approximately half of the RUP neutrophils were flagged as an unknown ROI class, suggesting imperfect parameter estimation from the training data set. This stands in agreement with a philosophy that when parameters are misspecified, it is safer to avoid classifying ROIs than to classify them wrong. Note that, in practice, it is always possible to fine-tune the parameters on additional images to increase the recall.

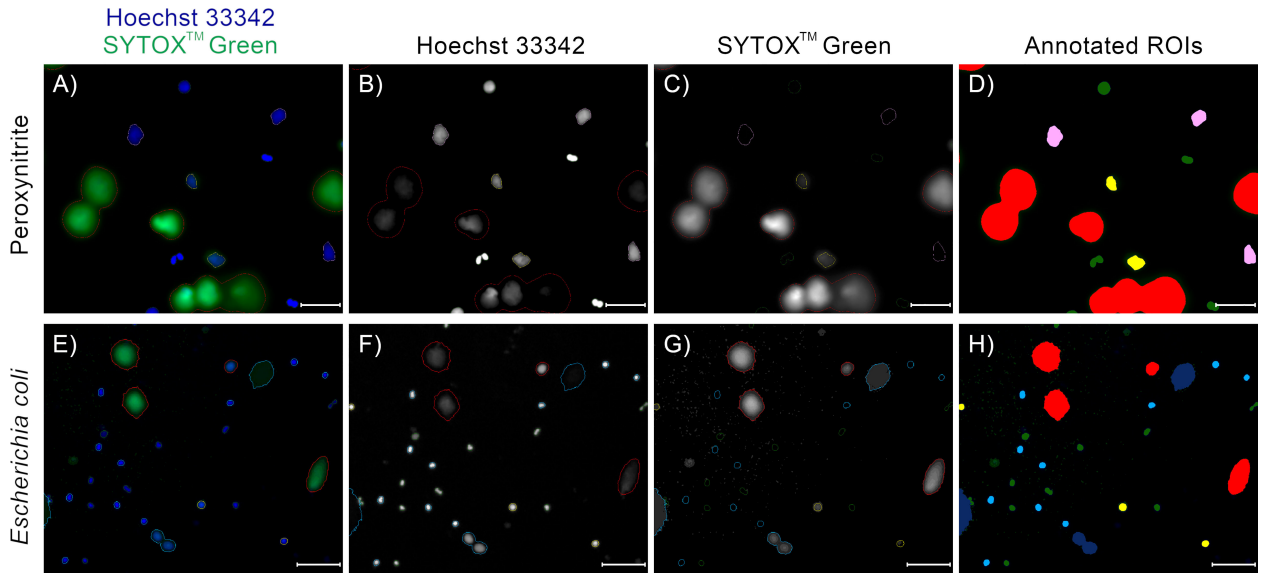

FIGURE 7
Examples of annotations of fluorescent microscopy images of NETs and neutrophils double-stained with Hoechst 33342 and SYTOX™ Green, with neutrophils acquired from different patients, NET formation induced with different stimuli, and different microscope magnifications. **(D, H)** Trapalyzer identified the following classes of objects: Red: Neutrophil Extracellular Traps; Green: PMN (polymorphonuclear) neutrophils; Light blue: RND (rounded nuclei) neutrophils; Pink: RUP (ruptured nuclear envelope) neutrophils; Yellow: PER (permeabilized plasma membrane) neutrophils; Dark blue: artifacts in the extracellular channel. **(A–D)** A fragment of an image from the benchmark data set (12). NET formation was triggered with 100 μM peroxynitrite. Scale bar = 75μm, magnification 400x. **(E–H)** A fragment of an image taken as a part of the neutrophil-*E. coli* co-culture study at t=120 min with multiplicity of infection equal 1. Scale bar = 125μm magnification 100x. In this example, two closely located emerging NETs in the bottom part of the image were flagged as a potential artifact for manual inspection due to low standard deviation of brightness in the extracellular channel. Lowering the standard deviation threshold results in their proper classification as NETs.

3.4.4 Quantifying NET area is more reliable than NET count

The recall value for neutrophil extracellular traps was 73%, caused by difficulties with matching Trapalyzer and manual annotations. Inspecting selected images showed that Trapalyzer missed fragments of NETs with a low brightness (on the verge of the background signal), causing low IoU values due to large differences between detected and manually generated bounding boxes. Moreover, NETs tend to merge if released by closely located cells and, although a human expert can detect such cases and identify individual nets, our approach to segmentation treats them as a single object. This agrees with observations made by other authors that the numbers and areas of individual NETs are difficult to quantify algorithmically, and quantifying the total image area covered by NETs is more reliable (10).

3.5 A detailed analysis of a neutrophil-E. coli co-culture

As an example application of Trapalyzer, we have performed a detailed analysis of the 120 fluorescent microscopy images of neutrophils incubated with or without *E. coli* bacteria, which we used to establish quantifiable classes of ROIs in the previous subsections. We have tuned the software's parameters on a set of selected 10 images and further adjusted them on images with large numbers of unclassified ROIs. The correctness of annotation was then validated by an expert on 5 images. An example annotation of a fragment of an image is shown in Figure 7. In total, Trapalyzer detected and annotated 16924 ROIs, including 10905 polymorphonuclear neutrophils, 733 neutrophils with a rounded nucleus, 266 neutrophils with a ruptured nuclear envelope, 2742 neutrophils with a permeabilized plasma membrane, 344 NETs, 698 clumps of bacteria, 265 artifacts on the SYTOX™ Green extracellular channel, and 971 unclassified components in the Hoechst 33342 total DNA channel.

3.5.1 Population-level results support the current model of NET formation

The total number of cells detected by Trapalyzer stayed approximately constant over the duration of the experiment (Supplementary Figure S2), in agreement with the fact that only a few cells release NETs, showing that the experimental conditions and image acquisition methods were consistent. We observed a gradual decrease of the number of PMN neutrophils over time and the transition to RND, RUP, and PER cell morphology types (Supplementary Figure S1), in agreement with the observations made for individual cells in (8). NETs were formed continuously throughout the experiment and their number seemed to grow linearly in all experimental conditions, including the control group without bacteria (Supplementary Figure S2). However, the rate of NET formation is higher in the co-cultures than in the control, indicating that the presence of bacteria successfully induced NET formation.

3.5.2 ROI-level results suggest an additional stage of NET formation

The properties of ROIs classified as neutrophils at different stages of NET formation are shown in Figure 8. Different classes were clearly separated by the ROI features used in our classification workflow, which confirms their distinct natures. We observed a gradual increase in cell size as NET formation progressed. The average brightness was the highest for RND neutrophils, likely due to chromatin decondensation and increased dye affinity, and decreased after the rupture of the nuclear envelopewhen the chromatin occupied a larger area. A visibly bi-modal distribution of the brightness of RND neutrophils suggests that there may be an additional stage NET formation, which causes this group to be composed of two different types of cell morphologies. This phenomenon requires further studies.

3.5.3 Mathematical modeling of the dynamics of a neutrophil population poses additional challenges

Neutrophils stayed viable for a prolonged period of time in the negative control without bacteria. From the perspective of mathematical modeling, this means that traditional models based on ordinary differential equations may not be suitable to describe an *in vitro* cultured population of neutrophils. More sophisticated mathematical techniques,such as delay differential equations, may be required to model the dynamics of NET formation in such experiments.

3.5.4 A small number of false positives did not influence the overall conclusions

The number of bacterial groups grew exponentially in time when bacteria were present in the sample (Supplementary Figure S2). This suggests that, in our experimental conditions, neutrophils had a limited capability to eliminate pathogens. We have observed a small number of false positive results in the control group without bacteria. In 8 out of 40 images for this experimental condition there were between one and three improperly detected clumps of bacteria, corresponding to image artifacts and misclassified neutrophil cells. In comparison, in the experimental condition with four bacterial cells per neutrophil, there were up to 100 bacterial groups for t=180 min. As a consequence, the number of false positive detections of bacterial clumps was comparatively small and did not influence the overall conclusions.

4 Discussion

Software tools designed for the analysis of microscopic images of neutrophils and neutrophil extrcellular traps (NETs) can be roughly partitioned into two groups. The first group consists of tools based on machine learning, such as convolutional neural networks (CNNs) or support vector machines (SVMs). The second group consists of tools based on classical image processing techniques, such as edge detection, image filtering etc.

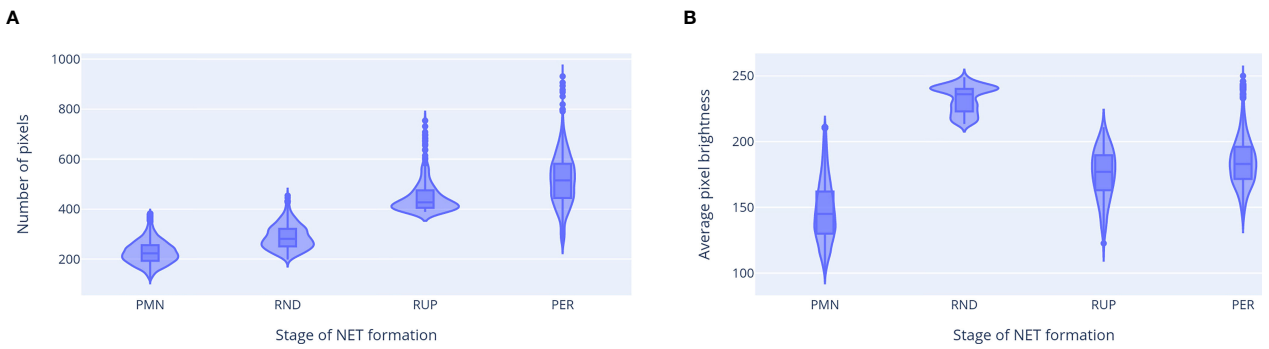

FIGURE 8
Properties of ROIs classified as neutrophils at different stages of NET formation. **(A)** ROI area (in number of pixels). **(B)** Average pixel brightness in the total DNA channel. The third feature, average brightness on the extracellular channel, had a non-zero value only for the neutrophils with permeabilized plasma membrane. Abbreviations of NET formation stages: PMN, polymorphonuclear; RND, rounded nuclei; RUP, ruptured nuclear envelope; PER, permeabilized plasma membrane.

Trapalyzer employs the latter approach. It detects ROIs using a thresholding operation and classifies them as NETs, neutrophils at different stages of NET formation, or clumps of bacteria based on a handful of features such as ROI area and average brightness. An ROI is assigned to a class if it matches it unambiguously according to a scoring function.

Our reasons to make Trapalyzer machine learning-free are twofold. First, machine learning algorithms require extensive training data sets on which they learn how to distinguish between different types of objects. Preparing such a data set can take many days for a trained expert. The algorithm is then capable of classifying objects in new images only as long as their morphology closely resembles the objects encountered in the training data set. This is particularly limiting in case of NETs, because their morphologies may differ depending on the experimental conditions, such as the substance used to stimulate neutrophils to release the traps (7). Even minor changes in experimental conditions, such as microscope magnification or exposure time, may require a retraining of the algorithm by a machine learning expert. This negates one of the purposes of such tools, which is to make analyses easier, faster, and less laborsome.

Despite the varying morphology, NETs retain certain characteristic features - large size, signal in the extracellular channel - that can be used to detect and quantify them. Identifying such features and using them in Trapalyzer makes the software more robust to small variations in morphology and more general in terms of applications to different experiments. A change in microscope magnification or exposure time requires only a simple change of a few parameters instead of retraining of the whole algorithm. On the other hand, since the parameter values depend on the equipment used in a particular laboratory, we do not include a default set of parameters in Trapalyzer. Instead, we provide an easy to follow tutorial with a step-by-step procedure of tuning them, available on the project's website.

The second reason to avoid the use of machine learning algorithms is that they typically operate on a black-box basis, meaning that the way they arrive at their classification is unknown and often too complex to be understood by humans (21). As a consequence, if a neural network misclassifies a given type of ROIs in a given experiment, it is either difficult or impossible to identify why this happens and how to fix it. On the other hand, digital image processing techniques and simplified algorithms used in Trapalyzer provide control over the classification process without sacrificing the precision of the results. The user may freely decide which cell types are of interest in a given experiment and which features to use for classification. If an ROIs is misclassified by Trapalyzer, it is easy to check which parameter of the software has an improper value and adjust it.

In this work, we detect and classify polymorphonuclear neutrophils solely based on their size and average brightness. Due to their characteristic shapes, some measure of ROI circularity could potentially also be a characteristic feature of this morphology. Two common measures of this feature are the ratio of the ROI area to squared perimeter and the ratio of the ROI area to squared diameter. However, none of those measures was capable of distinguishing polymorphonuclear neutrophils from other stages of NET formation and improve the accuracy of classification. This is because some segments corresponding to those cells are elongated but otherwise highly regular, and both circularity measures are high in such cases. We did not find any mathematical characterization of the irregular shape of polymorphonuclear neutrophils that would be useful for our purposes.

Trapalyzer is designed for studies based on double staining of neutrophils with DNA-binding dyes and live imaging of unfixed samples. Despite the characteristic morphology of NETs in such images, their identification based solely on DNA staining may not always be sufficient. This technique is complementary to, but not a substitute of, immunohistological staining which confirms the presence of characteristic proteins ornamenting DNA threads, such as neutrophil elastase, histones, or myeloperoxidase. Immunofluorescent labeling is especially important when novel or uncommon inducers of NET release are studied (12, 13). Nevertheless, once the formation of NETs is confirmed by immunostaining, double-staining of the DNA provides a robust and easy way to quantify the phenomenon of NET release.

To our knowledge, Trapalyzer is the only currently available computer program capable of quantifying not only NETs in terms of their number and area, but also the numbers of neutrophils at different stages of NET formation, in experiments where extensive training data sets are not available. Currently, Trapalyzer can only be

applied to cultures of isolated neutrophils. Extending the software capabilities to handle co-incubation of neutrophils with other types of cells, e.g. cancer cells, is a potential direction of future developments.

Data availability statement

The raw data supporting the conclusions of this article will be made available by the authors, without undue reservation.

Ethics statement

Ethical review and approval was not required for the study on human participants in accordance with the local legislation and institutional requirements. Written informed consent for participation was not required for this study in accordance with the national legislation and the institutional requirements.

Author contributions

MC and AG conceived the study. MC, GB and AM-H designed the software. GB implemented the software. MC and AM-H designed the co-culture experiment. AM-H and WK performed the experiment. MC analyzed the experimental data and wrote the draft manuscript. AG and UD supervised the work. All authors have read and approved the manuscript.

Funding

This work has been supported by the bilateral grant of the Medical University of Warsaw and the University of Warsaw, grant number 1WW/NUW1/18.

Conflict of interest

The authors declare that the research was conducted in the absence of any commercial or financial relationships that could be construed as a potential conflict of interest.

Publisher's note

Supplementary material

The Supplementary Material for this article can be found online at: https://www.frontiersin.org/articles/10.3389/fimmu.2023.1021638/full#supplementary-material

References

1. Pruchniak MP, Arazna M, Demkow U. Life of neutrophil: from stem cell to neutrophil extracellular trap. *Respir Physiol Neurobiol* (2013) 187:68–73. doi: 10.1016/j.resp.2013.02.023

2. Hidalgo A, Chilvers ER, Summers C, Koenderman L. The neutrophil life cycle. *Trends Immunol* (2019) 40:584–97. doi: 10.1016/j.it.2019.04.013

3. Brinkmann V, Reichard U, Goosmann C, Fauler B, Uhlemann Y, Weiss DS, et al. Neutrophil extracellular traps kill bacteria. *Science* (2004) 303:1532–5. doi: 10.1126/science.1092385

4. Azzouz L, Cherry A, Riedl M, Khan M, Pluthero FG, Kahr WH, et al. Relative antibacterial functions of complement and nets: nets trap and complement effectively kills bacteria. *Mol Immunol* (2018) 97:71–81. doi: 10.1016/j.molimm.2018.02.019

5. Jorch SK, Kubes P. An emerging role for neutrophil extracellular traps in noninfectious disease. *Nat Med* (2017) 23:279–87. doi: 10.1038/nm.4294

6. Brinkmann V, Zychlinsky A. Neutrophil extracellular traps: is immunity the second function of chromatin? *J Cell Biol* (2012) 198:773–83. doi: 10.1083/jcb.201203170

7. Boeltz S, Amini P, Anders HJ, Andrade F, Bilyy R, Chatfield S, et al. To net or not to net: current opinions and state of the science regarding the formation of neutrophil extracellular traps. *Cell Death Differentiation* (2019) 26:395–408. doi: 10.1038/s41418-018-0261-x

8. Thiam HR, Wong SL, Qiu R, Kittisopikul M, Vahabikashi A, Goldman AE, et al. Netosis proceeds by cytoskeleton and endomembrane disassembly and pad4-mediated chromatin decondensation and nuclear envelope rupture. *Proc Natl Acad Sci* (2020) 117:7326–37. doi: 10.1073/pnas.1909546117

9. van Breda SV, Vokalova L, Neugebauer C, Rossi SW, Hahn S, Hasler P. Computational methodologies for the in vitro and *in situ* quantification of neutrophil extracellular traps. *Front Immunol* (2019) 1562. doi: 10.3389/fimmu.2019.01562

10. Coelho LP, Pato C, Friaes A, Neumann A, von Köckritz-Blickwede M, Ramirez M, et al. Automatic determination of net (neutrophil extracellular traps) coverage in fluorescent microscopy images. *Bioinformatics* (2015) 10:2364–70. doi: 10.1093/bioinformatics/btv156

11. Elsherif L, Sciaky N, Metts CA, Modasshir M, Rekleitis I, Burris CA, et al. Machine learning to quantitate neutrophil netosis. *Sci Rep* (2019) 31:1–12. doi: 10.1038/s41598-019-53202-5

12. Manda-Handzlik A, Fiok K, Cieloch A, Heropolitanska-Pliszka E, Demkow U. Convolutional neural networks–based image analysis for the detection and quantification of neutrophil extracellular traps. *Cells* (2020) 9:508. doi: 10.3390/cells9020508

13. Rebernick R, Fahmy L, Glover C, Bawadekar M, Shim D, Holmes CL, et al. Dna area and netosis analysis (dana): a high-throughput method to quantify neutrophil extracellular traps in fluorescent microscope images. *Biol Procedures Online* (2018) 20:1–9. doi: 10.1186/s12575-018-0072-y

14. Mohanty T, Sørensen OE, Nordenfelt P. Netquant: automated quantification of neutrophil extracellular traps. *Front Immunol* (2018) 8:1999. doi: 10.3389/fimmu.2017.01999

15. Brinkmann V, Goosmann C, Kühn LI, Zychlinsky A. Automatic quantification of in vitro net formation. *Front Immunol* (2013) 3:413. doi: 10.3389/fimmu.2012.00413

16. de Buhr N, von Köckritz-Blickwede M. How neutrophil extracellular traps become visible. *J Immunol Res* (2016). doi: 10.1155/2016/4604713

17. Lelliott PM, Momota M, Lee MS, Kuroda E, Iijima N, Ishii KJ, et al. Rapid quantification of nets in vitro and in whole blood samples by imaging flow cytometry. *Cytometry Part A* (2019) 95:565–78. doi: 10.1002/cyto.a.23767

18. Billinton N, Knight AW. Seeing the wood through the trees: a review of techniques for distinguishing green fluorescent protein from endogenous autofluorescence. *Analytical Biochem* (2001) 291:175–97. doi: 10.1006/abio.2000.5006

19. Bokota G, Sroka J, Basu S, Das N, Trzaskoma P, Yushkevich Y, et al. Partseg: a tool for quantitative feature extraction from 3d microscopy images for dummies. *BMC Bioinf* (2021) 41:1–15. doi: 10.1186/s12859-021-03984-1

20. Bystrzycka W, Moskalik A, Sieczkowska S, Manda-Handzlik A, Demkow U, Ciepiela O. The effect of clindamycin and amoxicillin on neutrophil extracellular trap (net) release. *Central-European J Immunol* (2016) 14:1–5. doi: 10.5114/ceji.2016.58811

21. Rudin C, Radin J. *Why are we using black box models in AI when we don't need to? a lesson from an explainable AI competition*. Harvard Data Science Review (2019). doi: 10.1162/99608f92.5a8a3a3d

frontiers | Frontiers in Medicine

TYPE Methods
PUBLISHED 17 January 2024
DOI 10.3389/fmed.2023.1274482

OPEN ACCESS

EDITED BY
Quan Nguyen,
The University of Queensland, Australia

REVIEWED BY
Fabrizio Martelli,
National Institute of Health (ISS), Italy
Cedric Clouchoux,
WITSEE, France

*CORRESPONDENCE
Uwe Ritter
✉ uwe.ritter@ukr.de

†These authors have contributed equally to this work and share first authorship

RECEIVED 08 August 2023
ACCEPTED 24 November 2023
PUBLISHED 17 January 2024

CITATION
Stüve P, Nerb B, Harrer S, Wuttke M, Feuerer M, Junger H, Eggenhofer E, Lungu B, Laslau S and Ritter U (2024) Analysis of organoid and immune cell co-cultures by machine learning-empowered image cytometry.
Front. Med. 10:1274482.
doi: 10.3389/fmed.2023.1274482

Analysis of organoid and immune cell co-cultures by machine learning-empowered image cytometry

Philipp Stüve[1†], Benedikt Nerb[1,2†], Selina Harrer[1], Marina Wuttke[1], Markus Feuerer[1,2], Henrik Junger[3], Elke Eggenhofer[3], Bianca Lungu[4], Simina Laslau[4] and Uwe Ritter[1,2*]

[1]Division of Immunology, LIT – Leibniz Institute for Immunotherapy, Regensburg, Germany, [2]Chair for Immunology, University of Regensburg, Regensburg, Germany, [3]Department of Surgery, University Hospital Regensburg, Regensburg, Germany, [4]TissueGnostics SRL, Iași, Romania

Organoids are three-dimensional (3D) structures that can be derived from stem cells or adult tissue progenitor cells and exhibit an extraordinary ability to autonomously organize and resemble the cellular composition and architectural integrity of specific tissue segments. This feature makes them a useful tool for analyzing therapeutical relevant aspects, including organ development, wound healing, immune disorders and drug discovery. Most organoid models do not contain cells that mimic the neighboring tissue's microenvironment, which could potentially hinder deeper mechanistic studies. However, to use organoid models in mechanistic studies, which would enable us to better understand pathophysiological processes, it is necessary to emulate the *in situ* microenvironment. This can be accomplished by incorporating selected cells of interest from neighboring tissues into the organoid culture. Nevertheless, the detection and quantification of organoids in such co-cultures remains a major technical challenge. These imaging analysis approaches would require an accurate separation of organoids from the other cell types in the co-culture. To efficiently detect and analyze 3D organoids in co-cultures, we developed a high-throughput imaging analysis platform. This method integrates automated imaging techniques and advanced image processing tools such as grayscale conversion, contrast enhancement, membrane detection and structure separation. Based on machine learning algorithms, we were able to identify and classify 3D organoids within dense co-cultures of immune cells. This procedure allows a high-throughput analysis of organoid-associated parameters such as quantity, size, and shape. Therefore, the technology has significant potential to advance contextualized research using organoid co-cultures and their potential applications in translational medicine.

KEYWORDS

organoid, lymphocytes, co-culture, imaging, Matrigel®

1 Introduction

Cell-based assays are invaluable tools in clinical research for studying the interactions between immune, stromal, and parenchymal cells *in vitro*. However, most of these *in vitro* models cannot entirely mimic complex *in vivo* processes since 2D cell-monolayer models do not contain a tissue-specific microenvironment (1). During the last decades, stem cell- or adult

tissue progenitor cell-derived organoids have emerged as suitable *in vitro* applications in translational research of human chronic diseases (2, 3). Organoids are self-organized, 3D multicellular tissue cultures, serving as artificial model systems of organs (2, 4–7). They can be generated *in vitro* from almost every murine and human tissue, such as the liver, intestine, and brain (8). Since organoids also resemble many features of native human organs, such as functionality and structure, they are also referred to as "mini-organs" (2).

A requirement for conducting mechanistic studies with organoids is to develop experimental systems that accurately replicate the functional and structural complexity *in vivo*. Various scientific techniques, such as molecular analysis, gene editing, and imaging, can be used to characterize functional organoid models (9). Based on these experimental protocols, organoid technology offers a wide range of immunological applications, varying from basic research, including the analysis of tissue biology, tumor immunology, and host-pathogen interactions, to screening of drugs in regenerative medicine (3).

However, classical organoid cultures lack cells from the adjacent tissue microenvironment, such as immune, parenchymal, and stromal cells, thus potentially limiting mechanistic studies. Therefore, co-culturing organoids with cells from their adjacent tissue is necessary to gain a higher level of physiologically contextualized organoid research (3).

Several experimental *in vitro* systems are currently available to investigate the involvement of immune cells in stem cell development and organoid formation (reviewed in (3)). In the context of tumor research, tumor organoids can be used either for the identification of tumor-reactive T cells (10) or for testing organoid-cytolysis induced by chimeric antigen receptor (CAR)-engineered lymphocytes in combination with immune checkpoint inhibitors (11–13). Other co-culture systems of organoids, which simulate the microenvironment of the intestinal lamina propria, are also used to investigate the crosstalk between intestinal immune cells and epithelial stem cells in the context of tissue development or inflammation (14–18). Most recently, a relevant interaction between T cells and intestinal stem cell development has also been proposed (15, 17, 18).

Organoid co-cultures may also be a promising tool for basic and translational research, as potential communication between organoids and other cell subsets can be investigated. This setup would allow the characterization of immune- or parenchymal-derived factors that are expected to modulate organoid development. To this end, high-throughput brightfield imaging of the entire culture wells can be performed, generating time-lapse and end-point analyses (19). However, the quantification of experimental parameters, such as organoid number, size, and shape, still remains challenging due to the following reasons: Firstly, 3D stereoscopic organoid cultures are embedded in Matrigel® or other appropriate extracellular matrix gels, such as Hydrogel® or Geltrex® (20). Thus, organoids grow at different focus levels and may appear out of focus under fixed focus conditions during microscopy (21). Secondly, due to their heterogeneous differentiation status, the organoids have different shapes and dimensions (21). Thirdly, dense cell clusters of proliferating immune cells are similar to organoids and have the potential to generate interfering imaging signatures, leading to false positive results.

Most of the previously published image-processing algorithms were developed for the analysis of organoid cell cultures in the absence of additional cell subsets (compare Table 1). To date, no high-throughput image analysis workflow is published that are capable of identifying and quantifying organoids within co-cultures. Thus, we developed an organoid detection application (Organoid App), which provides a reliable and effective tool for the high-throughput identification, validation, and quantification of organoids in co-cultures with immune cells. In order to realize this methodological project, we used extrahepatic cholangiocyte organoid (ECO) cultures (6, 26), which served as a model system for studying homeostasis and regeneration as they contain both stem cells and differentiated epithelial cells (27). These ECOs were co-cultured with polarized human effector T cells. For the development of our Organoid App, we used the commercially available StrataQuest image cytometry platform.

In summary, our Organoid App enables the exploration of complex questions concerning the influence of human immune cell subsets and other compounds on organoid growth and development. This advancement offers great potential for addressing challenging applications in the field of translational medicine.

2 Materials and equipment

Detailed information about material and equipment is summarized in Table 2. Materials including hardware components and *in vitro* culturing of organoids are described below.

2.1 Hardware and software components

End-point analysis of organoid co-cultures (Figures 1A,B) were conducted using the automated TissueFAXSiPLUS (TissueGnostics, Vienna, Austria; Objective: EC Plan Neofluar 5x/0,25 M27, Zeiss, Oberkochen, Germany) system, including scanning with the appropriate TissueFAXS-plates software module (TissueGnostics). The time-lapse image acquisition was performed with the Incucyte® SX5 Live-Cell Analysis System (Sartorius, Goettingen, Germany) (Figure 1C). The Incucyte® Organoid Analysis Module (Cat. No. 9600-0034) was operated with the following settings: segmentation radius of 200 µm, segmentation sensitivity of 50, segmentation edge split with edge sensitivity of 70, cleanup with hole fill of 500,000 µm^2 and adjusted pixel size of −4. Additionally, filters for organoid quantification were set for a minimal area of 19,000 µm^2 and maximal eccentricity of 0.8. Image analysis by the OrganoSeg (22), software was conducted according the instructions given by the developer[1] (28). As mentioned in the OrganoSeg manual[2] (28), the following settings were used for optimal organoid detection. Given the fact that the ideal parameters of "Intensity threshold" and "Window size" vary from image to image, they had to be adapted for each individual image. Images with different levels of complexity were analyzed according the following parameters: Level #1 – Segmentation, "Out-of-focus correction" (default: ON), "Differential interference contrast (DIC) correction" (default: OFF); "Intensity threshold" 0.1172; "Window size" 90; "Size threshold" 699. Level #2: – Segmentation, "Out-of-focus correction" (default: ON), "DIC correction" (default: OFF); "Intensity

1 https://github.com/JanesLab/OrganoSeg.git

2 https://github.com/JanesLab/OrganoSeg/blob/main/BortenMA_OrganoSeg_Readme_GitHub.pdf

TABLE 1 Organoid detection pipelines.

Name	Organoid model	Imaging pipeline	Organoids analysis	Co-culture	Ref.
OrganoSeg	- Colorectal cancer - Pancreas	- Grayscale images (brightfield, phase-contrast, differential-interference contrast) - One Focus level	Size, distributions and morphology	No	(22)
OrgaQuant	Intestinal epithelium	- Grayscale images (brightfield) - One Focus level	Diameter in pixel	No	(23)
OrganoidTracker	Small intestinal epithelium	- Immune fluorescent labeled H2B-mCherry - One Focus level	Tracking	No	(24)
DNN	Alveolar	- Grayscale images (brightfield) - Merged z-stacks	Tracking number	No	(21)
OrganoID	Pancreatic cancer	- Grayscale images (brightfield) - One Focus level	Area tracking	No	(25)
D-CryptO	Colon culture	- Grayscale images (brightfield) - Merged z-stacks	Size diameter number	No	(1)

threshold" 0.82987; "Window size" 20; "Size threshold" 513. Level #3 – Segmentation, "Out-of-focus correction" (default: ON), "DIC correction" (default: OFF); "Intensity threshold" 1; "Window size" 100; "Size threshold" 699. After automatic segmentation, no organoids were manually removed or combined using "Spheroid editing toolbar." Analysis desktop configuration: device name DESKTOP-R2MMV91, Processor Intel(R) Xeon(R) W-2133 CPU @ 3.60 GHz 3.60 GHz, Installed RAM 24.0 GB (23.7 GB usable), System type 64-bit operating system, x64-based processor, Edition Windows 10 Pro for Workstations.

2.2 Generation of extrahepatic cholangiocyte organoids (ECOs)

For organoid generation (Regensburg University, ethical committee, reference 16-101-5-101), gallbladder tissues (2 cm^2 or less) were washed twice with cold Earle's Balanced Salt Solution (EBSS; Cat. No.: 24010043, Gibco/Thermo Fisher Scientific Inc., Schwerte, Germany), cut into small pieces, and digested in 4 mL digestion solution: 25 mg/mL Collagenase from clostridium histolyticum (Cat. No.: C9891-100 mg SIGMA/Merck KGaA, Darmstadt, Germany) in EBSS for 20 min at 37°C with soft shaking and filtered through a 70 µM Nylon CellStrainer (Cat. No.: 130-098-462 Miltenyi, Bergisch Gladbach, Germany). Dissociated cells were centrifuged at 1500 rpm (470 g) for 5 min at 4°C and washed twice with Base-medium (antibiotic-antimycotic 100x, Cat. No.: 15240-062, Gibco/Thermo Fisher Scientific Inc., New York, USA, 100 U/mL penicillin, 100 µg/mL streptomycin, AmphotericinB 1 µg/mL, L-Glutamine 2 mM Cat. No.: G7513-100 mL SIGMA/Merck KGaA, Darmstadt, Germany, HEPES 50 mM Cat. No.: H0887-100 mL, SIGMA/Merck and Advanced DMEM F12 Cat. No.: 12634028, Gibco/Thermo Fisher Scientific Inc). Organoid cultures were established according to previously published methods (6, 26). In brief, cell pellets were resuspended in organoid culture medium mixed with Matrigel® (Cat. No.: 356230 Corning, Corning, New York, United States of America) in a 50/50 ratio. Matrigel® was allowed to solidify for 15 min at 37°C before adding organoid culture medium. Organoid culture medium was based on ADV/DMEM-F12 (Cat. No.: 12634010, Gibco) supplemented with 1 M Hepes (Cat. No.: P05-01100, PAN-Biotech, Aidenbach, Germany), 100 mM L-Glutamin (Cat. No.: P04-80100, PAN-Biotech), 3.6% Anti-Anti (Cat. No.: 15240062, Gibco, Fisher Scientific GmbH, Schwerte, Germany), 1% N_2 serum-free supplement (Cat. No.: 17502-048, Gibco) 1% B27 serum-free supplement (Cat. No.: 12587-010, Gibco), 1 mM N-Acetyl L-Cystein (Cat. No.: A9165, Sigma/Merck KGaA, Darmstadt, Germany), 10 nM Gastrin I (Cat. No.: G9145, Sigma/Merck KGaA) and the following growth factors: 1 µg/mL of recombinant human R-spondin 1 (Cat. No.: 120-38, Peprotech, Hamburg, Germany), 10 mM Nicotinamin (Cat. No.: N0636, Sigma/Merck KGaA), 5 µM A83-01 (Cat. No.: 9094360, BioGems/Hölzel Diagnostika GmbH, Hohenzollernring, Germany), 10 µM Forskolin (Cat. No.: 1099, R&D/Bio-Techne, Wiesbaden, Germany), 50 ng/mL human epidermal growth factor (EGF, Cat. No.: AF-1000 Peprotech), 50 ng/mL human hepatocyte growth factor (HFG, Cat. No.: 100-39, Peprotech) and 100 ng/mL human fibroblast growth factor-10 (FGF-10, Cat. No.: 100-26, Peprotech). For the first 72 h after thawing, 10 µM of Y-27632 (Cat. No.: BioGems/Hölzel Diagnostika GmbH) was added to the media and only 25 ng/mL of HGF was used. Medium

TABLE 2 Key resources.

Biological samples: recombinant proteins		
Reagent or resource	**Source**	**Identifier**
human R-Spondin 1	Peprotech	Cat. No.: 120-38
human EGF	Peprotech	Cat. No.: AF-1000
human HFG	Peprotech	Cat. No.: 100-39
human FGF-10	Peprotech	Cat. No.: 100-26
human EGF-10	Peprotech	Cat. No.: AF-1000
IL-2	Novartis	Proleukin® S
Software and Algorithms		
OrganoSeg	Borten et al.,	https://github.com/JanesLab/OrganoSeg
StrataQuest v7.1.1.138	TissueGnostics	https://tissuegnostics.com/products/contextual-image-analysis/strataquest
Incucyte® Organoid Analysis ModuleIncucyte	Sartorius	https://www.sartorius.com/en/products/live-cell-imaging-analysis/live-cell-analysis-software/incucyte-organoid-analysis-software
TissueFAXS-plates software v7.1.6245.120	TissueGnostics	https://tissuegnostics.com/products/scanning-and-viewing-software/tissuefaxs-imaging-software
GraphPadPrism 9.5.1 for macOS	GraphPad Software, LLC.	https://www.graphpad.com
Plastic material		
48-well plate	Corning/Merck KgaA	Cat. No.: CLS3548
CellStrainer	Miltenyi	Cat. No.: 130-098-462
Critical cell culture components		
Matrigel®	Corning	Cat. No.: 356230
HEPES	PAN-Biotech	Cat. No.: P05-01100
L-Glutamin	PAN-Biotech	Cat. No.: P04-80100
Antibiotic-antimycotic	Gibco	Cat. No.: 15240062
N_2 serum-free supplement	Gibco	Cat. No.: 17502-048
B-27 serum-free supplement	Gibco	Cat. No.: 12587-010
N-Acetyl L-Cystein	Sigma/Merck KgaA	Cat. No.: A9165
Gastrin I	Sigma/Merck KgaA	Cat. No.: G9145
Nicotinamin	Sigma/Merck KgaA	Cat. No.: N0636
A83-01	BioGems/ Hölzel Diagnostika GmbH	Cat. No.: 9094360
Forskolin	R&D/Bio-Techne	Cat. No.: 1099
Y-27632	BioGems/ Hölzel Diagnostika GmbH	Cat. No.: 1293823
DPBS	Gibco	Cat. No.: 14190-094
TexMACS™ Medium	Miltenyi Biotec	Cat. No.: 130-097-196
T Cell TransAct™	Miltenyi Biotec	Cat. No.: 130-111-160
ADV/DMEM-F12	Gibco	Cat. No.: 12634010
EBSS	Gibco/Thermo Fisher Scientific Inc.,	Cat. No.: 24010043
Collagenase	SIGMA/Merck KgaA	Cat. No.: C9891
Cell separation reagents		
Pancoll®	PAN-Biotech	Cat. No.: P04-601000
biotinylated anti-human CD8 (clone HIT8a)	BioLegend	Cat. No.: 300904
anti-biotin ultrapure microbeads	Miltenyi Biotec	Cat. No.: 130-105-637
Imaging hardware		
TissueFAXSiPlus	TissueGnostics	https://tissuegnostics.com/products/fluorescence-brightfield-cytometer/tissuefaxs-i-plus
Incucyte® SX5 Live-Cell Analysis System	Sartorius	https://www.sartorius.com/en/products/live-cell-imaging-analysis/live-cell-analysis-instruments/sx5-live-cell-analysis-instrument?&utm_source=google&utm_medium=cpc&utm_campaign=incucyte&utm_term=brand&utm_content=search&gad=1&gclid=CjwKCAjw-7OlBhB8EiwAnoOEk3ycK0ZXXZanqBUwI_8aUyKfrOQNgP3NbvxddlEF7IIGWCaaQMbVhRoC0TsQAvD_BwE

10.3389/fmed.2023.1274482

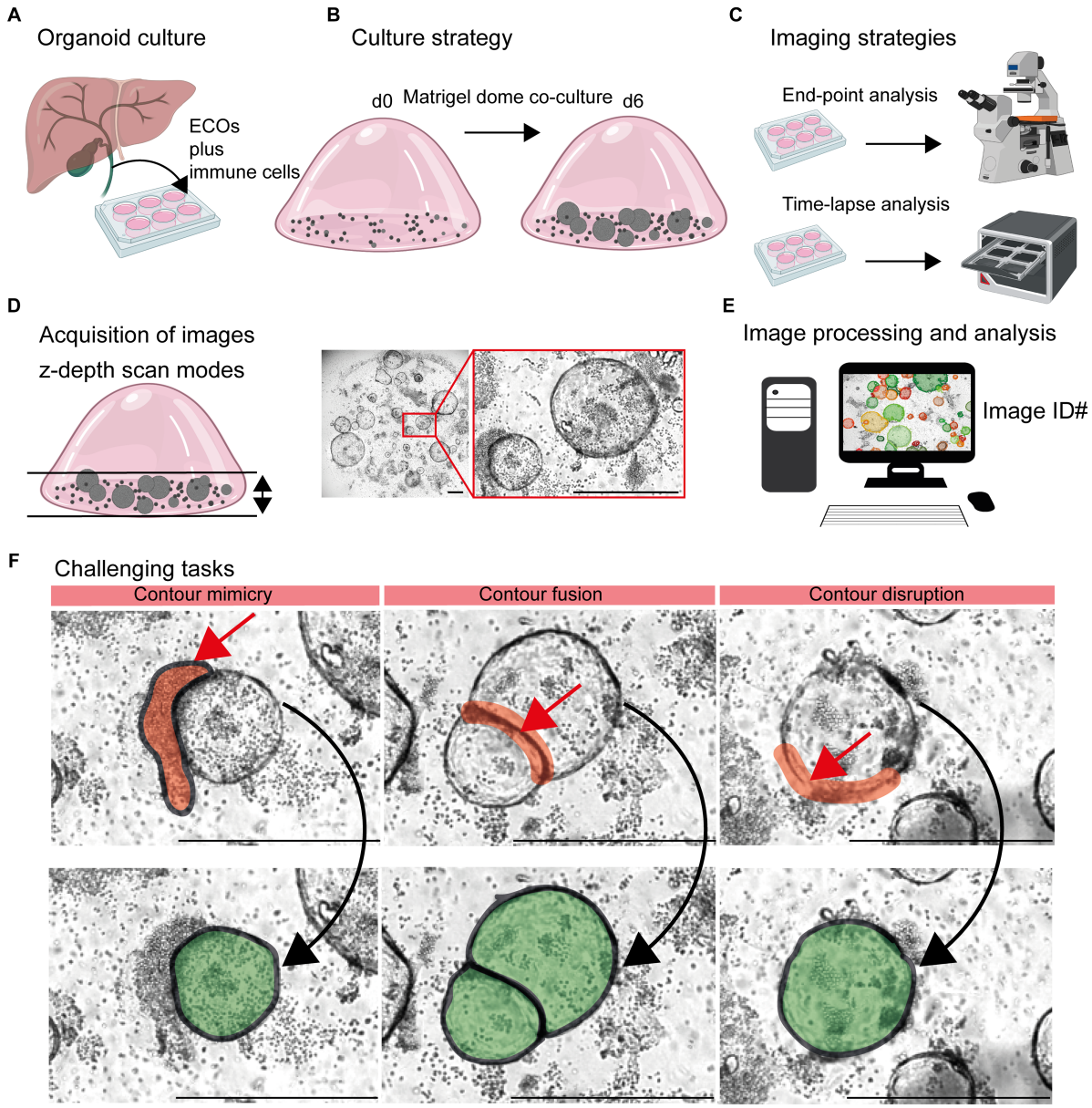

FIGURE 1
Detection of organoids in co-cultures of organoids and immune cells. **(A)** Organoid culture: Extrahepatic cholangiocyte organoids (ECOs) were generated from gallbladder tissue. **(B)** Culture strategy: ECOs and immune cells embedded in Matrigel® were co-cultured for a period of 6 days. Details are given in Section 2.2 and 2.3. **(C)** Imaging strategies: Culture plates are incubated within cell incubators for end-point analysis or the Incucyte® system, allowing an incubation and imaging for a period of 6 days. **(D)** Acquisition of images: Capturing red, green and blue (RGB) images with z-depth enables the generation of images with high plasticity. **(E)** Image processing and analysis: Import of images and image identification information (ID: well number and time point) in suitable devices for subsequent detection and quantification of organoids by the StrataQuest-supported Organoid App. **(F)** Challenging tasks: The main challenging tasks of organoid detection are depicted. Upper row: Red arrows indicate contour mimicry (left), contour fusing (middle) or contour disruption (right). Red areas highlight the regions that might interfere with a precise detection of organoids. Lower row: The aimed precision of organoid detection is highlighted in green. The bars represent 500 µm.

was changed every 3–4 days. Organoids were split every week by mechanical dissociation into small fragments and transferred to fresh Matrigel®.

2.3 Organoid co-culture with immune cells

For the isolation of $CD8^+$ T cells from human blood, leukocyte reduction chambers (provided by Transfusion Medicine, University Hospital Regensburg; ethical committee, reference number 13-0240-101 and 19-1414-101) were used. Leukocytes were initially diluted three times in DPBS (Cat. No.: 14190-94, Gibco), and the resulting blood and PBS mixture was split in two fractions and underlaid with an equal amount of Pancoll® (Cat. No.: P04-601000, PAN-Biotech, PAN-Biotech GmbH, Aidenbach, Germany). Samples were centrifuged at 1,000xg for 20 min at RT, with acceleration set to four and brake to zero. The PBMC layer was isolated and washed twice by centrifugation steps. $CD8^+$ T cells were isolated by column-based

magnetic separation using biotinylated anti-human $CD8^+$ (clone HIT8a, Cat. No.: 300904 Biolegend, Koblenz, Germany) and anti-biotin ultrapure microbeads (Cat. No.: 130-105-637, Miltenyi Biotec, Bergisch Gladbach, Germany), followed by fluorescence-activated cell sorting of viable $CD8^+$ T cells.

100,000 cells/well were seeded in TexMACS™ medium (Cat. No.: 130-097-196, Miltenyi Biotec) supplemented with 1% Penicillin/Streptomycin and activated with T Cell TransAct™ (1:100) (Cat. No.: 130-128-785, Miltenyi Biotec) in the presence of a cytokine mix for effector T-cell differentiation. Due to ongoing confidential work on this topic, further details about the T-cell phenotype cannot be provided. The absence of this confidential information is not relevant to the presentation of the developed Organoid App and will be discussed in follow up studies in detail.

After 4 days, $CD8^+$ effector T cells were harvested and rested in TexMACS™ medium with 100 U/mL IL-2 (Proleukin® S Novartis, Nürnberg, Germany) for three days. Subsequently, 200,000 T cells were stimulated with T Cell TransAct™ (Miltenyi Biotec) o/n before harvesting the cells. Organoids were harvested and washed with PBS to remove Matrigel®. For co-culture experiments, organoids and effector T cells were mixed in a ratio of 20 organoids/10,000 effector T cell in organoid culture medium without growth factors. The mixes were pelleted and resuspended in a 50/50 mixture of Matrigel® and organoid culture medium supplemented with growth factors as described above. Then, 25 µL of the mixture was seeded in the center of the wells of a 48-well plate (Cat. No.: CLS3548, Corning/Merck KGaA) and incubated at 37°C for 15 min to allow matrix solidification and dome formation. Finally, 300 µL of organoid culture medium supplemented with growth factors and 100 U/mL IL-2 was added and co-cultured by 37°C and 5% CO_2 in the Incucyte® SX5 Live-Cell Analysis Instrument (EssenBioscience/Sartorius, Göttingen, Germany). Scans of the individual wells were scheduled every 8 h over a period of 6 days. To assess the influence of the growth factor EGF on organoid growth, organoid co-cultures were cultured with or without 50 ng/mL human EGF.

2.4 Statistical analysis of data

Raw data (*.xls or *.xlsx) were imported into GraphPadPrism 9 macOS for subsequent graphical presentation and statistical analysis. Multiple *t*-tests (Multiple Mann–Whitney tests; unpaired; nonparametric), one way ANOVA tests (Kuruskal-Wallis test, Dune's multiple comparison) and Šídák's multiple comparisons test were used for statistical analysis.

2.5 Calculation of precision and recall

For the evaluation of the potential of software's to detect organoids, we verified the software-based results manually be counting true positive (TP), false positive (FP) and false negative (FN) signals. The parameters precision (positive predictive value) and recall (sensitivity) have been calculated according the formula: Precision = TP/(TP + FP); Recall = TP/(TP + TN) (29). Consequently, the following parameter associated questions could be addressed. Precision: What proportion of the positive identifications were actually correct? Recall: What proportion of true positives was correctly identified?

3 Methods

3.1 Probing technical limitations of automated detection and quantification of organoids in co-cultures

The influence of immune cells on the growth of organoids is gaining more and more acceptance in the field (3, 8, 11–18, 30, 31). In this study, we chose the ECO organoid model in combination with lymphocytes embedded in Matrigel® domes to generate time-lapse and end-point images for subsequent analysis (Figures 1A–E).

Based on the 3D structure of Matrigel® domes, a combination of multiple images taken at different focus distances was performed [TissueFAXSiPLUS: z-stacks, $n = 4$, range 310 µm; Incucyte®: brightfield organoid scan mode, object driven focus, z-depth < 2.9 mm (32)]. This allows for a high-contrast visualization of both organoids and lymphocytes embedded within different layers of the Matrigel® dome (Figure 1D; Supplementary Figure S1).

Based on these initial data, an accurate detection of organoids within heterogeneous and dense *in vitro* cultures remains challenging due to three main aspects (Figures 1D, F). Firstly, clusters of immune cells that are located close to organoid structures can mimic organoid morphology based on their cellular density. Therefore, the detection algorithms could recognize false positive structures based on contour mimicry. Secondly, when organoids are in close proximity to each other, the algorithm may recognize them as a 'single organoid structure' due to contour fusion, which underestimates the actual organoid number. Thirdly, the integrity of organoid contours can be disrupted due to inadequate imaging quality or the presence of overlapping immune cells.

To address these challenges, high-throughput software pipelines that can accurately detect organoid structures in complex samples would be a valuable asset in studying the immunological aspects of organoid growth. Several software tools have been released to identify and characterize organoids cultured in the absence of other cellular components (Table 1). Based on our knowledge, no imaging workflows have been developed to quantify organoid-immune cell co-culture systems in a high-throughput manner. Thus, we questioned whether existing codes or commercial software tools can distinguish between organoid structures and densely clustered immune cells.

Scientists can quantify organoids using different tools, such as ImageJ or handwritten notes. These results are quite accurate, but can also show variations, depending on who counted the organoids (Figures 2A,F). However, it is exceedingly challenging and time consuming to precisely determine the organoid's area and density utilizing manual techniques. Furthermore, this manual approach is unsuitable for high-throughput analyses. We used automated approaches, such as customized Incucyte® software packages and the OrganoSeg (22) detection algorithm, to identify and quantify organoids within co-cultures. Images of increasing complexity (level #1 – #3) have been included in this study. Our findings showed that the detection of organoids by both existing software tools is not optimized for heterogeneous co-cultures. All analyzed images, ranging

10.3389/fmed.2023.1274482

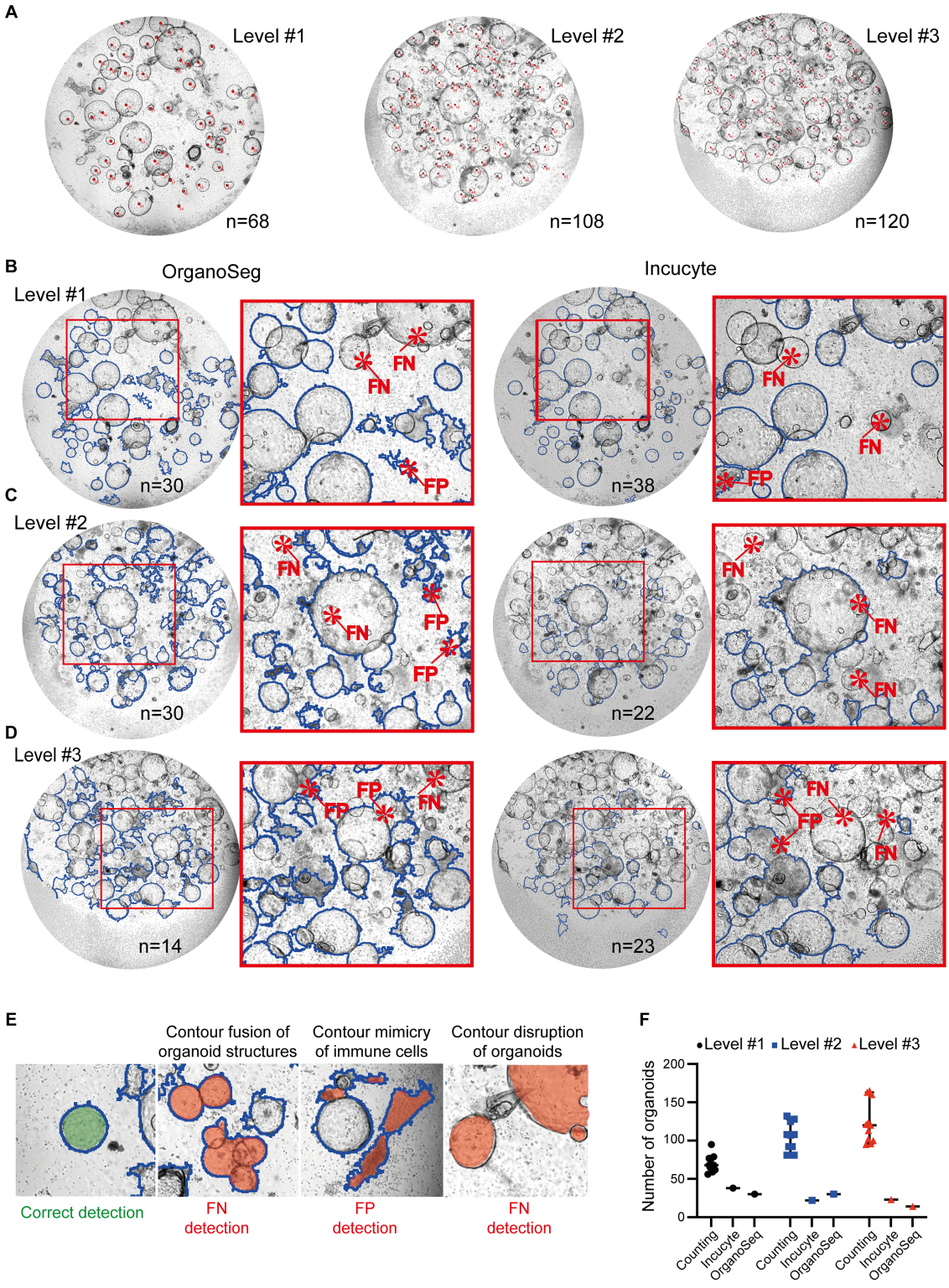

FIGURE 2
Quantification of organoids within immune cell co-cultures. Images of immune cell/organoid co-cultures representing different degrees of complexity (levels #1-#3) have been analyzed. **(A)** Organoids from level #1 – #3 were counted manually by four different scientists using the ImageJ counting function or written notes on the original pictures. Each image was counted 11 times. Representative images with organoids marked by red dots are shown. The depicted number represents the median number of organoids within the field of view. **(B–D)** Automated analysis of different degrees of complexity (levels #1-#3). Left: Images were analyzed using OrganoSeg. Right: Images were analyzed using the manufacturers' Incucyte® Organoid Analysis Module. Blue outlines visualize organoids which are detected by the respective software. Detailed software settings are described in Section 2.1. Red highlight false negative (FN) or false positive (FP) detections of organoids. **(E)** Representative examples of correct organoid detections (blue outline; filled with green). The filled red area indicates "organoid structures" that are detected FN or FP. **(F)** Comparison of organoid numbers, analyzed by the different software tools (counting: median plus 95% confidence interval is shown; Incucyte® and OrganoSeg analysis: each dot represents an analysis).

from intermediate (level #1; Figure 2B), to high (level #2; Figure 2C), to very high complexity (level #3; Figure 2D) showed false negative (FN) and/or false positive (FP) organoid structures. The most prominent FP and FN detection problems are given in Figure 2E. In comparison to manual counting by ImageJ ($n = 68$ in level #1, $n = 108$ in level#2, $n = 120$ in level #3), the Incucyte® and OrganoSeg software tools only highlighted a few ($n < 39$) organoid structures (Figure 2F). The calculated values for precision and recall, which are basic concepts for evaluating the performance of detection algorithms, show very low levels (Incucyte®: level #1 precision = 0.43/recall = 0.43, level #2 precision = 0.00/recall = 0.00, level #3 precision = 0.10/recall = 0.042; Organoseg: level #1 precision = 0.33/recall = 0.37, level #2 precision = 0.06/recall = 0.08, level #3 precision = 0.00/recall = 0.00; data not shown). This indicates very strong limitations regarding the detection of organoids. Despite the fact that the automated tools failed to accurately identify organoids, we plotted the number of "organoid structures" that were identified by the software (Figure 2F). In line with the unacceptable levels of recall and precision, those organoid numbers do not reflect the real situation (Figure 2F). Thus, we can conclude that the tested software tools or algorithms are limited in their ability to correctly recognize organoids under co-culture conditions (Figure 2). Therefore, our objective was to develop a high-throughput pipeline for the identification and quantification of organoid structures in lymphocyte co-cultures.

3.2 Image acquisition and data import for subsequent organoid detection by the StrataQuest-supported Organoid App

To improve the identification and quantification of organoid structures in lymphocyte co-cultures, we developed a StrataQuest-supported Organoid App. This software allows the processing of different image configurations and formats, ranging from time-lapse to end-point analysis of organoid development in co-cultures. In this context, an appropriate image sample identification code (ID) is mandatory for automated StrataQuest analysis, regardless of the image source. This ID must contain information about the plate number, well number, stimulation, and time point. Imported images obtained from alternative systems, such as Incucyte®, exhibit the following characteristics: 8-bit depth, resolution of 1,536 × 1,152 pixels, and a file size of approximately 4.5 MB. Consequently, a microscope field of view (FOV)-correction to 2,560×2,000 pixel must be performed by the StrataQuest software before starting the analysis. A simplified workflow of the organoid detection is summarized below and visualized in Figure 3.

3.2.1 Generation of a virtual channel

The input image is converted into a virtual grayscale image (Figure 3A; Step #1). This step is mandatory for an optimal signal (high grayscale-values) to noise (low grayscale-values) separation. The contours of organoids with high contrast intensities become prominent and represent the key element for subsequent organoid detection, as well as for separating the inner areas from the surrounding environment.

3.2.2 Background correction

A median filter is employed to create a suitable background model that is then subtracted from the grayscale image (Figure 3A; Step #2). This helps to reduce or eliminate non-uniform and high background signals, such as those arising from immune cells and other non-organoid structures.

3.2.3 Grayscale image enhancement

A membrane detection algorithm is used to identify the contour areas of putative organoid-like structures. The software automatically enhances the intensity and contrast of the organoid borders (Figure 3A; Step #3) and processes them for subsequent verification and detection. After converting the original image to grayscale (Figure 3A, Step #2), the contours of the organoids exhibit a high level of intensity. As a result of this image processing, the membrane shows a higher grayscale intensity compared to the rest of the structures, including background and immune cells. This allows the algorithm to search for changes in intensity (higher or lower) within a defined set of growth steps. Finally, the algorithm detects shifts in intensity from a lower to a higher value and then back to a lower value and can define the shapes of maximum intensities that represent the border structure of the organoid. The output of this process is a black and white masked image in which the white areas represent the membrane-like structures identified by the membrane detection algorithm. The grayscale image is then supplemented with the identified membrane in order to highlight the contours of the organoids. This enhancement produces a refined grayscale image, utilized as the input for training the classifier.

3.2.4 Classifier training by machine learning

Machine learning refers to the classification engine operated by the Organoid App, which can use representative images for each complexity category defined by the user. The machine learning process focuses on the dissection of real "organoid contour" and non-organoid structures, such as immune cells, which we call "tissue" in this publication. The enhanced grayscale image was used as the input image to facilitate the detection of the organoid contour (Figure 3A, Step #4; Supplementary Figure S2). After providing possible organoid boundaries and structures, the classifier is trained to identify all structures that are "real organoids". In parallel, the classifier recognizes a so-called "tissue" that consists of immune cells and/or background. Various features such as intensity, morphology, Haralick texture, and environmental context, including Gaussian and median filters, are used to train the classifier by marking structures of interest and contaminating background signals (Supplementary Figure S2). The results are displayed as coded map images, where each organoid structure is marked with a color corresponding to its assigned boundary (Figure 3A, Step #5). Real-time detection and visualization of organoids during classifier training enables quality control of the classifier. The machine learning program supported by the Organoid App can be repeated until optimal recognition of organoids is achieved in the selected training images.

3.2.5 Organoid contour and background detection

The contour mask (generated by the classifier) is highlighted in blue (Figure 3A; Step #5). Each disjunct object which generates a contour/organoid seed is assigned a unique image ID. The term "seeds" refers to an initial value that is used to initialize a random number generator algorithm, which then generates a sequence of random numbers based on that seed. These contour/organoid candidates are evaluated by morphological and intensity-based

10.3389/fmed.2023.1274482

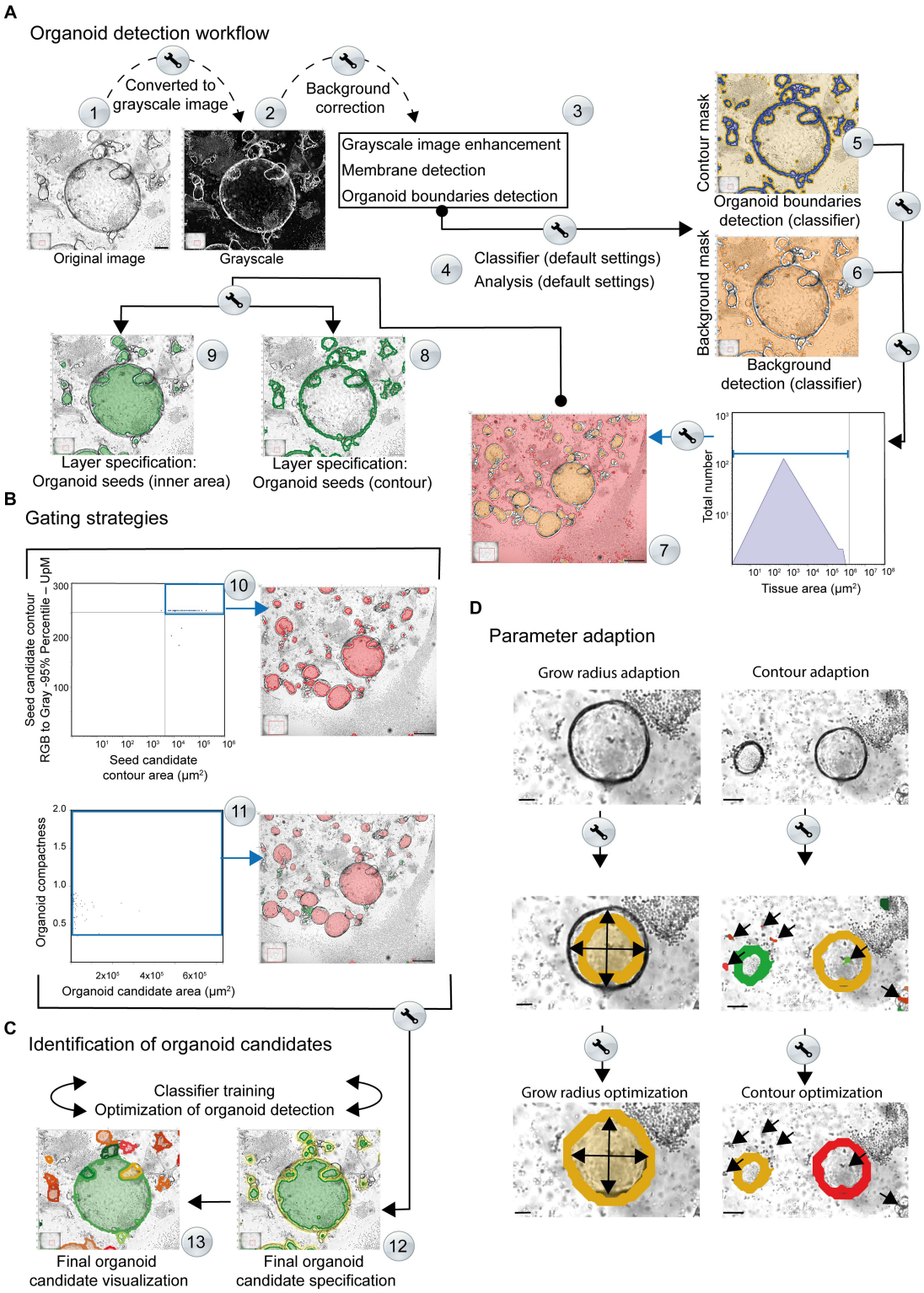

FIGURE 3
Simplified overview of the organoid detection workflow using the StrataQuest-powered Organoid App. The principal steps are depicted. Details are given in the main text. **(A)** After converting the original images to grayscale, a median filter is applied to create a background layer, which is then subtracted from the grayscale image (Step #1). This step helps to reduce interfering signals and eliminates non-uniform and high background signals (Step #2). An additional membrane detection step is integrated, for accurate discrimination of the organoid boundary (Step #3). The enhanced grayscale image is subjected to the machine learning procedure (classifier; Step #4) to identify the contours (contour mask, highlighted in blue) as well as the tissue or background (background mask; highlighted in orange). This analysis provides a boundary specification for the organoids (contours mask: blue area, background mask: orange area). By combining the input data from steps #5 and #6, a final organoid specification can be performed. Organoid boundaries (blue areas) and background (orange areas) are separated for individual images (Steps #5 and #6) and are further processed. Organoid candidates are generated (highlighted in orange, Step #7). A two-layer specification of the contour of the organoid cores (Step #8,

(Continued)

FIGURE 3 (Continued)
highlighted by green lines) and the inner region of the organoids (Step #9, highlighted by filled green areas) is used for further recognition of the organoids. **(B)** Gating strategies. Representative gating and back gating tools for quality controls are depicted. Upper row: The histogram shows the range of structures that are processed by the software for subsequent organoid detection. The gate (blue square) captures signals that serve as basis for further evaluation. The back-gating function can be used to highlight (orange) all structures representing the defined gate in the original image (Step #10). Lower row: The organoid compactness signature is used to define the final detection parameters (Step #11). The gate (blue square) captures all signals that serve as final basis for quantification of organoid area, number and shape. The bar represents 500 µm. **(C)** Identification of organoid candidates. Representative specifications are depicted (Step #12). The organoid contours (yellow) and areas (green) are highlighted. Individual organoids are visualized by the software by randomly selected colors (Step #13). **(D)** Parameter adaption. Right side: the growing masks of organoid seeds and the corresponding limits of the growth radii can be adjusted until the exact limit of the organoid candidates is reached. Upper image: original. Middle image: the organoid detection (orange area) based on default growing parameters is shown. The arrows highlight the growing mask. An adaption of the organoid seeds' grow radius (value = 280.00) and the organoid grow radius (value = 90.00) revealed an optimal detection of the organoid area (filled inner orange area). The bars represent 50 µm. Right side: the contour areas of organoid candidates can be adapted. Upper image: original. Middle image: the organoid detection (orange and blue contour line) based on default settings of contour area settings is shown. Wrong positive structures (immune cells contours red; highlighted by arrows) area detected as possible organoid structures. An adaption of the contour area (parameter adaption: remove contours below 20 µm^2) revealed an optimal detection of the organoid contours (orange area and red contour line). The bars represent 100 µm. Middle row: based on the contour area of organoid seeds (x-axis) and their corresponding intensity (y-axis) potential seeds candidates (inner area) can be determined for subsequent organoid detection. The upper right gate includes potential seeds candidates highlighted in red by back gating. These structures are further processed for organoid detection.

measurements (Figure 3A; Step #5). The background detection (highlighted in orange) allows the subtraction of structures that are not associated with organoids. This mask (including immune cells and debris), which is generated by the classifier, assigns a unique processing ID to each disjunct object, generating candidates for organoid seeds (Figure 3A; Step #6). The background mask (generated by the classifier) is labeled in red and separated from the actual organoid inner areas based on size criteria (Figure 3A; Step #7).

3.2.6 Organoid body detection (seeds; inner area)

To visualize organoid bodies, seeds can be used to generate random gray intensities or patterns for labeling and distinguishing different organoids or regions of interest within an image. These candidates are evaluated using morphological and intensity-based measurements. To implement this process, the background gate (Figure 3A; Step #7) is used for subtracting the background for subsequent analyses. Based on the area (indicated gate) a unique ID is assigned to each disjunct object. Contours of the organoids are also used to validate the seeds (green contour; Figure 3A; Step #8). The candidates (Figure 3A; Step #9) are evaluated by morphological and intensity-based measurements, by two subsequent intervals. First, raw organoid body selection is performed by selecting the small tissue objects, which might represent potential organoids inner areas. Second, a more accurate organoid seed selection is performed by evaluating the intensities around the seeds from the previous step. A valid seed is surrounded by a calculated organoid contour (compare diagram: Seed candidate contour area (Figure 3B; Step #10, upper right quadrant)). The selected seeds are processed further using morphological operations (compactness) to better represent the inner area of organoids (Figure 3B; Step #11).

3.2.7 Organoid detection and parameter adaption

The identified seeds (compare diagram: Organoid candidate area (µm^2) vs. compactness; (Figure 3B; Step #11)) are combined with small contours, corresponding to small organoids where the inner area identification is very difficult or impossible. Organoid structures can now be detected based on two criteria: body; highlighted in green (Figure 3C; Step #12) and contour; highlighted in yellow (Figure 3C; Step #12). The resulting organoids are highlighted by the Organoid App in randomized colors (Figure 3C; Step #13). If the detection of organoids within the group of selected images is insufficient regarding FN or FP organoid structures, the classifier can be retrained again to achieve optimal automated detection of organoid candidates.

3.2.8 Growing mask adaption and deletion of background signals

The raw organoid seed detection is combined with the contour mask, generated by the classifier, to create a growing mask (Figure 3D). Reconstruction of the organoids is performed by a growing algorithm that determines the final seeds on the growing mask. The growing step limits are defined by the parameter "Organoid – Grow Radius adaptation" (Figure 3D). For a precise adaption of organoid detection, it is also possible to adjust distinct growing masks accordingly. Additionally, an appropriate contour-size adaption enables the exclusion of background signals (Figure 3D). The identified organoids can be automatically categorized according to distinct areas.

4 Results

4.1 Quality control

The Organoid App was developed based on images of organoid co-cultures with immune cells (Figure 2A; level #1). Therefore, the default settings of the machine learning engine can be used to start the organoid detection procedure. Based on the heterogeneous quality of images and the varying density of organoids within cell culture plates, a project-specific adaption of the machine learning classifier is recommended to increase the quality of analysis.

Even though the default settings for organoid detection allow the identification of most organoids, some are not recognized (false-negative). In addition, organoid-like structures may be incorrectly identified (false-positive) as organoids (Figure 4A; top row). After appropriate classifier training and machine learning, the ability to recognize organoids in co-cultures is further improved (Figure 4A; lower row). Based on the high-throughput analysis of growing organoids from day 0 to day 6, the organoids exhibit varying densities and structures. Due to the significant variability and artifacts present in culture plates, the Organoid App has only very minor limitations, with high values of precision and recall (level #1 precision = 0.92/recall = 0.95, level #2 precision = 0.91/recall = 0.91, level #3 precision = 0.95/recall = 0.93; data not shown). This indicates that the

10.3389/fmed.2023.1274482

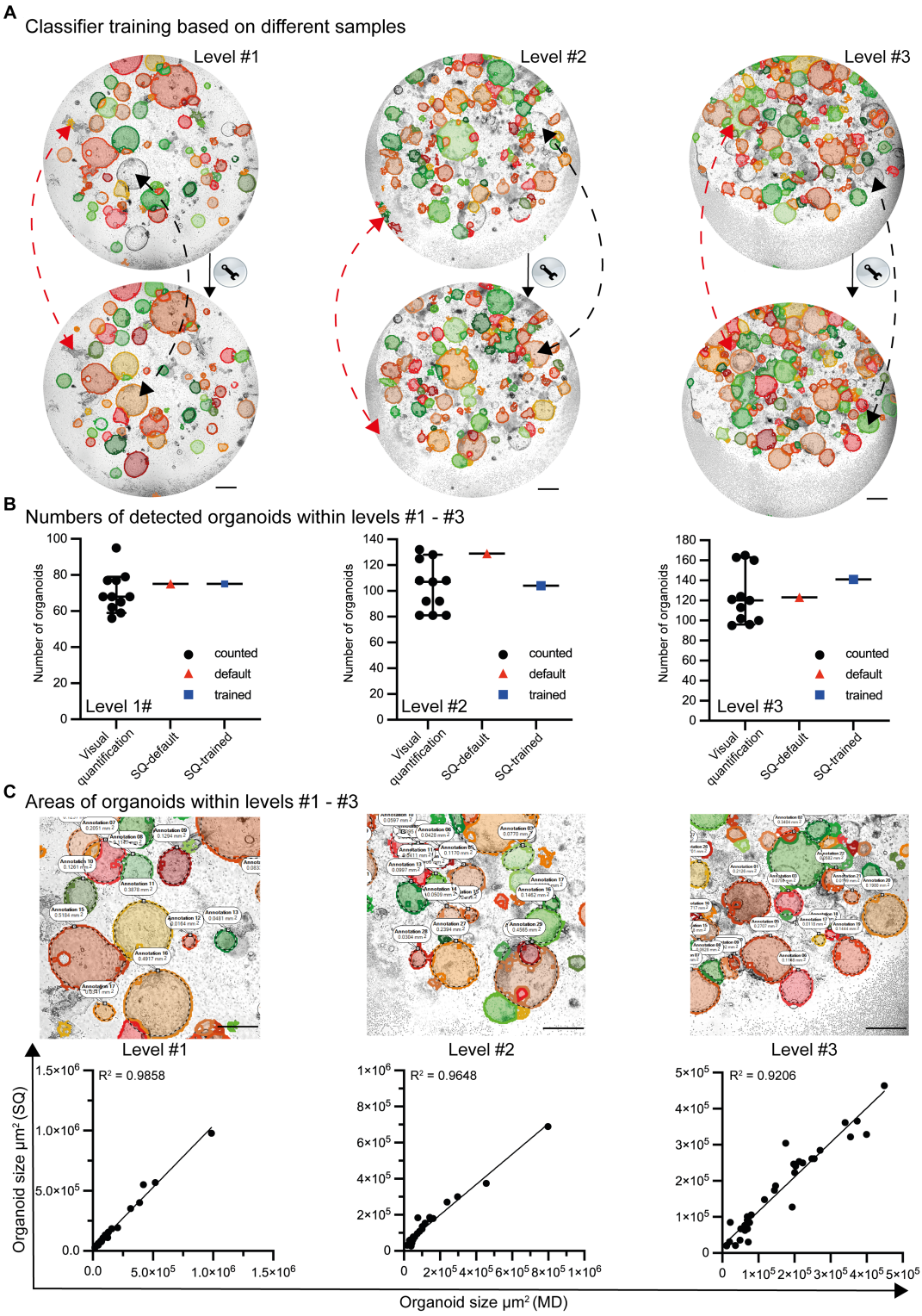

FIGURE 4
Classifier training and quality control by the StrataQuest-supported Organoid App. **(A)** Images with different levels of complexity (level #1 to #3) were analyzed by the default settings of the Organoid App (upper row) and after machine learning-based (lower row) classifier training. Representative modifications are highlighted by red and black dotted lines. The red lines indicate corrections of formerly false positive structures. The black lines indicate corrections of formerly false negative structures. The bars represent 500 µm. **(B)** The number of organoids is presented according to the indicated method of analysis. Visual quantification: the median and 95% confidence interval is shown. Each symbol represents an individual counting result (compare Figure 2). StrataQuest [(SQ)-default and SQ-trained: Each dot represents an analysis]. **(C)** The quality of area measurement is shown. Upper row: Areas detected by the StrataQuest based Organoid App (filled structures) and manually delineated boundaries (annotations and dotted black lines) of organoids. Representative images of different complexities (levels #1 to #3) are depicted. The bars represent 500 µm. Lower row: Linear regression plots, comparing the areas of organoids in µm^2. The x-axis indicates the areas of manual delineation (MD). The *y*-axis indicates the areas of automated analysis performed by StrataQuest (SQ) using the Organoid App. Images with different complexities (level #1 to #3) were analyzed. A linear regression model was used to calculate the value of variation between the data. The R^2 values are depicted.

Organoid App correctly identifies the majority of organoids. The identification and separation of overlapping organoids and technical artifacts remains indeed a real challenge, but has been largely solved with this application (Figures 4A,B).

The number of organoids detected by both the standard (StrataQuest (SQ)-default) and trained (SQ-trained) algorithm lies within the 95% confidence interval of the manually counted organoid numbers (Figure 4B). This result can be explained by the fact that after classifier training the number of false positives structures decreased (compare Figure 4A red arrows), whereas the detection rate of previously undetected organoids increased (compare Figure 4A black arrows).

In addition to the validation of the organoid detection count, the accuracy of the organoid area determination was verified. Randomly selected organoids were manually delineated and measured. These data were compared with the areas calculated by the Organoid App recognition algorithms. The corresponding linear regression graphs revealed a highly significant correlation between the Organoid App-based and manual-area measurements (Figure 4C). Our organoid application achieves a high degree of accuracy in organoid detection, closely paralleling the accuracy of the human eye (Figure 4C; Supplementary Figure S3B).

4.2 Characterization of organoid development within co-cultures in the presence of exogeneous compounds

A pilot study was conducted to evaluate the ability of the Organoid App to identify an aberration in organoid development under different growth conditions. In this context, we focused on two central aspects. First, we tested whether organoid growth can be monitored over time. Second, we addressed whether the simultaneous presence of a growth factor and immune cells can affect organoid differentiation in terms of size and compactness. To this end, we have included the epidermal growth factor (EGF) in our study, as EGF has already been used in a number of studies on organoid differentiation (27, 33–36).

Images were acquired over a period of 6 days with the Incucyte® SX5 Live-Cell Analysis System and imported into StrataQuest. An initial screening of the data revealed that the number and size of the organoids changed significantly over the course of a 6-day culture period. Even the density of immune cells in the *in vitro* system exhibited substantial fluctuations due to cell proliferation, as illustrated in Figure 5A. To ensure accurate detection of organoids by the Organoid App, we trained the classifier on a set of six representative images. These selected images were imported and merged into a single dataset. Based on this dataset, it was feasible to achieve a comprehensive training covering the full range of cell culture heterogeneity, including organoid density, overlapping structures and imaging quality (Figure 5B). After appropriate classifier training, image analysis was conducted.

StrataQuest allows the export of meta data in different file formats such as *.pdf, *.xls and *.xlsx for subsequent graphical display and statistical analysis (Figure 5C). This enables the import and further processing by other software tools. Consequently, adequate statistical analyses and data visualization can be performed. Our analysis showed an increase in the absolute number of organoids over time, both in untreated and EGF-treated culture conditions (Figure 5D). However, the total number of organoids was reduced in the presence of EGF (Figure 5D).

To determine whether the development of organoids with a distinct size was affected by EGF, organoids of different sizes were analyzed. This characterization revealed that the number of organoids (day 1–day 6) with a size between 18,000 μm^2 and 60,000 μm^2 is impaired in the presence of EGF (Figure 5E). The number of organoids with a size between 60,000 μm^2 and 120,000 μm^2 was only partially (day 3 and day 4) affected by EGF (Figure 5E). In contrast, EGF does not influence the development of organoids below 18,000 μm^2 or above 120,000 μm^2 in general (Supplementary Figure S4).

The Organoid App also enables the determination of individual organoid sizes within the co-culture system. Comparing day 2 with day 5 of organoid co-culture, the average size of organoids increased, independent of EGF (Figure 5F; upper dot plots). We also analyzed the influence of EGF on organoids growth on day 2 and 5 and found that while EGF had no effect on the size distribution of organoids on day 5 (Figure 5F: lower right dot plot), on day 2 EGF led to a very slight increase in average organoid size (Figure 5F: lower left dot plot).

In addition to the quantification of organoid number and size, the compactness of individual organoids can be determined. Compactness can be assessed using various quantitative metrics, such as the ratio of the organoid's volume to its surface area or the degree of sphericity. These measurements provide information about the overall structural integrity and density of organoids. A high compactness value indicates a well-developed cohesive circular organoid structure, while a lower value may indicate a diffuse arrangement of cells within an amorph organoid. We found increased compactness at day 2 compared to day 5 (Figure 5G), indicating that the organoids become less compact during culture.

Based on these first proof-of-principle experiments, it can be concluded that a sound quantification of organoid number, size and compactness in co-cultures with immune cells is possible by using the Organoid App in high-throughput analysis. Our study also confirms that the Organoid App effectively detects subtle differences in the chosen culture conditions. We found that EGF has the potential to affect the development of distinct organoid subsets (Figure 5H).

We have also incorporated the Incucyte® software for subsequent quantification of organoids in co-cultures, despite its obvious limitations in organoid detection (compare Figure 2B; right column). These data revealed that the Incucyte® software was not able to detect the differences in organoid growth between untreated and EGF-treated co-cultures, which could only be identified by the Organoid App (Figures 6A,B). Due to the limitations of the Incucyte® software (Figure 6C), these data cannot be used to further interpret the effect of EGF on organoid growth. The Organoid App, powered by StrataQuest and capable of detecting and quantifying of organoids, showed that EGF can dampen the growth of organoids in co-culture systems (Figures 6A,B). These data are consistent with the data shown in Figure 5D. Further analysis and comparison of organoid growth with OrganoSeg was not performed due to the limitations of this algorithm in organoid detection.

5 Discussion

The debate on whether or not engineered cell-based *in vitro* models, such as organoids, can faithfully reproduce the structures and

10.3389/fmed.2023.1274482

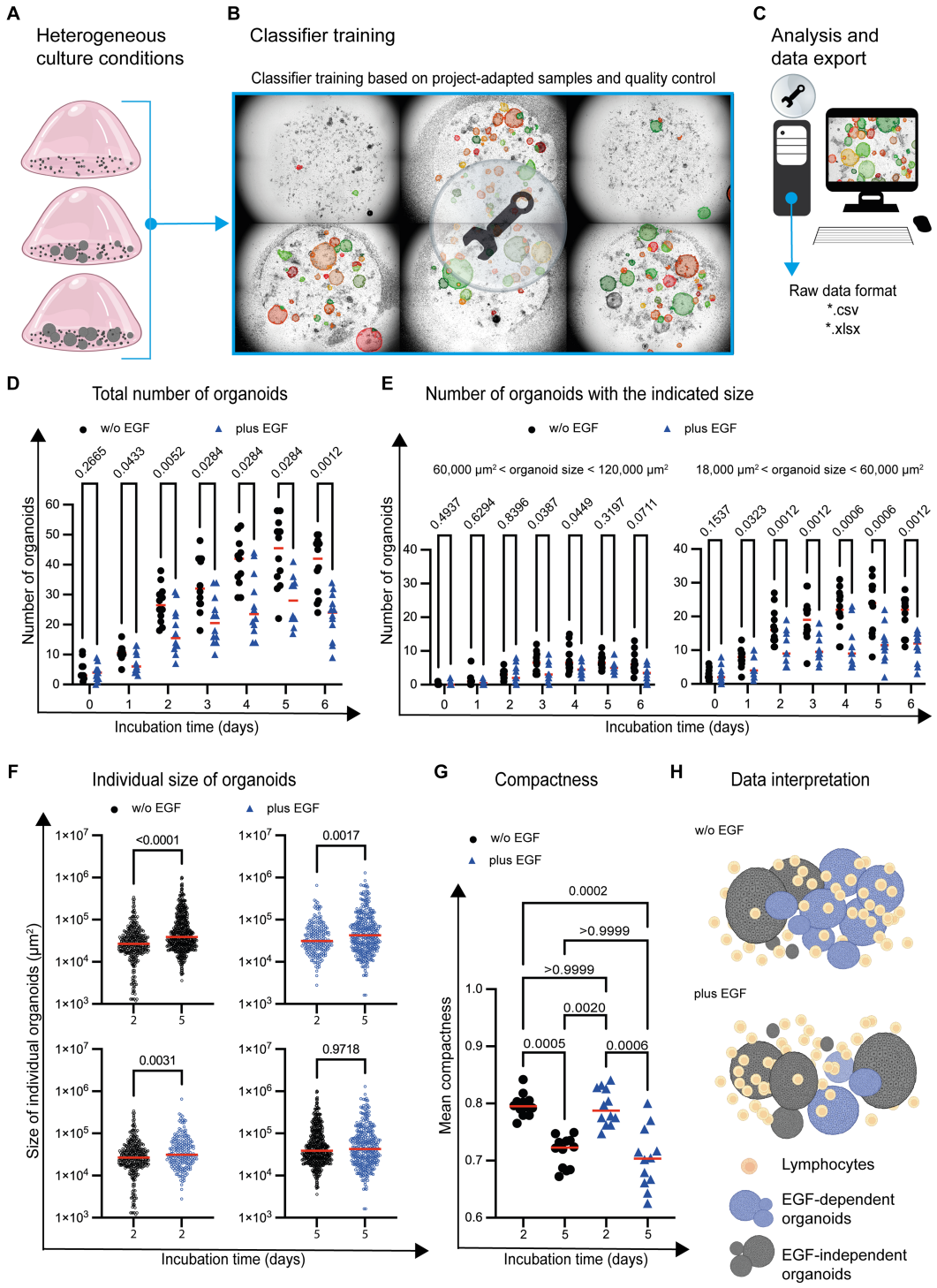

FIGURE 5
Organoid development in the presence of immune cells and EGF. **(A)** Graphical examples of different organoid growth conditions are depicted. **(B)** Based on the given complexity, the classifier is trained by using images (n =6) representing the range of the given cell culture complexity. **(C)** The analysis of the entire project (n =170 images) is based on the project-specific classification and detection settings. **(D)** The total number of organoids and **(E)** organoids within a distinct size range are depicted. Each symbol represents the total number of organoids within one well. Quadruplicates from n =3 different donors are shown. The red horizontal line highlights the median. Multiple t-test (Multiple Mann–Whitney tests; unpaired; nonparametric) have been used to compare organoid cultures in the absence (w/o EGF; black circle) and presence (plus EGF; blue filled triangle) of EGF. The p values are indicated. **(F)** The individual size of organoids at day 2 and day 5 is shown. Each dot represents the size of one single organoid within the culture wells. The horizontal line highlights the median. Quadruplicates from n =3 donors are shown. Multiple t-test (Multiple Mann–Whitney tests; unpaired; nonparametric) have been used to compare organoid co-cultures in the absence (w/o EGF; blue circle) and presence (plus EGF; blue circle) of EGF. The p values are indicated. **(G)** The mean of organoid candidates' compactness at day 2 and day 5 is shown. Each dot represents the area of a single organoid. The horizontal line represents the median. Quadruplicates from n =3 donors have been implemented in the data analysis. One way ANOVA tests (Kuruskal-Wallis test, Dune's multiple comparison) have been used comparing organoid cultures in the absence (w/o EGF; black circle) and presence (plus EGF; blue filled triangle) of EGF. The p values are indicated. **(H)** The diagram illustrates a potential interpretation of the data: The development of organoids with an intermediate size (highlighted in blue) between 18,000 µm² and 60,000 µm² is reduced in the presence of EGF. The growth of the blue organoids is EGF-dependent (EGF-dependent organoids). Gray organoids can grow in the absence of EGF (EGF-independent organoids).

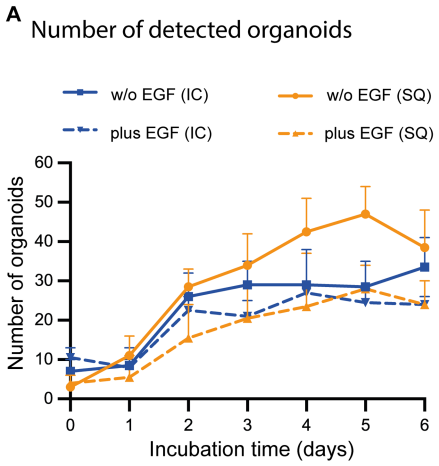

B Statistical analysis

Šídák's multiple comparisons test	Mean Diff.	95,00% CI of diff.	Below threshold?	Summary	Adjusted P Value
Day 4					
SQ (w/o EGF) vs. IC (w/o EGF)	11,08	-1,532 to 23,70	No	ns	0,1402
SQ (w/o EGF) vs. SQ (plus EGF)	15,25	0,8255 to 29,67	Yes	*	0,0303
SQ (w/o EGF) vs. IC (plus EGF)	15,92	4,557 to 27,28	Yes	**	0,0015
IC (w/o EGF) vs. SQ (plus EGF)	4,167	-10,13 to 18,47	No	ns	>0,9999
IC (w/o EGF) vs. IC (plus EGF)	4,833	-6,313 to 15,98	No	ns	0,9952
SQ (plus EGF) vs. IC (plus EGF)	0,6667	-12,73 to 14,06	No	ns	>0,9999
Day 5					
SQ (w/o EGF) vs. IC (w/o EGF)	13,67	-0,7823 to 28,12	No	ns	0,0774
SQ (w/o EGF) vs. SQ (plus EGF)	16,33	1,220 to 31,45	Yes	*	0,025
SQ (w/o EGF) vs. IC (plus EGF)	19,83	5,332 to 34,33	Yes	**	0,0025
IC (w/o EGF) vs. SQ (plus EGF)	2,667	-7,975 to 13,31	No	ns	>0,9999
IC (w/o EGF) vs. IC (plus EGF)	6,167	-2,933 to 15,27	No	ns	0,5671
SQ (plus EGF) vs. IC (plus EGF)	3,5	-7,254 to 14,25	No	ns	>0,9999
Day 6					
SQ (w/o EGF) vs. IC (w/o EGF)	4,083	-10,38 to 18,54	No	ns	>0,9999
SQ (w/o EGF) vs. SQ (plus EGF)	15,5	1,977 to 29,02	Yes	*	0,0139
SQ (w/o EGF) vs. IC (plus EGF)	15,08	2,036 to 28,13	Yes	*	0,013
IC (w/o EGF) vs. SQ (plus EGF)	11,42	-1,555 to 24,39	No	ns	0,1377
IC (w/o EGF) vs. IC (plus EGF)	11	-1,446 to 23,45	No	ns	0,1322
SQ (plus EGF) vs. IC (plus EGF)	-0,4167	-11,50 to 10,66	No	ns	>0,9999

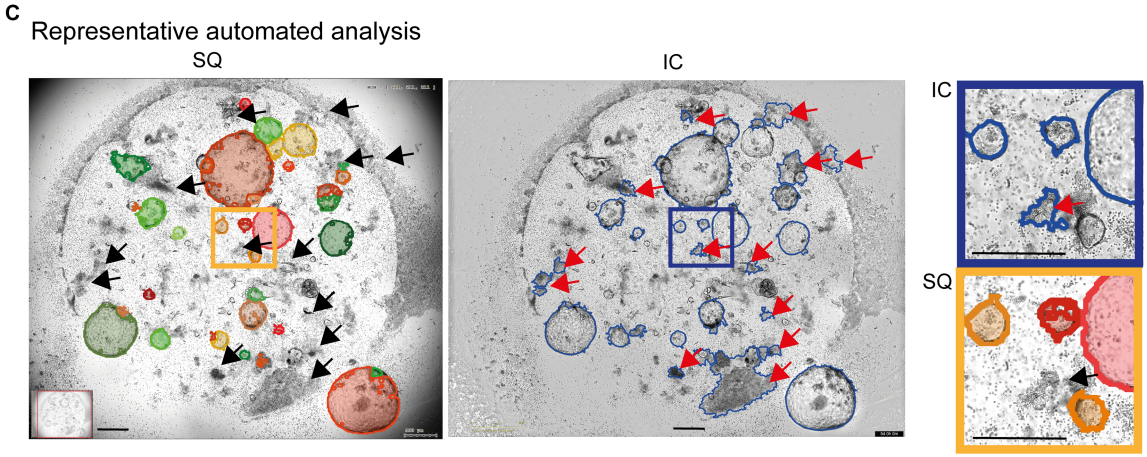

FIGURE 6
Comparison of automated organoid detection applications. **(A)** The total number of organoids determined by the StrataQuest Organoid App (SQ; orange lines; plus, EGF solid, w/o EGF dotted) and Incucyte® (blue lines; plus EGF solid, w/o EGF dotted) is shown. The median from quadruplicates of $n = 3$ different donors plus the 95% confidence interval is depicted. **(B)** The Šídák's multiple comparisons test highlights the statistical data of selected samples. **(C)** Representative analysis (day 5 w/o EGF) are shown. Left: StrataQuest-supported Organoid App (black arrows highlight correct exclusion of organoid- mimicking contours). Middle: Incucyte® analysis (red arrows highlight wrong detection of organoid-mimicking contours). Right: Inserts with higher amplification are depicted. The bars represent 500 µm.

functions of the original organ *in vivo* is ongoing (37, 38). Although organoid systems are limited in their ability to mimic the properties of complex *in vivo* tissues relevant to physiological or pathological processes in tissues, organoid cultures are still useful tools for studying fundamental mechanistic questions (39). Healthy and pathologically altered tissues, however, are composed of different cell types. Therefore, adding tissue-specific stromal or immune cells to organoid cultures may improve the physiological context of organoid development. Developing multicellular organoid models that better represent *in vivo* micro-environments is still challenging, but progress is already evident (39–42).

In addition to the complexity of the multicellular organoid model system itself, the strength of the analytic data is influenced by the image quality and structural diversity of the acquired objects. Even when image quality is excellent, the subsequent processing is still limited by other factors such as contour mimicry, fusion, and superposition of structures. These artifacts may result in the incorrect identification of organoid structures causing false negative or false positive data and therefore low values of recall and precision. Consequently, it is crucial to display organoid boundaries with maximum contrast to achieve clear visual delineation, which can be accomplished with our newly developed Organoid App.

Although machine learning classifiers are highly sophisticated, technical limits remain. We do not believe that any currently available algorithm will accurately detect 100% of the target structures since optical structure recognition involves the analysis and interpretation of visual data. While significant progress has been made in the fields of computer vision and image processing, achieving "100% accuracy" in optical structure detection remains a theoretical ideal rather than a practical expectation.

Several challenges hinder the achievement of perfect accuracy in optical structure detection. Artifacts and variability within optical data, caused by imaging conditions like illumination or sensor limitations, can lead to significant detection errors. Complex and overlapping optical patterns and structures make an accurate detection difficult, potentially resulting in incorrect outcomes. Algorithm limitations also pose challenges, as diverse algorithms have individual strengths and weaknesses and may not cover all scenarios effectively.

Additionally, human subjectivity in defining and recognizing optical structures introduces variability due to differences in expert criteria for setting detection thresholds.

Despite this technical hurdle, our data demonstrates that the Organoid App can accurately detect organoids in co-cultures. This was achieved by separating the organoid structures from the other contaminating structures such as immune cells and imaging artifacts. Even though the Organoid App occasionally fails to correctly recognize a minority of overlapping structures, most of them are detected correctly. In contrast to other software solutions such as Incucyte® or OrganoSeg, we were able to precisely detect organoids in co-cultures with immune cells for the first time. Therefore, we utilized the Organoid App to examine organoid growth under varying conditions. In this context, we questioned whether the Organoid App is able to highlight differences regarding the growth of organoids under the given co-culture conditions.

The term "growth of organoids" can be used to either address the numerical expansion of organoid structures, or the increase in size of a single organoid. Organoids are usually derived from progenitor cells which have the potential to differentiate into complex and self-organized structures (7, 43, 44). Exactly these early multicellular organoid precursors may be different in terms of their potential for organoid formation and subsequent growth. Accordingly, it can be assumed that the growth of individual organoids is determined by their cellular composition and the ability of the respective precursor cells to form organoids (2). Thus, the number of detected organoids can reflect the potential of organoid precursors to replicate and to survive under the given conditions. The increase in organoid size indicates the potential of organoid associated cells to replicate. In order to make a statement about organoid growth, both parameters should be taken into account. It is quite possible that the number of organoids can increase without an expansion in size. To confirm or exclude heterogeneity in organoid growth, it is also necessary to consider the parameter of individual organoid sizes within the co-culture. Various organoid-associated parameters, such as quantity, average size, and individual size, and compactness might therefore offer a promising approach for a more detailed characterization of organoid development within culture conditions.

Due to these facts, we evaluated time-lapse images of organoid co-cultures with immune cells in order to determine the effect of the growth factor EGF on organoid development. Based on the data we have generated with the Organoid App, we can conclude that organoids can be formed and detected under the given culture conditions. However, EGF is capable of suppressing organoid growth within the selected culture conditions. While the effect of EGF on ECO differentiation and growth has not been analyzed yet, there are a variety of reports on the use of EGF for organoid differentiation in the absence of differentiated immune cells (27, 33–36). Our results show that the combination of immune cells and EGF results in a reduced expansion of organoids within the co-culture. In this context, it is noticeable that the total number of organoids with a distinct size is reduced. This suggests that certain organoids are still able to grow effectively in the presence of EGF. The increase in organoid size could be due to increased cell-proliferation within the organoid bodies and/or accumulation of extracellular matrix components within the organoid structures. Thus, it can be assumed that individual organoids react differently to EGF. This effect might be explained by the fact that the composition of organoids regarding stem cells and other cell subsets is not homogeneous. While we could detect an increase in organoid size between day 2 and 5, regardless of the presence of EGF, the size of individual organoids was increased slightly in the presence of EGF on day 2 but not on day 5. In addition, we evaluated the compactness of the organoids in culture and found a reduction of compactness on day 5 compared to day 2, independent of the presence of EGF. This is an indication of a possible transformation to less "circular" organoids.

The initial pilot experiment studying the effects of EGF on organoid development in co-cultures with immune cells yielded these primary results. EGF shows a detrimental impact on individual organoids over the culturing period, leading to a decrease in the number of organoids of certain sizes. However, despite this reduction, certain organoids within the co-culture exhibit an increase in size when exposed to EGF. Hence, EGF appears to impact the early-stage organoid development in co-culture with $CD8^+$ effector T cells, leading to a reduced proportion of organoids capable of growth under specific immune cell culture conditions. It is known that conventional human T lymphocytes do not express the EGFR (45). However, distinct differentiated T-cell subsets such as regulatory T cells, can express the EGFR and benefit from other EGFR ligands such as amphiregulin (46, 47). The expression of EGFR by T cells that are in close proximity to organoids, as well as their potential role in regulating EGF-dependent organoid formation, remains unknown and warrants further investigation.

In summary, our presented high-throughput imaging solution offers great potential for further analysis and detection of organoids within co-culture systems. The Organoid App can be helpful in the development of innovative diagnostic and therapeutic strategies by enabling the study of organoids in the presence of human immune cells and exogenous substances such as drugs or cytokines.

Data availability statement

The original contributions presented in the study are included in the article/Supplementary material, further inquiries can be directed to the corresponding author.

Ethics statement

The studies involving human samples were approved by Ethical committee (Regensburg University). Organoids: Regensburg University, reference number reference number 16-101-5-101. CD8 T cells: Regensburg University, reference number 13-0240-101 and 19-1414-101. The studies were conducted in accordance with the local legislation and institutional requirements. The participants provided their written informed consent to participate in this study.

Author contributions

PS: Methodology, Software, Visualization, Writing – review & editing. BN: Data curation, Formal analysis, Investigation, Methodology, Software, Validation, Writing – review & editing. SH: Data curation, Formal analysis, Writing – review & editing. MW: Methodology, Software, Writing – review & editing. MF: Methodology,

Software, Writing – review & editing. HJ: Funding acquisition, Writing – review & editing. EE: Validation, Writing – review & editing. BL: Methodology, Software, Writing – review & editing. SL: Methodology, Software, Writing – review & editing. UR: Conceptualization, Data curation, Formal analysis, Investigation, Methodology, Software, Supervision, Validation, Visualization, Writing – original draft, Writing – review & editing.

Funding

The author(s) declare financial support was received for the research, authorship, and/or publication of this article. This work was supported by the Else-Kröner-Fresenius Stiftung 2020_EKEA.110 to HJ and the Bavarian Research Network (bayresq.net; Bavarian State Ministry for Science and the Arts) to MF and UR.

Acknowledgments

We thank Lydia Schneider (Department of Surgery, University Hospital Regensburg) for technical support. Lisa Schmidleithner (Department for Immunology, LIT-Leibniz Institute for Immunotherapy, Universitätsklinikum Regensburg Franz-Josef-Strauß-Allee 11, 93053 Regensburg) for critical reading and improving of the manuscript. Icons in the figures have been created with BioRender.com.

Conflict of interest

BL and SL were employed by TissueGnostics GmbH. UR acts as a scientific consultant for the company TissueGnostics.

The remaining authors declare that the research was conducted in the absence of any commercial or financial relationships that could be construed as a potential conflict of interest.

The author(s) declared that they were an editorial board member of Frontiers, at the time of submission. This had no impact on the peer review process and the final decision.

Publisher's note

Supplementary material

The Supplementary material for this article can be found online at: https://www.frontiersin.org/articles/10.3389/fmed.2023.1274482/full#supplementary-material

References

1. Abdul L, Xu J, Sotra A, Chaudary A, Gao J, Rajasekar S, et al. D-Crypto: deep learning-based analysis of Colon organoid morphology from Brightfield images. *Lab Chip*. (2022) 22:4118–28. doi: 10.1039/d2lc00596d

2. Lancaster MA, Knoblich JA. Organogenesis in a dish: modeling development and disease using organoid technologies. *Science*. (2014) 345, 345:1247125. doi: 10.1126/science.1247125

3. Bar-Ephraim YE, Kretzschmar K, Clevers H. Organoids in immunological research. *Nat Rev Immunol*. (2020) 20:279–93. doi: 10.1038/s41577-019-0248-y

4. Sato T, Clevers H. Growing self-organizing Mini-guts from a single intestinal stem cell: mechanism and applications. *Science*. (2013) 340:1190–4. doi: 10.1126/science.1234852

5. Wells JM, Spence JR. How to make an intestine. *Development*. (2014) 141:752–60. doi: 10.1242/dev.097386

6. Huch M, Gehart H, van Boxtel R, Hamer K, Blokzijl F, Verstegen MM, et al. Long-term culture of genome-stable Bipotent stem cells from adult human liver. *Cells*. (2015) 160, 160:299–312. doi: 10.1016/j.cell.2014.11.050

7. Huch M, Koo BK. Modeling mouse and human development using organoid cultures. *Development*. (2015) 142:3113–25. doi: 10.1242/dev.118570

8. Sullivan KM, Ko E, Kim EM, Ballance WC, Ito JD, Chalifoux M, et al. Extracellular microenvironmental control for organoid assembly. *Tissue Eng Part B Rev*. (2022) 28:1209–22. Epub 20220621. doi: 10.1089/ten.TEB.2021.0186

9. Drost J, van Jaarsveld RH, Ponsioen B, Zimberlin C, van Boxtel R, Buijs A, et al. Sequential Cancer mutations in cultured human intestinal stem cells. *Nature*. (2015) 521, 521:43–7. doi: 10.1038/nature14415

10. Dijkstra KK, Cattaneo CM, Weeber F, Chalabi M, van de Haar J, Fanchi LF, et al. Generation of tumor-reactive T cells by co-culture of peripheral blood lymphocytes and tumor organoids. *Cells*. (2018) 174:1586–1598.e12. doi: 10.1016/j.cell.2018.07.009

11. Schnalzger TE, de Groot MH, Zhang C, Mosa MH, Michels BE, Roder J, et al. 3d model for Car-mediated cytotoxicity using patient-derived colorectal Cancer organoids. *EMBO J*. (2019) 38:928. doi: 10.15252/embj.2018100928

12. Kong JCH, Guerra GR, Millen RM, Roth S, Xu H, Neeson PJ, et al. Tumor-infiltrating lymphocyte function predicts response to neoadjuvant Chemoradiotherapy in locally advanced rectal Cancer. *JCO Precis Oncol*. (2018) 2:1–15. doi: 10.1200/PO.18.00075

13. Chakrabarti J, Holokai L, Syu L, Steele NG, Chang J, Wang J, et al. Hedgehog signaling induces Pd-L1 expression and tumor cell proliferation in gastric Cancer. *Oncotarget*. (2018) 9:37439–57. doi: 10.18632/oncotarget.26473

14. Rogoz A, Reis BS, Karssemeijer RA, Mucida D. A 3-D Enteroid-based model to study T-cell and epithelial cell interaction. *J Immunol Methods*. (2015) 421:89–95. doi: 10.1016/j.jim.2015.03.014

15. Schreurs R, Baumdick ME, Sagebiel AF, Kaufmann M, Mokry M, Klarenbeek PL, et al. Human fetal Tnf-alpha-cytokine-producing Cd4(+) effector memory T cells promote intestinal development and mediate inflammation early in life. *Immunity*. (2019) 50:462–476.e8. doi: 10.1016/j.immuni.2018.12.010

16. Schreurs R, Baumdick ME, Drewniak A, Bunders MJ. *In vitro* co-culture of human intestinal organoids and Lamina Propria-derived Cd4(+) T cells. *STAR Protoc*. (2021) 2:100519. doi: 10.1016/j.xpro.2021.100519

17. Takashima S, Martin ML, Jansen SA, Fu Y, Bos J, Chandra D, et al. T cell-derived interferon-gamma programs stem cell death in immune-mediated intestinal damage. *Sci Immunol*. (2019) 4:8556. doi: 10.1126/sciimmunol.aay8556

18. Biton M, Haber AL, Rogel N, Burgin G, Beyaz S, Schnell A, et al. T helper cell cytokines modulate intestinal stem cell renewal and differentiation. *Cells*. (2018) 175:1307–1320.e22. doi: 10.1016/j.cell.2018.10.008

19. Fei K, Zhang J, Yuan J, Xiao P. Present application and perspectives of organoid imaging technology. *Bioengineering (Basel)*. (2022) 9:30121. doi: 10.3390/bioengineering9030121

20. Kozlowski MT, Crook CJ, Ku HT. Towards organoid culture without Matrigel. *Commun Biol*. (2021) 4:1387. doi: 10.1038/s42003-021-02910-8

21. Bian X, Li G, Wang C, Liu W, Lin X, Chen Z, et al. A deep learning model for detection and tracking in high-throughput images of organoid. *Comput Biol Med*. (2021) 134:104490. doi: 10.1016/j.compbiomed.2021.104490

22. Borten MA, Bajikar SS, Sasaki N, Clevers H, Janes KA. Automated Brightfield morphometry of 3d organoid populations by Organoseg. *Sci Rep*. (2018) 8:5319. doi: 10.1038/s41598-017-18815-8

23. Kassis T, Hernandez-Gordillo V, Langer R, Griffith LG. Orgaquant: human intestinal organoid localization and quantification using deep convolutional neural networks. *Sci Rep*. (2019) 9:48874. doi: 10.1038/s41598-019-48874-y

24. Kok RNU, Hebert L, Huelsz-Prince G, Goos YJ, Zheng X, Bozek K, et al. Organoidtracker: efficient cell tracking using machine learning and manual error correction. *PLoS One*. (2020) 15:e0240802. doi: 10.1371/journal.pone.0240802

25. Matthews JM, Schuster B, Kashaf SS, Liu P, Ben-Yishay R, Ishay-Ronen D, et al. Organoid: a versatile deep learning platform for tracking and analysis of single-organoid dynamics. *PLoS Comput Biol*. (2022) 18:e1010584. doi: 10.1371/journal.pcbi.1010584

26. Sampaziotis F, Justin AW, Tysoe OC, Sawiak S, Godfrey EM, Upponi SS, et al. Reconstruction of the mouse extrahepatic biliary tree using primary human extrahepatic Cholangiocyte organoids. *Nat Med*. (2017) 23:954–63. doi: 10.1038/nm.4360

27. Sampaziotis F, Muraro D, Tysoe OC, Sawiak S, Beach TE, Godfrey EM, et al. Cholangiocyte organoids can repair bile ducts after transplantation in the human liver. *Science*. (2021) 371:839–46. doi: 10.1126/science.aaz6964

28. Lab J. (2022). Bortenma_Organoseg. Available at: https://github.com/JanesLab/OrganoSeg.git

29. Olson L, Delen D. *Advanced data mining techniques. 1st* ed. Berlin: Springer (2008). 180 p.

30. Haider S, Beristain AG. Human organoid systems in modeling reproductive tissue development, function, and disease. *Hum Reprod*. (2023):20230429. doi: 10.1093/humrep/dead085

31. Betge J, Jackstadt R. From organoids to bedside: advances in modeling, decoding and targeting of colorectal Cancer. *Int J Cancer*. (2023) 152:1304–13. doi: 10.1002/ijc.34297

32. Ganguly K, Bhatia R, Rauth S, Kisling A, Atri P, Thompson C, et al. Mucin 5ac serves as the Nexus for Beta-catenin/C-Myc interplay to promote glutamine dependency during pancreatic Cancer Chemoresistance. *Gastroenterology*. (2022) 162:253–268.e13. doi: 10.1053/j.gastro.2021.09.017

33. Michalopoulos GK, Bowen WC, Mule K, Stolz DB. Histological organization in hepatocyte organoid cultures. *Am J Pathol*. (2001) 159:1877–87. doi: 10.1016/S0002-9440(10)63034-9

34. Abud HE, Watson N, Heath JK. Growth of intestinal epithelium in organ culture is dependent on Egf signalling. *Exp Cell Res*. (2005) 303:252–62. doi: 10.1016/j.yexcr.2004.10.006

35. Michalopoulos GK, Bowen WC, Mule K, Luo J. Hgf-, Egf-, and dexamethasone-induced gene expression patterns during formation of tissue in hepatic organoid cultures. *Gene Expr*. (2003) 11:55–75. doi: 10.3727/000000003108748964

36. Amarachintha SP, Mourya R, Ayabe H, Yang L, Luo Z, Li X, et al. Biliary organoids uncover delayed epithelial development and barrier function in biliary atresia. *Hepatology*. (2022) 75:89–103. doi: 10.1002/hep.32107

37. Yan HHN, Chan AS, Lai FP, Leung SY. Organoid cultures for Cancer modeling. *Cell Stem Cell*. (2023) 30:917–37. doi: 10.1016/j.stem.2023.05.012

38. Sang Y, Miller LC, Nelli RK, Gimenez-Lirola LG. Harness organoid models for Virological studies in animals: a cross-species perspective. *Front Microbiol*. (2021) 12:725074. doi: 10.3389/fmicb.2021.725074

39. Zhao Z, Chen X, Dowbaj AM, Sljukic A, Bratlie K, Lin L, et al. Organoids. *Nat Rev Methods Primers*. (2022) 2:174. doi: 10.1038/s43586-022-00174-y

40. Sun CP, Lan HR, Fang XL, Yang XY, Jin KT. Organoid models for precision Cancer immunotherapy. *Front Immunol*. (2022) 13:770465. doi: 10.3389/fimmu.2022.770465

41. Mackenzie NJ, Nicholls C, Templeton AR, Perera MP, Jeffery PL, Zimmermann K, et al. Modelling the tumor immune microenvironment for precision immunotherapy. *Clin Transl Immunology*. (2022) 11:e1400. doi: 10.1002/cti2.1400

42. Sabapathy V, Costlow G, Venkatadri R, Dogan M, Kumar S, Sharma R. Advances and challenges in kidney organoids. *Curr Stem Cell Res Ther*. (2022) 17:226–36. doi: 10.2174/1574888X16666210804113626

43. Simian M, Bissell MJ. Organoids: a historical perspective of thinking in three dimensions. *J Cell Biol*. (2017) 216:31–40. doi: 10.1083/jcb.201610056

44. Reis RL. 2nd consensus conference on definitions on biomaterials science. *J Tissue Eng Regen Med*. (2020) 14:561–2. doi: 10.1002/term.3016

45. Lozano T, Chocarro S, Martin C, Lasarte-Cia A, Del Valle C, Gorraiz M, et al. Genetic modification of Cd8(+) T cells to express Egfr: potential application for adoptive T cell therapies. *Front Immunol*. (2019) 10:2990. doi: 10.3389/fimmu.2019.02990

46. Zaiss DM, van Loosdregt J, Gorlani A, Bekker CP, Grone A, Sibilia M, et al. Amphiregulin enhances regulatory T cell-suppressive function via the epidermal growth factor receptor. *Immunity*. (2013) 38:275–84. doi: 10.1016/j.immuni.2012.09.023

47. Wang S, Zhang Y, Wang Y, Ye P, Li J, Li H, et al. Amphiregulin confers regulatory T cell suppressive function and tumor invasion via the Egfr/Gsk-3beta/Foxp3 Axis. *J Biol Chem*. (2016) 291:21085–95. doi: 10.1074/jbc.M116.717892

Frontiers in Medicine

Translating medical research and innovation into improved patient care

A multidisciplinary journal which advances our medical knowledge. It supports the translation of scientific advances into new therapies and diagnostic tools that will improve patient care.

Discover the latest Research Topics

See more →

Frontiers

Avenue du Tribunal-Fédéral 34
1005 Lausanne, Switzerland
frontiersin.org

Contact us

+41 (0)21 510 17 00
frontiersin.org/about/contact